

# Carbon Nanomaterials and Related Nanostructures: Synthesis, Characterization, and Application

Guest Editors: Jinlong Jiang, Jun Yang, Jian Lin, Zhenghong Huang, and S. C. Wang





---

# **Carbon Nanomaterials and Related Nanostructures: Synthesis, Characterization, and Application**

Journal of Nanomaterials

---

**Carbon Nanomaterials and Related  
Nanostructures: Synthesis, Characterization,  
and Application**

Guest Editors: Jinlong Jiang, Jun Yang, Jian Lin,  
Zhenghong Huang, and S. C. Wang



---

Copyright © 2014 Hindawi Publishing Corporation. All rights reserved.

This is a special issue published in "Journal of Nanomaterials." All articles are open access articles distributed under the Creative Commons Attribution License, which permits unrestricted use, distribution, and reproduction in any medium, provided the original work is properly cited.

## Editorial Board

Katerina E. Aifantis, Greece  
Nageh K. Allam, USA  
Margarida Amaral, Portugal  
Xuedong Bai, China  
Lavinia Balan, France  
Enrico Bergamaschi, Italy  
Theodorian Borca-Tasciuc, USA  
C. Jeffrey Brinker, USA  
Christian Brosseau, France  
Xuebo Cao, China  
Shafiq Chowdhury, USA  
Kwang-Leong Choy, UK  
Cui ChunXiang, China  
M. A. Correa-Duarte, Spain  
Shadi A. Dayeh, USA  
Claude Estourns, France  
Alan Fuchs, USA  
Lian Gao, China  
Russell E. Gorga, USA  
Hongchen Chen Gu, China  
Mustafa O. Guler, Turkey  
John Zhanhu Guo, USA  
Smrati Gupta, Germany  
Michael Harris, USA  
Zhongkui Hong, China  
Michael Hu, USA  
David Hui, USA  
Y.-K. Jeong, Republic of Korea  
Sheng-Rui Jian, Taiwan  
Wanqin Jin, China  
Rakesh K. Joshi, UK  
Zhenhui Kang, China  
Fathallah Karimzadeh, Iran  
Alireza Khataee, Iran  
Do Kyung Kim, Republic of Korea

Alan K. T. Lau, Hong Kong  
Burtrand Lee, USA  
Benxia Li, China  
Jun Li, Singapore  
Xing-Jie Liang, China  
Shijun Liao, China  
Gong Ru Lin, Taiwan  
J. -Y. Liu, USA  
Tianxi Liu, China  
Songwei Lu, USA  
Daniel Lu, China  
Jue Lu, USA  
Ed Ma, USA  
Gaurav Mago, USA  
Santanu K. Maiti, India  
Sanjay R. Mathur, Germany  
Vikas Mittal, United Arab Emirates  
Weihai Ni, Germany  
Sherine Obare, USA  
Atsuto Okamoto, Japan  
Abdelwahab Omri, Canada  
Edward Andrew Payzant, USA  
Kui-Qing Peng, China  
Anukorn Phuruangrat, Thailand  
Mahendra Rai, India  
Suprakas Sinha Ray, South Africa  
Ugur Serincan, Turkey  
Huaiyu Shao, Japan  
Donglu Shi, USA  
Vladimir Sivakov, Germany  
Marinella Striccoli, Italy  
Bohua Sun, South Africa  
Saikat Talapatra, USA  
Nairong Tao, China  
Titipun Thongtem, Thailand

Somchai Thongtem, Thailand  
Alexander Tolmachev, Ukraine  
Valeri P. Tolstoy, Russia  
Tsungh-Yen Tsai, Taiwan  
Takuya Tsuzuki, Australia  
Raquel Verdejo, Spain  
Mat U. Wahit, Malaysia  
Shiren Wang, USA  
Yong Wang, USA  
Ruiping Wang, Canada  
Cheng Wang, China  
Zhenbo Wang, China  
Jinquan Wei, China  
Ching-Ping Wong, Hong Kong  
Xingcai Wu, China  
Guodong Xia, Hong Kong  
Zhi Li Xiao, USA  
Ping Xiao, UK  
Shuangxi Xing, China  
Yangchuan Xing, USA  
N. Xu, China  
Doron Yadlovker, Israel  
Yingkui Yang, China  
Khaled Youssef, USA  
Kui Yu, Canada  
William W. Yu, USA  
Haibo Zeng, China  
Tianyou Zhai, Japan  
Renyun Zhang, Sweden  
Bin Zhang, China  
Yanbao Zhao, China  
Lianxi Zheng, Singapore  
Chunyi Zhi, Hong Kong

# Contents

**Carbon Nanomaterials and Related Nanostructures: Synthesis, Characterization, and Application,**

Jinlong Jiang, Jun Yang, Jian Lin, Zhenghong Huang, and S. C. Wang

Volume 2014, Article ID 319165, 1 page

**Transparent Electrodes with Nanotubes and Graphene for Printed Optoelectronic Applications,**

Marcin Słoma, Grzegorz Wróblewski, Daniel Janczak, and Małgorzata Jakubowska

Volume 2014, Article ID 143094, 7 pages

**Influence of 1D and 2D Carbon Fillers and Their Functionalisation on Crystallisation and Thermomechanical Properties of Injection Moulded Nylon 6,6 Nanocomposites,** Fabiola Navarro-Pardo, Ana L. Martínez-Hernández, Victor M. Castaño, José L. Rivera-Armenta, Francisco J. Medellín-Rodríguez, Gonzalo Martínez-Barrera, and Carlos Velasco-Santos

Volume 2014, Article ID 670261, 13 pages

**First-Principle Study of H<sub>2</sub> Adsorption on LaFeO<sub>3</sub> (110) Surface,** Yu-Hong Chen, Bing-Wen Zhang,

Liang Yang, Mei-Ling Zhang, Cai-Rong Zhang, Long Kang, and Yong-Chun Luo

Volume 2014, Article ID 758985, 8 pages

**Single- and Multiwalled Carbon Nanotubes with Phosphorus Based Flame Retardants for Textiles,**

D. Wesolek and W. Gieparda

Volume 2014, Article ID 727494, 6 pages

**Application of Multiwalled Carbon Nanotube Nanofluid for 450 W LED Floodlight,** Bui Hung Thang,

Le Dinh Quang, Nguyen Manh Hong, Phan Hong Khoi, and Phan Ngoc Minh

Volume 2014, Article ID 347909, 6 pages

**Preparation and Application of Conductive Textile Coatings Filled with Honeycomb Structured Carbon Nanotubes,** Filip Govaert and Myriam Vanneste

Volume 2014, Article ID 651265, 6 pages

**Improved Efficiency of Graphene/Si Heterojunction Solar Cells by Optimizing Hydrocarbon Feed Rate,**

Zexia Zhang, Tongxiang Cui, Ruitao Lv, Hongwei Zhu, Kunlin Wang, Dehai Wu, and Feiyu Kang

Volume 2014, Article ID 359305, 7 pages

**Silicon-Encapsulated Hollow Carbon Nanofiber Networks as Binder-Free Anodes for Lithium Ion Battery,** Ding Nan, Zheng-Hong Huang, Ruitao Lv, Yuxiao Lin, Lu Yang, Xiaoliang Yu, Ling Ye, Wanci Shen, Hongyu Sun, and Feiyu Kang

Volume 2014, Article ID 139639, 10 pages

**An Overview on Structure and Field Emission Properties of Carbon Nitride Films,** Qiong Wang and Jinlong Jiang

Volume 2014, Article ID 203837, 8 pages

**Study on the Microstructure and Electrical Properties of Boron and Sulfur Codoped Diamond Films Deposited Using Chemical Vapor Deposition,** Zhang Jing, Li Rongbin, Wang Xianghu, and Wei Xicheng

Volume 2014, Article ID 109869, 7 pages

**Microstructure Changes of Ti-Al-C Films Deposited by Filtered Cathodic Vacuum Arc**, Xianjuan Pang, Xiaoqiang Liu, and Bo Jin  
Volume 2014, Article ID 286484, 6 pages

**Nanopolycrystalline Diamond Sintered from Onion-Like Carbon**, Qin Zou, Ming-Zhi Wang, Wen Gong, Qiang-Hua Yu, Yan-Guo Li, and Yu-Cheng Zhao  
Volume 2014, Article ID 271494, 8 pages

**Tribological Performance and Lubrication Mechanism of Alkylimidazolium Dialkyl Phosphates Ionic Liquids as Lubricants for  $\text{Si}_3\text{N}_4$ - $\text{Ti}_3\text{SiC}_2$  Contacts**, Hai-zhong Wang, Dan Qiao, Song-wei Zhang, Da-peng Feng, and Jin-jun Lu  
Volume 2014, Article ID 548658, 8 pages

**Tribological Performance of Silahydrocarbons Used as Steel-Steel Lubricants under Vacuum and Atmospheric Pressure**, Hai-Zhong Wang, Song-Wei Zhang, Dan Qiao, Da-Peng Feng, and Wei-Min Liu  
Volume 2014, Article ID 852386, 8 pages

**The Long-Term Fate and Toxicity of PEG-Modified Single-Walled Carbon Nanotube Isoliquiritigenin Delivery Vehicles in Rats**, Bo Han, Mingming Zhang, Ting Tang, Qiusheng Zheng, Keyu Wang, Le Li, and Wen Chen  
Volume 2014, Article ID 257391, 8 pages

**Asymmetric Electrodes Constructed with PAN-Based Activated Carbon Fiber in Capacitive Deionization**, Mingzhe Li, Yingzhi Chen, Zheng-Hong Huang, and Feiyu Kang  
Volume 2014, Article ID 204172, 6 pages

**Carbon Nanofibers from Carbon Nanotubes by 1.2 keV  $\text{Ar}^+$  Sputtering at Room Temperature**, Shuang-Xi Xue, Qin-Tao Li, Xian-Rui Zhao, Qin-Yi Shi, Zhi-Gang Li, and Yan-Ping Liu  
Volume 2014, Article ID 313095, 5 pages

**Synthesis, Characterization, and Tribological Behavior of Oleic Acid Capped Graphene Oxide**, Tiedan Chen, Yanqiu Xia, Zhengfeng Jia, Zhilu Liu, and Haobo Zhang  
Volume 2014, Article ID 654145, 8 pages

**3D Hollow Sn@Carbon-Graphene Hybrid Material as Promising Anode for Lithium-Ion Batteries**, Xiaoyu Zheng, Wei Lv, Yan-Bing He, Chen Zhang, Wei Wei, Ying Tao, Baohua Li, and Quan-Hong Yang  
Volume 2014, Article ID 974285, 6 pages

**Electronic Structures and Optical Properties of Phenyl  $\text{C}_{71}$  Butyric Acid Methyl Esters**, Cai-Rong Zhang, Li-Heng Han, Jian-Wu Zhe, Neng-Zhi Jin, Yu-Lin Shen, Li-Hua Yuan, You-Zhi Wu, and Zi-Jiang Liu  
Volume 2013, Article ID 612153, 8 pages

**Preparation of  $\text{BiFeO}_3$ -Graphene Nanocomposites and Their Enhanced Photocatalytic Activities**, J. F. Dai, T. Xian, L. J. Di, and H. Yang  
Volume 2013, Article ID 642897, 5 pages

## Editorial

# Carbon Nanomaterials and Related Nanostructures: Synthesis, Characterization, and Application

**Jinlong Jiang,<sup>1</sup> Jun Yang,<sup>2</sup> Jian Lin,<sup>3</sup> Zhenghong Huang,<sup>4</sup> and S. C. Wang<sup>5</sup>**

<sup>1</sup> Department of Physics, Lanzhou University of Technology, Lanzhou 730050, China

<sup>2</sup> State Key Laboratory of Solid Lubrication, Lanzhou Institute of Chemical Physics, Chinese Academy of Sciences, Lanzhou 730000, China

<sup>3</sup> Department of Mechanical Engineering & Materials Science, Rice University, Houston, TX 77005, USA

<sup>4</sup> School of Materials Science and Engineering, Tsinghua University, Beijing 100084, China

<sup>5</sup> National Centre for Advanced Tribology at Southampton, University of Southampton, Southampton SO17 1BJ, UK

Correspondence should be addressed to Jinlong Jiang; [jinlong@lut.cn](mailto:jinlong@lut.cn)

Received 24 July 2014; Accepted 24 July 2014; Published 31 August 2014

Copyright © 2014 Jinlong Jiang et al. This is an open access article distributed under the Creative Commons Attribution License, which permits unrestricted use, distribution, and reproduction in any medium, provided the original work is properly cited.

Since the discovery of buckyballs in 1985, the family of carbon materials has been rapidly growing. From zero-dimensional (0D) fullerene, 1D carbon nanotubes (CNTs), and recent 2D graphene to traditional 3D nanoporous carbon and nanodiamond, carbon nanomaterials exhibit a variety of structures and forms due to the existence of three hybridization forms, namely,  $sp^3$ ,  $sp^2$ , and  $sp^1$ , of carbon atoms.

In recent years, they have increasingly gained interests from both scientific and industrial communities due to the unique physical and chemical properties. They show diverse potential applications in structure, electronics, energy, environment, water, and others. The purpose of this special issue is to report some latest research results on synthesis, characterization, and applications of carbon nanomaterials and related nanostructures. The accepted papers cover various carbon materials, namely, CNTs, graphene, carbon nanofibers, nanodiamonds, amorphous carbon films, carbon nanocomposite, graphite-like layered materials, and so on. These papers cover a wide range of topics related to synthesis and applications of these carbon nanomaterials in mechanics and tribology, thermal management, energy conversion (photoelectronic devices, solar cells, and photocatalysis), energy storage (lithium-ion batteries), and drug delivery fields. Moreover, two papers present theoretical calculation of carbon nanomaterials in electronic, optical, and surface adsorption properties using density functional theory.

The guest editors hope that this special issue will be of great interest to readers.

## Acknowledgments

We would like to thank all the authors for their contributions to this special issue as well as the reviewers for their constructive comments to the manuscripts. We also want to express our sincere thanks to the editorial board members of Journal of Nanomaterials for the support and help in preparation of this special issue.

Jinlong Jiang  
Jun Yang  
Jian Lin  
Zhenghong Huang  
S. C. Wang

## Research Article

# Transparent Electrodes with Nanotubes and Graphene for Printed Optoelectronic Applications

Marcin Słoma,<sup>1,2</sup> Grzegorz Wróblewski,<sup>1</sup> Daniel Janczak,<sup>1</sup> and Małgorzata Jakubowska<sup>1,2</sup>

<sup>1</sup> *Institute of Metrology and Biomedical Engineering, Faculty of Mechatronics, Warsaw University of Technology, św. A. Boboli 8, 02-525 Warsaw, Poland*

<sup>2</sup> *Institute of Electronic Materials Technology, Wólczyńska 133, 01-919 Warsaw, Poland*

Correspondence should be addressed to Marcin Słoma; [marcin.sloma@mchtr.pw.edu.pl](mailto:marcin.sloma@mchtr.pw.edu.pl)

Received 1 March 2014; Revised 20 June 2014; Accepted 20 June 2014; Published 24 July 2014

Academic Editor: Zheng-Hong Huang

Copyright © 2014 Marcin Słoma et al. This is an open access article distributed under the Creative Commons Attribution License, which permits unrestricted use, distribution, and reproduction in any medium, provided the original work is properly cited.

We report here on printed electroluminescent structures containing transparent electrodes made of carbon nanotubes and graphene nanoplatelets. Screen-printing and spray-coating techniques were employed. Electrodes and structures were examined towards optical parameters using spectrophotometer and irradiation meter. Electromechanical properties of transparent electrodes are exterminated with cyclical bending test. Accelerated aging process was conducted according to EN 62137 standard for reliability tests of electronics. We observed significant negative influence of mechanical bending on sheet resistivity of ITO, while resistivity of nanotube and graphene based electrodes remained stable. Aging process has also negative influence on ITO based structures resulting in delamination of printed layers, while those based on carbon nanomaterials remained intact. We observe negligible changes in irradiation for structures with carbon nanotube electrodes after accelerated aging process. Such materials demonstrate a high application potential in general purpose electroluminescent devices.

## 1. Introduction

Transparent electrodes are used in a variety of applications in modern electronic systems. This includes touch screens [1–5], transparent cathodes for photovoltaics [6–10], window heaters [11–14], electromagnetic shielding [15], or even speakers [16–18]. The most common application is front electrode for almost all types of displays: LCDs, OLEDs, and thick film electroluminescent structures (TFELs) [19–22]. Commonly used materials are transparent conductive oxides (TCO), for example, indium tin oxide (ITO) [23, 24], ZnO [25–27], and antimony thin oxide (ATO) [28–30]. Alternatively metallic electrodes made of Ag nanostructures are introduced [31–33]. In many cases there is an additional need to provide the elasticity of an electrode, where TCOs cannot be implemented because of their low mechanical strength. There are also some other disadvantages of using TCOs like expensive coating technique (sputtering), only effective for mass production, and high sensitivity to harsh environmental conditions which are causing the decrease of

conductivity [34]. Above-mentioned reasons led researchers to alternative materials for transparent conductive layers (TCL) like conductive polymers (PEDOT:PSS) [7, 9] or graphene layers [35–39]. Conjugated polymers are known for their low resistance to environmental factors, like humidity or oxygen [40, 41], and graphene films are produced with CVD method, which still creates problems in mass production of large area electrodes. In this field also other solutions are introduced, like carbon nanotubes [4, 5, 10].

We present fabrication of TFEL structures with the use of elaborated transparent electrodes with oligo walled carbon nanotubes (OWCNTs) and graphene nanoplatelets (GNPs). Structures were subjected to series of experiments: transmittance measurements of electrodes and bending tests for evaluation of resistivity stability, irradiance comparison of structures with different colors of luminophores (orange, blue, and blue-green) and different types of electrodes (ITO, OWCNT, and GNP-CNT), and accelerated aging of electroluminescent structures demonstrating influence on mechanical properties of TCLs.

## 2. Materials and Preparation

TFEL structures were prepared on diverse transparent electrodes deposited on PET foil. ITO on PET was acquired commercially. Composite layers with CNTs, GNPs, and GNP + CNT were coated on PET foil using spray-coating method. Luminophore, dielectric, and silver electrode layers were screen-printed on top of transparent electrodes.

**2.1. Materials.** First type of nanomaterial investigated in research was CCVD grown oligowalled carbon nanotubes, commercially available from Cheap Tubes Inc. (USA). Observed Raman spectra (Figure 1(a)) are typical for multiwalled carbon nanotubes with small diameters. Additional scanning electron microscopy (SEM) observations (Figure 1(b)) allowed confirming assumptions that we have carbon nanotubes of small diameter with length around 10–20  $\mu\text{m}$ , organized in bundles.

Second type of nanomaterial investigated in research was graphene nanoplatelets from the same supplier. Again, Raman analysis indicates that material consists of few layer graphene structures (Figure 2(a)) which was confirmed by scanning electron microscopy observations (Figure 2(b)). Mean diameter of graphene nanoplatelets was in range of 5 to 15  $\mu\text{m}$ . According to supplier GNPs were obtained by chemical method, employing oxidization of graphite with the mixture of  $\text{H}_2\text{SO}_4$ ,  $\text{NaNO}_3$ , and  $\text{KMnO}_4$ , known as Hummer's and Offerman method. Obtained graphene oxide was further exfoliated and reduced by hydrazine.

For elaborated structures, luminophore powders from GTP (USA) were acquired: GG45 High Brite-green, GG25 Super Brite-blue-green, and GG13 High Brite-orange, with mean particle size in range of 20–30  $\mu\text{m}$ . For dielectric compositions barium titanate  $\text{BaTiO}_3$  nanopowder from IAM (Germany) was used. Performed SEM observations and granulometric analysis (Figure 3) showed that the average grain size is 137 nm, though there were also larger grains observed. For metallic electrode commercial silver lacquer L-121 from ITME (Poland) was used.

Final compositions consist of functional filler (CNTs, GNPs, luminophores or dielectric powders) and polymer vehicle. To prepare polymer vehicle poly(methyl methacrylate) (PMMA)  $M_w$  350 000 from Sigma-Aldrich was dissolved in diethylene glycol butyl ether acetate with magnetic mixer for 48 hours at 40°C. Obtained this way 8 wt.% solution of PMMA in solvent was used as vehicle for luminophore and dielectric powders. Spray-coating inks contain 0.02 wt.% solution of PMMA in organic solvent, to achieve desired low viscosity.

**2.2. Preparation.** To obtain final compositions, carbon nanomaterials and luminophore/dielectric powders were dispersed in corresponding polymer vehicles.

Spray-coating CNT and GNP inks were prepared by mixing carbon fillers and polymer vehicle in an ultrasonic bath for 30 min in 25°C. Nanotube ink contained 0.31 wt.% OWCNT in vehicle, and GNP ink contained 0.35 wt.% platelets with additional 0.1 wt.% OWCNT in vehicle.

Luminophore powders (60 wt.%) were mixed with the 8 wt.% PMMA vehicle with pestle and mortar followed by homogenization on three-roll mill to break remaining agglomerates. The dielectric paste consisted of 76.3 wt.%  $\text{BaTiO}_3$  and additional 0.8 wt.% of MALIALM SC-0505K surfactant from NOF Corp. (Japan).

**2.3. Printing.** TFEL structure consists of PET substrate with TCL and three main layers printed on top: luminophore, dielectric, and last metallic electrode. Schematic illustration of such structure is presented in Figure 4.

Transparent electrodes were made using spray-coating method. Airbrush gun with 350  $\mu\text{m}$  nozzle diameter was supplied with compressed air (pressure 0,5 MPa) and spraying was done with 100 mm distance between the nozzle and the PET substrate. Screen-printing was made using polyester screen with density 67 T for luminophore, dielectric, and silver layers. Double dielectric layer was printed to ensure that no electric breakdowns in capacitor structure will take place. Spray-coated and screen-printed layers were cured in a chamber dryer in 125°C for 30 min.

## 3. Experimental

Elaborated TFEL structures are supplied with alternating voltage from HV generator, indicated with peak-to-peak values. Main interest in the conducted experiments was focused on comparison of properties of composite carbon nanomaterials electrodes with ITO. Irradiance measurements from all types of structures were conducted with the same supply parameters, measured with Thorlabs PM100D power meter equipped with S121C sensor. Additionally optical properties measurements of all TCLs were taken in 400–900 nm spectrum on Lambda 40 spectrophotometer from Perkin-Elmer. Sheet resistivity measurements were done with Keithley 2636A dual-channel source measure unit and four-probe method. Mechanical bending tests were performed on specially adapted laboratory stand, with 350 cycles per minute and bending to 0,14  $\text{mm}^{-1}$  curvature. Bent sample was attached from one side to a static fixture and on the other side to a movable grip which caused a warp around symmetry axis. Accelerated aging process was conducted according to EN 62137 standard for reliability tests of electronics in Heraeus HT 7012 S2 thermal shock chamber. The thermal cycle was set to 125°C for upper and –40°C for lower temperatures, respectively, and cycled equally in 1-hour period with 5-second temperature shift. Tests were conducted without additional humidification or addition of aggressive atmospheres.

## 4. Results and Discussion

Printed electroluminescent structures were fully functional and were emitting a color light according to luminophore type. Structures with TCLs filled only with GNPs were not functional, which is related to high sheet resistivity of that TCL (around 1,5  $\text{M}\Omega/\text{sq}$ ). This is significantly higher value than reported from previous experiments [42–44]. Reported

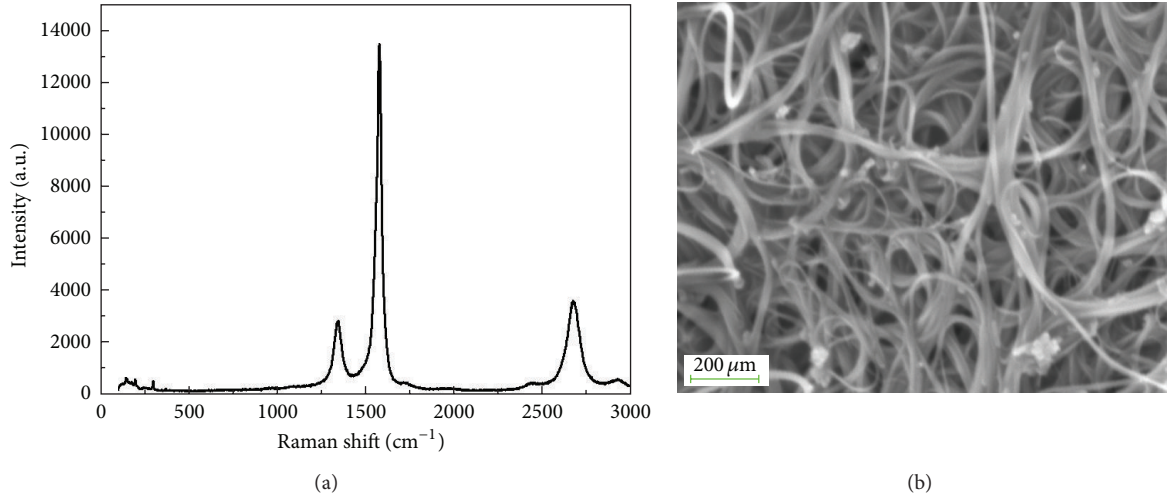


FIGURE 1: (a) Raman spectra and (b) SEM micrograph of OWCNT material.

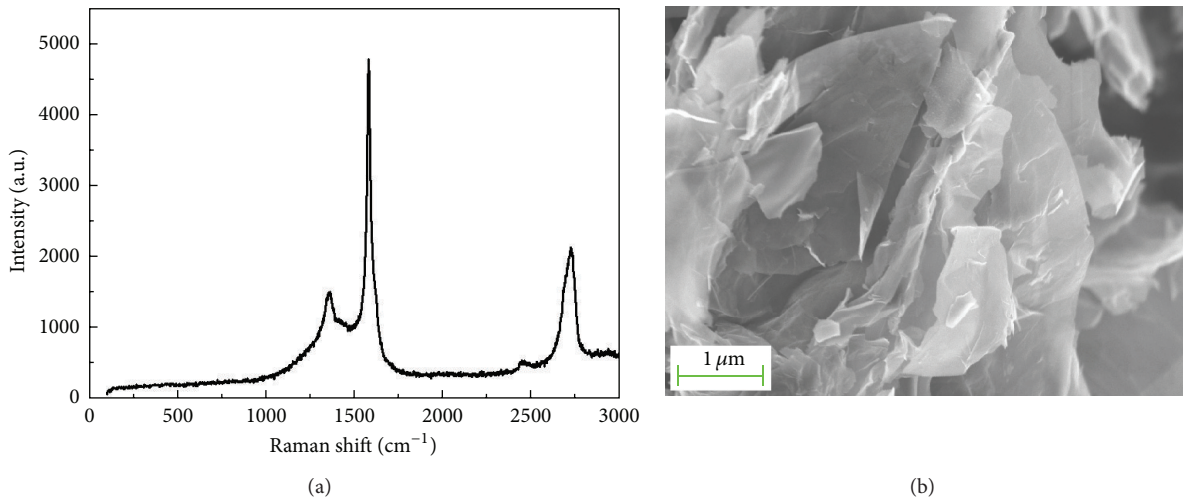


FIGURE 2: (a) Raman spectra and (b) SEM micrograph of GNP material.

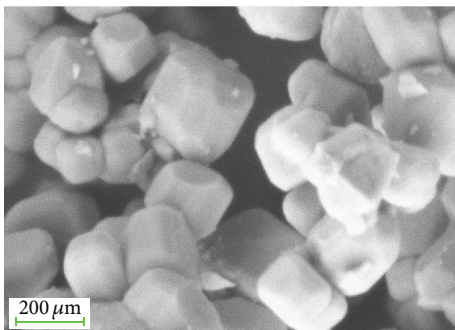


FIGURE 3: SEM micrograph of BaTiO<sub>3</sub> dielectric powder.

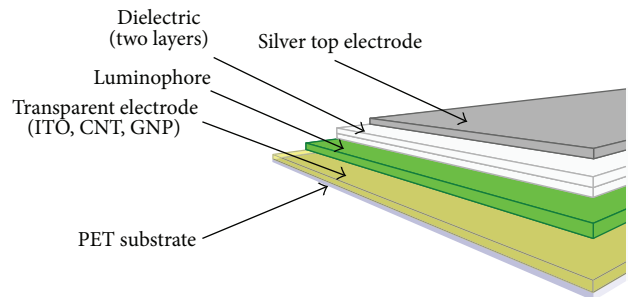


FIGURE 4: Visualization of printed TFEL.

types of layers are generally deposited without additional binder, and while they exhibit resistances below thousands of ohms, they are vulnerable to mechanical factors-peel under scratching or bending-what authors observed in another

experiment with GNP and CNT layers deposited without polymer binder or fired at elevated temperature. From that perspective it is possible to use such layers in encapsulated systems, such as capacitors or rigid solar cells, but they do not meet requirements for elastic electronic applications.



FIGURE 5: Printed electroluminescent structures with three types of TCL (from top): ITO, CNTs, and GNPs + CNTs. Colors (from left): orange, green, and blue-green. Inaccurate color mapping and intensities are related to camera technical restrictions.

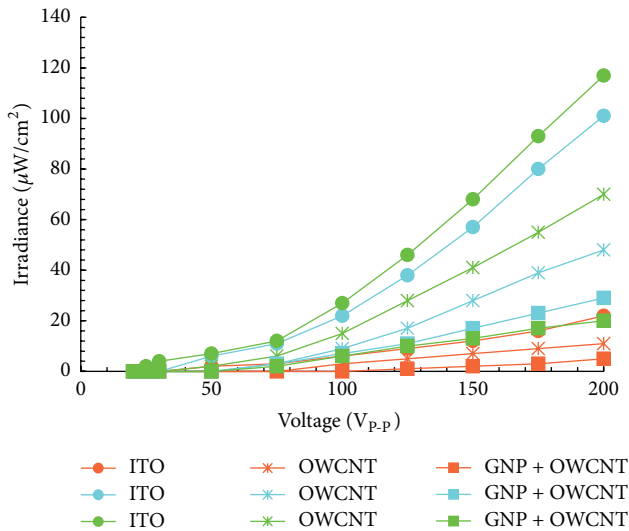


FIGURE 6: The relationships between irradiance and supply voltage amplitude for the frequency  $f = 500$  Hz.

Although GNP layers exhibited extremely high resistivity, small addition of OWCNTs (0.1 wt.%) allowed lowering resistivity by more than order of magnitude, resulting in functional structures. Picture of working electroluminescent structures is presented in Figure 5.

Thickness of obtained TCL layers was controlled during coating process and remained on the level of 500 nm. Comparable thickness of all layers allows direct comparison of

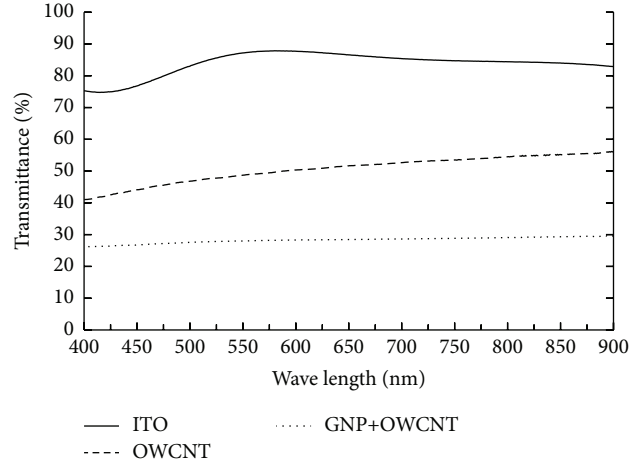


FIGURE 7: The relationship between optical transmittance value of TCLs and wavelength.

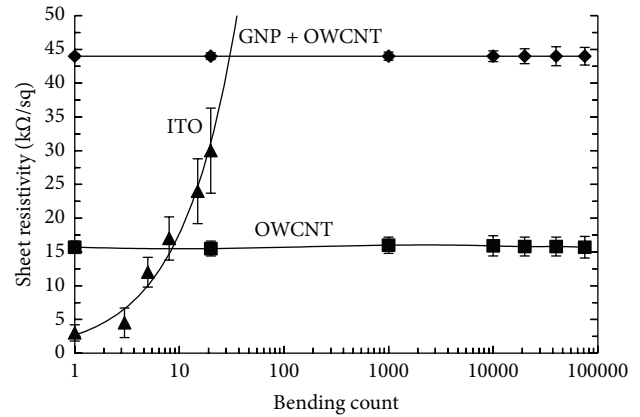


FIGURE 8: Sheet resistivity changes during cyclical mechanical stress test for TCLs.

their properties. Final TFEL structure with screen-printed luminophore, dielectric, and silver layers was 35  $\mu\text{m}$  thick.

**4.1. Irradiance Measurements.** Measurements of irradiance flux from all types of structures revealed significant dissimilarities (Figure 6). Emission from luminophores varies depending on different colors. While highest obtained irradiance for blue and blue-green is around  $100 \mu\text{W}/\text{cm}^2$ , for orange luminophore it stays below  $30 \mu\text{W}/\text{cm}^2$ . Moreover, elaborated elements with nanotube based TCLs have at most 60% of irradiance compared with ITO based structures. This is related to lower optical transmittance of composite layers, what we confirmed in the next experiment.

**4.2. Transmittance Measurements.** Transparent electrodes were measured with spectrophotometer to draw optical transmittance spectrum. As we can see in Figure 7, ITO has higher values of transmittance, but on uneven level, while CNT based electrodes have linear relation, with minor decay in lower wavelengths. Interestingly graphene based layers

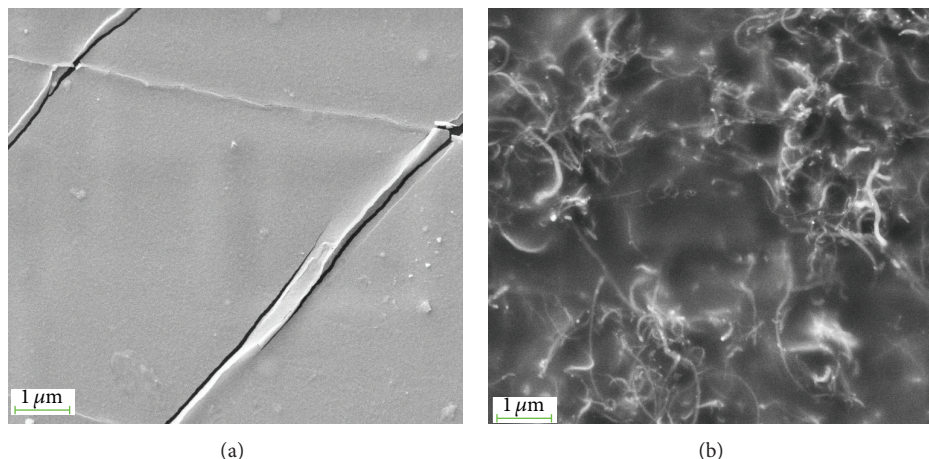


FIGURE 9: SEM micrographs of ITO and OWCNT layers after cyclical bending tests.

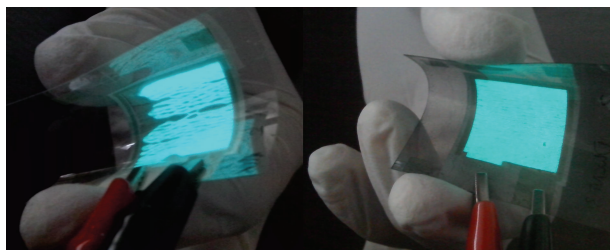


FIGURE 10: TFEL structures on ITO (left) and OWCNTs (right) after thermal shock cycles.

have wavelength independent value of transmittance, which is also known for monolayer graphene [45] and not for any other transparent electrodes.

**4.3. Electromechanical Properties.** Periodical mechanical stress test was performed on all transparent electrodes. Direct comparison of results is presented in Figure 8. Mechanical stress has relatively low influence on resistance of printed composite electrodes, while ITO samples did not survive the test. Sheet resistivity of CNT and GNP based electrodes remained almost unchanged after 75 000 bending cycles, while sheet resistivity of ITO layer increased more than 10 times just after 20 bends, and shortly after that noted higher resistivity than GNP + CNT layers

High mechanical endurance of composite electrodes emerges from carbon nanomaterials, strengthening structure of the layers. Applied mechanical stress does not have any effect on structure of CNTs or GNPs, and additionally very high length-to-diameter ratio of nanotubes and high area of graphene platelets prevent losing electrical contact between separate particles. Sputtered ITO with domain-based polycrystalline structure is less resilient to this type of stresses and is easily destroyed. Detailed observations of microstructure revealed cracked ITO structure, while there were no visible defects in layers with nanomaterials (Figure 9).

**4.4. Accelerated Aging.** We have not observed influence of the accelerated aging process on the irradiance, but we observed degradation of mechanical properties in ITO based structures. After 200 thermal cycles a delamination of luminophore layer from ITO was observed, for all kinds of used luminophores. Adhesion loss resulting in delamination is negative phenomena in case of elastic electronic structures that we have demonstrated in Figure 10. Structures with carbon based layers (OWCNT, GNP + OWCNT) did not exhibit such problems.

## 5. Conclusions

Electroluminescent structures with carbon nanotubes and graphene nanoplatelets based transparent electrodes were obtained using screen-printing and spray-coating techniques. Although elaborated structures with nanomaterials have lower luminance than typically ITO based structures, they exhibit much higher resilience to mechanical factors and have stable parameters after aging process. Such composite layers sustain heavy mechanical stress or environmental factors and in that field overcome significantly ITO electrodes. While electrical and optical properties are still superior for ITO layers, optimization processes are on the way. Selection of nanotubes with higher length-to-diameter aspect ratio and thinner graphene platelets will improve optical properties of TCLs. Addition of dispersing agents for elaborated composite layers is goal to improve electrical properties. The results presented in this paper demonstrate that printed TCLs with carbon nanomaterials might be good substitute for ITO layers in elastic optoelectronic application. Presented results are very promising, but we need to improve electrical and optical properties of these new electronic materials.

## Conflict of Interests

The authors declare that there is no conflict of interests regarding the publication of this paper.

## Acknowledgment

This work was supported by The Polish National Centre for Research and Development through GRAF-TECH/07 Project no. 513L 1142 0907 000.

## References

- [1] C. H. Hong, J. H. Shin, B. K. Ju et al., "Index-matched indium tin oxide electrodes for capacitive touch screen panel applications," *Journal of Nanoscience and Nanotechnology*, vol. 13, no. 11, pp. 7756–7759, 2013.
- [2] S. Yong-Hee, C. Chung-Ki, and K. Han-Ki, "Resistance and transparency tunable Ag-inserted transparent InZnO films for capacitive touch screen panels," *Thin Solid Films*, vol. 548, pp. 641–645, 2013.
- [3] B. Han, K. Pei, Y. Huang et al., "Uniform self-forming metallic network as a high-performance transparent conductive electrode," *Advanced Materials*, vol. 26, no. 6, pp. 873–877, 2014.
- [4] D. S. Jung, S. Lee, K. H. Lee et al., "A temperature-independent multi-walled carbon-nanotube sheet electrode for transparent touch screen," in *Proceedings of the 19th International Workshop on Active-Matrix Flatpanel Displays and Devices (AM-FPD '12)*, pp. 99–100, Kyoto, Japan, July 2012.
- [5] K. Kim, K. Shin, J.-H. Han et al., "Deformable single wall carbon nanotube electrode for transparent tactile touch screen," *Electronics Letters*, vol. 47, no. 2, pp. 118–120, 2011.
- [6] Y. Wang, X. Zhang, Q. Huang, C. Wei, and Y. Zhao, "Room temperature deposition of highly conductive and transparent hydrogen and tungsten co-doped ZnO films for thin film solar cells applications," *Solar Energy Materials and Solar Cells*, vol. 110, pp. 94–97, 2013.
- [7] J. G. Tait, B. J. Worfolk, S. A. Maloney et al., "Spray coated high-conductivity PEDOT:PSS transparent electrodes for stretchable and mechanically-robust organic solar cells," *Solar Energy Materials and Solar Cells*, vol. 110, pp. 98–106, 2013.
- [8] R. V. Salvatierra, C. E. Cava, L. S. Roman, and A. J. G. Zarbin, "ITO-free and flexible organic photovoltaic device based on high transparent and conductive polyaniline/carbon nanotube thin films," *Advanced Functional Materials*, vol. 23, no. 12, pp. 1490–1499, 2013.
- [9] Y. H. Kim, C. Sachse, M. L. MacHala, C. May, L. Müller-Meskamp, and K. Leo, "Highly conductive PEDOT:PSS electrode with optimized solvent and thermal post-treatment for ITO-free organic solar cells," *Advanced Functional Materials*, vol. 21, no. 6, pp. 1076–1081, 2011.
- [10] M. Sibiński, K. Znajdek, M. Słoma, and B. Guzowski, "Carbon nanotube transparent conductive layers for solar cells application," *Optica Applicata*, vol. 41, no. 2, pp. 375–381, 2011.
- [11] T. Kim, Y. W. Kim, H. S. Lee, H. Kim, W. S. Yang, and K. S. Suh, "Uniformly interconnected silver-nanowire networks for transparent film heaters," *Advanced Functional Materials*, vol. 23, no. 10, pp. 1250–1255, 2013.
- [12] R. Gupta, S. Walia, M. Hösel et al., "Solution processed large area fabrication of Ag patterns as electrodes for flexible heaters, electrochromics and organic solar cells," *Journal of Materials Chemistry A*, vol. 2, pp. 10930–10937, 2014.
- [13] D. Kim, L. Zhu, D. Jeong et al., "Transparent flexible heater based on hybrid of carbon nanotubes and silver nanowires," *Carbon*, vol. 63, pp. 530–536, 2013.
- [14] C. Hudayaa, J. H. Parka, W. Choia, and J. K. Leeb, "Characteristics of fluorine-doped tin oxide as a transparent heater on PET prepared by ECR-MOCVD," *ECS Transactions*, vol. 53, no. 4, pp. 161–166, 2013.
- [15] H. Mingjun, G. Jiefeng, D. Yucheng et al., "Flexible transparent PES/silver nanowires/PET sandwich-structured film for high-efficiency electromagnetic interference shielding," *Langmuir*, vol. 28, no. 18, pp. 7101–7106, 2012.
- [16] S. C. Xu, B. Y. Man, S. Z. Jiang et al., "Flexible and transparent graphene-based loudspeakers," *Applied Physics Letters*, vol. 102, no. 15, Article ID 151902, 2013.
- [17] J. W. Suk, K. Kirk, Y. Hao, N. A. Hall, and R. S. Ruoff, "Thermoacoustic sound generation from monolayer graphene for transparent and flexible sound sources," *Advanced Materials*, vol. 24, no. 47, pp. 6342–6347, 2012.
- [18] K. Y. Shin, J. Y. Hong, and J. Jang, "Flexible and transparent graphene films as acoustic actuator electrodes using inkjet printing," *Chemical Communications*, vol. 47, no. 30, pp. 8527–8529, 2011.
- [19] T. Minami, "Present status of transparent conducting oxide thin-film development for indium-tin-oxide (ITO) substitutes," *Thin Solid Films*, vol. 516, no. 17, pp. 5822–5828, 2008.
- [20] B. Y. Oh, M. C. Jeong, T. H. Moon et al., "Transparent conductive Al-doped ZnO films for liquid crystal displays," *Journal of Applied Physics*, vol. 99, no. 12, Article ID 124505, 2006.
- [21] S. Pang, Y. Hernandez, X. Feng, and K. Müllen, "Graphene as transparent electrode material for organic electronics," *Advanced Materials*, vol. 23, no. 25, pp. 2779–2795, 2011.
- [22] Y. Kavanagh, M. J. Alam, and D. C. Cameron, "The characteristics of thin film electroluminescent displays produced using sol-gel produced tantalum pentoxide and zinc sulfide," *Thin Solid Films*, vol. 447–448, pp. 85–89, 2004.
- [23] M. G. Helander, Z. B. Wang, J. Qiu et al., "Chlorinated indium tin oxide electrodes with high work function for organic device compatibility," *Science*, vol. 332, no. 6032, pp. 944–947, 2011.
- [24] K. Takehara, K. Takeda, K. Nagata et al., "Transparent electrode for UV light-emitting-diodes," *Physica Status Solidi (C)*, vol. 8, no. 7–8, pp. 2375–2377, 2011.
- [25] Y. Liu, Y. Li, and H. Zeng, "ZnO-based transparent conductive thin films: doping, performance, and processing," *Journal of Nanomaterials*, vol. 2013, Article ID 196521, 9 pages, 2013.
- [26] D. Lee, W. K. Bae, I. Park, D. Y. Yoon, S. Lee, and C. Lee, "Transparent electrode with ZnO nanoparticles in tandem organic solar cells," *Solar Energy Materials and Solar Cells*, vol. 95, no. 1, pp. 365–368, 2011.
- [27] N. M. Kiasari, J. Shen, B. Gholamkhash, S. Soltanian, and P. Servati, "Well-aligned zinc oxide nanowire arrays for transparent electrode applications," in *Proceedings of the 24th Annual Meeting on IEEE Photonic Society (PHO '11)*, pp. 561–562, October 2011.
- [28] I. S. Song, S. W. Heo, J. H. Lee, J. R. Haw, and D. K. Moon, "Study on the wet processable antimony tin oxide (ATO) transparent electrode for PLEDs," *Journal of Industrial and Engineering Chemistry*, vol. 18, no. 1, pp. 312–316, 2012.
- [29] L. Luo, D. Bozyigit, V. Wood, and M. Niederberger, "High-quality transparent electrodes spin-cast from preformed antimony-doped tin oxide nanocrystals for thin film optoelectronics," *Chemistry of Materials*, vol. 25, no. 24, pp. 4901–4907, 2013.
- [30] F. Chen, N. Li, Q. Shen, C. Wang, and L. Zhang, "Fabrication of transparent conducting ATO films using the ATO sintered targets by pulsed laser deposition," *Solar Energy Materials and Solar Cells*, vol. 105, pp. 153–158, 2012.

- [31] I. Moreno, N. Navascues, M. Arruebo, S. Irusta, and J. Santamaria, "Facile preparation of transparent and conductive polymer films based on silver nanowire/polycarbonate nanocomposites," *Nanotechnology*, vol. 24, no. 27, 2013.
- [32] T. Feng, Y. Wang, K. Wang, M. Qian, Y. Chen, and Z. Sun, "A facile method for preparing transparent, conductive, and paper-like silver nanowire films," *Journal of Nanomaterials*, vol. 2011, Article ID 935218, 5 pages, 2011.
- [33] A. J. Morfa, E. M. Akinoglu, J. Subbiah, M. Giersig, and P. Mulvaney, "Transparent metal electrodes from ordered nanosphere arrays," *Journal of Applied Physics*, vol. 114, no. 5, Article ID 054502, 2013.
- [34] M. M. Hamasha, T. Dhakal, K. Alzoubi et al., "Stability of ITO thin film on flexible substrate under thermal aging and thermal cycling conditions," *IEEE/OSA Journal of Display Technology*, vol. 8, no. 7, pp. 385–390, 2012.
- [35] L. G. de Arco, Y. Zhang, C. W. Schlenker, K. Ryu, M. E. Thompson, and C. Zhou, "Continuous, highly flexible, and transparent graphene films by chemical vapor deposition for organic photovoltaics," *ACS Nano*, vol. 4, no. 5, pp. 2865–2873, 2010.
- [36] G. Kalita, K. Wakita, M. Umeno, Y. Hayashi, and M. Tanemura, "Large-area CVD graphene as transparent electrode for efficient organic solar cells," in *Proceedings of the 38th IEEE Photovoltaic Specialists Conference (PVSC '12)*, pp. 3137–3141, June 2012.
- [37] X. Li, G. Zhang, X. Bai et al., "Highly conducting graphene sheets and Langmuir-Blodgett films," *Nature Nanotechnology*, vol. 3, no. 9, pp. 538–542, 2008.
- [38] L. Gomez de Arco, Y. Zhang, C. W. Schlenker, K. Ryu, M. E. Thompson, and C. Zhou, "Continuous, highly flexible, and transparent graphene films by chemical vapor deposition for organic photovoltaics," *ACS Nano*, vol. 4, no. 5, pp. 2865–2873, 2010.
- [39] Y. Choi, S. J. Kang, H. Kim, W. M. Choi, and S. Na, "Multilayer graphene films as transparent electrodes for organic photovoltaic devices," *Solar Energy Materials and Solar Cells*, vol. 96, no. 1, pp. 281–285, 2012.
- [40] K. Kawano, R. Pacios, D. Poplavskyy, J. Nelson, D. D. C. Bradley, and J. R. Durrant, "Degradation of organic solar cells due to air exposure," *Solar Energy Materials and Solar Cells*, vol. 90, no. 20, pp. 3520–3530, 2006.
- [41] P. Verge, F. Vidal, P. Aubert et al., "Thermal ageing of poly(ethylene oxide)/poly(3,4-ethylenedioxythiophene) semi-IPNs," *European Polymer Journal*, vol. 44, no. 11, pp. 3864–3870, 2008.
- [42] Y. Zhu, W. Cai, R. D. Piner, A. Velamakanni, and R. S. Ruoff, "Transparent self-assembled films of reduced graphene oxide platelets," *Applied Physics Letters*, vol. 95, no. 10, Article ID 103104, 2009.
- [43] A. Yu, I. Roes, A. Davies, and Z. Chen, "Ultrathin, transparent, and flexible graphene films for supercapacitor application," *Applied Physics Letters*, vol. 96, no. 25, Article ID 253105, 2010.
- [44] J. Zhao, S. Pei, W. Ren, L. Gao, and H. Cheng, "Efficient preparation of large-area graphene oxide sheets for transparent conductive films," *ACS Nano*, vol. 4, no. 9, pp. 5245–5252, 2010.
- [45] L. A. Falkovsky, "Optical properties of graphene," *Journal of Physics: Conference Series*, vol. 129, no. 1, 2008.

## Research Article

# Influence of 1D and 2D Carbon Fillers and Their Functionalisation on Crystallisation and Thermomechanical Properties of Injection Moulded Nylon 6,6 Nanocomposites

**Fabiola Navarro-Pardo,<sup>1,2,3</sup> Ana L. Martínez-Hernández,<sup>2,3</sup> Victor M. Castaño,<sup>2</sup> José L. Rivera-Armenta,<sup>4</sup> Francisco J. Medellín-Rodríguez,<sup>5</sup> Gonzalo Martínez-Barrera,<sup>6</sup> and Carlos Velasco-Santos<sup>2,3</sup>**

<sup>1</sup> *Facultad de Química, Universidad Autónoma del Estado de México, Posgrado en Ciencia de Materiales, Km. 12 de la Carretera Toluca-Atlaconulco, 50200 San Cayetano, Toluca, MEX, Mexico*

<sup>2</sup> *Centro de Física Aplicada y Tecnología Avanzada, Universidad Nacional Autónoma de México, Boulevard Juriquilla No. 3001, Juriquilla, 76230 Santiago de Querétaro, QRO, Mexico*

<sup>3</sup> *Instituto Tecnológico de Querétaro, División de Estudios de Posgrado e Investigación, Avenida Tecnológico s/n, Esquina Gral. Mariano Escobedo, Colonia Centro Histórico, 76000 Santiago de Querétaro, QRO, Mexico*

<sup>4</sup> *Instituto Tecnológico de Ciudad Madero, División de Estudios de Posgrado e Investigación, Juventino Rosas y Jesús Urueta, Colonia Los Mangos, 89440 Ciudad Madero, TAMPS, Mexico*

<sup>5</sup> *Universidad Autónoma del San Luis Potosí, Facultad de Ciencias Químicas, Avenida Manuel Nava 6, Zona Universitaria, 78210 San Luis Potosí, SLP, Mexico*

<sup>6</sup> *Facultad de Química, Universidad Autónoma del Estado de México, Laboratorio de Investigación y Desarrollo de Materiales Avanzados, Km. 12 de la Carretera Toluca-Atlaconulco, 50200 San Cayetano, Toluca, MEX, Mexico*

Correspondence should be addressed to Carlos Velasco-Santos; [cylaura@gmail.com](mailto:cylaura@gmail.com)

Received 15 February 2014; Revised 21 June 2014; Accepted 23 June 2014; Published 22 July 2014

Academic Editor: Jinlong Jiang

Copyright © 2014 Fabiola Navarro-Pardo et al. This is an open access article distributed under the Creative Commons Attribution License, which permits unrestricted use, distribution, and reproduction in any medium, provided the original work is properly cited.

Carbon nanotubes (CNTs) and graphene were used as reinforcing fillers in nylon 6,6 in order to obtain nanocomposites by using an injection moulding process. The two differently structured nanofillers were used in their pristine or reduced form, after oxidation treatment and after amino functionalisation. Three low nanofiller contents were employed. Crystallisation behaviour and perfection of nylon 6,6 crystals were determined by differential scanning calorimetry and wide angle X-ray diffraction, respectively. Crystallinity was slightly enhanced in most samples as the content of the nanofillers was increased. The dimensionality of the materials was found to provide different interfaces and therefore different features in the nylon 6,6 crystal growth resulting in improved crystal perfection. Dynamical, mechanical analysis showed the maximum increases provided by the two nanostructures correspond to the addition of 0.1 wt.% amino functionalised CNTs, enhancing in 30% the storage modulus and the incorporation of 0.5 wt.% of graphene oxide caused an increase of 44% in this property. The latter also provided better thermal stability when compared to pure nylon 6,6 under inert conditions. The superior properties of graphene nanocomposites were attributed to the larger surface area of the two-dimensional graphene compared to the one-dimensional CNTs.

## 1. Introduction

Carbon nanotubes (CNTs) and graphene have raised great interest because of their unique physical, chemical, and mechanical properties [1–5]. A variety of polymer nanocomposites employing these nanomaterials have been developed

and these works have shown promising results in this field of application [6–12]. Despite the great potential of both carbon allotropes for their use as nanofillers, dispersion and strong interfacial adhesion between the nanofiller and the matrix remain the key challenge for effective reinforcement of polymers [8, 9, 12–14]. Extensive research has been made on

the chemical functionalisation of these carbon nanomaterials [7–14]. The modifications imparted to these nanomaterials dictate their properties and therefore have an impact on the nanocomposites obtained from them [15–17]. Functionalisation of these nanomaterials prevents their aggregation and improves their dispersion in polymer matrices resulting in efficient stress transfer between both phases [9, 13]. Functional groups at the surface of CNTs or graphene make the strongest interfacial interactions with the polymer matrix [7, 8, 11]. The use of polymers with functional groups in their monomer units also favours these aspects; nylon 6,6 contains amide groups separated by methylene units in its structure. The ordered array of polymer chains packed due to hydrogen bonding and the subsequent folding of these chains into sheets due to Van der Waals forces provide a degree of crystallinity to this polyamide [18]. Furthermore, several studies have shown that the addition of a second phase in polymer matrices modifies the crystallisation behaviour of polymers [8–10, 16–19]. Additionally, it is well known that the properties of semicrystalline polymers are strongly dependent on their crystalline structure [7–9].

CNTs dominate the research among carbon based materials used as reinforcing agents in polymers. On the other hand, graphene based nanocomposites have been gaining more importance because of the superior properties of this nanofiller. Only a few works have shown the influence between both differently dimensional structures on the crystallisation behaviour or the mechanical properties of polymers [17, 20–22]. Lamastra et al. [21] reinforced poly( $\epsilon$ -caprolactone) with electrospun poly(methyl methacrylate) (PMMA) fibres containing CNTs and graphene nanoplatelets. The nanocomposites reinforced with well-exfoliated graphene sheets showed the best results in the mechanical properties providing an increase of 180% in yield strength when compared to the pure matrix. Chatterjee et al. [22] reinforced nylon 12 spun fibres with both carbon nanofillers; CNTs and graphene favoured the increase in the equatorial percentage crystallinity of nylon 12 and graphene showed to be the best reinforcing filler with an improvement of 400% in elastic modulus. Recent works concerning the influence provided by both carbon structures on crystallisation and thermomechanical properties have been based on pristine materials [20–23]. Our research group has investigated these effects on electrospun nanocomposites containing functionalised 1D and 2D carbon fillers, showing the differences between both carbon nanomaterials [7, 8].

Injection moulding is a very important technique for industrial purposes, because it is a fast and an automated process for large scale manufacture of complex products at minimum cost. Injection moulded automotive parts reinforced with CNTs or graphene could be a potential application of the type of nanocomposites developed in this work. Comprehensive understanding of both carbon nanostructures is needed in order to optimise the processing conditions in industrial processes and achieve desirable properties. The aim of this work is to investigate the influence of one-dimensional (1D) and two-dimensional (2D) structures of carbon on the crystallisation and the thermomechanical properties of nylon 6,6 nanocomposites obtained by the injection moulding

process using different nanofiller contents. The effect that functionalisation provides to the properties mentioned above is also presented.

## 2. Materials and Methods

Chemical vapour deposition multiwalled carbon nanotubes (Sunnano Company), with 10–30 nm in outer diameter, 1–10  $\mu\text{m}$  length, and purity above 80%, were refluxed for three hours at 80°C in a 3:1 molar solution of nitric acid ( $\text{HNO}_3$ , 70%, Sigma-Aldrich) and sulphuric acid ( $\text{H}_2\text{SO}_4$ , 98%, J. T. Baker). The solution was filtered and washed with distilled water until achieving neutral pH. Finally, the oxidised carbon nanotubes (OCNT) were dried overnight at 80°C [8].

Graphene oxide (GO) was obtained from graphite using the modified Hummers method [1], in which 23 mL of  $\text{H}_2\text{SO}_4$  was added into a reaction flask submerged in an ice bath and kept there until it reached 0°C. 1 g graphite (Number 70230, Electron Microscopy Science) and 3 g potassium permanganate ( $\text{KMnO}_4$ , Merck) were added slowly followed by stirring at 35°C for two hours and then diluted with 46 mL of distilled water for 15 minutes under stirring. After that, a solution of 5 mL of hydrogen peroxide ( $\text{H}_2\text{O}_2$ , 30%, J.T. Baker) in 135 mL of distilled water was added to reduce residual  $\text{KMnO}_4$ . A solution of 2.5 mL hydrochloric acid (HCl, 37%, Sigma-Aldrich) in 100 mL of distilled water was added to remove metal ions followed by filtration with excess water to remove acid. Finally, the graphite oxide was dried overnight at 60°C. In order to obtain GO, 0.5 g of graphite oxide (batches of 100 mg) was redispersed into water (10 mL per batch) for being exfoliated using sonication for three hours in an ultrasound bath (Autoscience 10200B, at a frequency of 40 Hz); the resulting GO dispersion was filtrated and dried overnight at 60°C. Reduced graphene oxide (RGO) was obtained by adding 0.25 g Hexamethylenetetramine (HMTA, Sigma-Aldrich) to 0.25 g GO dispersed in water and kept under stirring at 100°C for 10 hours [2]. The RGO was filtered and washed with distilled water until reaching neutral pH and dried overnight at 60°C.

An acid-base titration with sodium hydroxide (NaOH, 98%, Sigma-Aldrich) was used to determine the concentration of acidic surface groups [3]. The oxidised carbon materials were added into 25 mL of a 0.04 N NaOH solution and stirred for 48 h to allow the acidic groups on the nanomaterials to neutralise with the basic solution. The mixture was titrated with a 0.04 N HCl solution to determine the excess NaOH in the solution and the concentration of the carboxylates on OCNT and GO. The concentrations of acidic surface sites were 6.5 mmol/g in OCNT and 5.4 mmol/g in GO. The nanomaterials were functionalised as follows: a 1:1 molar ratio solution of carbon nanomaterial and 1-ethyl-3-[3-dimethylaminopropyl]carbodiimide hydrochloride (EDAC, 99%, Sigma-Aldrich) was kept under stirring at 80°C in dimethylamine excess for 6 h. The material obtained was washed until neutral pH and dried overnight at 60°C. The functionalised carbon nanotubes and graphene were labelled as f-CNT and f-Ge, respectively.

Nylon 6,6 (Ultramid A3K, BASF) was dried at 60°C for 12 hours. Prior to injection moulding, the pellets were mixed with the carbon nanofillers and agitated so that the charged particles are deposited on the surface of nylon pellets due to electrostatic forces. Three nanofiller contents were chosen: 0.1, 0.3, and 0.5 wt.%. The mixed blends were moulded into a  $50 \times 44 \times 2 \text{ mm}^3$  aluminium mould by an injection machine (AB-200, AB Machinery) at a moulding temperature of 270°C and pressure of 110 psi. After injection, the mould was set to cool down for three minutes before opening and removing the sample. The first ten samples of each run were discarded in order to stabilise the process. The rest of the samples were chosen for their characterisation.

Fourier transform infrared spectroscopy (FTIR) was carried out on a Bruker Tensor 37 spectrometer fitted with a diamond ATR device (resolution  $1 \text{ cm}^{-1}$ ). A differential scanning calorimeter (DSC), Perkin Elmer DSC-7, was used to determine the crystallinity and the nucleating behaviour of nanocomposites. This was calibrated with an indium standard using a constant nitrogen flow both in the sample and in the reference chambers. All samples weighed approximately 6 mg and were sealed within aluminium pans. The samples were heated up to 280°C for five minutes and then they were cooled down at  $10^\circ\text{C}/\text{min}$ . The percentage of crystallinity ( $X_c$ ) was calculated by integrating the melting curves for obtaining the sample heat of fusion and dividing by the heat of fusion of 100% crystalline nylon 6,6, taken as  $197 \text{ J/g}$  [24]. Wide angle X-ray diffraction (WAXD) measurements were obtained in PANalytical X'Pert Pro X-ray diffraction equipment with Cu  $K\alpha$  radiation ( $k = 0.154 \text{ nm}$ ). The scanning rate was  $0.05^\circ/\text{s}$ . The diffraction patterns were fitted using Gaussian functions in Origin 8.5 in order to obtain a broad amorphous halo and sharp peaks from the reflections of the crystalline peaks, as it has been reported by other research groups [25–27]. This procedure was used to evaluate the crystallinity index (CI) obtained by the following equation:

$$\text{CI} = \frac{A_c}{A_c + A_a}, \quad (1)$$

where  $A_c$  is the integrated area underneath the crystalline peaks and  $A_a$  is the integrated area of the amorphous halo [25, 27]. The crystallite sizes perpendicular to the diffraction (hkl) planes,  $L_{\text{hkl}}$  in nanometres, were obtained by applying Scherrer's equation:

$$L_{\text{hkl}} = \frac{k\lambda}{\beta \cos \theta}, \quad (2)$$

where  $k$  is the Scherrer factor, taken as 0.891 [19, 28],  $\lambda$  is the X-ray wavelength,  $\beta = (B^2 - b_0^2)^{1/2}$  is the pure line breadth,  $B$  is a measured half width of the experimental peak,  $b_0$  is the instrumental broadening factor which is 0.12 for the diffractometer employed, and  $\theta$  is the Bragg angle. Thermomechanical properties of the nanocomposites were determined using a dynamic mechanical analyser (DMA), TA Instruments DMA 2980. Samples of  $30 \times 10 \times 2 \text{ mm}^3$  were analysed in dual cantilever mode from room temperature to  $200^\circ\text{C}$  at a frequency of 1 Hz and a heating rate of  $5^\circ\text{C}/\text{min}$ . Thermogravimetric analysis (TGA) was carried out using an SDT Q600

V20.5 Build 15 equipment. 10 mg of the samples was placed into alumina pans and heated up from 25 to  $600^\circ\text{C}$  under a nitrogen flow of  $100 \text{ mL}/\text{min}$ . Scanning electron microscopy (SEM) investigation was performed using a JEOL JSM 6060 microscope with an acceleration voltage of 25 kV. The samples were cryogenically broken in liquid nitrogen and gold was sputter-coated on the fractured surface.

### 3. Results and Discussion

FTIR spectroscopy has been used for determining the structural units present in pure nylon 6,6 and nanofiller reinforced injection moulded samples. The FTIR spectra are presented in Figure 1(a) showing the samples with the highest content of carbon nanofillers. The peak at  $\sim 935 \text{ cm}^{-1}$  is due to the amide axial deformation of C–C=O [29]. The angular deformation of C=O occurs at  $\sim 1140 \text{ cm}^{-1}$  [30]. The angular deformation out of plane of amide III is located at  $\sim 1200 \text{ cm}^{-1}$  [29]. The C–C skeletal vibration is shown at  $\sim 1275 \text{ cm}^{-1}$  [29]. The amide III band/CH<sub>2</sub> wagging is located at  $\sim 1368 \text{ cm}^{-1}$  [31]. The peaks in the  $2800\text{--}3000 \text{ cm}^{-1}$  region correspond to the CH<sub>2</sub> stretching and to the N–H axial deformation [29]. The peak at  $\sim 3300 \text{ cm}^{-1}$  is due to the N–H stretching vibrations [30]. Our research group has explained the interactions of the functionalised carbon nanomaterials with the nylon 6,6 matrix as seen in FTIR spectra [8]. In this case these interactions are not as noticeable as the ones found in the electrospun nanocomposites recently developed. However, as displayed in Figure 1(b), bands corresponding to methylene stretching and related to conformational changes are red shifted when the nanofillers are incorporated [32]; this change to lower frequencies is clearer in the band located at  $\sim 2930 \text{ cm}^{-1}$ , indicating that the addition of carbon nanomaterials affects the polymer chain order. There is ongoing work to explain the behaviour of the perfection in the short-range ordered structures by this technique; however, their discussion is beyond the scope of this paper.

The melting and crystallisation temperatures of the injection moulded nanocomposites are shown in Tables 1 and 2. All melting thermograms showed a broad peak at  $\sim 260^\circ\text{C}$  attributed to the melting of  $\alpha$ -crystals [33]. There was also a very slight broad shoulder on the low temperature side at  $\sim 250^\circ\text{C}$  indicating crystallite morphological changes [19] or melting of small and less stable crystalline units [24]. There were no significant variations in the melting temperature between nylon 6,6 and the nanofiller reinforced samples. As shown in Table 1, the crystallinity in the nanocomposites in most cases increased marginally as a function of nanofiller content, except in f-CNT based nanocomposites. This can be explained from a kinetic point of view. The nucleation in the polymer is a rate-limiting process and the addition of nanofillers increases the nucleation rate during cooling and hence the fractional crystallinity [33]. The opposite behaviour provided by f-CNT has also been found in our previous research of electrospun nanocomposites [7]. As described in this previous publication, oxidised carbon nanofillers were used for obtaining the amino functionalised ones where the amount of carboxylic groups in OCNT was higher

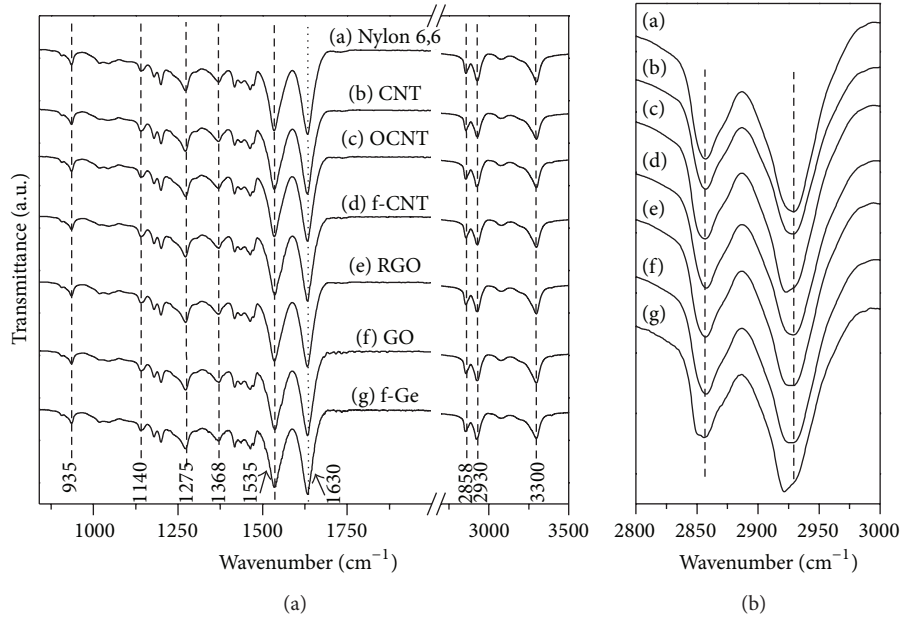


FIGURE 1: FTIR spectra of (a) nylon 6,6 and nanocomposites containing 0.5 wt.% nanofillers and (b) zoom in of the 2800–3000  $\text{cm}^{-1}$  region.

TABLE 1: Crystallisation properties obtained from melting curves of DSC.

Nylon 6,6	Melting temperature, °C			Percentage of crystallinity, %		
	263.77			37.68		
Nanofiller	Weight %			Weight %		
	0.1	0.3	0.5	0.1	0.3	0.5
CNT	263.8	264.9	263.2	37.8	38.1	38.1
OCNT	263.8	263.8	263.2	38.8	39.1	39.3
f-CNT	262.6	263.8	263.8	42.0	38.5	38.1
RGO	264.3	264.4	264.3	38.0	38.8	38.9
GO	263.2	263.2	263.2	39.1	40.9	41.0
f-Ge	264.3	263.2	263.2	38.1	40.8	41.0

TABLE 2: Crystallisation temperatures obtained from crystallisation curves of DSC.

Nylon 6,6		231.8°C					
Nanofiller	Weight %			Nanofiller	Weight %		
	0.1	0.3	0.5		0.1	0.3	0.5
CNT	235.2	234.6	235.2	RGO	234.0	234.0	234.0
OCNT	235.2	234.6	235.7	GO	233.5	233.5	233.5
f-CNT	234.0	234.0	234.6	f-Ge	233.5	233.5	232.9

than in GO. Assuming the same amount of  $-\text{COOH}$  was converted to  $-\text{NH}_2$ , the increasing content of amino groups with the addition of f-CNT hindered the diffusion and arrangement of long polymer chains resulting in a decrease in crystallinity. This can be also related to poor dispersion of f-CNT as it will be seen later in the nanocomposite mechanical response. Figure 2 reveals nylon 6,6 crystallisation peaks became broader and decreased in intensity upon addition of nanofillers. This has been attributable to a wider crystal size

distribution in the polymer [16]. In addition, the nanocomposites showed a very modest increase in crystallisation temperatures ( $T_c$ ), as seen in Table 2. The increase was more evident in CNT based nanocomposites; these samples displayed slightly higher  $T_c$  than graphene based nanocomposites. Other authors [17, 34] have shown more noticeable results regarding the nucleating effect of CNTs and graphene based nanofillers using higher content of nanomaterials. Xu et al. [20] studied poly(L-lactide) nanocomposites using FTIR and found that the induction process of crystallisation due to graphene is slower than the process due to CNTs because lattice matching plays a dominant role in surface-induced crystallisation. The polymer chains adsorbed on the surface of graphene need more time to adjust their conformations, making the induction process more complex [20]. In contrast, the crystallisation thermograms obtained from the injection moulded nanocomposites show interesting differences between both nanofillers. Graphene based nanocomposites displayed sharper crystallisation curves than CNT based nanocomposites, as shown by the lower values of full width at

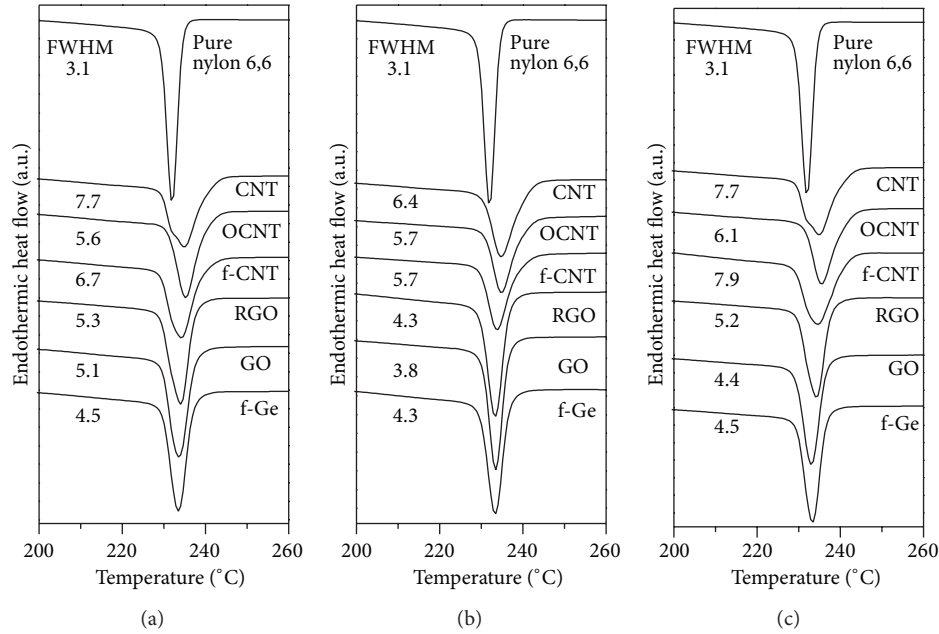


FIGURE 2: Cooling thermograms of nylon 6,6 and nanocomposites containing (a) 0.1 wt.%, (b) 0.3 wt.%, and (c) 0.5 wt.% nanofillers.

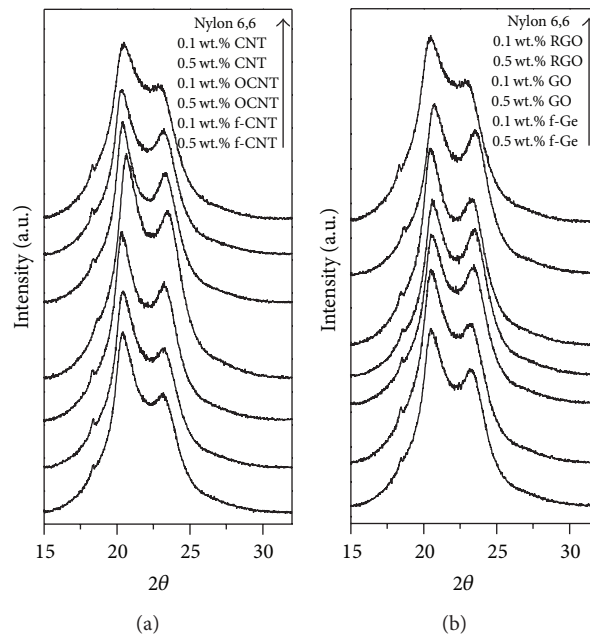


FIGURE 3: X-ray diffractograms of nylon 6,6, (a) carbon nanotube based nanocomposites and (b) graphene based nanocomposites.

half maximum (FWHM) included in Figure 2. This indicates that while CNTs accelerate the nucleation process, most nylon 6,6 crystals are grown in a shorter time in graphene based nanocomposites. Similar behaviour in crystallisation thermograms and crystallisation rate has been found in polypropylene nucleated with exfoliated graphite [35]. This effect can be attributed to the large surface area of graphene favouring the reduction of interfacial free energy.

The crystallinity of the samples was also characterised by WAXD. The diffraction patterns are displayed in Figure 3.

This polymer has two characteristic diffraction signals located at  $\sim 20^\circ$  and  $\sim 23^\circ$ . The spacing of them is approximately 0.44 nm and 0.37 nm, respectively. The former is a project value of the interchain distance within the hydrogen-bonded sheet and the latter represents the intersheet distance [18]. These peaks correspond to the (100) and (010/110) crystalline planes of  $\alpha$ -crystals which have a triclinic unit cell [19, 24]. The values of CI are included in Table 3; these values agree with the  $X_c$  calculated from DSC analyses. Furthermore, Figure 3 shows that the polymer crystalline peaks are

TABLE 3: Crystallisation properties obtained from WAXD.

Nylon 6,6	$L_{(100)}$ , nm			$L_{(010/110)}$ , nm			CI		
	4.46			4.01			0.37		
Nanofiller	Weight, %			Weight, %			Weight, %		
	0.1	0.3	0.5	0.1	0.3	0.5	0.1	0.3	0.5
CNT	5.08	5.28	5.37	4.10	3.75	4.15	0.38	0.39	0.39
OCNT	4.99	4.91	5.10	4.16	4.18	4.01	0.38	0.39	0.40
f-CNT	5.07	5.06	4.87	3.83	3.97	3.94	0.41	0.41	0.40
RGO	4.86	4.92	5.03	4.34	4.30	4.05	0.38	0.39	0.39
GO	4.88	4.75	4.82	4.25	4.21	4.22	0.39	0.40	0.40
f-Ge	4.78	4.91	4.56	4.01	4.20	4.24	0.39	0.40	0.40

TABLE 4: Thermal properties of nylon 6,6 and the nanocomposites.

Nylon 6,6	Glass transition temperature, °C			Temperature at which 10 weight % loss occurs, °C		Temperature at which 50 weight % loss occurs, °C	
	71.8			387.4		421.2	
Nanofiller	Weight, %			Weight, %		Weight, %	
	0.1	0.3	0.5	0.1	0.5	0.1	0.5
CNT	78.3	78.0	76.4	387.5	386.6	418.8	418.7
OCNT	77.7	79.3	80.0	389.5	389.2	421.1	421.6
f-CNT	81.4	78.7	77.7	388.1	387.6	421.1	421.3
RGO	76.9	80.9	79.9	391.4	390.9	422.5	421.5
GO	78.1	72.8	78.9	388.7	392.8	418.6	426.0
f-Ge	78.3	77.7	79.6	390.6	389.6	421.7	422.0

sharper after addition of nanofillers, indicating an increase in crystallite size meaning enhanced crystal perfection. Table 3 also shows the increased crystallite size values when compared to pure polymer. Typically, the addition of nucleating agents is expected to produce smaller and less perfect crystals. However other composite studies have shown similar results as in this case [16, 34, 36]. Sandler et al. [34] explained that the early nucleation leaves more space for the heteronucleated crystals to grow before homonucleation within the rest of the matrix leads to impingement. The crystal sizes indicate that the preferential growth of nylon 6,6 crystalline structures is in the perpendicular direction of (100) plane in all samples.

Figure 4 shows the plots of storage modulus versus temperatures of nylon 6,6 and the nanocomposites, showing the percentage increases in this property compared to pure polymer (values taken at 30°C). These results demonstrate the polymer enhanced stiffness imposed by the carbon nanofillers and also these storage modulus values match the crystallinity trend upon nanofiller addition. The predominant effect in this property can be attributed to the addition of the rigid carbon nanofillers [21]. Besides, the functionalisation effect in the mechanical response is evident in CNT based nanocomposites; polymer reinforced with pristine CNTs showed that the modulus increased up to 17% at the highest content. After oxidation CNTs at the same loading provide a better dispersion in the matrix resulting in an increase of 27% compared to pure nylon 6,6. Amino functionalised CNTs could have been agglomerated at high content

and consequently the modulus was enhanced only by a 17% at a 0.5 wt.% loading; however the incorporation of 0.1 wt.% of this nanofiller provided a 30% enhancement in the storage modulus. Graphene based nanocomposites showed the best mechanical response. Both RGO and f-Ge increased the modulus up to ~30% at the highest content. The very similar results in these nanocomposites can be related to the reduction method employed in this work. The infrared analysis shown in our previous publication gave a hint of a few amine groups adsorbed on the graphene surface due to the reducing agent used [8]; this provided a better dispersion of the nanofiller and favoured the mechanical properties. The incorporation of 0.5 wt.% GO resulted in an increase up to 44% in nylon 6,6 storage modulus. Previous studies have shown that graphene provides better mechanical performance when compared to CNTs [21, 22]. The large 2D structure of graphene allows the polymer to have a larger interfacial area which favours stress transfer between both materials. Nylon nanocomposites obtained from solution mixing and melt compounding techniques have shown similar modulus results when using higher content of CNTs or graphene [37–40].

The glass transition temperatures ( $T_g$ ) can be evaluated using the  $\tan \delta$  plot obtained from DMA, which is related to the reduction of vibration of material, that is, damping [41]. Table 4 shows the values of this property which were obtained from the maximum of the  $\tan \delta$  plots displayed in Figure 5. There was no consistent effect produced by the carbon structures, functionalisation, or content in the glass transition

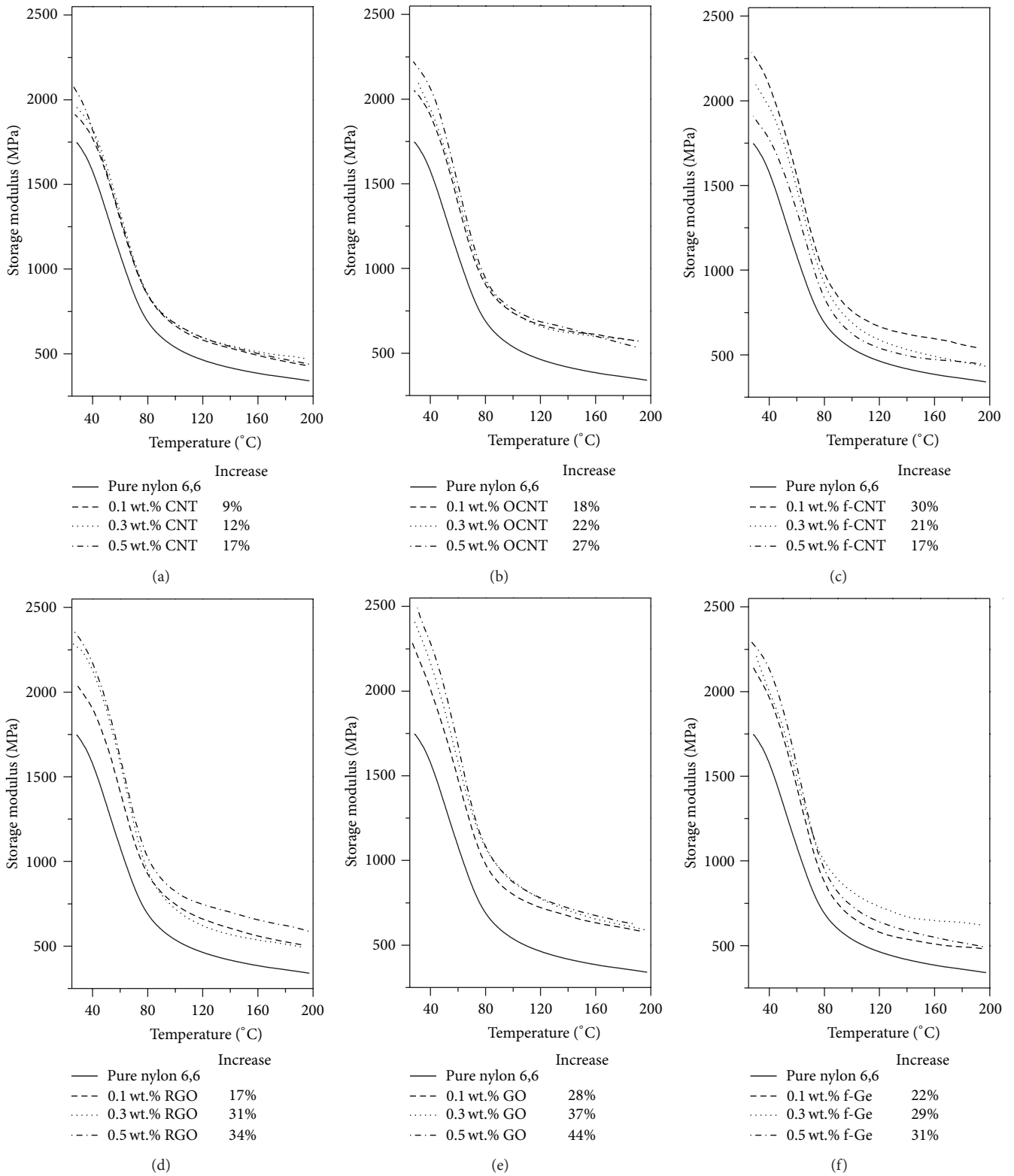


FIGURE 4: Storage modulus of nylon 6,6 and (a), (b), and (c) carbon nanotube based nanocomposites and (d), (e), and (f) graphene based nanocomposites.

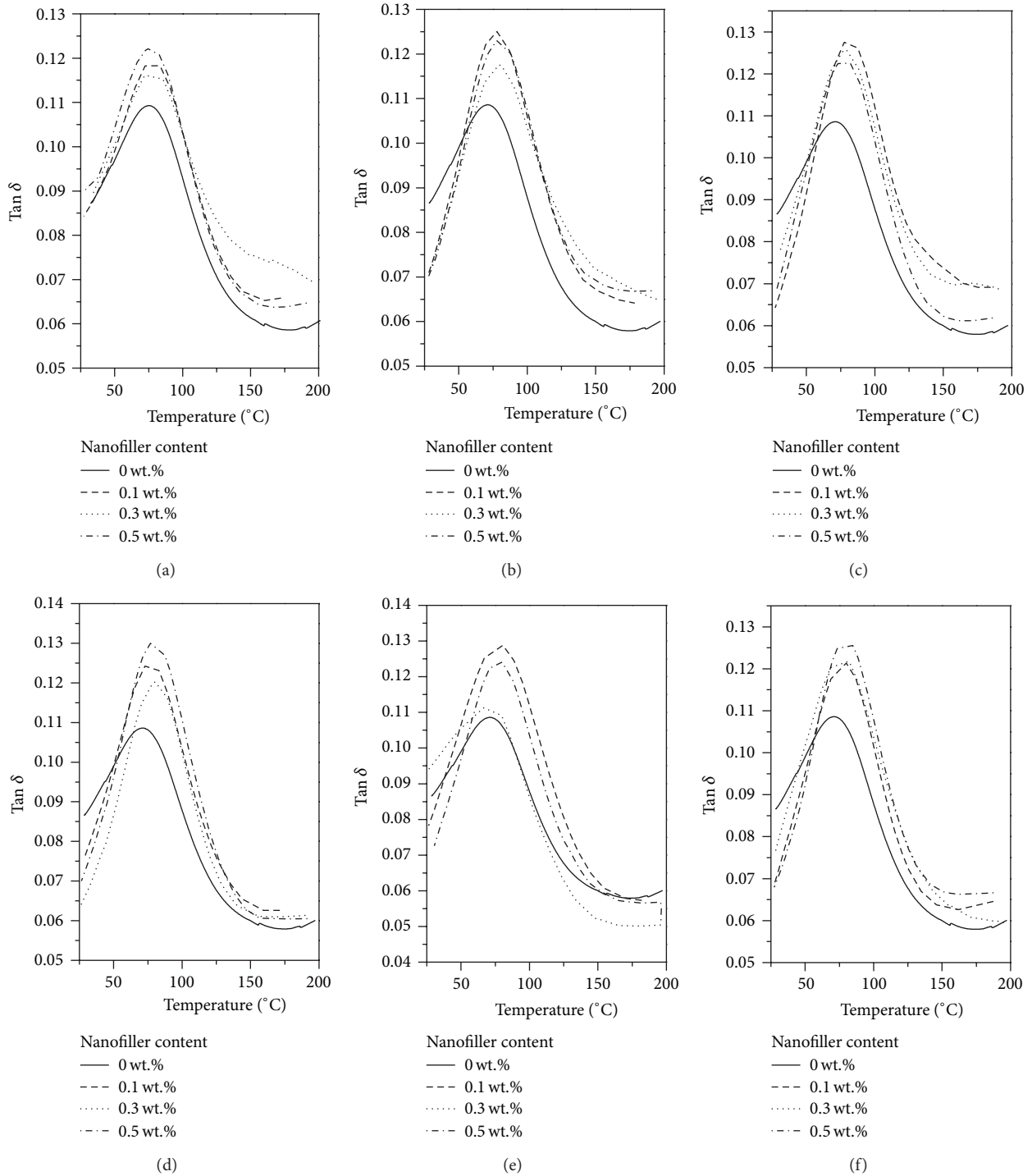


FIGURE 5:  $Tan \delta$  of nylon 6,6 and (a) CNT, (b) OCNT, and (c) f-CNT nanocomposites and (d) RGO, (e) GO, and (f) f-Ge nanocomposites.

of polymer, as has also been observed in other works [12, 42]. However there is a moderate increase in this property caused by the restriction in molecular mobility of the matrix imposed by the nanofillers and also the enhanced stiffness of graphene composites caused a damping variation and hence the nanocomposite  $T_g$  was increased [12, 41]. This property was enhanced up to  $\sim 9^{\circ}C$  when incorporating 0.1 wt.% f-CNT or 0.3 wt.% RGO. The temperature of decomposition

( $T_d$ ) of the lowest and highest filler content in the nylon 6,6 was investigated; Table 4 also summarises the results obtained from TGA measurements. The temperatures at which 10% and 50% weight loss occurred were the criteria for determining the thermal stability. In most cases, the nanocomposite  $T_d$  remained unchanged. Enhanced thermal stability has been associated to the filler good dispersion in the polymer; the nanofillers act as restriction sites reducing segmental

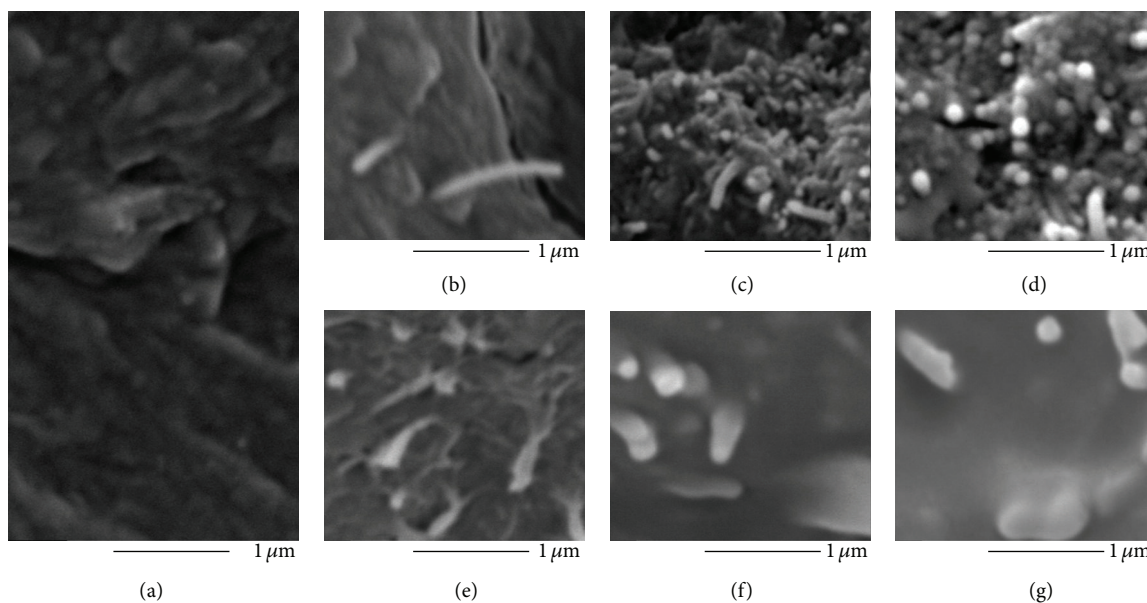


FIGURE 6: SEM micrograph of fracture surface of (a) neat nylon 6,6 and higher magnification micrographs of fracture surface of nanocomposites containing 0.5 wt. % of (b) CNT, (c) OCNT, (d) f-CNT, (e) RGO, (f) GO, and (g) f-Ge.

mobility of the polymer chains. The reduced mobility in turn assists in preventing scission of chains driven by thermal excitation [43]. Liu et al. [44] obtained well-dispersed nanocomposites of PMMA/CNTs and TGA analyses showed that  $T_d$  is similar to that of the polymer when a nitrogen atmosphere was used. Other studies [12, 40, 43] have indicated that the  $T_d$  of nanocomposites is comparable to the matrix when tested under an inert atmosphere. Li et al. [40] concluded that the presence of CNTs hinders the thermooxidation of nylon 6 under air and thus increases the thermal stability of the polymer. However, this effect was not found for all the CNTs/nylon 6 composites under nitrogen atmosphere without the participation of oxygen [40]. Despite the results obtained, the GO addition into nylon 6,6 enhanced this property. The GO nanocomposites displayed an increase of  $\sim 6^\circ\text{C}$  and  $\sim 5^\circ\text{C}$  at 10 wt.% and 50 wt.% loss, respectively, for the highest nanofiller content.

Figures 6, 7, and 8 show the cryogenic fracture surface of pure polymer and nanocomposites. High magnification micrographs are included in Figure 6 showing the embedding of the carbon nanomaterials in the polymer matrix and protruding of some of them. Figures 6(b), 6(c), and 6(d) show a few CNTs pulled-out of nylon 6,6 matrix. On the other hand, Figures 6(e), 6(f), and 6(g) exhibit the presence of graphene sheets with the edges emerging out of the matrix. The presence of graphene sheets was corroborated by the size of these platelets; GO prepared via chemical routes and sonication typically yield GO sheets with diameters of hundreds of nanometers and rarely exceed a few microns [45]. Therefore, this observation is supported by taking into account that all the graphene based materials employed in this work were obtained from GO (either by reduction or further

functionalisation), by doing a close examination of TEM images obtained in previous works [7, 8] and also by comparing SEM images of nanocomposites reported by other research groups [46, 47]. Furthermore, the micrographs of neat polymer (Figure 6(a)) and nanocomposites (Figures 7 and 8) show the sample morphology and dispersion of the nanofillers in the reinforced samples. The surface of the nanocomposites appeared coarser than that of the neat polymer by showing many fracture ditches indicating that the nanofillers prevented the crack propagation, as it has been found by other studies of carbon based nanocomposites [37, 44]. The 1D carbon reinforcements were well dispersed within the matrix as shown by the bright dots attributed to the broken ends of the nanotubes. A few pulled-out nanotubes are shown in the pristine CNT based nanocomposites as indicated by the red arrows in Figures 7(a) and 7(b). The functionalisation of the nanofillers diminished the presence of pulled-out nanotubes indicating the good interfacial interaction with the matrix, as seen in Figures 7(c) to 7(f). Nevertheless, the sample containing 0.5 wt.% f-CNT showed the thickest bright dots, indicating the presence of nanotube agglomerates in this nanocomposite, as it was shown by the response in the mechanical analysis. Figure 8 shows the graphene sheets protruding out of the fracture surface and some of them are indicated by red arrows. The rest of the bright dots appearing in these micrographs can be attributed to the edges of the graphene sheets or small nanosheets. These features show that the graphene sheets were well dispersed and embedded in the nylon matrix. The surface of the nanocomposite containing 0.5 wt.% f-Ge showed the smoothest surface; however, the graphene sheets were coated with polymer, indicating strong polymer interaction.

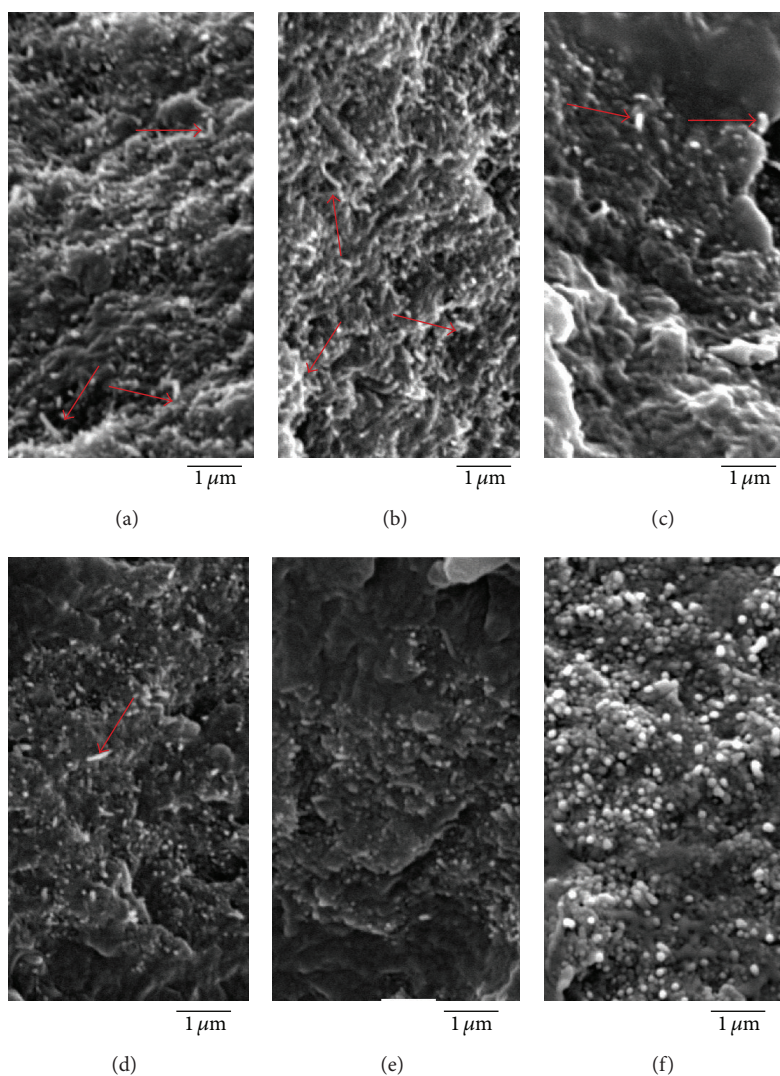


FIGURE 7: SEM micrographs of (a) 0.1 wt.% CNT, (b) 0.5 wt.% CNT, (c) 0.1 wt.% OCNT, (d) 0.5 wt.% OCNT, (e) 0.1 wt.% f-CNT, and (f) 0.5 wt.% f-CNT nanocomposites.

#### 4. Conclusions

Nylon 6,6 was reinforced using 1D and 2D carbon nanofillers. The addition of the nanofillers provided a very little increase in the crystallinity of the polymer and there was no significant influence in this property attributed to the functionalisation of the nanofillers. The crystallisation curves revealed the effect in crystal growth when using differently structured carbon nanofillers. CNT based nanocomposites were crystallised at higher temperatures than graphene based nanocomposites. However the crystal growth in graphene based nanocomposites was faster. The method employed for obtaining the nanocomposites is compatible with current industrial processes and revealed interesting crystal features. All nanofillers favoured the perfection of the crystals. The stiffness of the polymer was increased and the improvement was more noticeable in graphene based nanocomposites. The mechanical response of most nanocomposites was enhanced as the nanofiller content increased. f-CNT nanocomposites

showed an opposite behaviour due to the agglomeration of the nanotubes at high content as confirmed by SEM images; however, the modulus was 30% higher than nylon 6,6 when using 0.1 wt.% of this nanofiller. GO showed to be the best reinforcing material at all contents when compared with the rest of the nanofillers. In addition, the nanocomposite containing 0.5 wt.% GO improved the thermal stability by  $\sim 5^{\circ}\text{C}$ . Graphene based composites showed the best thermo-mechanical properties owned to the dimensionality of this material. Examination of the neat polymer and nanocomposite fracture surfaces revealed differences between the two types of carbon nanofillers as well as interesting features for the different functionalised reinforcements.

#### Conflict of Interests

The authors declare that there is no conflict of interests regarding the publication of this paper.

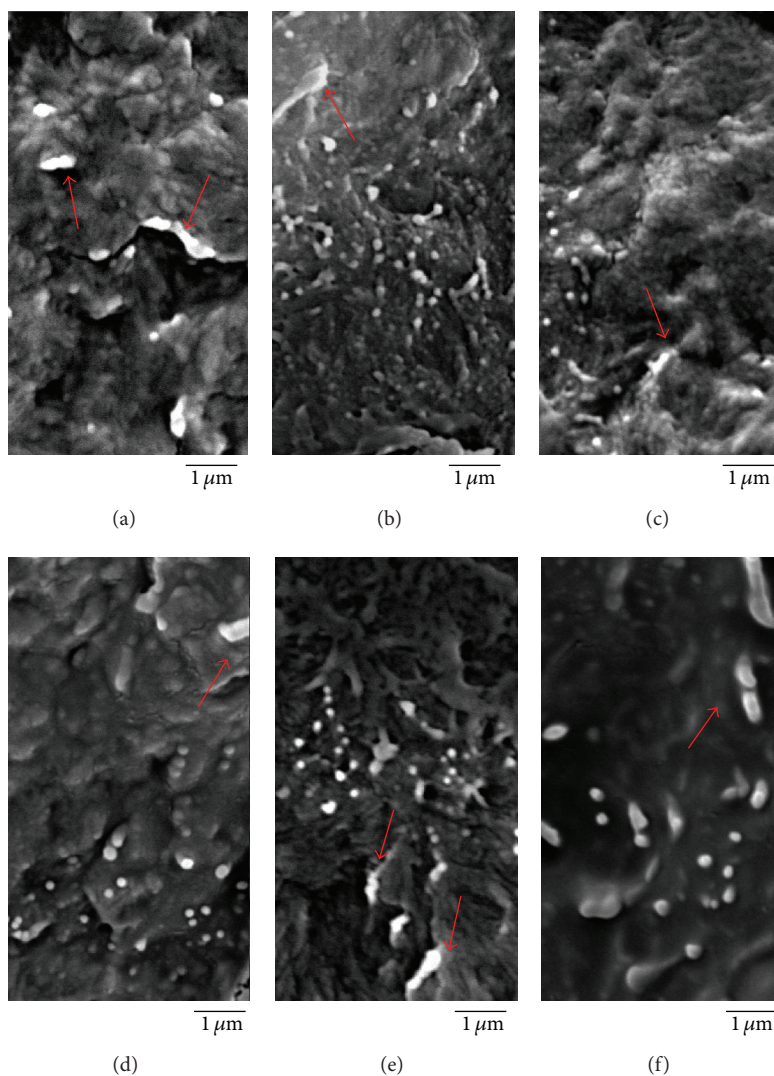


FIGURE 8: SEM micrographs of (a) 0.1 wt.% RGO, (b) 0.5 wt.% RGO, (c) 0.1 wt.% GO, (d) 0.5 wt.% GO, (e) 0.1 wt.% f-Ge, and (f) 0.5 wt.% f-Ge nanocomposites.

## Acknowledgments

The authors are grateful to O. Davalos Montoya for her help in DSC analyses, A. L. Rodríguez Villanueva for her assistance in WAXD measurements, and F. Ureña-Nuñez for his help in TGA measurements. They are also grateful to A. del Real López for her assistance in SEM and R. Preza for his technical assistance. Ph.D. student F. Navarro-Pardo is thankful to CONACYT for the Grant no. 213733 and to Universidad Autónoma de Estado de México for the use of facilities. Authors are grateful to PROMEP due to its financial support in this research.

## References

- [1] S. Park, J. An, R. D. Piner et al., "Aqueous suspension and characterization of chemically modified graphene sheets," *Chemistry of Materials*, vol. 20, no. 21, pp. 6592–6594, 2008.
- [2] X. Shen, L. Jiang, Z. Ji, J. Wu, H. Zhou, and G. Zhu, "Stable aqueous dispersions of graphene prepared with hexamethylenetetramine as a reductant," *Journal of Colloid and Interface Science*, vol. 354, no. 2, pp. 493–497, 2011.
- [3] V. Datsyuk, M. Kalyva, K. Papagelis et al., "Chemical oxidation of multiwalled carbon nanotubes," *Carbon*, vol. 46, no. 6, pp. 833–840, 2008.
- [4] H. L. Guo, X. F. Wang, Q. Y. Qian, F. B. Wang, and X. H. Xia, "A green approach to the synthesis of graphene nanosheets," *ACS Nano*, vol. 3, no. 9, pp. 2653–2659, 2009.
- [5] W. Chen, L. Yan, and P. R. Bangal, "Preparation of graphene by the rapid and mild thermal reduction of graphene oxide induced by microwaves," *Carbon*, vol. 48, no. 4, pp. 1146–1152, 2010.
- [6] A. L. Martínez -Hernández, C. Velasco-Santos, and V. M. Castaño, "Carbon nanotubes composites: processing, grafting and mechanical and thermal properties," *Current Nanoscience*, vol. 6, no. 1, pp. 12–39, 2010.

- [7] F. Navarro-Pardo, G. Martínez -Barrera, A. L. Martínez -Hernández et al., "Nylon 6,6 electrospun fibres reinforced by amino functionalised 1D and 2D carbon," *IOP Conference Series: Materials Science and Engineering*, vol. 40, Article ID 012023, 2012.
- [8] F. Navarro-Pardo, G. Martínez -Barrera, A. L. Martínez -Hernández et al., "Effects on the thermo-mechanical and crystallinity properties of nylon 6, 6 electrospun fibres reinforced with one dimensional (1D) and two dimensional (2D) carbon," *Materials*, vol. 6, pp. 3494–3513, 2013.
- [9] C. Rong, G. Ma, S. Zhang et al., "Effect of carbon nanotubes on the mechanical properties and crystallization behavior of poly(ether ether ketone)," *Composites Science and Technology*, vol. 70, no. 2, pp. 380–386, 2010.
- [10] X. Chen, X. Chen, M. Lin, W. Zhong, X. Chen, and Z. Chen, "Functionalized multi-walled carbon nanotubes prepared by in situ polycondensation of polyurethane," *Macromolecular Chemistry and Physics*, vol. 208, no. 9, pp. 964–972, 2007.
- [11] G. Mago, C. Velasco-Santos, A. L. Martinez-Hernandez, D. M. Kalyon, and F. T. Tisher, "Effect of functionalization on the crystallization behavior of MWNT-PBT nanocomposites," *Materials Research Society Symposium Proceedings*, vol. 1056, pp. 295–300, 2008.
- [12] P. Song, Z. Cao, Y. Cai, L. Zhao, Z. Fang, and S. Fu, "Fabrication of exfoliated graphene-based polypropylene nanocomposites with enhanced mechanical and thermal properties," *Polymer*, vol. 52, pp. 4001–4010, 2011.
- [13] J. Shen, B. Yan, M. Shi et al., "Synthesis of graphene oxide-based biocomposites through diimide-activated amidation," *Journal of Colloid and Interface Science*, vol. 356, pp. 543–549, 2011.
- [14] J. Shen, M. Shi, B. Yan et al., "Covalent attaching protein to graphene oxide via diimide-activated amidation," *Colloids and Surfaces B: Biointerfaces*, vol. 81, no. 2, pp. 434–438, 2010.
- [15] M. Seredych, J. A. Rossin, and T. J. Bandoz, "Changes in graphite oxide texture and chemistry upon oxidation and reduction and their effect on adsorption of ammonia," *Carbon*, vol. 49, no. 13, pp. 4392–4402, 2011.
- [16] A. R. Bhattacharyya, P. Pötschke, L. Häußler, and D. Fischer, "Reactive compatibilization of melt mixed PA6/SWNT composites: mechanical properties and morphology," *Macromolecular Chemistry and Physics*, vol. 206, no. 20, pp. 2084–2095, 2005.
- [17] Y. S. Yun, Y. H. Bae, D. H. Kim, J. Y. Lee, I. J. Chin, and H. J. Jin, "Reinforcing effects of adding alkylated graphene oxide to polypropylene," *Carbon*, vol. 49, no. 11, pp. 3553–3559, 2011.
- [18] Y. Lu, Y. Zhang, G. Zhang, M. Yang, S. Yan, and D. Shen, "Influence of thermal processing on the perfection of crystals in polyamide 66 and polyamide 66/clay nanocomposites," *Polymer*, vol. 45, no. 26, pp. 8999–9009, 2004.
- [19] L. Li, C. Y. Li, C. Ni, L. Rong, and B. Hsiao, "Structure and crystallization behavior of nylon 66/multi-walled carbon nanotube nanocomposites at low carbon nanotube contents," *Polymer*, vol. 48, no. 12, pp. 3452–3460, 2007.
- [20] J. Z. Xu, T. Chen, C. L. Yang et al., "Isothermal crystallization of poly(L-lactide) induced by graphene nanosheets and carbon nanotubes: a comparative study," *Macromolecules*, vol. 43, no. 11, pp. 5000–5008, 2010.
- [21] F. R. Lamastra, D. Puglia, M. Monti et al., "Poly( $\epsilon$ -caprolactone) reinforced with fibres of poly(methyl methacrylate) loaded with multiwall carbon nanotubes or graphene nanoplatelets," *Chemical Engineering Journal*, vol. 196, pp. 140–148, 2012.
- [22] S. Chatterjee, F. A. Nüesch, and B. T. Chu, "Crystalline and tensile properties of carbon nanotube and graphene reinforced polyamide 12 fibers," *Chemical Physics Letters*, vol. 557, pp. 92–96, 2013.
- [23] S. Chatterjee, F. A. Nüesch, and B. T. T. Chu, "Comparing carbon nanotubes and graphene nanoplatelets as reinforcements in polyamide 12 composites," *Nanotechnology*, vol. 22, no. 27, Article ID 275714, 2011.
- [24] D. J. Lin, C. L. Chang, C. K. Lee, and L. P. Cheng, "Fine structure and crystallinity of porous nylon 66 membranes prepared by phase inversion in the water/formic acid/nylon 66 system," *European Polymer Journal*, vol. 42, no. 2, pp. 356–367, 2006.
- [25] N. S. Murthy, "Recent developments in polymer characterization using X-ray diffraction," *The Rigaku Journal*, vol. 20, no. 1, pp. 15–24, 2004.
- [26] A. Marcellan, A. R. Bunsell, L. Laiarinandrasana, and R. Piques, "A multi-scale analysis of the microstructure and the tensile mechanical behaviour of polyamide 66 fibre," *Polymer*, vol. 47, no. 1, pp. 367–378, 2006.
- [27] N. Dencheva, Z. Denchev, M. J. Oliveira, and S. S. Funari, "Relationship between crystalline structure and mechanical behavior in isotropic and oriented polyamide 6," *Journal of Applied Polymer Science*, vol. 103, no. 4, pp. 2242–2252, 2007.
- [28] H. P. Klug and L. E. Alexander, *X-Ray Diffraction Procedures for Polycrystalline and Amorphous Materials*, John Wiley & Sons, New York, NY, USA, 2nd edition, 1974.
- [29] L. M. Guerrini, M. C. Branciforti, T. Canova, and R. E. S. Bretas, "Electrospinning and characterization of polyamide 66 nanofibers with different molecular weights," *Materials Research*, vol. 12, no. 2, pp. 181–190, 2009.
- [30] J. Coates, "Interpretation of infrared spectra, a practical approach," in *Encyclopedia of Analytical Chemistry*, R. A. Meyers, Ed., pp. 1–22, John Wiley & Sons, New York, NY, USA, 2000.
- [31] J. Charles, G. R. Ramkumaar, S. Azhagiri, and S. E. Gunasekaran, "FTIR and thermal studies on nylon-66 and 30% glass fibre reinforced nylon-66," *Journal of Chemistry*, vol. 6, no. 1, pp. 23–33, 2009.
- [32] T. Ishisue, M. Okamoto, and K. Tashiro, "Real-time investigation of crystallization in nylon 6-clay nano-composite probed by infrared spectroscopy," *Polymer*, vol. 51, pp. 5585–5591, 2010.
- [33] C. Caamaño, B. Grady, and D. E. Resasco, "Influence of nanotube characteristics on electrical and thermal properties of MWCNT/polyamide 6, 6 composites prepared by melt mixing," *Carbon*, vol. 50, no. 10, pp. 3694–3707, 2012.
- [34] J. K. W. Sandler, S. Pegel, M. Cadek et al., "A comparative study of melt spun polyamide-12 fibres reinforced with carbon nanotubes and nanofibres," *Polymer*, vol. 45, no. 6, pp. 2001–2015, 2004.
- [35] C. I. Ferreira, C. Dal Castel, M. A. S. Oviedo, and R. S. Mauler, "Isothermal and non-isothermal crystallization kinetics of polypropylene/exfoliated graphite nanocomposites," *Thermochimica Acta*, vol. 553, pp. 40–48, 2013.
- [36] S. Kumar, T. Rath, R. N. Mahaling, and C. K. Das, "Processing and characterization of carbon nanofiber/syndiotactic polystyrene composites in the absence and presence of liquid crystalline polymer," *Composites A*, vol. 38, no. 5, pp. 1304–1317, 2007.
- [37] F. C. Chiu and G. F. Kao, "Polyamide 46/multi-walled carbon nanotube nanocomposites with enhanced thermal, electrical, and mechanical properties," *Composites Part: A*, vol. 43, pp. 208–218, 2012.
- [38] F. C. Chiu and I. N. Huang, "Phase morphology and enhanced thermal/mechanical properties of polyamide 46/graphene

- oxide nanocomposites,” *Polymer Testing*, vol. 31, pp. 953–962, 2012.
- [39] H. Meng, G. X. Sui, P. F. Fang, and R. Yang, “Effects of acid- and diamine-modified MWNTs on the mechanical properties and crystallization behavior of polyamide 6,” *Polymer*, vol. 49, no. 2, pp. 610–620, 2008.
- [40] J. Li, L. Tong, Z. Fang, A. Gu, and Z. Xu, “Thermal degradation behavior of multi-walled carbon nanotubes/polyamide 6 composites,” *Polymer Degradation and Stability*, vol. 91, no. 9, pp. 2046–2052, 2006.
- [41] R. K. Layek, S. Samanta, D. P. Chatterjee, and A. K. Nandi, “Physical and mechanical properties of poly(methyl methacrylate) functionalized graphene/poly(vinylidene fluoride) nanocomposites: piezoelectric  $\beta$ -polymorph formation,” *Polymer*, vol. 51, pp. 5846–5856, 2010.
- [42] S. Vadukumpully, J. Paul, N. Mahanta, and S. Valiyaveetil, “Flexible conductive graphene/poly(vinyl chloride) composite thin films with high mechanical strength and thermal stability,” *Carbon*, vol. 49, no. 1, pp. 198–205, 2011.
- [43] H. Deng, E. Bilotti, R. Zhang et al., “Improving tensile strength and toughness of melt processed polyamide 6/multiwalled carbon nanotube composites by in situ polymerization and filler surface functionalisation,” *Journal of Applied Polymer Science*, vol. 120, no. 1, pp. 133–140, 2011.
- [44] J. Liu, A. Rasheed, M. L. Minus, and S. Kumar, “Processing and properties of carbon nanotube/ poly( methyl methacrylate) composite films,” *Journal of Applied Polymer Science*, vol. 112, no. 1, pp. 142–156, 2009.
- [45] M. Cai, D. Thorpe, D. H. Adamson, and H. C. Schniepp, “Methods of graphite exfoliation,” *Journal of Materials Chemistry*, vol. 22, pp. 24992–25002, 2012.
- [46] Y. Mao, S. Wen, Y. Chen et al., “High performance graphene oxide based rubber composites,” *Scientific Reports*, vol. 3, article 2508, 2013.
- [47] D. Cai and M. Song, “Recent advance in functionalized graphene/polymer nanocomposites,” *Journal of Materials Chemistry*, vol. 20, pp. 7906–7915, 2010.

## Research Article

# First-Principle Study of H<sub>2</sub> Adsorption on LaFeO<sub>3</sub>(110) Surface

Yu-Hong Chen,<sup>1,2</sup> Bing-Wen Zhang,<sup>1</sup> Liang Yang,<sup>1</sup>  
Mei-Ling Zhang,<sup>1</sup> Cai-Rong Zhang,<sup>1,2</sup> Long Kang,<sup>2</sup> and Yong-Chun Luo<sup>2</sup>

<sup>1</sup> School of Science, Lanzhou University of Technology, Lanzhou 730050, China

<sup>2</sup> State Key Laboratory of Gansu Advanced Non-Ferrous Metal Materials, Lanzhou University of Technology, Lanzhou 730050, China

Correspondence should be addressed to Yu-Hong Chen; lzchenyh@163.com

Received 15 January 2014; Revised 6 May 2014; Accepted 12 May 2014; Published 21 July 2014

Academic Editor: Jinlong Jiang

Copyright © 2014 Yu-Hong Chen et al. This is an open access article distributed under the Creative Commons Attribution License, which permits unrestricted use, distribution, and reproduction in any medium, provided the original work is properly cited.

The adsorption of H<sub>2</sub> molecule on LaFeO<sub>3</sub>(110) surface was studied by first-principle calculations. Based on the adsorption sites, adsorption energies, and electronic structures, it can be found that one H atom can be adsorbed on O atom and form -OH with the O atom, which is the most stable structure. One H atom can be adsorbed on one Fe atom, which makes Fe<sup>3+</sup> turn to Fe<sup>2+</sup>. Two H atoms can form H<sub>2</sub>O molecule with O atom, which makes it possible to form oxygen vacancy on the surface.

## 1. Introduction

Nickel-metal (NI-MH) batteries have been widely studied for its favorable property such as high capacity, fast charge and discharge rate, environmental compatibility, and long stable periods [1]. Cathode material has a great effect on the performance of NI-MH batteries. Traditional negative materials are hydrogen storage alloys including AB<sub>5</sub>, AB<sub>2</sub>, AB, and Mg-based alloys [2, 3]. Although AB<sub>5</sub>-type alloys have been widely applied in various devices, it has high cost and low capacity. Therefore, a lot of researches have been carried out to develop new negative materials to reduce the cost and improve the capacity. In recent years, Perovskite ABO<sub>3</sub> has attracted a lot of attention as potential negative materials [4, 5].

The capacity of perovskite ABO<sub>3</sub> as cathode material is much higher than that of traditional materials. Mandal et al. [6] have developed an unprecedented intake of hydrogen by BaMnO<sub>3</sub>/Pt to the extent of 1.25 w.% at moderate temperatures (190–260°C) and ambient pressure. Esaka et al. [7] have proposed perovskite-type oxides ACe<sub>1-x</sub>M<sub>x</sub>O<sub>3-δ</sub> (A = Sr or Ba, M = rare earth element) prepared by a conventional solid-state reaction method as innovative electrode materials for Ni-MH batteries. Deng et al. [8] have reported that the reversible capacity of perovskite La<sub>1-x</sub>Sr<sub>x</sub>FeO<sub>3</sub> was more than 500 mAh/g at a discharge current density of 31.25 mA/g when the temperature rises to 333 K, which is much higher

than that of AB<sub>5</sub> alloys [9]. Considering the high capacity and abundance of La, perovskite LaFeO<sub>3</sub> has been studied widely as potential negative materials for Ni-MH batteries. Deng et al. [10] have reported that before the 20th cycle, the discharge capacity of LaFeO<sub>3</sub> keeps steady at about 80 mAh/g, 160 mAh/g, and 350 mAh/g at 298 K, 313 K, and 333 K, respectively. However, the electrochemical hydrogen storage mechanism of the perovskite oxide still remains uncertain, and it requires more investigation to know how the H atoms combine with the perovskite oxide. In this research, we employed density functional theory (DFT) to investigate the slab character of LaFeO<sub>3</sub> and hydrogen adsorption on the slab aiming to explain the adsorption mechanism of reaction and provide theoretical guidance for correlative experiment.

## 2. Models and Computational Methods

**2.1. Models.** In this paper, we employed the slab model which is widely used in surface calculation. The structure of LaFeO<sub>3</sub> belongs to orthorhombic crystal system, whose space group is Pbnm [11]. As for LaFeO<sub>3</sub>(110) slab, there are two kinds of models which we defined as Model I and Model II. Taking accuracy and speed in consideration, we simulate the LaFeO<sub>3</sub>(110) surface with a 4-layer model and for further discussion a 7-layer model will be studied for improving and comparison. The structure parameter of H<sub>2</sub> molecule which

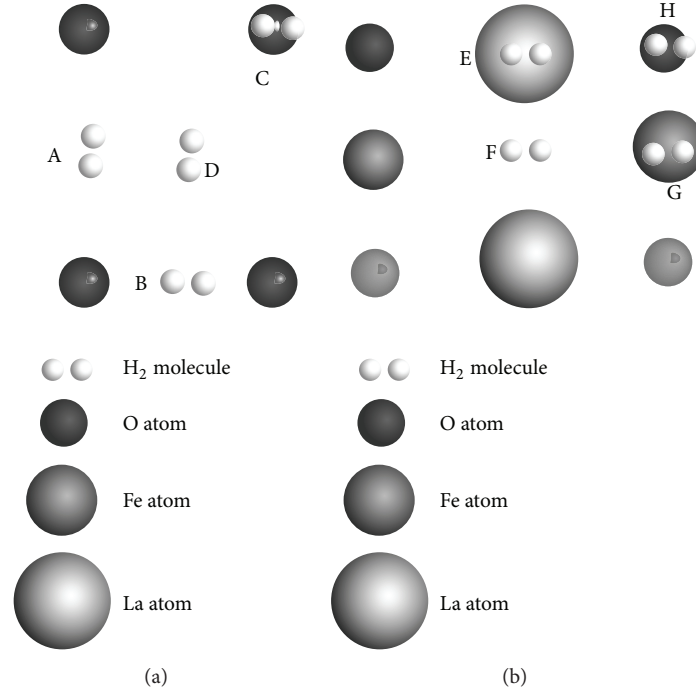


FIGURE 1: Vertical view of all symmetrical adsorption sites: (a) Model I (b) Model II. ((A): O long bridge; (B): O short bridge; (C): O top; (D): O cave; (E): La top; (F): La bridge; (G): Fe top; (H): O top).

is about to be adsorbed is  $0.741 \text{ \AA}$  and the thickness of vacuum is set at  $20 \text{ \AA}$ . When the model is set up, 8 favorable sites are taken in calculation, which is shown in Figure 1.  $\text{H}_2$  molecule is put on all the sites separately parallel to the crystal surface.

**2.2. Computational Methods.** The first-principle calculations are performed with Cambridge serial total energy package (CASTEP) in the framework of density functional theory (DFT), which is based on the plane-wave pseudopotential. The exchange and correlation energy were treated within the generalized gradient approximation (GGA) of Perdew-Burke-Ernzerhof (PBE). The electron-ion interaction is described with ultrasoft pseudopotential (UUSP). After testing the model with  $k$ -point grid set  $a \times a \times 1$  ( $a = 3, 4, 5, 6$ ), it is decided to use the supercells consisting of  $5 \times 5 \times 1$  unit cell for the doped system calculations. All the calculations are carried out non-spin-polarized with a kinetic energy cutoff of  $340 \text{ eV}$ , and the convergence criteria for energy and displacement are  $2 \times 10^{-6} \text{ eV/atom}$  and  $10^{-3} \text{ \AA}$ , respectively. The calculated structure parameters of  $\text{H}_2$  molecule are  $0.746 \text{ \AA}$ , which agrees well with experimental results [12].

Moreover, the structure parameters of  $\text{LaFeO}_3(110)$  surface is  $a = b = c = 3.926 \text{ \AA}$ , which is the same as experimental results.

### 3. Results and Discussions

**3.1. Decision of the Adsorption Sites of  $\text{H}_2$  Molecule on  $\text{LaFeO}_3(110)$  Surface.** Table 1 lists the energies and structure parameters of all possible sites. It is defined that  $r_{\text{H-H}}$ ,  $r_{\text{H-O}}$ ,

$r_{\text{H-Fe}}$ , and  $r_{\text{H-La}}$  are the shortest distances of H atoms, H atom and O atom, H atom and Fe atom, and H atom and La atom, respectively. The dissociation energy of  $\text{H}_2$  molecule is defined as the following equation:

$$E = -(E_{\text{H}_2} - 2E_{\text{H}}). \quad (1)$$

$E_{\text{H}_2}$  and  $E_{\text{H}}$  represent the energy of  $\text{H}_2$  molecule and H atom, respectively. The adsorption energy of  $\text{H}_2$  molecule is defined in the following equation:

$$E_{\text{ads}} = E_{\text{H}_2} + E_{\text{clean}} - E_{\text{slab}/\text{H}_2}. \quad (2)$$

$E_{\text{clean}}$  and  $E_{\text{slab}/\text{H}_2}$  represent the energy of clean crystal surface and the surface with two adsorbed H atoms, respectively. According to the definitions above, it can be inferred that (1) the structure of  $\text{LaFeO}_3(110)/\text{H}_2$  is stable when  $E_{\text{ads}}$  is positive, and the bigger the  $E_{\text{ads}}$  is, the more stable the structure will be; (2) it means that the  $\text{H}_2$  molecule has been dissociated when  $E$  is positive.

According to the results in Table 1, the adsorption of  $\text{H}_2$  molecule on sites a, b, c, h, and f belong to chemical adsorptions, and they are physical adsorptions when  $\text{H}_2$  molecule is put on the other sites.

All the chemical adsorption sites are shown in Figure 2. The data in the figure are representative of distances between H atoms, whose unit is  $\text{ \AA}$ . By analysing the data in Table 1 and adsorption in Figure 2, we can find the following.

- (1) On both site a and site b, the  $\text{H}_2$  molecule is dissociated into two H atoms and then each H atom is absorbed by O atom, which is a chemical adsorption.

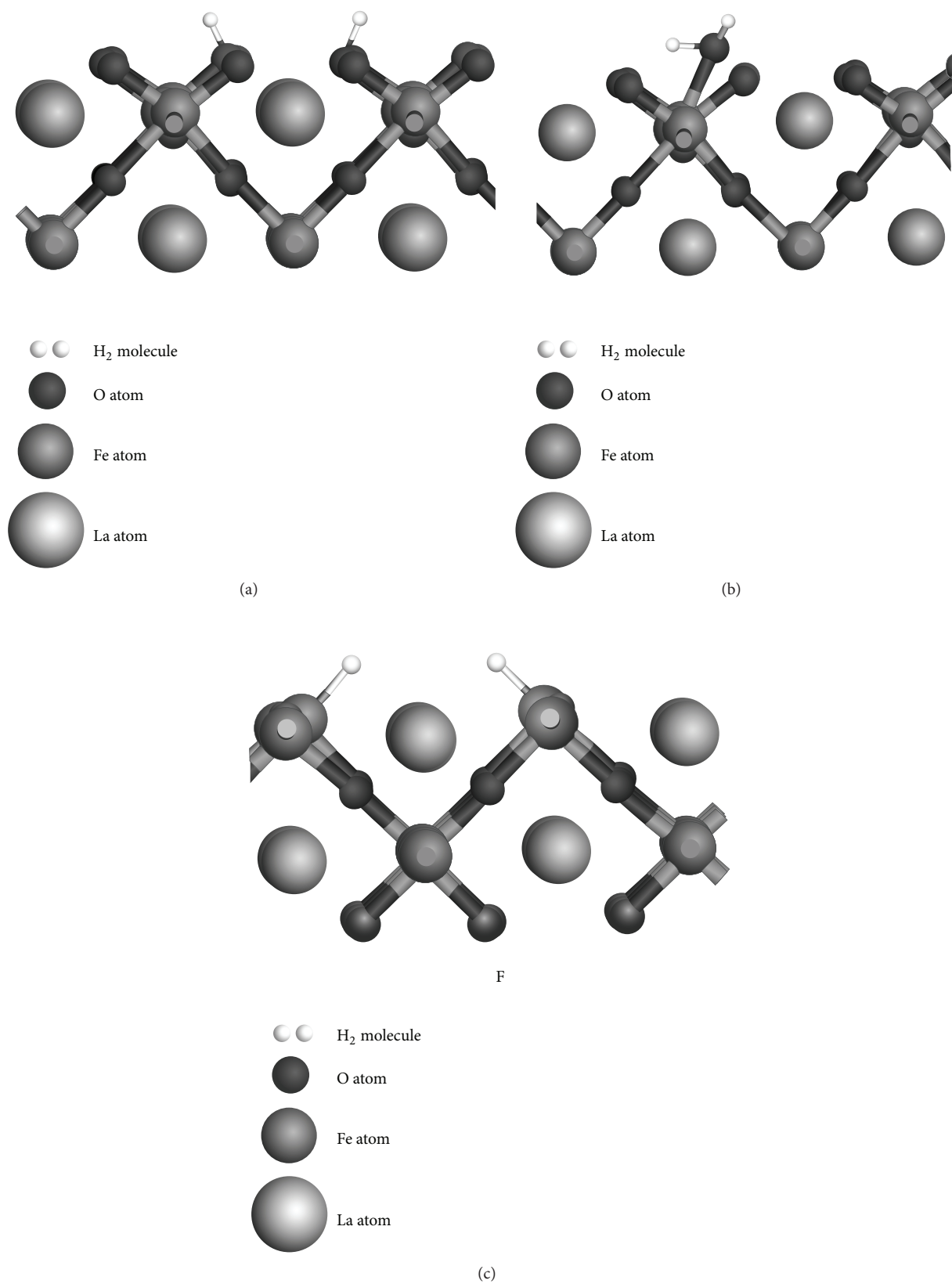


FIGURE 2: Figure 2: All the sites where a chemical adsorption occurs. Model I: (a) O short bridge; (b) O top. Model II: (F) La bridge.

TABLE 1: Energies and structure parameters of possible sites.

LaFeO <sub>3</sub> (110) surface	Possible adsorption sites	$r_{\text{H-H}}/\text{\AA}$	$r_{\text{H-O}}/\text{\AA}$	$r_{\text{H-Fe}}/\text{\AA}$	$r_{\text{H-La}}/\text{\AA}$	$E_{\text{ads}}/\text{eV}$	$E/\text{eV}$
	Free H <sub>2</sub>	0.746	—	—	—	—	4.502
Model I	O long bridge (a)	3.431	0.980	2.389	3.456	3.130	-1.854
	O short bridge (b)	3.471	0.982	2.373	3.505	3.507	-1.878
	O top (c)	1.613	0.981	2.202	3.877	2.389	1.220
	O cave (d)	0.760	17.335	18.359	18.677	0.370	4.495
Model II	La top (e)	0.765	18.411	19.500	19.213	0.357	4.494
	La bridge (f)	2.968	2.677	1.571	2.853	1.898	-1.542
	Fe top (g)	0.760	16.978	17.477	18.359	0.248	4.495
	O top (h)	4.784	2.229	1.587	2.966	1.829	-2.186

TABLE 2: Structure parameters and energies of the crystal surface.

Initial position of H <sub>2</sub>	$r_{\text{H-H}}/\text{\AA}$	$r_{\text{H-O}}/\text{\AA}$	$r_{\text{H-Fe}}/\text{\AA}$	$r_{\text{H-La}}/\text{\AA}$	$E_{\text{ads}}/\text{eV}$	$E/\text{eV}$
O top in Model II	2.968	2.677	1.571	2.853	1.898	-1.542
O short bridge in Model I	3.647	0.976	2.332	3.367	4.713	-1.956

- (2) On both site h and site f, after dissociation of the the H<sub>2</sub> molecule, each H atom is absorbed by Fe atom, which is chemical adsorption.
- (3) On site c, after adsorption, the structure parameters ( $r_{\text{H-H}} = 1.613 \text{\AA}$ ,  $r_{\text{H-O}} = 1.007 \text{\AA}$ ) are close to the experimental parameters that Gu et al. [13] have reported ( $r_{\text{H-H}} = 1.545 \text{\AA}$ ,  $r_{\text{H-O}} = 0.978 \text{\AA}$ ). We can infer that H<sub>2</sub>O molecule is formed, which makes it possible to form an oxygen vacancy if the H<sub>2</sub>O molecule gets rid of the crystal surface [14].

Considering the accuracy, a model consisting of 7 layers of atoms is adopted. Table 2 lists the structure parameters and energies of the crystal surface. According to the data in the table, the surface with H atoms absorbed on O atoms is more stable than that with H atoms absorbed on Fe atoms and both are chemical adsorptions.

**3.2. The Adsorption Mechanism of H<sub>2</sub> Molecule on O Short Bridge in Model I.** The following discussions are about the properties on O short bridge in Model I including Mulliken charge population, density of states, and electron localization function.

**3.2.1. Mulliken Charge Population.** It shows the information of interaction between the H<sub>2</sub> molecule and the crystal surface by analysing Mulliken charge population. Table 3 lists the Mulliken Charge population before and after adsorption, respectively. The H atoms get positive charges and the crystal surface is negatively charged after adsorption. The change of charges on the surface takes 69.5% of total change, which indicates that the H<sub>2</sub> molecules mainly interact with the atoms on the surface. Moreover, surface potential falls after adsorption, which means the structure is more stable.

**3.2.2. Density of States (DOS).** The information of interaction between atoms can be obtained by analysing the change of valance states and energies. Figure 3 lists density of states of

TABLE 3: Mulliken population on O short bridge in Model I.

Layer	Atom	Charges before adsorption	Charges after adsorption
First	H		0.40
	H		0.40
	O	-0.61	-0.68
	O	-0.61	-0.82
	O	-0.61	-0.82
Second	O	-0.61	-0.64
	O	-0.65	-0.65
	La	1.68	1.65
Third	Fe	0.77	0.76
	O	-0.69	-0.69
Fourth	O	-0.70	-0.70
	Fe	1.23	1.21
	La	0.28	0.29

H<sub>2</sub> molecule adsorption on O short bridge in Model I before and after adsorption, respectively. By analysing the data, we can find that the energy of highest occupied states (HOS) is between -6.5 eV and 3.0 eV, which is mainly caused by O 2p electrons and Fe 3d electrons. In contrast, the energy of HOS has changed to that which is between -8.0 eV and 0.5 eV after adsorption, which is mainly caused by H 1s electron, O 2p electrons, and Fe 3d electrons. The HOS of electrons moved to deeper levels after adsorption. That is to say, the structure becomes more stable after adsorption. And the H<sub>2</sub> molecule is dissociated absolutely after adsorption. In addition, H 1s not only overlaps but also resonates with O 2s and O 2p; it means that H atom forms -OH with O atom after adsorption.

**3.2.3. Electron Localization Function (ELF).** Properties of bonds between atoms can be analysed by ELF. The range of ELF is the interval from 0 to 1. The closer ELF to 1, the deeper

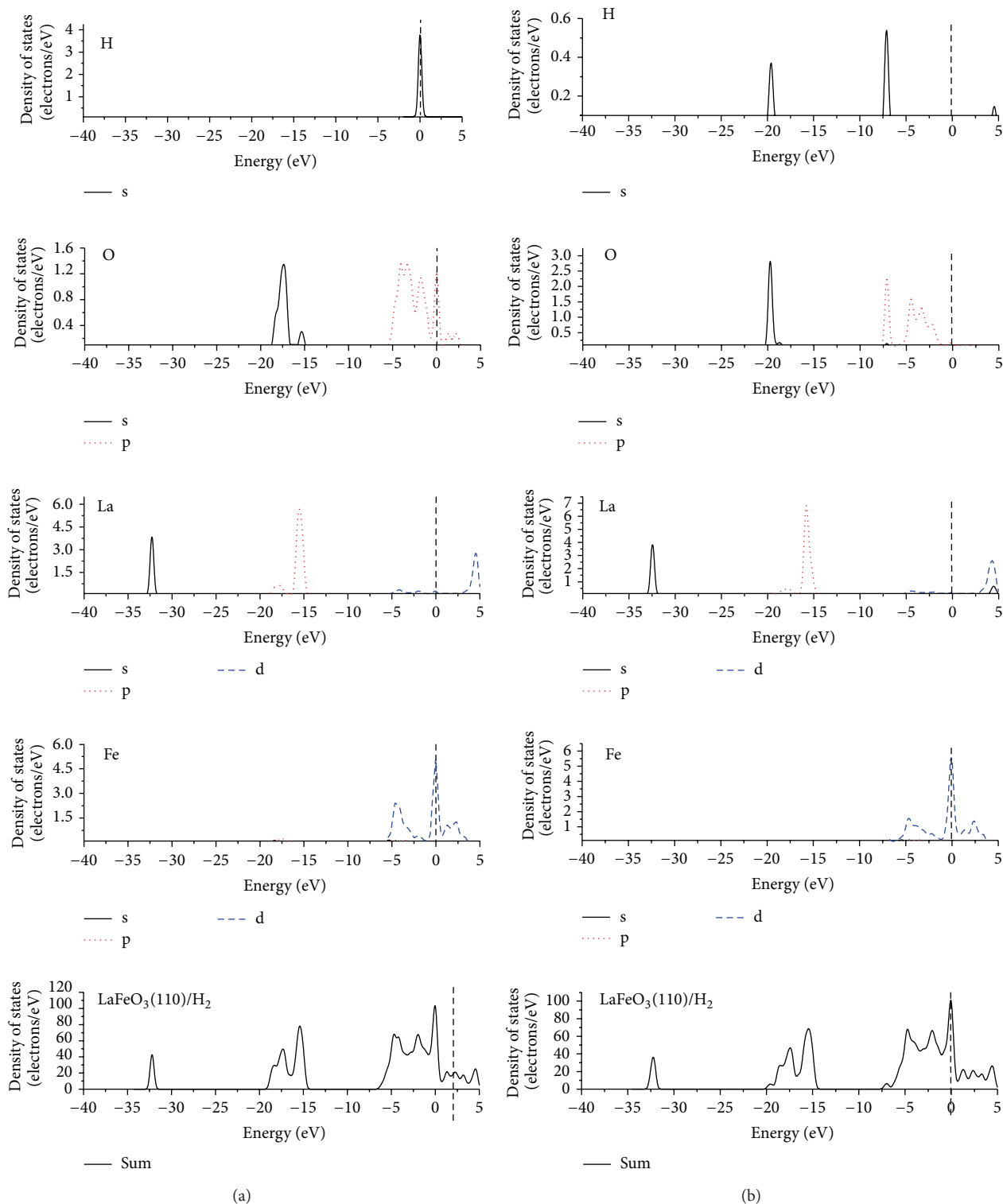


FIGURE 3: DOS on O short bridge in Model I (a) before adsorption and (b) after adsorption.

the electron localization degree. On the other hand, if ELF is close to zero, the electrovalent bond will be strong.

Figure 5(a) lists the ELF of  $\text{LaFeO}_3(110)$  surface with H atoms absorbed on O atoms and on the initial position of O short bridge in Model I. It is obvious that the ELF is close to 1,

which means the covalent bond between the H atom and the O atom is very strong.

3.3. Adsorption Mechanism of  $\text{H}_2$  Molecule on O Top in Model II. The following discussions are about the properties on

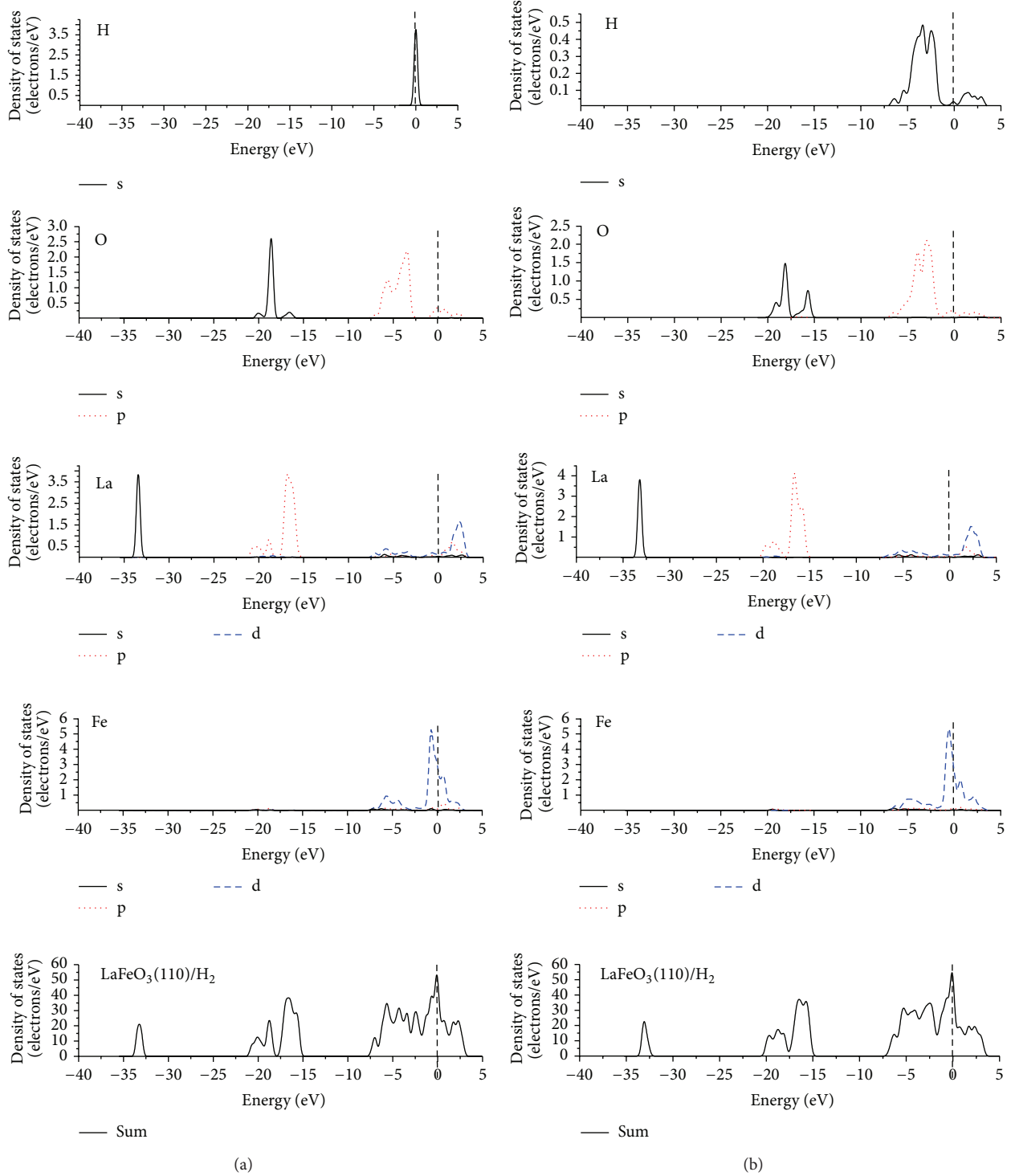


FIGURE 4: DOS on O top in Model II (a) before adsorption and (b) after adsorption.

O top in Model II including Mulliken charge population, density of states, and electron localization function.

**3.3.1. Mulliken Charge Population.** Table 4 lists the Mulliken charge population before and after adsorption, respectively. The H atoms get negative charges and the crystal surface gets

positive charges after adsorption. The Fe atoms, which absorb H atoms, lose charges after adsorption. It makes  $\text{Fe}^{3+}$  turn to  $\text{Fe}^{2+}$ . And that agrees with what Hoffmann et al. [15] have reported on change of valance states of B in perovskite  $\text{ABO}_3$ . Surface potential falls after adsorption, which means that the structure is more stable. Moreover, it is observed that the La

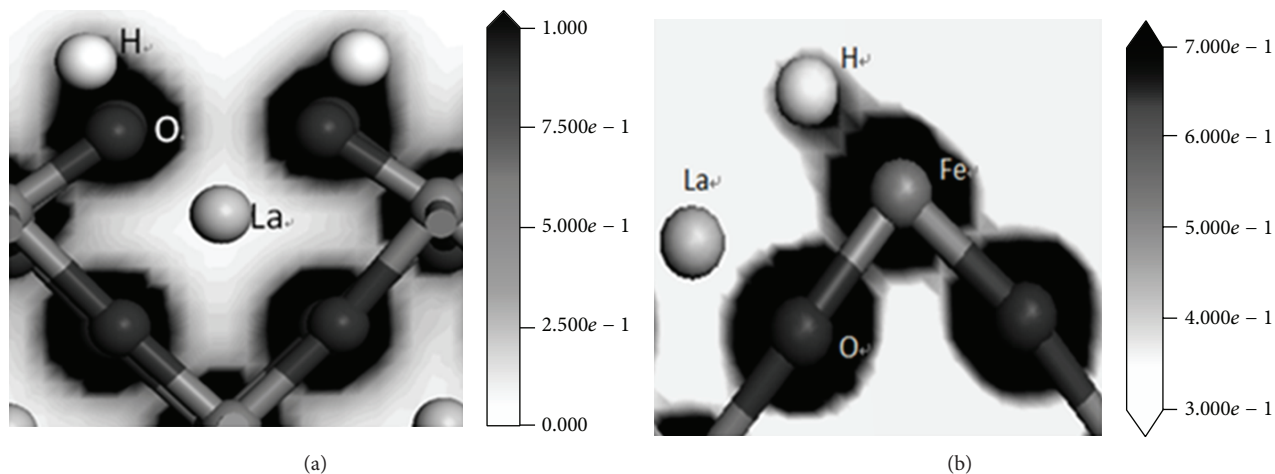


FIGURE 5: ELF on O top in two models: (a) Model I; (b) Model II.

TABLE 4: Mulliken population on O top in Model II.

Layer	Atom	Charges before adsorption	Charges after adsorption
First	H		-0.31
	H		-0.31
	O	-0.72	-0.74
	Fe	0.42	0.46
	Fe	0.42	0.48
	Fe	0.42	0.31
Second	Fe	0.42	0.34
	La	1.37	1.45
Third	O	-0.74	-0.73
	O	-0.69	-0.69
Fourth	Fe	0.62	0.62
	La	1.49	1.51
Fourth	O	-0.70	-0.70

atoms got charges after adsorption, which indicates that the valance states of La atoms have changed.

**3.3.2. Density of States (DOS).** Figure 4 lists the density of states of  $H_2$  molecule adsorption on O top in Model II before and after adsorption, respectively. By analysing the data, we get three conclusions. First, the energy of HOS of H atoms is decreased after adsorption and in contrast the energy of HOS of Fe atoms is increased after adsorption, which means that the H atoms get more stable and the Fe atoms get more excited after adsorption. Second, the peaks of density of states falls after adsorption, which means the energy of the surface is lower and the structure is more stable after adsorption. Third, after adsorption, the DOS of Fe atoms have changed, which means the charge population of Fe atoms have changed.

**3.3.3. Electron Localization Function (ELF).** Figure 5(b) lists the ELF of  $LaFeO_3(110)$  surface with H atoms absorbed on Fe atoms with the initial position of the  $H_2$  molecule being O top

in Model II. It is obvious that the ELF between the H atom and the Fe atom is about 0.5, which means that a metallic bond is formed after adsorption. And that agree with what Mandal et al. [6] have reported on the change of valance states of Mn.

## 4. Conclusions

The adsorption  $H_2$  on  $LaFeO_3(110)$  surface is studied.  $H_2$  is put on one symmetrical adsorption site, parallel to the surface, and then is calculated with first-principle methods. After analysing and discussing the results, we can find the following.

- (1) H atom can be absorbed on O atom and form  $-OH$ . There is a strong covalent bond between them after adsorption. The adsorption energy is 3.507 eV, which is higher than that on other sites.
- (2) Two H atoms can form  $H_2O$  molecule with an O atom. The adsorption energy is 1.220 eV, which is lower than that when H atom is absorbed on O atom or Fe atom. An Oxygen vacancy will be formed on the surface if the  $H_2O$  molecule gets rid of the surface.
- (3) H atoms can be absorbed on Fe atom and forms a metallic bond with it, which not only makes  $Fe^{3+}$  turn to  $Fe^{2+}$  but also makes the H atoms more stable and the Fe atoms more excited.
- (4) Although no H atom is absorbed on La atom, it is observed that the charge population has changed after adsorption, which indicates that the valance states of La may have changed.

## Conflict of Interests

The authors declare that there is no conflict of interests regarding the publication of this paper.

## Acknowledgments

The authors gratefully acknowledge the financial support from the Basic Scientific Research Foundation for Gansu Universities of China (Grant no. 05-0342), the Science and Technology Project of Lanzhou City (Grant no. 2011-1-10), and the Doctoral Foundation of Lanzhou University of Technology (Grant no. BS200901).

## References

- [1] D. J. Cuscueta, A. A. Ghilarducci, and H. R. Salva, "Design, elaboration and characterization of a Ni-MH battery prototype," *International Journal of Hydrogen Energy*, vol. 35, no. 20, pp. 11315–11323, 2010.
- [2] W. T. Wu and J. S. Do, "Characterization of AB<sub>5</sub>-type metal hydride modified by electroless plating nickel in forming process," *Advanced Materials Research*, vol. 306-307, pp. 139–142, 2011.
- [3] K. Young, T. Ouchi, J. Koch, and M. A. Fetcenko, "Compositional optimization of vanadium-free hypo-stoichiometric AB<sub>2</sub> metal hydride alloy for Ni/MH battery application," *Journal of Alloys and Compounds*, vol. 510, no. 1, pp. 97–106, 2012.
- [4] H. Zhang, N. Li, K. Li, and D. Xue, "Structural stability and formability of ABO<sub>3</sub>-type perovskite compounds," *Acta Crystallographica B: Structural Science*, vol. 63, no. 6, pp. 812–818, 2007.
- [5] G. A. Samara, "The relaxational properties of compositionally disordered ABO<sub>3</sub> perovskites," *Journal of Physics Condensed Matter*, vol. 15, no. 9, pp. R367–R411, 2003.
- [6] T. K. Mandal, L. Sebastian, J. Gopalakrishnan, L. Abrams, and J. B. Goodenough, "Hydrogen uptake by barium manganite at atmospheric pressure," *Materials Research Bulletin*, vol. 39, no. 14-15, pp. 2257–2264, 2004.
- [7] T. Esaka, H. Sakaguchi, and S. Kobayashi, "Hydrogen storage in proton-conductive perovskite-type oxides and their application to nickel-hydrogen batteries," *Solid State Ionics*, vol. 166, no. 3-4, pp. 351–357, 2004.
- [8] G. Deng, Y. G. Chen, M. D. Tao, C. L. Wu, X. Q. Shen, and H. Yang, "Electrochemical properties of La<sub>1-x</sub>Sr<sub>x</sub>FeO<sub>3</sub> ( $x = 0.2, 0.4$ ) as negative electrode of NiMH batteries," *Electrochimica Acta*, vol. 54, pp. 3910–3914, 2009.
- [9] F. C. Ruiz, P. S. Martínez, E. B. Castro, R. Humana, H. A. Peretti, and A. Visintin, "Effect of electrolyte concentration on the electrochemical properties of an AB<sub>5</sub>-type alloy for Ni/MH batteries," *International Journal of Hydrogen Energy*, vol. 38, no. 1, pp. 240–245, 2013.
- [10] G. Deng, Y. Chen, M. Tao et al., "Electrochemical properties and hydrogen storage mechanism of perovskite-type oxide LaFeO<sub>3</sub> as a negative electrode for Ni/MH batteries," *Electrochimica Acta*, vol. 55, no. 3, pp. 1120–1124, 2010.
- [11] M. B. Bellakki, B. J. Kelly, and V. Manivannan, "Synthesis, characterization, and property studies of (La, Ag) FeO<sub>3</sub> ( $0.0 \leq x \leq 0.3$ ) perovskites," *Journal of Alloys and Compounds*, vol. 489, no. 1, pp. 64–71, 2010.
- [12] M. C. Per, S. P. Russo, and I. K. Snook, "Anisotropic intracule densities and electron correlation in H<sub>2</sub>: a quantum Monte Carlo study," *The Journal of Chemical Physics*, vol. 130, no. 13, Article ID 134103, 2009.
- [13] J. D. Gu, A. M. Tian, and G. S. Yan, "Molecular dynamics simulation for the geometry of water molecule in liquid," *Chemical Journal of Chinese Universities*, vol. 15, pp. 886–890, 1994.
- [14] J. Sánchez-Benítez, M. J. Martínez-Lope, and J. A. Alonso, "Preparation at moderate pressures, crystal and magnetic structure and magnetotransport of the ferrimagnetic CeCu<sub>3</sub>Mn<sub>4</sub>O<sub>12</sub> perovskite," *Journal of Applied Physics*, vol. 107, no. 10, pp. 103904-1–103904-7, 2010.
- [15] J. Hoffmann, S. Schnittger, J. Norpoth, S. Raabe, T. Kramer, and C. Jooss, "Nanocomposite stability in Fe-, Co-, and Mn-based perovskite/spinel systems," *Journal of Materials Research*, vol. 27, no. 11, pp. 1462–1470, 2012.

## Research Article

# Single- and Multiwalled Carbon Nanotubes with Phosphorus Based Flame Retardants for Textiles

**D. Wesolek and W. Gieparda**

*Institute of Natural Fibres and Medicinal Plants, Ulica Wojska Polskiego 71b, 60-630 Poznan, Poland*

Correspondence should be addressed to W. Gieparda; [veronika.gieparda@iwnirz.pl](mailto:veronika.gieparda@iwnirz.pl)

Received 7 March 2014; Revised 12 June 2014; Accepted 19 June 2014; Published 8 July 2014

Academic Editor: Zheng-Hong Huang

Copyright © 2014 D. Wesolek and W. Gieparda. This is an open access article distributed under the Creative Commons Attribution License, which permits unrestricted use, distribution, and reproduction in any medium, provided the original work is properly cited.

Due to growing popularity of composites, modification methods to obtain the best properties are searched for. The aim of the study is to reduce the flammability of textile materials using nanocomposite polymer back-coating. Different types of carbon nanotubes (single- and multiwalled) and different phosphorus flame retardants (ammonium polyphosphates and melamine polyphosphate) were introduced into the resin and then the fabrics were covered by the obtained composites. Homogeneous dispersion of multiwalled carbon nanotubes in the polyurethane resin was obtained by sonification, which was confirmed by scanning electron microscopy. Flammability tests of fabrics coated by modified polyurethane resin were carried out using pyrolysis combustion flow calorimeter (PCFC) and thermal stability of textiles was evaluated. Also, organoleptic estimation of coatings was conducted (flexibility and fragility). The use of polymer nanocomposites with phosphorus flame retardants as a back-coating for textiles effectively reduces flammability and improves thermal stability of the fabric. Furthermore, the synergistic effect between carbon nanotubes and phosphorus compound occurs. The resulting coatings are flexible and do not crack or change the feel of fabrics.

## 1. Introduction

Rapid development of the economy increases demand for new engineering materials. Traditional materials and textiles are increasingly often being replaced by modern composites and modified textiles showing improved useful properties. Improvement of existing and creation of new material properties are the most important reasons for functionalization of textiles. Many studies have investigated thermal stability and flammability of materials with addition of different types of flame retardants [1, 2]. Enhancement of thermal stability and fire resistance based on the use of polymer composites filled with various types of nanoadditives has been extensively developed in the recent years [2–4]. Many other materials besides polymer composites must fulfill requirements for flammability. More and more studies are being conducted to reduce the flammability of textiles [5, 6], as these materials are used in furniture, interior finishing, and the transport industry (seat fabrics) and in the production of clothing. Polymer nanocomposites offer possibility of developing a new class of back-coating for textiles.

Carbon nanotubes (CNT) are allotropes of carbon with a cylindrical nanostructure. The CNT walls resemble rolled-up graphite-like sheets with strong covalent  $sp^2$  bonds. These cylindrical carbon molecules have unusual properties, which are valuable for nanotechnology, electronics, optics, and other fields of materials science and technology [7].

There are a number of studies investigating these materials as a flame suppressing additive. Researchers such as Beyer [8, 9] Rahatekar et al. [10], Hapuarachchi and Peijs [11], Kashiwagi et al. [12–14], Schartel et al. [15, 16], and Bourbigot et al. [17] have been investigating flammability of various sets of polymeric composites together with multiwalled nanotubes composition.

Our previous studies on flammability of epoxy and polyurethane composites with nanoparticles brought interesting results of the flammability properties of nanocomposites [18, 19]. Also our studies on flammability of epoxy/CNTs composites with different fillers [20] such as expandable graphite, montmorillonite, or intumescent compositions showed that the addition of those fillers to epoxy/CNT composites had

a considerable effect on reduction of heat release rate and also on delaying time to ignition. Our latest studies on reduction of flammability in polyurethane resins with montmorillonite and carbon nanotubes as fillers [21] indicated that the use of the nanoscale particles in a polymer matrix can give satisfactory results in flammability tests.

The aim of this work is reducing flammability of textiles by using a polymer nanocomposite back-coating with addition of conventional phosphorus flame retardants. Different types of carbon nanotubes (single-walled—SWCNT, multi-walled—MWCNT) were added to polyurethane (PU) resin. When the dispersion of nanotubes was homogenous, then different flame retardants (melamine polyphosphate—MPP, ammonium polyphosphates APP423 and APP750) were added. After that the fabrics were coated by those composites.

## 2. Materials and Methods

2.1. *Materials.* The following materials were used:

- (i) polyurethane resin Edolan UH (PU) supplied by Tanatex Chemicals;
- (ii) two types of carbon nanotubes—single-walled carbon nanotubes (SWCNT) and multiwalled carbon nanotubes (MWCNT) supplied by a Belgian company Nanocyl S.A.;
- (iii) two types of ammonium polyphosphate: APP423 and APP750—supplied by Clariant;
- (iv) melamine polyphosphate (MPP) supplied by a Polish company Ciech;
- (v) fabrics made of natural fibers (f)—45% cotton/55% flax, surface mass 310 g/m<sup>2</sup>.

2.2. *Methods.* The dispersion of nanofillers was studied by scanning electron microscopy (SEM) on the Hitachi S-3400 N microscope.

Thermogravimetric analysis was carried out with a thermal analyser Setaram Setsys 1200 at 10°C/min under air atmosphere. The weight of the samples was close to 30 mg. The temperatures of the 5% weight loss were determined.

The effect of the polymer nanocomposite back-coating on the flammability of natural fibre fabric was analyzed by a pyrolysis combustion flow calorimeter (PCFC). The heating rate was 1°C/s. Pyrolysis temperature ranged between 75 and 750°C, and the combustion temperature was 900°C. The flow was a mixture of O<sub>2</sub>/N<sub>2</sub> 20/80 cm<sup>3</sup>/min and the sample weight at 5 (±0,01) mg. The specific heat release rate (HRR) and maximum specific heat release rate (HRR<sub>max</sub>) were determined.

2.3. *Sample Preparation.* The composites were prepared from polyurethane resin, single-walled nanotubes as well as multi-walled carbon nanotubes. The mixtures were homogenized for 2 hours by the ultrasonic processor. Conventional compounds reducing flammability were used in addition to CNT, including ammonium polyphosphates (APP 423 and APP 750) and melamine polyphosphate (MPP). The above-mentioned flame retardants were added with using a high

speed homogenizer (20000 RPM). Such modified resins were applied on one side of the fabric surface in the form of a coating of the fabric surface using Mathis Labcoater. The coatings were dried at 80°C and then crosslinked at 140°C.

## 3. Results and Discussion

3.1. *Dispersion of Carbon Nanotubes.* The flammability of PU/CNT composites depends strongly on the homogeneous distribution of carbon nanotubes into the polymer matrix. The ultrasonification process used in the preparation of the composites ensures the proper distribution of multiwalled carbon nanotubes in the entire volume of the sample and prevents the formation of agglomerates (Figure 1(a)). However, in the case of SWNT, on the SEM pictures is visible that dispersion is slightly worse. Besides individual nanotubes, agglomerates can be observed in a few places (Figure 1(b)).

3.2. *Microcalorimetric Analysis.* Flammability studies with the pyrolysis combustion flow calorimeter showed that combustion of the fabrics coated by the composites with carbon nanotubes only is much less intensive in comparison with the pure fabric. After the addition of phosphorus compounds the combustion is further reduced. (Figures 2(a) and 2(b)) significant differences were not observed in the maximum heat release rate between fabrics coated by single- or multiwalled carbon nanotubes. Numerous reports in the literature demonstrated the superiority of SWCNT because of their better physical properties [22–25]. However, Kashiwagi et al. showed in their report the importance of obtaining adequate dispersion of this type of carbon nanotubes, in order to obtain a significant improvement of the flammability [12]. The result achieved in this study (a small difference in reducing the flammability of fabric coated by polymer nanocomposites with SWCNT and MWCNT) might also be related with insufficient dispersion, due to the fact that single-walled nanotubes were harder to undergo uniform dispersion in a polymer matrix. HRR<sub>max</sub> reduction for fabrics coated only by polyurethane/nanotubes was similar (regardless of the type of nanotubes—SWCNT or MWCNT) and reached approximately 20%. The addition of MPP to the composition caused large reduction of HRR<sub>max</sub>—from 200 W/g (pure fabric) to approximately 120 W/g. The addition of ammonium polyphosphates, in turn, reduced further this parameter, to approximately 90 W/g. Changes in the HRR<sub>max</sub> for the addition of 5% of flame retardants proceeded in a way comparable to that for 15% addition. So the 5% weight fraction of flame retardants seemed to be the optimal amount to reduce combustion of fabrics. The addition of APP 423 to coating with multiwalled carbon nanotubes is an exception with a significant reduction of heat release rate from 99 (5%) to 67 W/g (15%). Polyurethane with ammonium polyphosphate 423 was the best coating in the amount of 15% and multiwalled carbon nanotubes. The coating reduced the maximum heat release rate by 66% as compared to the neat fabric.

The curves of heat release rate (HRR) for selected samples are presented in Figure 3. The curve shapes are visibly

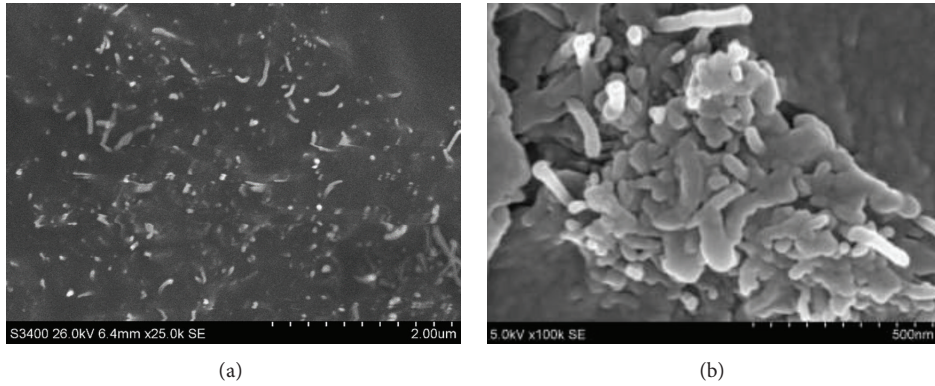


FIGURE 1: (a) SEM image of PU/MWCNT composite. (b) SEM image of PU/SWCNT composite.

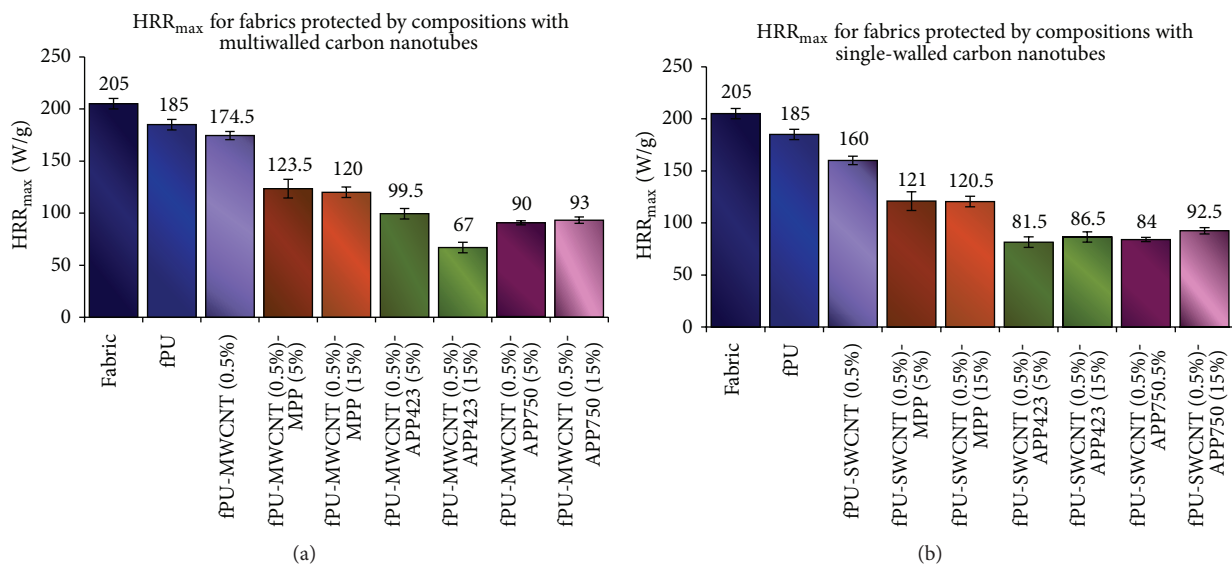


FIGURE 2: (a) HRR<sub>max</sub> for fabrics protected by compositions with multiwalled carbon nanotubes. (b) HRR<sub>max</sub> for fabrics protected by compositions with single-walled carbon nanotubes.

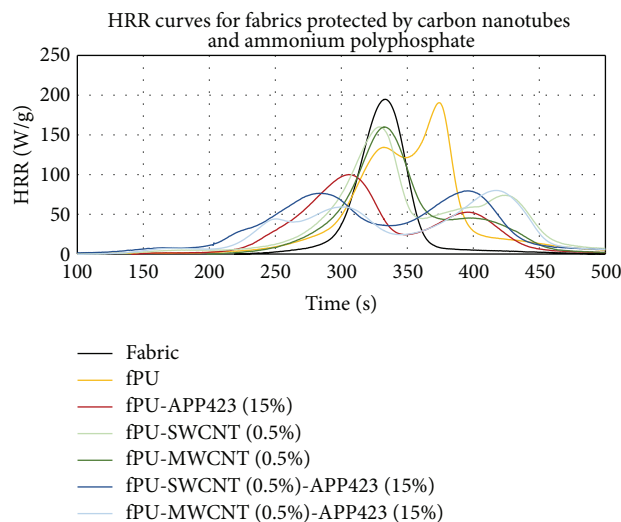


FIGURE 3: HRR curves for selected fabrics protected by nanofillers and phosphorous compounds.

different for the fabrics with polyurethane coating in comparison to the pure fabric. The coating by neat polyurethane resulted in forming of two HRR peaks, the first one was reduced with respect to the pure fabric by 30% and the second peak was similar to the pure fabric peak, but it occurred 60 seconds later. Introducing of the carbon nanotubes into the polyurethane, in turn, caused significant reduction in the second peak of heat release rate (from 200 W/g for fPU to 50–70 W/g for fPU-CNT depending on the type of carbon nanotubes), and further delayed this peak. The first peak increased in comparison to fPU but decreased in comparison to pure fabric. The addition of ammonium polyphosphate to polyurethane coating (without CNT) led to the reduction in the first peak by half in comparison to pure fabric. Synergistic effect between nanofiller and ammonium polyphosphates is visible when comparing HRR curves for fabric coated by PU/APP423 and PU/CNT with the curve for the fabric coated by PU/APP423/CNT. The addition of carbon nanotubes and APP 423 together into the polymer matrix reduced both peaks of heat release rate from 200 W/g (pure fabric) to 50 W/g (first peak) and 70 W/g (second peak) and it constituted the largest reduction in those peaks of all the samples.

During combustion, phosphorous flame retardants dilute the amount of gaseous combustibles by releasing water in the gas phase. Furthermore, APP is assumed to be an intumescent flame retardant which forms an expanded and foamed char layer. Thus, it can act a physical barrier to mass and heat transfer between the polymer and the superficial zone where the combustion of the polymer occurs. Presence of CNTs in this char layer might have strengthened the char and led to a synergistic effect. Observations of the residue recovered after combustion were performed by numerous researchers [26, 27] and this hypothesis has been confirmed. The char formed during combustion is much less cracked in the composites with APP and MWCNT.

Time to ignition for the protected fabrics showed reduction with respect to neat polymer. This behaviour is in agreement with the previously reported data [12, 28].

**3.3. Thermogravimetric Analysis.** Thermal stability of composites was analyzed by thermogravimetric analysis (TGA). In Figure 4 thermogravimetric curves in the range of 90–100% weight loss, for samples with different phosphorous compounds, are shown. The temperature of 5% weight loss was determined in order to compare the initial step of sample decomposition. Thermal decomposition of unprotected fabric began at  $T_d = 297^\circ\text{C}$  (5% weight loss) and decomposition of fabric covered with polyurethane at  $319^\circ\text{C}$ . A slight increase of the temperature to  $323^\circ\text{C}$  was observed for the fabric with the coating containing carbon nanotubes. In other cases, with the addition of phosphorous compounds, the decomposition of coated fabrics began at lower temperatures.

In Figure 5 selected thermogravimetric curves are shown (unprotected fabric, fabric protected by PU, PU/MWCNT, and PU/MWCNT/APP15%—the best composition). In natural fibres, the degradation involves two main steps (see the thermogravimetric curve for pure fabric). The first one is

the thermal depolymerisation of the hemicellulose and the cleavage of glycosidic linkages of cellulose ( $340\text{--}360^\circ\text{C}$ ) and the second one is related to the decomposition of the  $\alpha$ -cellulose ( $370\text{--}580^\circ\text{C}$ ) [29, 30]. The decomposition of lignin takes place in a broad range of temperature between 200 and 500 [31]. These two steps were also visible for fabrics coated by composites with polyurethane and carbon nanotubes. However, the second step begins at higher temperatures. Three steps of the degradation were visible for the fabrics coated by composites with carbon nanotubes and phosphorous additive. The first step started earlier and shifted to lower temperatures, while the second one was characterized by a very slow weight loss due to flame retardant action of polyphosphate. The third step was also milder and slower.

Flame retardants have two opposing functions in the thermal stability of the polymer nanocomposite, one is the catalytic effect towards the degradation of the polymer matrix which would accelerate thermal decomposition, and the other is its barrier effect and formation of char, which should improve the thermal stability by lowering the intensity of the combustion process. This is clearly visible in our studies. Thermal decomposition of fabrics protected by the polymer nanocomposite starts earlier but the combustion is slower and less intense.

Phosphorous compounds are intumescent flame retardants which improve thermal stability by changing pyrolytic path of the polymeric materials [32]. Under oxidative conditions, at temperatures above  $260^\circ\text{C}$ , APP starts to degrade producing phosphoric acid, which then is converted to polyphosphoric acid, which enhances cross-linking of polymer fragments to form a carbonaceous char protecting the underlying polymer from degradation [33]. When CNTs were incorporated to the mixture of PU/APP423 the intensity of degradation was significantly lowered. That synergistic effect was more pronounced at temperatures above  $350^\circ\text{C}$ . This can be attributed to efficient barrier effect of carbonaceous char formed by the incorporation of CNTs and APP fillers. The combination of CNTs and APP fillers leads to formation of stronger and more cohesive char, which can reduce the diffusion of volatile compounds [26].

**3.4. The Appearance of Fabrics.** It is important that the fabric after coating remained soft and flexible and the protecting coat itself was stable and did not crack. In order to evaluate the prepared samples in this respect, the organoleptic analysis of the coatings and fabrics was made. It was found that fabrics after treatment did not change in terms of flexibility, softness, and feel. The coatings did not crack.

## 4. Summary

The protection obtained in the form of coatings for natural fabrics improves the flammability properties. The addition of 0,5% of carbon nanotubes to the polyurethane resin coating decreases the value of maximum heat release rate by 20%. Enriching the composite coating additionally with phosphorous flame retardants used in the study results in a further reduction of  $\text{HRR}_{\text{max}}$ . Single-walled carbon nanotubes show

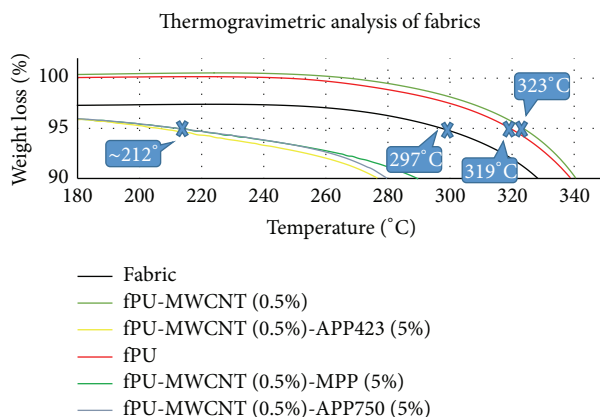


FIGURE 4: Thermogravimetric curves in the range of 90–100% weight loss for the protected fabrics with coatings containing different phosphorous compounds.

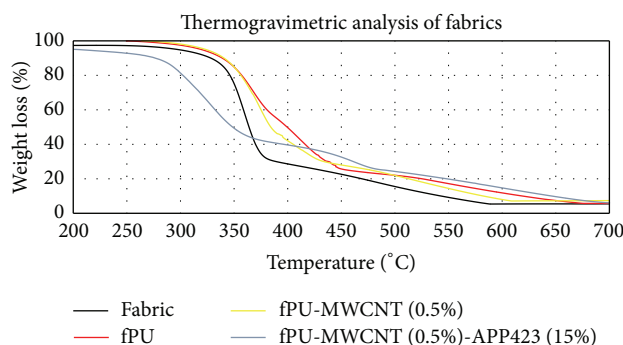


FIGURE 5: Thermogravimetric curves for the selected fabrics.

similar properties in terms of reduction of heat release rate to those of multiwalled carbon nanotubes. The thermal degradation of fabrics coated by polymer nanocomposites (without phosphorous compounds) starts at higher temperatures than in case of pure fabric. After addition of phosphorous flame retardants the temperatures of the 5% weight loss are reduced but the decomposition is much slower and milder.

The most advantageous composition in reducing fabrics flammability and in terms of the appearance of coating (flexibility and elasticity) is the composition containing polyurethane resin with ammonium polyphosphate 423 in the amount of 15% and 0,5% of multiwalled carbon nanotubes.

### Conflict of Interests

The authors declare that there is no conflict of interests regarding the publication of this paper.

### Acknowledgments

The study has been carried out within the Key Project—POIG.01.03.01-00-004/08 Functional nano- and microtextile materials—NANOMITEX cofinanced by the European Union with the financial resources of the European Regional Development Fund and the National Centre for Research

and Development within the framework of the Innovative Economy Operational Programme, 2007–2013, Priority 1. Research and development of modern technologies, Activity 1.3. Supporting R&D projects for enterprises undertaken by scientific organizations, Subactivity 1.3.1. Development projects.

### References

- [1] R. Jeenchan, N. Suppakarn, and K. Jarukumjorn, “Effect of flame retardants on flame retardant, mechanical, and thermal properties of sisal fiber/polypropylene composites,” *Composites Part B: Engineering*, vol. 56, pp. 249–253, 2014.
- [2] P. Rybiński and G. Janowska, “Influence synergetic effect of halloysite nanotubes and halogen-free flame-retardants on properties nitrile rubber composites,” *Thermochimica Acta*, vol. 557, pp. 24–30, 2013.
- [3] Z. Wu, H. Wang, X. Tian et al., “Mechanical and flame-retardant properties of styrene-ethylene-butylene-styrene/carbon nanotube composites containing bisphenol A bis(diphenyl phosphate),” *Composites Science and Technology*, vol. 82, pp. 8–14, 2013.
- [4] G. Huang, S. Wang, P. Song, C. Wu, S. Chen, and X. Wang, “Combination effect of carbon nanotubes with graphene on intumescent flame-retardant polypropylene nanocomposites,” *Composites A: Applied Science and Manufacturing*, vol. 59, pp. 18–25, 2014.

- [5] A. R. Horrocks, "Flame retardant challenges for textiles and fibres: new chemistry versus innovatory solutions," *Polymer Degradation and Stability*, vol. 96, no. 3, pp. 377–392, 2011.
- [6] A. R. Horrocks, "Textile flammability research since 1980—personal challenges and partial solutions," *Polymer Degradation and Stability*, vol. 98, no. 12, pp. 2813–2824, 2013.
- [7] R. Malik, N. Alvarez, M. Haase et al., "Chapter 13—carbon nanotube sheet: processing, characterization and applications," in *Nanotube Superfiber Materials*, chapter 13, pp. 349–387, 2014.
- [8] G. Beyer, "Short communication: carbon nanotubes as flame retardants for polymers," *Fire and Materials*, vol. 26, no. 6, pp. 291–293, 2002.
- [9] G. Beyer, "Carbon nanotubes—a new class of flame retardants for polymers," *Gummi, Fasern, Kunststoffe*, vol. 55, no. 9, pp. 596–549, 2002.
- [10] S. S. Rahatekar, M. Zammarano, S. Matko et al., "Effect of carbon nanotubes and montmorillonite on the flammability of epoxy nanocomposites," *Polymer Degradation and Stability*, vol. 95, no. 5, pp. 870–879, 2010.
- [11] T. D. Hapuarachchi and T. Peijs, "Multiwalled carbon nanotubes and sepiolite nanoclays as flame retardants for polylactide and its natural fibre reinforced composites," *Composites A: Applied Science and Manufacturing*, vol. 41, no. 8, pp. 954–963, 2010.
- [12] T. Kashiwagi, F. Du, K. I. Winey et al., "Flammability properties of polymer nanocomposites with single-walled carbon nanotubes: effects of nanotube dispersion and concentration," *Polymer*, vol. 46, no. 2, pp. 471–481, 2005.
- [13] T. Kashiwagi, E. Grulke, J. Hilding, R. Harris, W. Awad, and J. Douglas, "Thermal degradation and flammability properties of poly(propylene)/carbon nanotube composites," *Macromolecular Rapid Communications*, vol. 23, no. 13, pp. 761–765, 2002.
- [14] T. Kashiwagi, E. Grulke, J. Hilding et al., "Thermal and flammability properties of polypropylene/carbon nanotube nanocomposites," *Polymer*, vol. 45, no. 12, pp. 4227–4239, 2004.
- [15] B. Schartel, P. Pötschke, U. Knoll, and M. Abdel-Goad, "Fire behaviour of polyamide 6/multiwall carbon nanotube nanocomposites," *European Polymer Journal*, vol. 41, no. 5, pp. 1061–1070, 2005.
- [16] B. Schartel, U. Braun, U. Knoll et al., "Mechanical, thermal, and fire behavior of bisphenol a polycarbonate/multiwall carbon nanotube nanocomposites," *Polymer Engineering and Science*, vol. 48, no. 1, pp. 149–158, 2008.
- [17] S. Bourbigot, S. Duquesne, and C. Jama, "Polymer nanocomposites: how to reach low flammability?" *Macromolecular Symposia*, vol. 233, pp. 180–190, 2006.
- [18] M. Wladyka-Przybylak, D. Wesolek, W. Gieparda, A. Boczkowska, and E. Ciecierska, "Functionalization effect on physico-mechanical properties of multi-walled carbon nanotubes/epoxy composites," *Polymers for Advanced Technologies*, vol. 22, no. 1, pp. 48–59, 2011.
- [19] W. Gieparda, D. Wesolek, and S. Rojewski, "Montmorillonite and carbon nanotubes filled polyurethane back-coating for textiles with improved flammability properties and thermal stability," *Journal of Nanostructured Polymers and Nanocomposites*, vol. 8, no. 3, pp. 82–88, 2012.
- [20] M. Wladyka-Przybylak, D. Wesolek, W. Gieparda, and M. Przybylak, "Flame retardant effects of magnesium hydroxide and intumescent additives for epoxy/carbon nanotube composites," in *Proceedings of the 1st International Symposium on Flame Retardant Materials Technologies*, p. 174, Chengdu, China, 2010.
- [21] S. Rojewski, R. Gąsiorowski, W. Gieparda, D. Wesolek, and M. Wladyka-Przybylak, "Montmorillonite and carbon nanotubes as a reducing flammability fillers for polymers resins," in *Proceedings of the 4th ECNP Young Researcher Conference*, Paris, France, 2011.
- [22] R. Haggemueller, H. H. Gommans, A. G. Rinzler, J. E. Fischer, and K. I. Winey, "Aligned single-wall carbon nanotubes in composites by melt processing methods," *Chemical Physics Letters*, vol. 330, no. 3–4, pp. 219–225, 2000.
- [23] P. M. Ajayan, L. S. Schadler, C. Giannaris, and A. Rubio, "Single-walled carbon nanotube-polymer composites," *Strength and Weakness Advanced Materials*, vol. 12, pp. 750–753, 2000.
- [24] A. A. Mamedov, N. A. Kotov, M. Prato, D. M. Guldi, J. P. Wicksted, and A. Hirsch, "Molecular design of strong single-wall carbon nanotube/polyelectrolyte multilayer composites," *Nature Materials*, vol. 1, no. 3, pp. 190–194, 2002.
- [25] F. Du, J. E. Fischer, and K. I. Winey, "Coagulation method for preparing single-walled carbon nanotube/poly(methyl methacrylate) composites and their modulus, electrical conductivity, and thermal stability," *Journal of Polymer Science B: Polymer Physics*, vol. 41, no. 24, pp. 3333–3338, 2003.
- [26] S. Bourbigot, S. Duquesne, G. Fontaine, S. Bellayer, T. Turf, and F. Samyn, "Polymer nanocomposites with and without conventional flame retardants: Reaction to fire and synergy," *Molecular Crystals and Liquid Crystals*, vol. 486, pp. 325–339, 2008.
- [27] M. C. Costache, M. J. Heidecker, E. Manias et al., "The influence of carbon nanotubes, organically modified montmorillonites and layered double hydroxides on the thermal degradation and fire retardancy of polyethylene, ethylene-vinyl acetate copolymer and polystyrene," *Polymer*, vol. 48, no. 22, pp. 6532–6545, 2007.
- [28] M. Delichatsios, in *Proceedings of the 4th International Conference on Polymer Modification, Degradation and Stabilization (MoDeSt '06)*, F. La Mantia, Ed., Modest Society, Palermo, Italy, 2006.
- [29] K. C. Manikandan Nair, S. Thomas, and G. Groeninckx, "Thermal and dynamic mechanical analysis of polystyrene composites reinforced with short sisal fibres," *Composites Science and Technology*, vol. 61, no. 16, pp. 2519–2529, 2001.
- [30] C. Albano, J. González, M. Ichazo, and D. Kaiser, "Thermal stability of blends of polyolefins and sisal fiber," *Polymer Degradation and Stability*, vol. 66, no. 2, pp. 179–190, 1999.
- [31] N. E. Marcovich, M. M. Reboredo, and M. I. Aranguren, "Modified woodflour as thermoset fillers ii. Thermal degradation of woodflours and composites," *Thermochimica Acta*, vol. 372, no. 1–2, pp. 45–57, 2001.
- [32] B. Schartel, A. Weiß, H. Sturm et al., "Layered silicate epoxy nanocomposites: formation of the inorganic-carbonaceous fire protection layer," *Polymers for Advanced Technologies*, vol. 22, no. 12, pp. 1581–1592, 2011.
- [33] E. Kandare, B. K. Kandola, D. Price, S. Nazaré, and R. A. Horrocks, "Study of the thermal decomposition of flame-retarded unsaturated polyester resins by thermogravimetric analysis and Py-GC/MS," *Polymer Degradation and Stability*, vol. 93, no. 11, pp. 1996–2006, 2008.

## Research Article

# Application of Multiwalled Carbon Nanotube Nanofluid for 450 W LED Floodlight

**Bui Hung Thang,<sup>1</sup> Le Dinh Quang,<sup>1</sup> Nguyen Manh Hong,<sup>1,2</sup>  
Phan Hong Khoi,<sup>2</sup> and Phan Ngoc Minh<sup>1,2</sup>**

<sup>1</sup> Institute of Materials Science (IMS), Vietnam Academy of Science and Technology, A2 Building, 18 Hoang Quoc Viet Road, Cau Giay District, Hanoi 122102, Vietnam

<sup>2</sup> Center for High Technology Development (HTD), Vietnam Academy of Science and Technology, 2B Building, 18 Hoang Quoc Viet Road, Cau Giay District, Hanoi 122102, Vietnam

Correspondence should be addressed to Bui Hung Thang; [thangbh@ims.vast.vn](mailto:thangbh@ims.vast.vn) and Phan Ngoc Minh; [pnminh@vast.ac.vn](mailto:pnminh@vast.ac.vn)

Received 28 February 2014; Revised 17 June 2014; Accepted 17 June 2014; Published 1 July 2014

Academic Editor: Jinlong Jiang

Copyright © 2014 Bui Hung Thang et al. This is an open access article distributed under the Creative Commons Attribution License, which permits unrestricted use, distribution, and reproduction in any medium, provided the original work is properly cited.

Overheating of the high-power light emitting diode (LED) has a dramatic effect on the chip's lifetime. Heat dissipation for high-power LED is becoming a major challenge for researchers and technicians. Compared with the air cooling method, the liquid cooling method has many advantages and high efficiency because of higher specific heat capacity, density, and thermal conductivity. Carbon nanotubes with remarkable thermal properties have been used as additives in liquids to increase the thermal conductivity. In this work, multiwalled carbon nanotubes nanofluid (MWCNTs nanofluid) was used to enhance heat dissipation for 450 W LED floodlight. MWCNTs nanofluid was made by dispersing the OH functionalized MWCNTs in ethylene glycol/water solution. The concentration of MWCNTs in fluid was in the range between 0.1 and 1.3 gram/liter. The experimental results showed that the saturated temperature of 450 W LED chip was 55°C when using water/ethylene glycol solution in liquid cooling system. In the case of using MWCNTs nanofluid with 1.2 gram/liter of MWCNTs' concentration, the saturated temperature of LED chip was 50.6°C. The results have confirmed the advantages of the MWCNTs for heat dissipation systems for high-power LED floodlight and other high power electronic devices.

## 1. Introduction

In recent years, the problem of heat dissipation with features and strengthening functions of products has become more significant. Many approaches can improve the cooling system performance. The most feasible one is to enhance the heat transfer (dissipation) performance through the working fluid without modifying the mechanical designs or key components of the system. Recent studies have shown that the thermal conductivity of the suspension which contains suspended metallic or nonmetallic nanoparticles can be much higher than that of the base fluid, and it was called as "nanofluid" [1, 2]. On this basis, adding certain kinds of nanomaterials into base fluid is considered to be a novel approach to enhance the thermal conductivity in

heat transfer medium [3]. Results showed that the thermal conductivity enhancements of nanofluids could be influenced by multifaceted factors including the volume fraction of nanoparticles, the tested temperature, thermal conductivity of the base fluid, nanoparticles size, pretreatment process, and the additives of the fluids [4, 5].

Carbon nanotubes (CNTs) have attracted much attention because of their unique structure and remarkable mechanical, thermal, and electrical properties [6–10]. CNTs have been used as additives in liquids to increase the thermal conductivity, one of the most important issues in industry [11]. Owing to their very high thermal conductivity (2000 W/m·K compared to thermal conductivity of Ag 419 W/m·K) [12, 13], CNTs become one of the most suitable nanoadditives to fabricate the nanofluid for thermal dissipation in many industrial

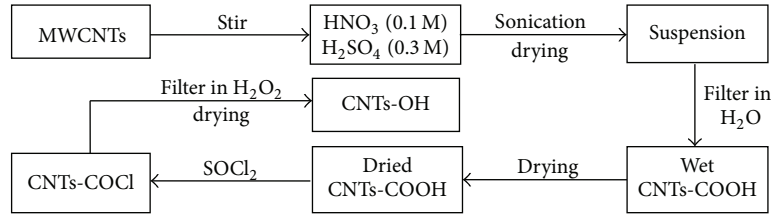


FIGURE 1: Process for functionalization of the MWCNTs with hydroxyl functional group.

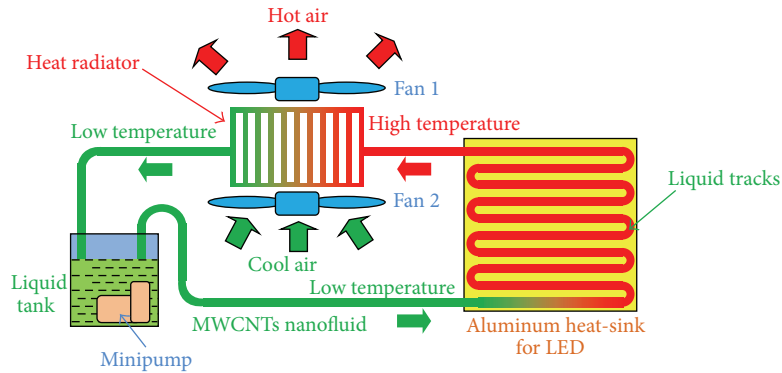


FIGURE 2: Scheme of cooling system using MWCNTs nanofluid for 450 W LED floodlight.

and consumer products [14, 15]. In this paper, we present the results on application of multiwalled carbon nanotube nanofluid (MWCNTs nanofluid) for 450 W LED floodlight.

## 2. Experiment

MWCNTs were produced at the IMS by thermal CVD technique on solid catalyst in a gas mixture of acetylene, hydrogen, and nitrogen. The diameter and length of the grown MWCNTs were in the range 15 nm–90 nm and several ten  $\mu\text{m}$ , respectively [16]. The stability of carbon nanotubes in fluids can be increased by introducing hydroxyl groups onto the surface of CNTs [17].

Process for functionalization of the MWCNTs with hydroxyl functional group ( $-\text{OH}$ ) was shown in Figure 1 with the following steps [16].

*Step 1.* MWCNTs were treated in the mixture of hot acid ( $\text{HNO}_3 : \text{H}_2\text{SO}_4$  in ratio 1 : 3) at  $60^\circ\text{C}$  in 6 h.

*Step 2.* The suspension obtained in Step 1 was dried in argon atmosphere at  $80^\circ\text{C}$  for 24 h.

*Step 3.* The mixture obtained in Step 2 was treated in the thionyl chloride ( $\text{SOCl}_2$ ) to obtain MWCNTs-COCl.

*Step 4.* The MWCNTs-COCl was filtered in hydrogen peroxide ( $\text{H}_2\text{O}_2$ ) and dried in argon atmosphere at  $80^\circ\text{C}$  for 24 h to obtain MWCNTs-OH.

The ethylene glycol/distilled water solution (EG/DW solution) was prepared by heat-magnetic stirring at  $50^\circ\text{C}$  and 6.5 rps (rounds per second) in 60 minutes. The percent by volume of ethylene glycol in EG/DW solution was 45%. In order to disperse MWCNTs-OH in EG/DW solution, we used the Tween-80 surfactant and Hielscher Ultrasonics vibration instrument. The MWCNTs-OH was dispersed in EG/DW solution with concentration from 0.1 to 1.3 g/L to obtain MWCNTs nanofluid. The prepared MWCNTs nanofluid had good stability by using functionalized carbon nanotube and the Tween-80 surfactant. This was caused by a hydrophobic-to-hydrophilic conversion of the surface nature due to the generation of a hydroxyl group, and the Tween-80 surfactant provides lower surface tension of liquids and increases immersion of CNTs [17–19].

We develop a heat dissipation system using MWCNTs nanofluid for a 450 W LED floodlight. Figure 2 is the schematic view of the heat dissipation system for 450 W LED floodlight using the MWCNTs nanofluid.

In Figure 2, the aluminum heat-sink was set to directly contact the 9 LED chips; the tracks inside the aluminum heat-sink were fabricated to allow fluid flows through it and absorb heat from the LED chips. The MWCNTs nanofluid was pumped into the aluminum heat-sink with  $3\text{ cm}^3/\text{s}$  of flow rate. The pump power consumption of cooling system was 1.8 W. The dimension and power consumption of fan were  $120 \times 120 \times 38\text{ mm}$  and 3.6 W, respectively. The volume of the liquid tank was 500 mL. The heat radiator was made by aluminum material, and dimensions of heat radiator were

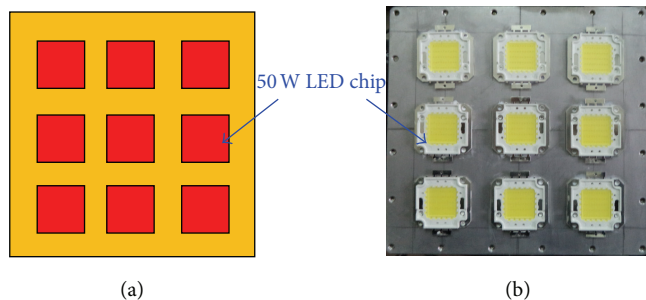


FIGURE 3: Scheme (a) and real image (b) of aluminum heat-sink with 9 LED chips.

150 × 120 × 25 mm, respectively. Figure 3 is scheme and real image of 9 LED chips, which were mounted on the aluminum heat-sink. The dimension of aluminum heat-sink and LED chip was 210 mm × 210 mm × 17 mm and 40 mm × 40 mm × 3 mm, respectively. The powers of LED chip and power consumption of LED floodlight were 50 W and 450 W, respectively.

The environmental temperature was kept at 20°C for all measurements by using air conditioner. The temperature of LED chip was directly measured by using an attached temperature sensor and WH7016E Electronic Digital Temperature Controller.

### 3. Results and Discussions

The existence of carboxyl (COOH) and hydroxyl (OH) functional groups bonded to the ends and sidewalls of the CNTs was demonstrated by Raman and Fourier transform infrared (FTIR) spectra. Raman scattering is a powerful technique to probe the changes of surface and structure of MWCNTs. The Raman scattering spectra were clearly seen such that the two bands around 1583.10 and 1333.69  $\text{cm}^{-1}$  in the spectra were assigned to the tangential mode (G-band) and the disorder mode (D-band), respectively. The D-band intensity was increased in the functionalized MWCNTs compared to pristine MWCNTs. The peak intensity ratio ( $I_D/I_G$ ) at D-band and G-band of 0.99 and 1.87 corresponding to MWCNTs-COOH and MWCNTs-OH exceeded those of pristine MWCNTs ( $I_D/I_G = 0.79$ ). The intensity ratio of D lines and G lines is different, suggesting some changes of the surface and structure of MWCNTs. This result indicates that some of the  $\text{sp}^2$  carbon atoms (C=C) were converted to  $\text{sp}^3$  carbon atoms (C-C) at the surface of the MWCNTs after the acid treatment in  $\text{HNO}_3/\text{H}_2\text{SO}_4$ . The intensity ratio of MWCNTs-OH is higher than that of MWCNTs-COOH indicating that by two chemical treatment processes, the new defects were formed on the surface of MWCNTs [20].

The typical FTIR spectrum of MWCNTs-COOH shows some important peak after MWCNT was treated by mixture of  $\text{H}_2\text{SO}_4$  and  $\text{HNO}_3$ . The vibration of O-H bonding in carboxyl group was shown on peak 3431.81  $\text{cm}^{-1}$ . It expanded more than that of O-H bonding of  $\text{H}_2\text{O}$ . Peak 1707.31  $\text{cm}^{-1}$

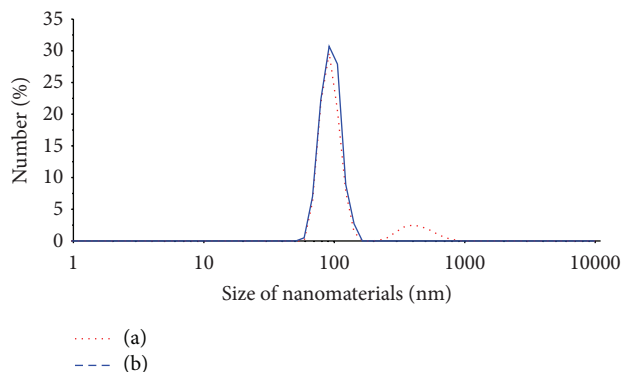


FIGURE 4: Spectra of the MWCNTs-OH size distribution in EG/DW solutions by number with 10 minutes of ultrasonication time: (a) immediately after the sonication; (b) 72 hours after the sonication.

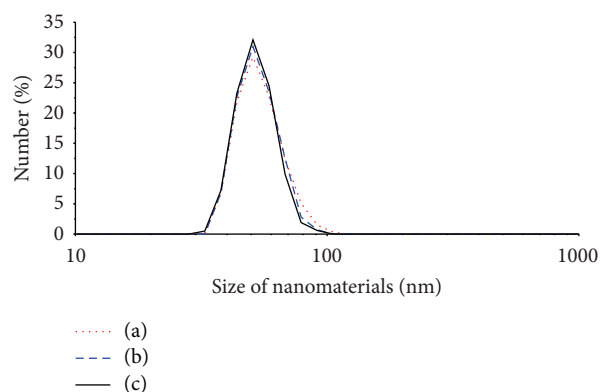


FIGURE 5: Spectra of the MWCNTs-OH size distribution in EG/DW solutions by number after 72 hours from the sonication: line (a) 20 minutes of sonication; line (b) 30 minutes of sonication; line (c) 40 minutes of sonication.

showed the existence of vibration of C=O bonding in carboxyl group. This exhibits the importance of proving the existence of carboxyl (COOH) functional groups that appeared due to the oxidation resulting from nitric and sulfuric acids. It clearly shows that the kinds of acids functionalized the surface of MWCNTs. The FTIR transmittance spectra of MWCNTs-OH show that the peak of conjugated O-H stretching vibration mode appeared at 3431.81  $\text{cm}^{-1}$ , and the central position of O-H peak shifted to a lower frequency as well; the expansion of vibration peak and the disappearance of vibration peak of C=O bonding at 1707.31  $\text{cm}^{-1}$  indicated the generation of hydroxyl groups on surface of MWCNTs [20].

In order to evaluate the dispersion of MWCNTs-OH in EG/DW solutions, we used the Malvern Zetasizer Nano ZS Instrument. Figure 4 is the spectra of the MWCNTs-OH size distribution in EG/DW solutions by number with 10 minutes of ultrasonication. Line (a) in Figure 4 showed that immediately after the ultrasonication, the MWCNTs-OH was still gathering into large bundles with two peaks at 437 nm and 93.5 nm. The 437 nm peak was corresponding



FIGURE 6: The 450 W LED floodlight using MWCNTs nanofluid for heat dissipation.

to the large bundles of MWCNTs-OH, whereas the 93.5 nm peak was corresponding to the individual of the MWCNTs-OH in EG/DW solutions. In order to remove large bundles from EG/DW solutions, the solutions were settled in 72 hours. Line (b) in Figure 4 showed that after 72 hours from the ultrasonication, the 437 nm peak disappeared, which means that there were no longer large bundles of MWCNTs-OH in EG/DW solutions. However, the MWCNTs were still gathering into small bundles with the size distribution from 70 nm to 170 nm.

Figure 5 was the spectra of the MWCNTs-OH size distribution in EG/DW solution by number with 20, 30, and 40 minutes of sonication. In the case of 20 minutes of ultrasonic vibration time (showed as line (a) in Figure 5), the spectra of the MWCNTs-OH size distribution by number were from 18 nm to 95 nm. This result showed that MWCNTs-OH was better dispersed in EG/DW solutions with 20 minutes of ultrasonic vibration time. However, the range of spectra did not match with 15–90 nm of the diameter of MWCNTs-OH. In the case of 30 minutes or 40 minutes of ultrasonic vibration time, the MWCNTs-OH was well dispersed in EG/DW solutions shown as line (b) and line (c) in Figure 5. The spectra of the MWCNTs-OH size distribution by number in line (b) and line (c) matched with 15–90 nm of the diameter of MWCNTs-OH. The results showed that the ultrasonic vibration time more than 30 minutes is required for well dispersion of MWCNTs-OH in EG/DW solutions, so we chose 30 minutes of ultrasonic vibration time for all subsequent experiments [20].

Figure 6 is the 450 W LED floodlight using MWCNTs nanofluid for heat dissipation. The experimental results of heat dissipation for the 450 W LED floodlight with different concentrations of CNTs in nanofluid were shown in Figure 7. The temperature of the LED chip was 20°C at initial time, and then the temperature of the LED chip was saturated after 40 minutes of working time. When using water/EG solution for heat dissipation, the saturated temperature of the LED

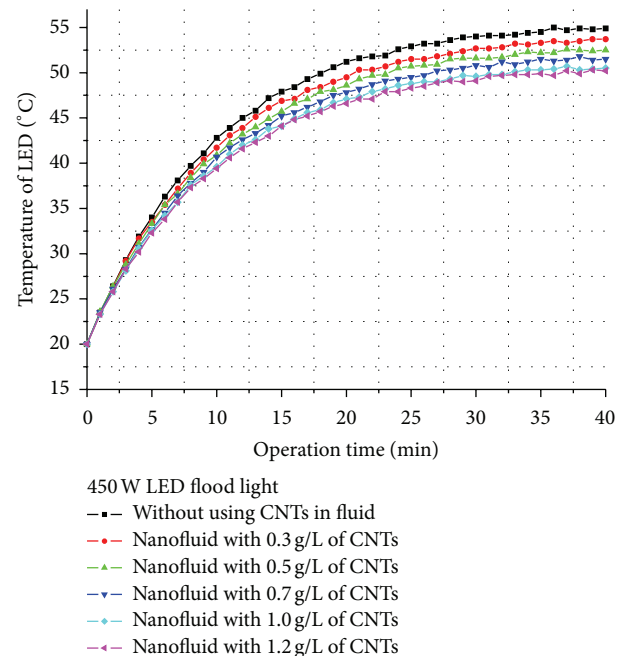


FIGURE 7: The temperature of 450 W LED floodlight measured as a function of operation time with different concentrations of CNTs in nanofluid.

chip was about 55°C. The saturated temperature of the LED chip reached 53.7°C, 52.5°C, 51.9°C, and 50.6°C when using nanofluids with 0.3 g/L, 0.5 g/L, 0.7 g/L, 1.0 g/L, and 1.2 g/L of CNTs concentration, respectively. These results indicated that by mixing CNTs-OH with 1.2 g/L of concentration in the nanofluid, the saturated temperature of LED chip decreased by 4.5°C compared to fluid without CNTs. According to the datasheet of the LED chip, if the operating temperature drops 10°C the lifetime of LED chips increases approximately

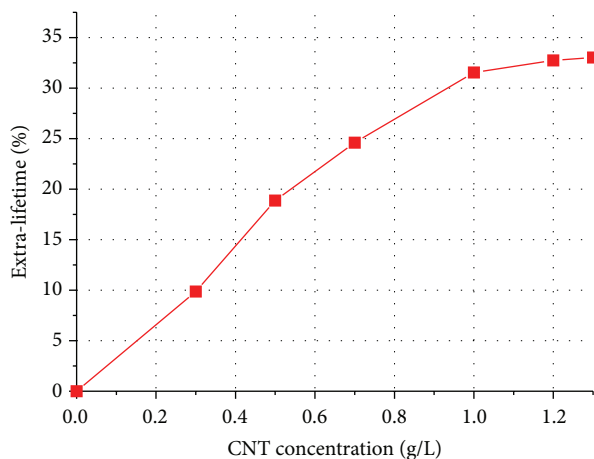


FIGURE 8: The dependence of extra-lifetime percent of 450 W LED on CNTs concentration in nanofluid.

2 times. Thus, the lifetime of LED was estimated as the following expression:

$$L \approx L_0 \cdot 2^{\Delta t/10}, \quad (1)$$

where  $L_0$ ,  $L$ , and  $\Delta t$  indicated the basic-lifetime, the extended-lifetime, and the temperature reduction of LED, respectively. Thus, the extra-lifetime percent of LED is determined by the expression:

$$\%L = \frac{L - L_0}{L_0} \cdot 100\% = (2^{\Delta t/10} - 1) \cdot 100\%. \quad (2)$$

From (2), the extra-lifetime percent of LED was estimated as shown in Figure 8. It clearly showed that the lifetime of LED is extended when the CNTs concentration is increased. The extra-lifetime percent of LED reached a saturated value at 33% with 1.2 g/L of CNTs concentration. The extra-lifetime percent of LED almost did not increase with 1.3 g/L of CNTs concentration. Thus, we have chosen 1.2 g/L for the optimal concentration of CNTs for the 450 W LED floodlight.

#### 4. Conclusions

The heat dissipation efficiency of the 450 W LED floodlight using the MWCNTs nanofluid was examined and evaluated. The temperature of the LED chip was saturated after 40 minutes of working time. By mixing CNTs-OH with 1.2 g/L of concentration in the nanofluid, the saturated temperature of LED chip decreased by 4.5°C compared to fluid without CNTs. The extra-lifetime percent of LED also reached a saturated value at 33% with 1.2 g/L of optimal CNTs concentration. The experimental results have confirmed the advantage of the MWCNTs based liquid in heat dissipation for 450 W LED floodlight and other high-power electronic devices.

#### Conflict of Interests

The authors declare that there is no conflict of interests regarding the publication of this paper.

#### Acknowledgments

The authors acknowledge financial support from the Vietnam National Foundation for Science and Technology Development (NAFOSTED) under Grant no. 103.99-2012.35. The authors also would like to thank the VAST Program for Young Scientist for the financial support (Project no. VAST.DLT.05/13-14).

#### References

- [1] S. U. S. Choi and J. A. Eastman, "Enhancing thermal conductivity of fluids with nanoparticles," in *Proceedings of the International Mechanical Engineering Congress and Exhibition*, San Francisco, Calif, USA, 1995.
- [2] Y.-H. Hung, J.-H. Chen, and T.-P. Teng, "Feasibility assessment of thermal management system for green power sources using nanofluid," *Journal of Nanomaterials*, vol. 2013, Article ID 321261, 11 pages, 2013.
- [3] M. Dong, L. P. Shen, H. Wang, H. B. Wang, and J. Miao, "Investigation on the electrical conductivity of transformer oil-based AlN nanofluid," *Journal of Nanomaterials*, Article ID 842963, 7 pages, 2013.
- [4] A. M. Hussein, K. V. Sharma, R. A. Bakar, and K. Kadrigama, "The effect of nanofluid volume concentration on heat transfer and friction factor inside a horizontal tube," *Journal of Nanomaterials*, vol. 2013, Article ID 859563, 12 pages, 2013.
- [5] K. Tseng, H. Lee, C. Liao, K. Chen, and H. Lin, "Rapid and efficient synthesis of silver nanofluid using electrical discharge machining," *Journal of Nanomaterials*, vol. 2013, Article ID 174939, 6 pages, 2013.
- [6] V. N. Popov, "Carbon nanotubes: properties and application," *Materials Science and Engineering R: Reports*, vol. 43, no. 3, pp. 61–102, 2004.
- [7] P. N. Minh and P. H. Khoi, "Carbon nanotube: a novel material for applications," *Journal of Physics: Conference Series*, vol. 187, Article ID 012002, 2009.
- [8] S. K. Singhal, M. Lal, Lata, S. R. Kabi, and R. B. Mathur, "Synthesis of Cu/CNTs nanocomposites for antimicrobial activity," *Advances in Natural Sciences: Nanoscience and Nanotechnology*, vol. 3, no. 4, Article ID 045011, 10 pages, 2012.
- [9] A. S. Hoang, H. N. Nguyen, H. T. Bui, A. T. Tran, V. A. Duong, and V. B. Nguyen, "Carbon nanotubes materials and their application to guarantee safety from exposure to electromagnetic fields," *Advances in Natural Sciences: Nanoscience and Nanotechnology*, vol. 4, no. 2, Article ID 025012, 5 pages, 2013.
- [10] H. T. Bui, V. C. Nguyen, V. T. Pham, T. T. T. Ngo, and N. M. Phan, "Thermal dissipation media for high power electronic devices using a carbon nanotube-based composite," *Advances in Natural Sciences: Nanoscience and Nanotechnology*, vol. 2, Article ID 025002, 4 pages, 2011.
- [11] N. M. Phan, H. T. Bui, M. H. Nguyen, and H. K. Phan, "Carbon-nanotube-based liquids: a new class of nanomaterials and their applications," *Advances in Natural Sciences: Nanoscience and Nanotechnology*, vol. 5, no. 1, Article ID 015014, 5 pages, 2014.
- [12] R. Walvekar, I. A. Faris, and M. Khalid, "Thermal conductivity of carbon nanotube nanofluid—experimental and theoretical study," *Heat Transfer—Asian Research*, vol. 41, no. 2, pp. 145–163, 2012.
- [13] B. H. Thang, P. N. Hong, P. V. Trinh et al., "Simulation of thermal dissipation in a  $\mu$ -processor using carbon nanotubes

- based composite,” *Computational Materials Science*, vol. 49, no. 4, pp. S302–S306, 2010.
- [14] Y. Ding, H. Alias, D. Wen, and R. A. Williams, “Heat transfer of aqueous suspensions of carbon nanotubes (CNT nanofluids),” *International Journal of Heat and Mass Transfer*, vol. 49, no. 1-2, pp. 240–250, 2006.
- [15] B. H. Thang, P. van Trinh, N. van Chuc, P. H. Khoi, and P. N. Minh, “Heat dissipation for microprocessor using multiwalled carbon nanotubes based liquid,” *The Scientific World Journal*, vol. 2013, Article ID 305957, 6 pages, 2013.
- [16] N. D. Dung, N. Van Chuc, N. T. T. Tam, N. H. Quang, P. H. Khoi, and P. N. Minh, “Carbon-nanotube growth over iron nanoparticles formed on CaCO<sub>3</sub> support by using hydrogen reduction,” *Journal of the Korean Physical Society*, vol. 52, no. 5, pp. 1372–1377, 2008.
- [17] S. Mukherjee and S. Paria, “Preparation and stability of nanofluids—a review,” *IOSR Journal of Mechanical and Civil Engineering*, vol. 9, no. 2, pp. 63–69, 2013.
- [18] L. Chen and H. Xie, “Surfactant-free nanofluids containing double- and single-walled carbon nanotubes functionalized by a wet-mechanochemical reaction,” *Thermochimica Acta*, vol. 497, no. 1-2, pp. 67–71, 2010.
- [19] S. S. Chougule and S. K. Sahu, “Thermal performance of automobile radiator using carbon nanotube-water nanofluid—experimental study,” *Journal of Thermal Science and Engineering Applications*, vol. 6, no. 4, Article ID 041009, 2014.
- [20] B. H. Thang, P. Van Trinh, L. D. Quang, N. T. Huong, P. H. Khoi, and P. N. Minh, “Heat dissipation for Intel core i5 processor using multiwalled carbon nanotubes based ethylene glycol,” in *Proceedings of the 2nd International Conference on Advanced Electromaterial (ICAE '13)*, ICC, Jeju, Republic of Korea, November 2013, Accepted for publication in Journal of Korean Physical Society, 2014.

## Research Article

# Preparation and Application of Conductive Textile Coatings Filled with Honeycomb Structured Carbon Nanotubes

**Filip Govaert and Myriam Vanneste**

*Centexbel, Belgian Textile Research Centre, Technologiepark 7, 9052 Gent, Belgium*

Correspondence should be addressed to Filip Govaert; [fgo@centexbel.be](mailto:fgo@centexbel.be)

Received 28 February 2014; Revised 6 June 2014; Accepted 7 June 2014; Published 18 June 2014

Academic Editor: Jun Yang

Copyright © 2014 F. Govaert and M. Vanneste. This is an open access article distributed under the Creative Commons Attribution License, which permits unrestricted use, distribution, and reproduction in any medium, provided the original work is properly cited.

Electrical conductive textile coatings with variable amounts of carbon nanotubes (CNTs) are presented. Formulations of textile coatings were prepared with up to 15 wt % of CNT, based on the solid weight of the binder. The binders are water based polyacrylate dispersions. The CNTs were mixed into the binder dispersion starting from a commercially available aqueous CNT dispersion that is compatible with the binder dispersion. Coating formulations with variable CNT concentrations were applied on polyester and cotton woven and knitted fabrics by different textile coating techniques: direct coating, transfer coating, and screen printing. The coatings showed increasing electrical conductivity with increasing CNT concentration. The coatings can be regarded to be electrically conductive (sheet resistivity  $< 10^3$  Ohm/sq) starting at 3 wt% CNT. The degree of dispersion of the carbon nanotubes particles inside the coating was visualized by scanning electron microscopy. The CNT particles form honeycomb structured networks in the coatings, proving a high degree of dispersion. This honeycomb structure of CNT particles is forming a conductive network in the coating leading to low resistivity values.

## 1. Introduction

Textile materials with integrated electrical conductivity make it possible to create intelligent articles with wide ranging applications in sports and work wear, healthcare, and for technical applications. Nowadays, electrically conductive textile applications are made by weaving, knitting, or attaching metal wires in the textile material [1–3]. The homogeneous distribution of the electric current over the total textile surface is poor and only located at the position of the metal wire. In case of electric connectors this specific location of the electric current is desired, but in devices for sensors or electric heating, this concentration of electric current is a source of concern. These high currents can lead to material defects. To avoid this, many wires are introduced to spread the current equally over the textile surface. Textile articles are subjected to processes and activities during their lifetime of use, that is, washing (tumble), drying, and flexing and exposed to varying (outdoor) conditions: humidity, extreme temperatures, irradiation by UV, rain, and so forth. When metal wires and devices are present in this textile, very

severe protection is necessary to avoid rapid degradation and corrosion of these materials. This protection is achieved by using insulation cabling, layered structures, and more stiff and thick materials to limit bending and stretching [4–6].

Conductive coatings or finishes for textiles are used in application such as conductive mattress covers for surgical tables or fabrics with shielding for electromagnetic radiation for military applications or work wear. In that case high loading of carbon black is needed to provide sufficient electrical conductivity, while hampering the final textile properties [7].

The integration of carbon nanotubes (CNTs) in coatings for textiles offer good perspectives to obtain electrically conductive textile materials without losing the basic properties of a textile, that is, light weight, stretchable and flexible, comfortable, and ease of use. Conductive textiles by incorporating CNT through a coating or dyeing process are already discussed [8–10]. This work assesses the usability of CNT in various textile materials and applications by investigating CNT as an additive in coatings for textiles. In this work, textile coatings with variable amounts of CNT were developed and applied by traditional textile application

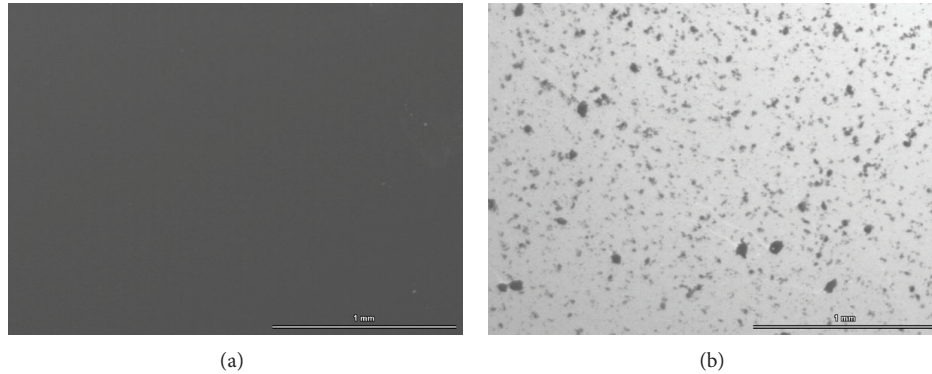


FIGURE 1: Microscopic evaluation of wet 1 wt% CNT coating formulations, with no CNTs visible (a) and agglomerates of CNTs (b).

processes, that is, direct coating, transfer coating, and screen printing. A high degree of dispersion of the CNT within the coating was observed over the entire concentration range and visualized by scanning electron microscopy. This study reveals the construction of a honeycomb conductive network of the CNT particles inside the coatings.

## 2. Materials and Methods

**2.1. Materials.** The CNTs were supplied by Nanocyl (Belgium) as an aqueous dispersion of 3% by weight. This dispersion is commercially available under the name of Aquacyl.

As binders, polyacrylate dispersions under the commercial name Lurapret from BASF (Germany) were used. Lurapret dispersions are used to make coatings for home and technical textiles and characterized by a good wash and chemical resistance and a long lifetime. For textile coating, thickeners are added to the formulation, prior to coating, to avoid complete penetration inside the textile material. An acrylate-based polymer synthetic thickener from BASF was used: Lutexal HIT. Furthermore pigment stabilizing agents based on alkoxyated surfactants were used to improve the dispersion of the CNT particles in the formulation.

The textile materials used in this study are polyester knitted and woven fabrics from various suppliers.

For transfer coating process, release paper from ArjoWiggins, UK (Primacast Mirror) was used.

**2.2. Coating Formulation.** Coating formulations were prepared by mixing different amounts of the CNT dispersion and binder dispersion with a laboratory overhead stirrer (IKA, Germany). The formulating was divided into two parts. Part one is the addition of the CNT dispersion to the binder dispersion. The CNT dispersion was added in small amounts and under constant mixing at slow speed (~1000 rpm). To avoid high thickening of the formulation paste, small amounts of water are added as well. In Part two, the dispersion was mixed at high speed (~10000 rpm) to obtain homogeneous dispersed CNT coating formulation. Finally, the vessel was placed in a desiccator and subjected to a vacuum process for 30 min with a maximum vacuum of -1 bar. This was done to avoid the introduction of air bubbles

in the coating formulation and afterwards in the coating on the fabric. The quality of the dispersion was controlled by optical microscopy. When agglomerates of CNT particles are observed, the dispersion was qualified as insufficient and not further used. In case a homogeneous black picture of the dispersion was observed, the dispersion was qualified as good. In Figure 1, images of these microscopic observations of both types of dispersions are showed.

**2.3. Coating Application.** The coating formulation was prepared for application by adding thickener to adjust the viscosity of the coating paste. The thickener was added in small amounts and by slow mixing (~500 rpm). Afterwards, the coating paste was subjected again to a vacuum process for 30 min with a maximum vacuum of -1 bar.

For the application of the coatings, a labcoater LTE-S from Mathis (Switzerland) was used. This labcoater is a combination of an applicator and a drying unit.

For the direct coating applications, the coatings were applied in a three-layered structure. First, a basecoat was applied with the technique of knife-in-air. In this way, a thin layer is applied that covers all pores and holes of the fabric. The coating was immediately dried during 3 min at 150°C. Next, two layers were applied by the technique of knife-on-roll. The knife gap was set at 200 μm. After application the coating is dried in two steps: first during 2 min at 80°C and next during 2 min at 150°C. This was done to have gradual evaporation of water and to avoid the formation of air bubbles in the coating. Coated fabrics of 300 × 400 mm were obtained after the application and curing processes. Several samples were prepared for conductivity measurements, characterization, and further testing.

For the transfer coating applications, two layers of a CNT based coating were applied on transfer paper and subsequently transferred to the textile material with a tie-coat. This tie-coat is based on a polyurethane dispersion. Drying is done in the same two-step procedure as described above for the direct coatings.

Finally the method of screen printing of CNT based formulations was evaluated as well. For this purpose a screen with the design of an electronic circuit was used.

**2.4. Microscopic Characterization.** Morphology analysis of surface and layer structure was carried out by means of an



FIGURE 2: Black acrylate-based coating containing 10 wt% CNT on a white polyester fabric.

optical microscope, LV100POL (Nikon, Japan) equipped with digital imaging camera and software, DS-Fil (Nikon, Japan).

Scanning electron microscopy (SEM) was used to visualize the CNT particles in the coatings and to evaluate the degree of dispersion of CNT. Two ultrahigh resolution field emission scanning electron microscopes were used, Jeol JSM-7600F and Jeol JSM-7500F (Jeol, Japan) in collaboration with Nanocyl.

### 3. Results and Discussion

**3.1. Coating Application.** The first method used for the application of the CNT containing coating formulations is the direct knife-on-roll coating process. In this process the coating paste passes through a gap between the textile substrate and a knife. This gap determines the amount or weight of coating that is applied onto the textile surface. The 15 different coating formulations containing 1 wt% of CNT up to 15 wt% were applied by this process in a 3-layered structure as explained in Section 2. The coatings for evaluating the sheet resistance were prepared by this direct knife coating procedure. A picture of a 3-layered coating system produced on roll-to-roll coating equipment is shown in Figure 2.

The binders used for this type of coatings are high quality polyacrylates for textile coating with good film forming properties, high adhesion, good flexibility, and scratch resistance. These properties are reflected in the coatings containing CNT. Microscopic investigations using an optical microscope equipped with digital imaging are shown in Figure 3. It is clearly seen on these 10 wt% samples that a homogeneous coating is obtained that is free of defects. Depending on the wt% of CNT in the coating, differences in surface morphology are observed. At low CNT concentration, the coating has a semigloss aspect. This is similar to the coating without CNT. From CNT amounts of 10 wt% and higher the coating has a more matt aspect, due to the high solid content or the low amount of binder present in such coatings.

The irregularities observed on the surface can be explained by the roughness of the textile substrate. This can be seen on the image of the cross section where the waviness of the coating is following the structure of the woven fabric. Depending on the type of application method (direct coating versus transfer coating) the coating morphology on the textile can be changed. By the method of transfer coating, the structure of the release paper will determine the surface structure of the top layer. In Figure 4, the cross section of a transfer coated layer system is depicted. As transfer paper, a high-gloss (mirror) type of paper was used. In this process,

two layers are subsequently applied on the glossy release paper and fully dried and cured. To transfer this coating system to a textile, a tie-coat (binder without CNT) is applied on this coating system and a piece of textile is rolled in this wet layer. After drying and curing, the textile together with the complete coating system can be released from the paper. With this application process, a smooth and flat coated surface is achieved, due to the use of a mirror type of release paper.

A third application that was tested in this study is the method of screen printing. For this purpose simple screen designs were used to evaluate the printing process. Initially, the same formulation and preparation method was used as for the direct coating application method. The formulation with 10 wt% CNT was prepared and applied. Initially no sharp design of the print was obtained. This is due to a slight flow of the formulation immediately after application. This flow is beneficial in knife coating application to obtain a smooth homogeneous film, but in printing application, this flow is not acceptable. The formulation was adapted for screen printing by adding a thixotropic thickener to the formulation. By adding 0.5 to 1% of Lutexal TX4744 (BASF) to the total formulation, prints with sharp borders and edges were obtained. Examples of such prints are depicted in Figure 5. With this method conductive tracks can be applied on textile fabrics. The resistivity of these tracks depends on the width and thickness of the printed lines.

**3.2. Sheet Resistance.** In order to assess the influence of the CNT concentration in the coating on the electrical conductivity, 15 coating formulations were prepared with different concentrations of CNT and the sheet resistance of dried and cured coatings measured. The 15 coating formulations consist of 1 wt% up to 15 wt % of CNT based on the solid weight of the binder. These formulations were used to apply a three-layered coating system on the fabric by the direct coating process (one layer knife-in-air, two layers knife-on-roll). The sheet resistance was measured directly on the coated samples with a four-probe sheet resistance measurement. The results obtained for an acrylic-based textile coating are shown in Figure 6. There is a direct relationship between the concentration of CNT in the coating and the sheet resistance as expected: increasing the amount of CNT in the coating decreases the sheet resistance. A sheet resistance down to 60  $\Omega$ /sq was measured at 10 wt% CNT.

As depicted in Figure 6, it can be seen that percolation starts between 3 and 4 wt%. The coatings can be regarded to be electrically conductive (sheet resistivity  $< 10^3$  Ohm/sq) starting at 3 wt% CNT. For industrial use, it is important to see that a broad range of electrical conductivity levels can be obtained by simply changing the amount of CNT in the coating. Above a concentration of 10 wt% CNT, no significant decrease of sheet resistance is measured.

**3.3. Dispersion of Carbon Nanotubes.** By a controlled preparation of CNT based formulations—slow addition of the CNT dispersion, counter the effect of viscosity increase by the addition of small amounts of water—a high degree of dispersion of the CNT in the binder matrix can be obtained. Mixtures of alkoxyates improve strongly the rheology of the formulation.

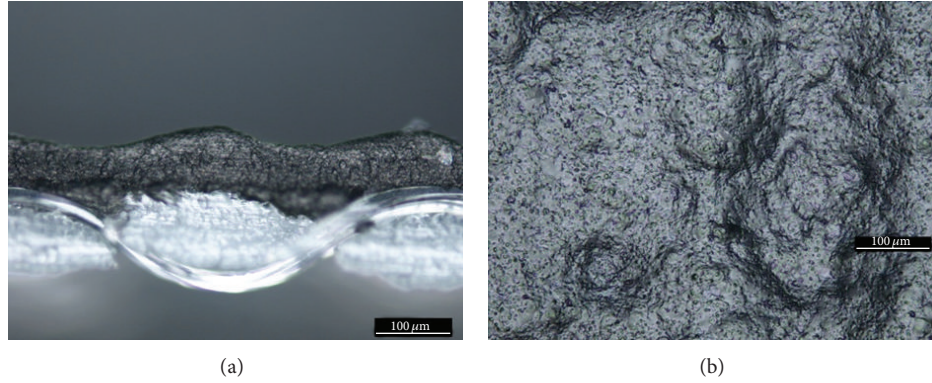


FIGURE 3: Microscopic images of coated textiles with a black acrylate-based coating containing 10 wt% CNT on a white polyester fabric: a cross section (a) and the surface (b).

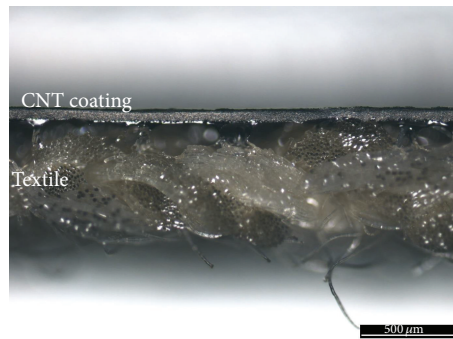


FIGURE 4: Microscopic image (cross section) of a coated textile with a black acrylate-based coating containing 10 wt% CNT on a polyester textile fabric by the transfer coating process.

Moreover by adding these alkoxyated surfactants to the formulation, the CNTs orientate during the coating drying process in a way that they form a honeycomb structure inside the binder matrix. This structure can be visualized by scanning electron microscopy images of applied coatings, depicted in Figure 7. The electrically conductive CNTs are highlighted during imaging and a structured network is visible.

This structure forms a continuous network inside the coating at a concentration of 10 wt% of CNT, based on the solid content. At lower CNT content, this network is inside the coating as well, but not homogeneously present over the complete surface. This is shown in Figure 8(a) for a coating with a CNT content of 6 wt%. The absence of a complete network results in a higher sheet resistance. At a concentration above 10 wt% of CNT in the coating, this network is in some areas overloaded with CNT, as shown in Figure 8(b) for a coating with a CNT content of 13 wt%.

The SEM analysis shows that a high degree of dispersion of carbon nanotubes can be observed. A network structure appears together with a high value of conductivity. From 3 wt% CNT the first network structure appears. This is also the concentration where a more linear relation between concentration and resistivity starts (see Figure 6). The most clear network structure can be observed at 10 and 11 wt%. Above this concentration saturation of carbon nanotubes in

some areas occurs and at 15% loss of structure is observed. The conductivity increases slightly from 4 wt% up to 14 wt% and drops slightly at 15 wt%.

The origin of this network can be explained by the fact that the CNT particles are homogeneously present in the acrylate binder dispersion. During the drying process of the wet coating, all the water evaporates and the acrylate particles move together surrounded by the CNT particles. The CNT particles settle between the acrylate particles forming a honeycomb structured network. In the SEM picture in Figure 9 one can observe the surface of an acrylate-based coating. This coating was completely dried at 30°C to avoid fusion of the acrylate particles at high temperature. In this picture the individual acrylate particles can be observed. The particles have an average particles size of approximately 180 nm. This size corresponds to honeycomb cell size that can be observed in Figure 7. Measurements show that these CNT cells have sizes between 160 and 230 nm. The most perfect CNT honeycomb cells have a diameter of approximately 180 nm.

#### 4. Conclusions

This work describes the introduction of electrical conductivity in textile materials by the use of textile coatings filled with carbon nanotubes. The preparation of coating

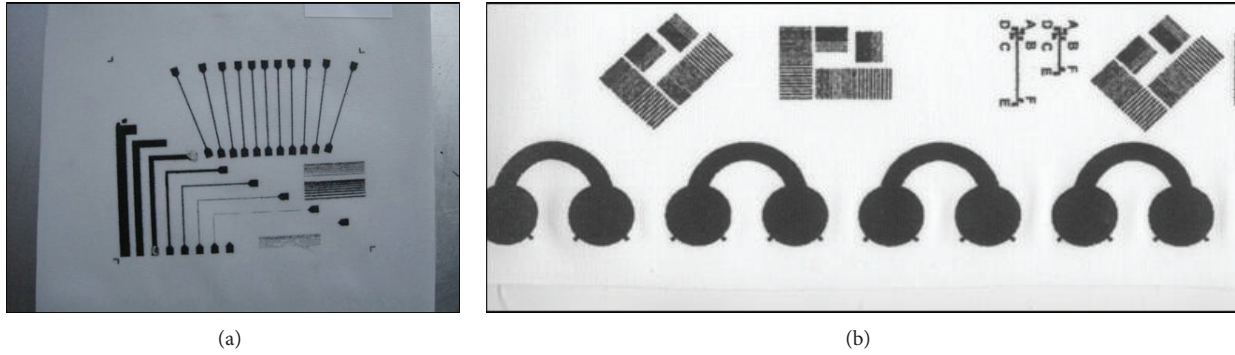


FIGURE 5: Screen printing of black acrylic-based coatings containing 10 wt% CNT on polyester (a) and cotton (b) textile fabric.

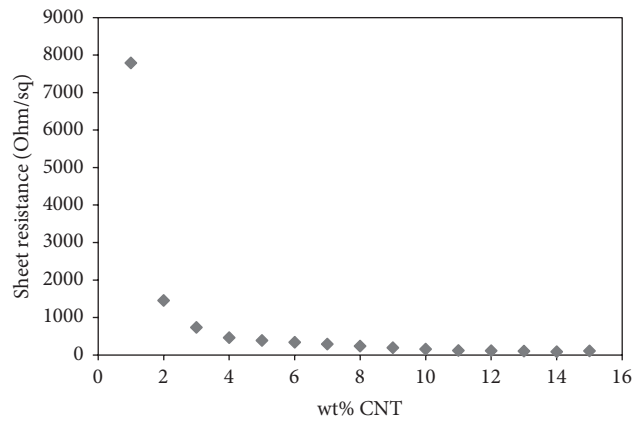


FIGURE 6: Sheet resistance of an acrylic-based textile coatings with different CNT loading (wt%).

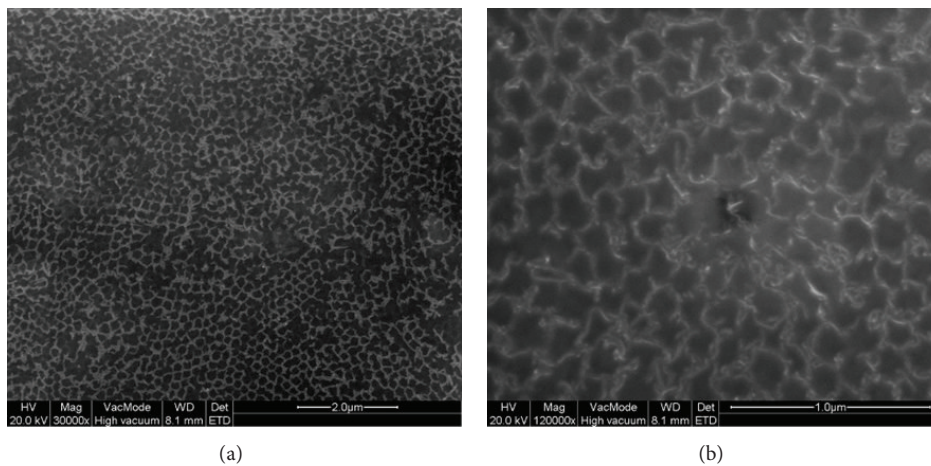


FIGURE 7: Scanning electron microscopy images of the surface of an acrylic-based coating containing 10 wt% CNT, in low (a) and high (b) magnification.

formulations of water based acrylic binders with CNT as the active filler material is demonstrated. It is important to control the viscosity of the formulation during the addition of the CNT. CNT acts as a thickener to the binder material during the preparation of the coating paste. This viscosity increase must be controlled by adding CNT in small amounts to the binder material and by adding water to counter the thickening effect. The application of these coating formulations was demonstrated by direct coating, transfer coating,

and screen printing. With the direct and transfer coating process, full coatings of one or more layers are applied over the complete textile surface. In direct coating, the textile structure is maintained, but with the transfer coating process, flat and smooth coating surfaces can be obtained onto a textile substrate. With screen printing, conductive tracks or designs are applied on the textile material. The level of conductivity of these layers or tracks can be defined by the coating composition. By varying the amount of CNT in

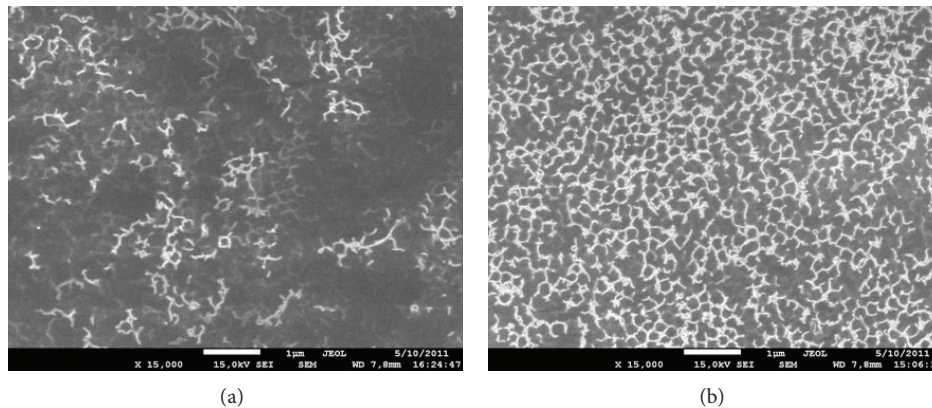


FIGURE 8: SEM images of the surface of an acrylate-based coating containing 6 wt% CNT (a) and 13 wt% CNT.

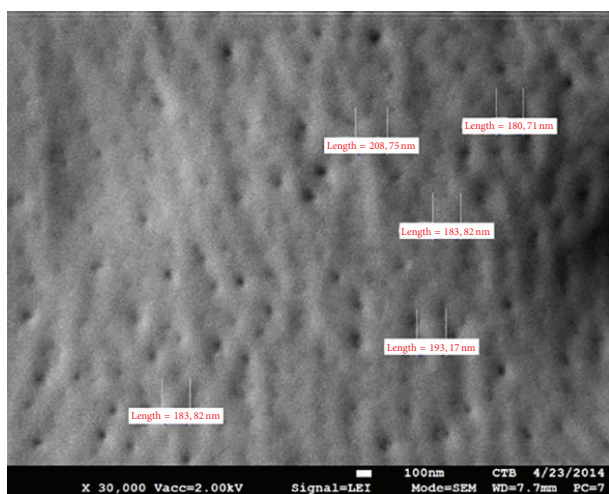


FIGURE 9: SEM image from the surface of an acrylate-based coating dried at 30°C with indication of the acrylate particle size.

the coating formulation, the range of conductivity can be tuned from antistatic (1 wt% CNT) up to high conductivity (10 wt% CNT). The high level of conductivity (low resistivity) was explained by a high degree of dispersion of the CNT particles in the coating. A network of honeycomb structured CNTs can be visualized by scanning electron microscopy. This structure is homogeneously present in the coating at a concentration from 10 wt% to 11 wt% of CNT. The CNT network can be explained by the fact that the CNT particles are homogeneously present in the acrylate binder dispersion. During the drying process of the coating formulation, the acrylate particles move together due to the evaporation of the water. The CNT particles are moving between the acrylate particles forming a honeycomb structured network. The cell size of this CNT network corresponds to the size of the acrylate particles.

### Conflict of Interests

The authors declare that there is no conflict of interests regarding the publication of this paper.

### Acknowledgments

The research results presented in this paper have been obtained in the research project IWT-095070 and IWT-120629, with the financial support of the Flemish government agency for Innovation by Science and Technology. The authors are grateful to Nanocyl for providing the CNT material and for the fruitful discussions, SEM measurements, and collaboration.

### References

- [1] R. F. Service, "Electronic textiles charge ahead," *Science*, vol. 301, no. 5635, pp. 909–911, 2003.
- [2] M. Catrysse, R. Puers, C. Hertleer, L. Van Langenhove, H. Van Egmond, and D. Matthys, "Towards the integration of textile sensors in a wireless monitoring suit," *Sensors and Actuators A: Physical*, vol. 114, no. 2-3, pp. 302–311, 2004.
- [3] I. Locher, T. Kirstein, and G. Tröster, "Temperature profile estimation with smart textiles," in *Proceedings of the 1st International Scientific Conference (Ambience '05)*, Tampere, Finland, September 2005.
- [4] E. R. Post, M. Orth, R. R. Russo, and N. Gershenfeld, "E-broderly: design and fabrication of textile-based computing," *IBM Systems Journal*, vol. 39, no. 3-4, pp. 840–860, 2000.
- [5] S. Coyle, K. -T. Lau, N. Moyna et al., "BIOTEX-biosensing textiles for personalised healthcare management," *IEEE Transactions on Information Technology in Biomedicine*, vol. 14, no. 2, pp. 364–370, 2010.
- [6] M. Billingham, "New ways to manage information," *Computer*, vol. 32, no. 1, pp. 57–64, 1999.
- [7] D. Negru, C.-T. Buda, and D. Avram, "Electrical conductivity of woven fabrics coated with carbon black particles," *Fibres and Textiles in Eastern Europe*, vol. 90, no. 1, pp. 53–56, 2012.
- [8] M. I. H. Panhuis, J. Wu, S. A. Ashraf, and G. G. Wallace, "Conducting textiles from single-walled carbon nanotubes," *Synthetic Metals*, vol. 157, no. 8-9, pp. 358–362, 2007.
- [9] B. S. Shim, W. Chen, C. Doty, C. Xu, and N. A. Kotov, "Smart electronic yarns and wearable fabrics for human biomonitoring made by carbon nanotube coating with polyelectrolytes," *Nano Letters*, vol. 8, no. 12, pp. 4151–4157, 2008.
- [10] R. Zhang, H. Deng, R. Valenca et al., "Carbon nanotube polymer coatings for textile yarns with good strain sensing capability," *Sensors and Actuators A: Physical*, vol. 179, pp. 83–91, 2012.

## Research Article

# Improved Efficiency of Graphene/Si Heterojunction Solar Cells by Optimizing Hydrocarbon Feed Rate

Zexia Zhang,<sup>1</sup> Tongxiang Cui,<sup>1</sup> Ruitao Lv,<sup>1</sup> Hongwei Zhu,<sup>1,2</sup> Kunlin Wang,<sup>1</sup> Dehai Wu,<sup>1</sup> and Feiyu Kang<sup>1,3</sup>

<sup>1</sup> Key Laboratory of Advanced Materials (MOE), School of Materials Science and Engineering, Tsinghua University, Beijing 100084, China

<sup>2</sup> Center for Nano and Micro Mechanics, Tsinghua University, Beijing 100084, China

<sup>3</sup> Graduate School at Shenzhen, Tsinghua University, Shenzhen, Guangdong 518055, China

Correspondence should be addressed to Ruitao Lv; lvruitao@tsinghua.edu.cn and Feiyu Kang; fykang@tsinghua.edu.cn

Received 7 March 2014; Accepted 24 April 2014; Published 15 June 2014

Academic Editor: Jinlong Jiang

Copyright © 2014 Zexia Zhang et al. This is an open access article distributed under the Creative Commons Attribution License, which permits unrestricted use, distribution, and reproduction in any medium, provided the original work is properly cited.

Four different graphene films were synthesized via chemical vapor deposition by using acetonitrile with feed rates of 0.01, 0.02, 0.04, and 0.06 mL/min. Heterojunction solar cells were assembled by transferring as-synthesized graphene films onto *n*-Si. Solar cells based on graphene samples produced at 0.01, 0.02, 0.04, and 0.06 mL/min demonstrate power conversion efficiencies of 2.26%, 2.10%, 1.02%, and 0.94%, respectively. When HNO<sub>3</sub> was used to dope the graphene films, the corresponding photovoltaic efficiencies were increased to 4.98%, 4.19%, 2.04%, and 1.74%, respectively. Mechanism for the improved efficiency of graphene/Si heterojunction solar cells was also investigated.

## 1. Introduction

The application of graphene in photovoltaics has attracted tremendous research interest due to its unique two-dimensional structure [1, 2], high light transmittance [3], and excellent carrier mobility [4, 5]. Indium tin oxide (ITO) is a commercialized transparent electrode for solar cells [6], but ITO suffers from many drawbacks, such as high cost, limited resource of indium and brittle textures [7]. It was shown that graphene could be a possible candidate for replacing ITO in organic solar cells [3, 8]. Furthermore, graphene also shows the potential to replace platinum (Pt) in dye-sensitized solar cells (DSSCs) [9, 10]. As is known, the role of Pt in DSSCs is to catalyze the reduction of I<sub>3</sub><sup>-</sup> to I<sup>-</sup> at counter electrode [11]. However, Pt is very costly and has limited supply on the earth. Replacement of Pt by other inexpensive and abundant materials is also very important. Pt-free counter electrode was developed recently by using graphene supported nickel nanoparticles as catalyst, and the corresponding solar cell efficiency had an increase of 10% than that of Pt-based DSSCs [11]. In addition, graphene could also be used as an active layer

for *p-n* junction and participate in the photo-carrier generation process [12]. Schottky junction solar cells had been assembled by transferring graphene onto various semiconducting substrates, such as Si [12], CdS [13], and CdSe [14]. A recent work showed that the initial efficiency of graphene/Si (G/Si) solar cell reached 1.9%, and it could be further improved to 8.6% by bis(trifluoromethanesulfonyl)imide [((CF<sub>3</sub>SO<sub>2</sub>)<sub>2</sub>)NH] doping [15].

Due to the simple design and efficient photovoltaic conversion, G/Si Schottky junction solar cells have attracted increasing interests and exciting progress has been achieved recently [16–18]. However, there are still many fundamental questions which need to be addressed. In particular, the influence of many factors on the performance of G/Si solar cells is still under investigation, such as chemical doping of graphene films [15, 19, 20], the environment gas flow [21, 22], and the thickness of graphene sheets [23]. Besides that, feed rate of hydrocarbon precursors is also an important factor in graphene synthesis [24, 25]. For example, our previous work has demonstrated that graphene and carbon films could be selectively synthesized by adjusting the feed rate of

acetonitrile [24]. Many impurities and agglomerates could be observed on graphene surface if the feed rate of hydrocarbon precursor was not optimized [25, 26]. However, the effect of hydrocarbon precursor feed rate on the photovoltaic performance of graphene has been rarely investigated.

In this work, four graphene films were obtained at different acetonitrile feed rates (0.01, 0.02, 0.04, and 0.06 mL/min). G/Si heterojunction solar cells based on these graphene films demonstrate efficiencies of 2.26%, 2.10%, 1.02%, and 0.94%, respectively. Moreover, the respective efficiencies could be enhanced to 4.98%, 4.19%, 2.04%, and 1.74% upon HNO<sub>3</sub> treatment. It is clearly shown that high feed rate of acetonitrile plays a negative role in the photovoltaic performance of graphene, and the reason for that is discussed in detail.

## 2. Experiment

**2.1. Synthesis of Graphene.** The experimental setup and procedure are described in detail elsewhere [24]. Cu foil is used as substrate, located in the middle of the quartz tube reactor, and gradually heated up to 900 °C in an Ar (300 mL/min) flow. H<sub>2</sub> is introduced into the reactor as the temperature reaches 900 °C, and the Cu substrate is annealed at 900 °C for 1 h to homogenize the crystal grain. After that, the temperature is raised to 1000 °C at a rate of 10 °C/min. Then, acetonitrile is fed into the reactor at a given rate (0.01, 0.02, 0.04, or 0.06 mL/min) in an Ar (2000 mL/min)/H<sub>2</sub> (30 mL/min) flow for 5 min. When the feeding of acetonitrile is cut off, the Cu foil is quickly moved to the low-temperature region of the reactor to ensure fast-cooling rate.

**2.2. Transfer of Graphene.** Samples of as-synthesized graphene on Cu foil were cut into pieces with sizes of ~6 mm × 6 mm and then etched in a mixed solution of FeCl<sub>3</sub>/HCl. After the Cu was completely etched away, the graphene films were floating on the surface of FeCl<sub>3</sub>/HCl solution. Then, the graphene films were rinsed with deionized water for several times and transferred onto arbitrary substrate for characterization and device fabrication.

**2.3. Characterization of Graphene.** Optical transmission spectra of graphene films were collected by a UV-2450 UV/vis optical spectrometer. The sheet resistance of the graphene films was measured using a four-probe resistivity test system. The morphologies of graphene samples were characterized by scanning electron microscope (SEM, JSM-6460 LV) and transmission electron microscope (TEM, JEOL-2010).

**2.4. Solar Cell Device Assembly and Evaluation.** The details of the solar cell assembly can be found in our previous work [27]. In a typical process, as-synthesized graphene film (with Cu substrate) was cut into pieces and then etched in a mixed solution of FeCl<sub>3</sub>/HCl. After 2~3 hours, the Cu substrate could be completely etched away at room temperature. The detached graphene film will float on the surface of the FeCl<sub>3</sub>/HCl solution. After being rinsed with deionized water for several times, the graphene film was transferred onto *n*-type Si wafer (with a square window of 3 mm × 3 mm

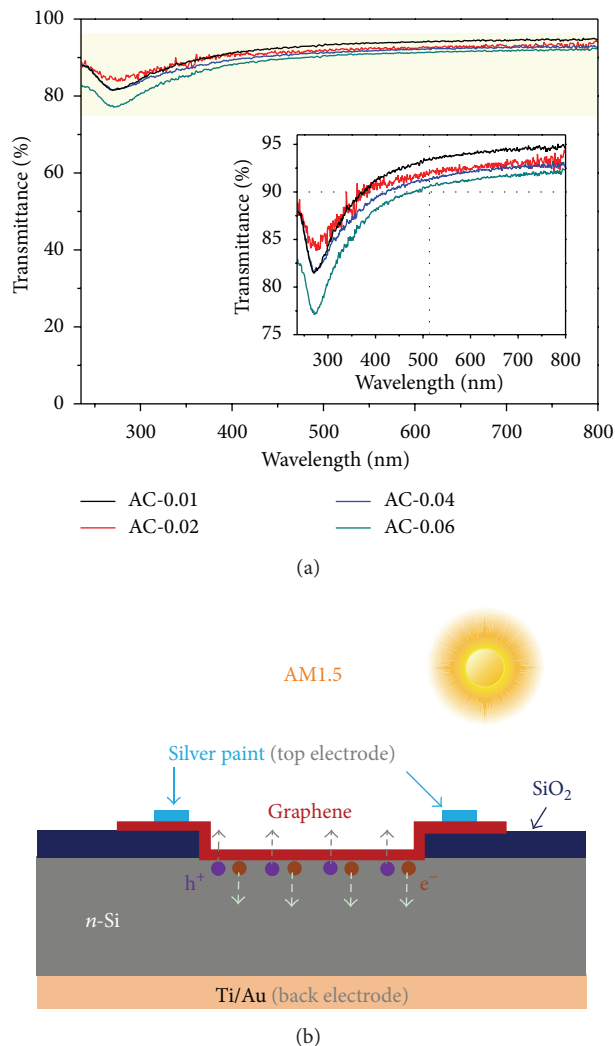


FIGURE 1: (a) Optical transmission spectra of different graphene samples. Inset is the enlarged spectra of the parts highlighted with light yellow color. (b) A schematic diagram of the solar cell device configuration. In this kind of device, photo-generated holes ( $h^+$ ) and electrons ( $e^-$ ) are driven by the built-in electric field into graphene and *n*-Si, respectively.

surrounded by insulating SiO<sub>2</sub>) to construct a heterojunction solar cell. Ag paste and Ti/Au were used as top and back electrodes, respectively. The assembled solar cell devices were evaluated with a solar simulator (Newport, at AM1.5, 100 mW/cm<sup>2</sup>) and a Keithley 2400 SourceMeter.

## 3. Results and Discussion

The graphene samples produced at acetonitrile feed rate of 0.01, 0.02, 0.04, and 0.06 mL/min were labelled as AC-0.01, AC-0.02, AC-0.04, and AC-0.06, respectively. The transmission spectra of the graphene samples produced at different feed rates were shown in Figure 1(a). All the samples show high transparency in the UV-Vis range with transmittances

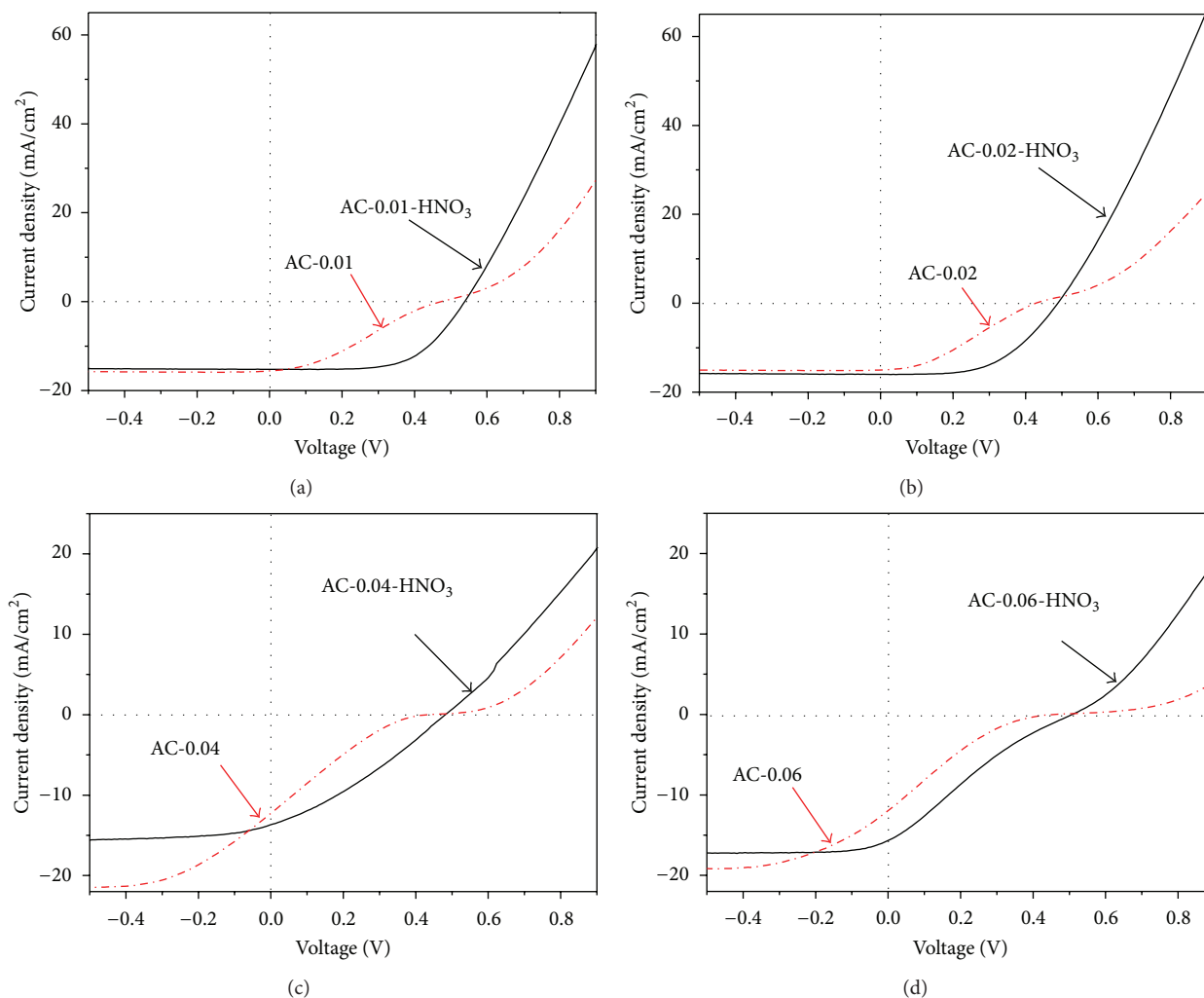


FIGURE 2: Light current density-voltage curves of solar cells based on different graphene samples before (red lines) and after HNO<sub>3</sub> (black lines) treatment. (a) AC-0.01, (b) AC-0.02, (c) AC-0.04, and (d) AC-0.06.

up to 90% at 550 nm wavelength. The sheet resistance of AC-0.01, AC-0.02, AC-0.04, and AC-0.06 is 1080, 1135, 1353, and 1415  $\Omega/\text{sq}$ , respectively. Raman spectra and high resolution TEM image (see Figure S1 in Supplementary Material available online at <http://dx.doi.org/10.1155/2014/359305>) were used to identify the layers of these samples, and the higher intensity of 2D-band than that of G-band in Figure S1(a) proves the graphene films are mainly few-layer ones (about less than 3 layer), which is also confirmed by HRTEM image (Figure S1(b)). The graphene samples are highly transparent and conductive, making them appealing in G/Si heterojunction solar cell applications.

G/Si heterojunction solar cells were assembled by transferring as-synthesized graphene films onto *n*-type Si. A schematic diagram of the G/Si heterojunction solar cell is shown in Figure 1(b). High purity silver paint is used to form ohmic contacts between graphene and silver wire, which is used as an electrode for electrical measurements. In this device, graphene films can act not only as the active part of Schottky junction, but also as the transparent anode

electrode. A space-charge region accompanied by a built-in electric field is formed at the interface of graphene and *n*-Si because of their work function difference. The photo-generated holes ( $h^+$ ) and electrons ( $e^-$ ) are driven by the built-in electric field into the graphene and *n*-Si, respectively.

The current density ( $J$ ) versus voltage ( $V$ ) curves of solar cells based on the graphene films produced at different acetonitrile feed rates are shown in Figure 2. The corresponding photovoltaic parameters, such as short circuit current density ( $J_{sc}$ ), open circuit voltage ( $V_{oc}$ ), filling factor (FF), and power conversion efficiency ( $\eta$ ), are listed in Table 1. As shown in Table 1, solar cells based on AC-0.01, AC-0.02, AC-0.04, and AC-0.06 demonstrate  $\eta$  of 2.26%, 2.10%, 1.02%, and 0.94%, respectively. The  $\eta$  of solar cells based on AC-0.01 and AC-0.02 shows comparable photovoltaic performance with previous report work about G/Si solar cells [12, 26, 28]. However, the efficiencies are still far from practical applications. HNO<sub>3</sub> was used to modify the graphene films and to enhance the photovoltaic performance of assembled solar cells. The assembled G/Si cells were placed above a vial

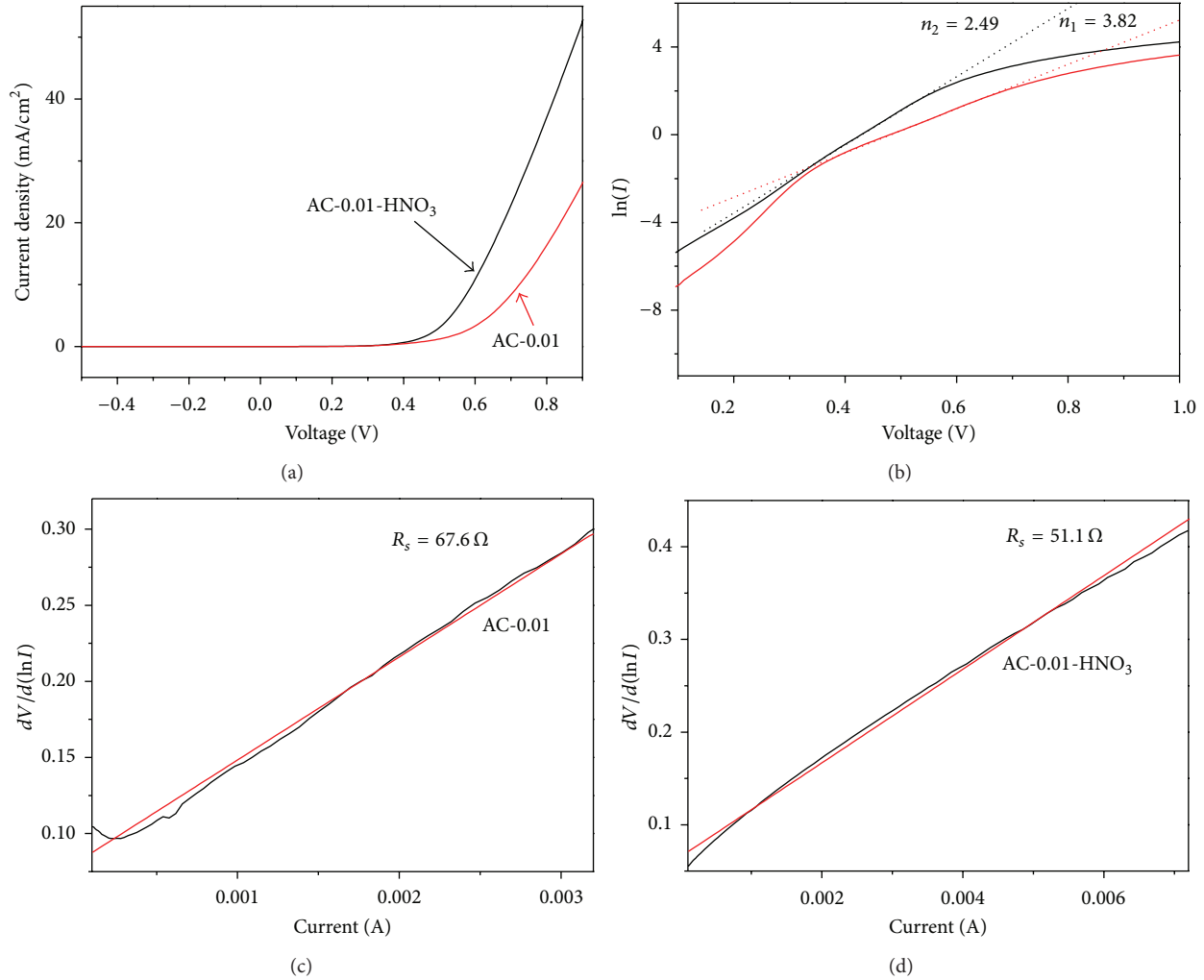


FIGURE 3: Mechanism for the efficiency improvement by HNO<sub>3</sub> treatment. (a) Dark current density-voltage curves of solar cells based on AC-0.01 before (red line) and after HNO<sub>3</sub> (black line) treatment. (b) Plots of  $\ln(I)$  versus voltage showing diode ideality factors before ( $n_1$ ) and after ( $n_2$ ) HNO<sub>3</sub> treatment. ((c), (d)) Linear fit of  $dV/d(\ln I)$  versus  $I$  shows the  $R_s$  of the AC-0.01 solar cell before and after HNO<sub>3</sub> treatment: (c) before HNO<sub>3</sub> treatment and (d) after HNO<sub>3</sub> treatment.

containing fuming HNO<sub>3</sub> (65 wt%). The treatment time was fixed at 1 min, in case of corrosion of silver and underlying Si at longer time [19]. Upon HNO<sub>3</sub> treatment, the efficiencies of solar cells based on AC-0.01, AC-0.02, AC-0.04, and AC-0.06 could be increased to 4.98%, 4.19%, 2.04%, and 1.74%, respectively. That means the efficiencies of the G/Si solar cells almost doubled upon HNO<sub>3</sub> treatment, which accords with previous reported works [19, 28]. The corresponding photovoltaic parameters after HNO<sub>3</sub> treatment are also listed in Table 1. The reasons why the efficiencies of G/Si solar cells could be enhanced by HNO<sub>3</sub> treatment are discussed as follows. Firstly, HNO<sub>3</sub> treatment could increase the work function of graphene film by *p*-doping [19]. As it was demonstrated in our previous work, increasing the work function of graphene is beneficial for a larger  $V_{oc}$  of the G/Si Schottky junction [19, 29]. It can be seen from Table 1, the  $V_{oc}$  of all the solar cells has an increase of  $\sim 55$  mV after HNO<sub>3</sub> treatment. Secondly, the conductivity of the graphene films

could also be increased by HNO<sub>3</sub> treatment because of *p*-doping [19, 30]. The sheet resistance of AC-0.01, AC-0.02, AC-0.04, and AC-0.06 reduced from 1080 to 581  $\Omega/\text{sq}$ , from 1135 to 598  $\Omega/\text{sq}$ , from 1353 to 707  $\Omega/\text{sq}$ , and from 1415 to 744  $\Omega/\text{sq}$ , respectively. The enhanced conductivity of graphene film is good for the increase of  $J_{sc}$  and reducing the internal resistance ( $R_s$ ) of the solar cell. The increase of  $J_{sc}$  could be observed in solar cells based on AC-0.02, AC-0.04, and AC-0.06 (Table 1). Interestingly, there is a slight decrease of  $J_{sc}$  in AC-0.01 solar cell (from 15.57 to 15.23  $\text{mA}/\text{cm}^2$ ), which might result from the slight corrosion of silver paint or silver wire. Thirdly, HNO<sub>3</sub> treatment could reduce the  $R_s$  of the solar cell and improve the quality of the G/Si Schottky junction, resulting in larger FF.

Dark current density-voltage curves of the AC-0.01 solar cell before (black curve) and after (red curve) HNO<sub>3</sub> treatment are shown in Figure 3(a). The dark curves exhibit rectifying characteristics, and we can qualitatively see from

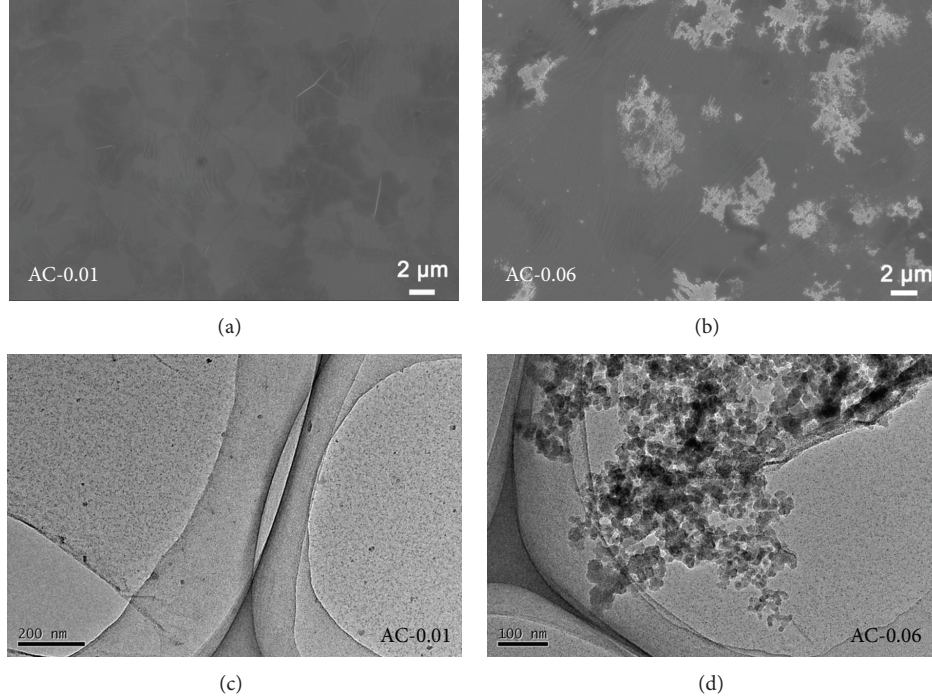


FIGURE 4: SEM and TEM images of AC-0.01 and AC-0.06. (a) SEM image of AC-0.01, (b) SEM image of AC-0.06, (c) TEM image of AC-0.01, and (d) TEM image of AC-0.06.

TABLE 1: Characteristics of G/Si solar cells based on different graphene samples before and after  $\text{HNO}_3$  treatment.

Samples	$V_{oc}$ (mV)	$J_{sc}$ (mA/cm <sup>2</sup> )	FF (%)	$\eta$ (%)
AC-0.01-original	472.4	15.57	30.78	2.26
AC-0.01- $\text{HNO}_3$	532.7	15.23	61.27	4.98
AC-0.02-original	427.2	15.00	32.83	2.10
AC-0.02- $\text{HNO}_3$	487.5	15.99	53.75	4.19
AC-0.04-original	427.2	12.07	19.69	1.02
AC-0.04- $\text{HNO}_3$	480.0	13.59	31.26	2.04
AC-0.06-original	450.0	11.79	17.78	0.94
AC-0.06- $\text{HNO}_3$	502.6	15.56	22.28	1.74

the curves that the quality of the Schottky junction is improved by  $\text{HNO}_3$  treatment. The diode ideality factor ( $n$ ) of the Schottky junction could be calculated by linear fit of  $\ln(I)$  versus voltage, where  $I$  is the dark current [31]. As shown in Figure 3(b), the  $n$  has been improved from 3.82 (without  $\text{HNO}_3$  treatment) to 2.49 (upon  $\text{HNO}_3$  treatment) for AC-0.01 solar cell, demonstrating the improvement of the Schottky junction quality [32]. The  $n$  for AC-0.02, AC-0.04, and AC-0.06 solar cells is improved by  $\text{HNO}_3$  treatment (Figure S2). In addition, a linear fit of  $dV/d(\ln I)$  versus  $I$  gives the  $R_s$  of the Schottky junction [12]. As to AC-0.01 solar cell, the  $R_s$  has dropped from  $67.6 \Omega$  in the pristine cell to  $51.1 \Omega$  in the  $\text{HNO}_3$ -treated cell, as shown in Figures 3(c) and 3(d). The  $R_s$  for the other three cells is also reduced by  $\text{HNO}_3$  treatment (Figure S3). The improvement of the Schottky junction quality and the decrease of  $R_s$  are beneficial

to the improvement of FF, which can be seen from Table 1, where the FF of all the cells was enhanced by the  $\text{HNO}_3$  treatment.

From Table 1, we also obtain the evident and important result that solar cells based on AC-0.01 and AC-0.02 demonstrate much better performance than those based on AC-0.04 and AC-0.06. Furthermore, the efficiency improvement by  $\text{HNO}_3$  treatment of AC-0.01, AC-0.02, and AC-0.04 is superior compared with that of AC-0.06. The typical SEM images of AC-0.01 and AC-0.06 are shown in Figures 4(a) and 4(b). As one can see, the surface of AC-0.01 is almost free of impurities, while there are many agglomerates located on the surface of AC-0.06. TEM image further confirms the surface of AC-0.01 is very clean (Figure 4(c)); while the agglomerates on the surface of AC-0.06 are irregularly shaped particles (Figure 4(d)). The photovoltaic performance difference of the G films might be due to the irregularly shaped agglomerates.

As can be seen from Table 1, the photovoltaic performance difference between AC-0.04, AC-0.06 and AC-0.01, AC-0.02 mainly results from their difference in  $J_{sc}$  and FF. The diode ideality factor of AC-0.02, AC-0.02- $\text{HNO}_3$ , AC-0.04, AC-0.04- $\text{HNO}_3$ , AC-0.06, and AC-0.02- $\text{HNO}_3$  is 3.87, 2.68, 4.12, 3.41, 4.57, and 3.69, respectively, as shown in Figure S3. The  $R_s$  of AC-0.02, AC-0.02- $\text{HNO}_3$ , AC-0.04, AC-0.04- $\text{HNO}_3$ , AC-0.06, and AC-0.06- $\text{HNO}_3$  is 70.6, 57.2, 82.9, 63.2, 136.6, and 79.2  $\Omega$ , respectively, as shown in Figure S2. The diode ideality factor and  $R_s$  of AC-0.04 and AC-0.06 are much poorer than these of AC-0.01 and AC-0.02, resulting in their lower FF. Our results are in agreement with previous report work that impurity on graphene surface results in poor diode behavior [33]. Graphene film also acts as a transparent

electrode in our G/Si Schottky junction solar cells. As mentioned above, higher feed rate graphene samples show lower visible light transmittance and larger sheet resistance, which are supposed to be caused by the impurities on their surface. Moreover, reduced light absorption and poor sheet resistance are harmful for the generation and transport of charge carriers; thus, the  $J_{sc}$  of AC-0.04 and AC-0.06 is lower than that of AC-0.01 and AC-0.02. It is shown that agglomerates on graphene surface show a negative effect on graphene conductivity and the  $R_s$  of G/Si solar cells, resulting in poor photovoltaic performance. Generally, optimization of the hydrocarbon precursor feed rate plays a vital role in photovoltaic application and improvement of graphene films.

#### 4. Conclusion

In summary, effect of acetonitrile feed rate on the growth and photovoltaic performance of graphene films was investigated. Graphene/Si solar cells based on graphene films produced with feed rates of 0.01, 0.02, 0.04, and 0.06 mL/min demonstrate efficiencies of 2.26%, 2.10%, 1.02%, and 0.94%, respectively. The respective efficiencies increased to 4.98%, 4.19%, 2.04%, and 1.74% upon  $HNO_3$  treatment. The efficiency improvement by  $HNO_3$  treatment is mainly due to the increase of the graphene work function and the decrease of the internal resistance. Graphene samples synthesized with high feed rate show poor photovoltaic performance, due to the coexistence of many impurities on their surface, which show a negative effect on the diode ideality factor and the internal resistance of the Schottky junctions and thus lead to low filling factors. Our results indicate that controlling feed rate of hydrocarbon precursor is an effective way for tailoring the morphologies and photovoltaic properties of graphene, which will open up opportunities for facilitating their applications in many fields, such as energy conversion/storage devices, catalyst support, sensors.

#### Conflict of Interests

The authors declare that they have no conflict of interests regarding the publication of this paper.

#### Acknowledgments

The authors are grateful to the financial supports from the National Natural Science Foundation of China (Grant no. 51372131) and 973 program of China (no. 2014CB932401).

#### References

- [1] A. K. Geim and K. S. Novoselov, "The rise of graphene," *Nature Materials*, vol. 6, no. 3, pp. 183–191, 2007.
- [2] L. Ai and J. Jiang, "Removal of methylene blue from aqueous solution with self-assembled cylindrical graphene-carbon nanotube hybrid," *Chemical Engineering Journal*, vol. 192, pp. 156–163, 2012.
- [3] Y. Wang, S. W. Tong, X. F. Xu, B. Ozyilmaz, and K. P. Loh, "Interface engineering of layer-by-layer stacked graphene anodes for high-performance organic solar cells," *Advanced Materials*, vol. 23, no. 13, pp. 1514–1518, 2011.
- [4] X. S. Li, W. W. Cai, J. H. An et al., "Large-area synthesis of high-quality and uniform graphene films on copper foils," *Science*, vol. 324, no. 5932, pp. 1312–1314, 2009.
- [5] Y.-M. Lin, C. Dimitrakopoulos, K. A. Jenkins et al., "100-GHz transistors from wafer-scale epitaxial graphene," *Science*, vol. 327, no. 5966, p. 662, 2010.
- [6] S. Ameen, M. S. Akhtar, H.-K. Seo, Y. S. Kim, and H. S. Shin, "Influence of Sn doping on ZnO nanostructures from nanoparticles to spindle shape and their photoelectrochemical properties for dye sensitized solar cells," *Chemical Engineering Journal*, vol. 187, pp. 351–356, 2012.
- [7] D. S. Hecht, L. Hu, and G. Irvin, "Emerging transparent electrodes based on thin films of carbon nanotubes, graphene, and metallic nanostructures," *Advanced Materials*, vol. 23, no. 13, pp. 1482–1513, 2011.
- [8] L. G. de Arco, Y. Zhang, C. W. Schlenker, K. Ryu, M. E. Thompson, and C. W. Zhou, "Continuous, highly flexible, and transparent graphene films by chemical vapor deposition for organic photovoltaics," *ACS Nano*, vol. 4, no. 5, pp. 2865–2873, 2010.
- [9] X. Wang, L. Zhi, and K. Mullen, "Transparent, conductive graphene electrodes for dye-sensitized solar cells," *Nano Letters*, vol. 8, no. 1, pp. 323–327, 2008.
- [10] M. Y. Yen, M. C. Hsiao, S. H. Liao et al., "Preparation of graphene/multi-walled carbon nanotube hybrid and its use as photoanodes of dye-sensitized solar cells," *Carbon*, vol. 49, no. 11, pp. 3597–3606, 2011.
- [11] R. Bajpai, S. Roy, N. Kulshrestha, J. Rafiee, N. Koratkar, and D. S. Misra, "Graphene supported nickel nanoparticle as a viable replacement for platinum in dye sensitized solar cells," *Nanoscale*, vol. 4, no. 3, pp. 926–930, 2012.
- [12] X. M. Li, H. W. Zhu, K. L. Wang et al., "Graphene-on-silicon schottky junction solar cells," *Advanced Materials*, vol. 22, no. 25, pp. 2743–2748, 2010.
- [13] Y. Ye, Y. Dai, L. Dai et al., "High-performance single CdS nanowire (nanobelt) Schottky junction solar cells with Au/graphene Schottky electrodes," *ACS Applied Materials & Interfaces*, vol. 2, no. 12, pp. 3406–3410, 2010.
- [14] Y. Ye, L. Gan, L. Dai et al., "A simple and scalable graphene patterning method and its application in CdSe nanobelt/graphene Schottky junction solar cells," *Nanoscale*, vol. 3, no. 4, pp. 1477–1481, 2011.
- [15] X. Miao, S. Tongay, M. K. Petterson et al., "High efficiency graphene solar cells by chemical doping," *Nano Letters*, vol. 12, no. 6, pp. 2745–2750, 2012.
- [16] Y. Lin, X. Li, D. Xie et al., "Graphene/semiconductor heterojunction solar cells with modulated antireflection and graphene work function," *Energy & Environmental Science*, vol. 6, no. 1, pp. 108–115, 2013.
- [17] X. Li, D. Xie, H. Park et al., "Anomalous behaviors of graphene transparent conductors in graphene-silicon heterojunction solar cells," *Advanced Energy Materials*, vol. 3, no. 8, pp. 1029–1034, 2013.
- [18] E. Shi, H. Li, L. Yang et al., "Colloidal antireflection coating improves graphene-silicon solar cells," *Nano Letters*, vol. 13, no. 4, pp. 1776–1781, 2013.
- [19] T. Feng, D. Xie, Y. Lin et al., "Efficiency enhancement of graphene/silicon-pillar-array solar cells by  $HNO_3$  and PEDOT-PSS," *Nanoscale*, vol. 4, no. 6, pp. 2130–2133, 2012.

- [20] X. Li, D. Xie, H. Park et al., "Ion doping of graphene for high-efficiency heterojunction solar cells," *Nanoscale*, vol. 5, no. 5, pp. 1945–1948, 2013.
- [21] G. Fan, L. Fan, Z. Li et al., "Hybrid effect of gas flow and light excitation in carbon/silicon Schottky solar cells," *Journal of Materials Chemistry*, vol. 22, no. 8, pp. 3330–3334, 2012.
- [22] X. Bai, J. Q. Wei, Y. Jia et al., "The influence of gas absorption on the efficiency of carbon nanotube/Si solar cells," *Applied Physics Letters*, vol. 102, no. 14, Article ID 143105, 2013.
- [23] K. Ihm, J. T. Lim, K. J. Lee et al., "Number of graphene layers as a modulator of the open-circuit voltage of graphene-based solar cell," *Applied Physics Letters*, vol. 97, no. 3, Article ID 032113, 2010.
- [24] T. Cui, R. Lv, Z.-H. Huang et al., "Effect of feed rate on the production of nitrogen-doped graphene from liquid acetonitrile," *Carbon*, vol. 50, no. 10, pp. 3659–3665, 2012.
- [25] M. Regmi, M. F. Chisholm, and G. Eres, "The effect of growth parameters on the intrinsic properties of large-area single layer graphene grown by chemical vapor deposition on Cu," *Carbon*, vol. 50, no. 1, pp. 134–141, 2012.
- [26] W. Liu, H. Li, C. Xu, Y. Khatami, and K. Banerjee, "Synthesis of high-quality monolayer and bilayer graphene on copper using chemical vapor deposition," *Carbon*, vol. 49, no. 13, pp. 4122–4130, 2011.
- [27] T. Cui, R. Lv, Z.-H. Huang et al., "Synthesis of nitrogen-doped carbon thin films and their applications in solar cells," *Carbon*, vol. 49, no. 15, pp. 5022–5028, 2011.
- [28] Z. Li, H. Zhu, D. Xie et al., "Flame synthesis of few-layered graphene/graphite films," *Chemical Communications*, vol. 47, no. 12, pp. 3520–3522, 2011.
- [29] T. Cui, R. Lv, Z.-H. Huang et al., "Low-temperature synthesis of multilayer graphene/amorphous carbon hybrid films and their potential application in solar cells," *Nanoscale Research Letters*, vol. 7, no. 1, article 453, 2012.
- [30] S. Bae, H. Kim, Y. Lee et al., "Roll-to-roll production of 30-inch graphene films for transparent electrodes," *Nature Nanotechnology*, vol. 5, no. 8, pp. 574–578, 2010.
- [31] Y. Jia, A. Y. Cao, X. Bai et al., "Achieving high efficiency silicon-carbon nanotube heterojunction solar cells by acid doping," *Nano Letters*, vol. 11, no. 5, pp. 1901–1905, 2011.
- [32] M. Bashahu and P. Nkundabakura, "Review and tests of methods for the determination of the solar cell junction ideality factors," *Solar Energy*, vol. 81, no. 7, pp. 856–863, 2007.
- [33] H. Park, P. R. Brown, V. Buloyic, and J. Kong, "Graphene as transparent conducting electrodes in organic photovoltaics: studies in graphene morphology, hole transporting layers, and counter electrodes," *Nano Letters*, vol. 12, no. 1, pp. 133–140, 2012.

## Research Article

# Silicon-Encapsulated Hollow Carbon Nanofiber Networks as Binder-Free Anodes for Lithium Ion Battery

Ding Nan,<sup>1,2</sup> Zheng-Hong Huang,<sup>1</sup> Ruitao Lv,<sup>1</sup> Yuxiao Lin,<sup>1</sup> Lu Yang,<sup>1</sup> Xiaoliang Yu,<sup>1</sup> Ling Ye,<sup>1</sup> Wanci Shen,<sup>1</sup> Hongyu Sun,<sup>1</sup> and Feiyu Kang<sup>1,3</sup>

<sup>1</sup> Key Laboratory of Advanced Materials (MOE), School of Materials Science and Engineering, Tsinghua University, Beijing 100084, China

<sup>2</sup> School of Materials Science and Engineering, Inner Mongolia University of Technology, Hohhot 010051, China

<sup>3</sup> City Key Laboratory of Thermal Management Engineering and Materials, Graduate School at Shenzhen, Tsinghua University, Shenzhen 518055, China

Correspondence should be addressed to Feiyu Kang; [fykang@mail.tsinghua.edu.cn](mailto:fykang@mail.tsinghua.edu.cn)

Received 28 February 2014; Accepted 12 April 2014; Published 3 June 2014

Academic Editor: Jinlong Jiang

Copyright © 2014 Ding Nan et al. This is an open access article distributed under the Creative Commons Attribution License, which permits unrestricted use, distribution, and reproduction in any medium, provided the original work is properly cited.

Silicon-encapsulated hollow carbon nanofiber networks with ample space around the Si nanoparticles (hollow Si/C composites) were successfully synthesized by dip-coating phenolic resin onto the surface of electrospun Si/PVA nanofibers along with the subsequent solidification and carbonization. More importantly, the structure and Si content of hollow Si/C composite nanofibers can be effectively tuned by merely varying the concentration of dip solution. As-synthesized hollow Si/C composites show excellent electrochemical performance when they are used as binder-free anodes for Li-ion batteries (LIBs). In particular, when the concentration of resol/ethanol solution is 3.0%, the product exhibits a large capacity of 841 mAh g<sup>-1</sup> in the first cycle, prominent cycling stability, and good rate capability. The discharge capacity retention of it was ~90%, with 745 mAh g<sup>-1</sup> after 50 cycles. The results demonstrate that the hollow Si/C composites are very promising as alternative anode candidates for high-performance LIBs.

## 1. Introduction

To meet the increasing demands of rapidly developing market from cell phone to electric vehicles for the Li-ion batteries (LIBs), new anode materials with higher capacity have attracted significant attention. Graphite, the most commonly used commercial anode material, has low theoretical specific capacity (372 mAh g<sup>-1</sup>) and poor rate capability. Silicon is considered as one of the most attractive and promising alternative anode materials to replace graphite in LIBs in the coming decades in virtue of its fascinating performance, such as relatively low working potential (~370 mV versus Li/Li<sup>+</sup>), rich abundance in earth, environmental benignity, and especially the highest theoretical capacity of 4212 mAh g<sup>-1</sup> among the existing anode materials [1]. However, there still exist several challenges which restrict the commercialization of such silicon anodes. Firstly, the large volumetric expansion (~400%) of silicon anodes upon the lithiation results in

high internal stress, causes mechanical fracture and pulverization of electrode and subsequent losses of electrical contact between the active material and current collector, and leads to poor reversibility and rapid fading of capacity. Secondly, the huge and repeated volume change during the charge/discharge process prevents the formation of a layer of stable solid electrolyte interface (SEI). Hence it can easily continuously grow through the cracks till being too thick for Li-ions to diffuse through, and in turn results in a low Coulombic efficiency and a decrease in capacity. Moreover, silicon anodes possess poor electrical conductivity [2, 3]. Such drawbacks lead to serious capacity fade during cycles and thus hinder the practical applications of silicon anodes.

In order to address abovementioned challenges, it would be crucial to release the mechanical strains, as well as reducing the diffusion length of Li-ions in Si electrode materials during charge/discharge process. Nanostructured Si would be a good solution. So far, many nanostructured silicon

and Si-based composites with various morphologies, such as nanoparticles [4–10], porous nanoparticles [11, 12], nanofilm [13–18], nanotubes [19–21], nanofibers [2, 22–37], and core-shell structures [3, 38–42] have been prepared and evaluated. Among them, one-dimensional (1D) nanostructured Si or Si-containing nanotubes, nanofibers, and core-shell structures showed very good electrochemical performance in virtue of the enhanced electric conductivity of the 1D nanostructures. Furthermore, they could easily form three-dimensional (3D) interconnected networks to buffer the huge volume changes of active Si, thereby preventing the degradation of the electrode integrity and the breakdown of electric conductive networks. However, such 1D silicon nanostructures were usually synthesized by using toxic  $\text{SiH}_4$  as silicon precursor and costly Au particles as catalysts [22, 24, 39, 40]. Moreover, the synthesis of them seemed to be too elaborate and suffered from low yield. Thus, the most straightforward and practical approach recently to overcome these shortcomings is to directly utilize the commercially available Si nanoparticles incorporated into carbon matrix, for example, carbon nanofibers via electrospinning method [26–29, 31–34]. Such products are typical interconnected nonwoven nanofiber networks with good mechanical integrity. The as-prepared free-standing fabrics can be directly used as anodes for LIBs without adding any other polymeric binders or conductive additives. They could increase the effective electrode-electrolyte interface area, facilitate the high-speed electron transport, and hold great potential to enhance the electrochemical performance. Nevertheless, in fact, their cycle stability is still inferior because the direct contact of carbon with silicon has the limited buffer capability, which is difficult to cope with about 400% of volume expansion.

More recently, to improve the cycling stability of silicon anode materials, some new nanostructures with Si nanoparticles encapsulated in continuous hollow carbon tubes have gained much attention due to the enhanced electrical conductivity and stable solid electrolyte interface (SEI). Moreover, particularly, the ample empty space inside the hollow tubes among the silicon nanoparticles allowed for silicon nanoparticles expansion freely during electrochemical cycling, supporting a stable cycling of the entire electrode as well as high charge and discharge rates [2, 3, 35–37, 42]. In addition, it is known that the low-cost phenolic resin (i.e., resol) has high carbon yield (over 50%) during carbonization and good anodic performance for LIBs by exhibiting a high reversible capacity of  $550 \text{ mAh g}^{-1}$  [43]. More importantly, the resol could be solidified by occurrence of polycondensation reaction thus keeping the original morphology by means of solidification process. It is very favorable to generate the tubular nanostructure.

With a motivation to further increase the cycling stability of the silicon anode materials, in this work, we put forward a facile strategy to synthesize novel silicon-encapsulated hollow carbon nanofiber networks with ample space around the Si nanoparticles (hollow Si/C composites) by dip-coating resol on the surface of electrospinning Si/PVA nanofibers along with the subsequent solidification and carbonization. These freestanding membranous hollow Si/C composites can

be used directly as anodes for LIBs without adding any carbon conductors or polymer binders. The as-prepared hollow Si/C composites display a high electrochemical performance with excellent cycle stability of  $\sim 90\%$  of discharge capacity retention after 50 cycles.

## 2. Experimental

**2.1. Materials Synthesis.** Firstly, polyvinyl alcohol (PVA, molecule weight = 80000) and deionized water were mixed in the ratio of 15 g PVA/135 g water. The mixture was stirred in water bath at  $90^\circ\text{C}$  for 2 h to form a homogenous solution. Meanwhile, silicon nanoparticles (n-Si, 0.04 mol, average particle size of 80 nm) were dispersed in deionized water (10 mL) with sodium linear alkylbenzenesulfonate by ultrasonication and magnetically stirred for 2 h. Then, the suspension and the former solution were mixed and agitated for 12 h to be used for the precursor of electrospinning for Si/PVA nanofibers.

A needle, with the inner diameter of 1 mm, was connected to a high voltage DC power and vertically clamped on an insulating glass stick. A piece of graphite paper was used as the collector. The height of the needle and the distance between the needle and the collector were adjustable. Typically, 20 kV of high positive voltage was adopted and the distance between the needle and collector was 15 cm. The precursor solution was electrospun into fiber networks at a constant flow rate of  $1.0 \text{ mL h}^{-1}$ . Then the Si/PVA nanofibers fabric was dipped into resol (thermosetting phenolic resin, molecule weight = 2080)/ethanol solution for 5 seconds to obtain the Si/PVA-Resol composites (abbreviated as Si/PVA-Resol- $n$  in text,  $n$  represents concentration of resol/ethanol solution (%)). Afterwards, the as-prepared Si/PVA-Resol composites were treated in air by a typical solidification process and then carbonized in Ar at  $600^\circ\text{C}$  for 1 h with a heating rate of  $5^\circ\text{C min}^{-1}$  to finally acquire the silicon-encapsulated hollow carbon nanofiber networks (i.e., hollow Si/C composites, denoted as H-Si/C- $n$ , where  $n$  represents the concentration of resol/ethanol solution (%)). The solidification process was performed according to a stepwise heating curing process, that is, the reaction time shortened with increasing temperature, while the low temperature reaction held for a long time. The total cure duration was about 25 h when heating the samples in air from room temperature up to  $180^\circ\text{C}$ .

**2.2. Materials Characterization and Electrochemical Evaluation.** The morphology and microstructure of samples were characterized using a scanning electron microscope (SEM, LEO 1530, Germany) and a transmission electron microscopy (TEM, JEOL 2010, Japan). Raman spectroscopy (Renishaw Invia RM200, England) was employed to study the structure of Si/PVA nanofibers. X-ray powder diffraction (XRD, Rigaku D/Max 2500PC, Japan) was used to characterize the crystal structures of the Si/PVA nanofibers and hollow Si/C composites. Thermogravimetric analysis (TGA) was performed to ascertain the carbon yield and Si content of samples on a TA instrument SDT-Q600 with temperature increments of

10°C min<sup>-1</sup> in Ar and air atmosphere. The specific surface area of samples was evaluated by N<sub>2</sub> adsorption measurement on a Belsorp Max apparatus (Japan) and determined by Brunauer-Emmett-Teller (BET) method.

The electrochemical performance was characterized by galvanostatic cycling and cyclic voltammetry at room temperature in a half cell, in which lithium foil was used as the counter electrode and 1 M LiPF<sub>6</sub> was dissolved in a mixture of ethyl carbonate (EC) and dimethyl carbonate (DMC) (1:1, v/v) as the electrolyte. The samples were used as working electrode directly without adding any nonactive materials such as polymer binders or electronic conductors. Celgard 2400 was used as separator. The test cells were galvanostatically cycled between 0.01 V and 1.5 V versus Li<sup>+</sup>/Li to evaluate the electrochemical performance (LAND battery tester, Wuhan Jinnuo Electronics Co., Ltd.). Cyclic voltammetry was measured between 0.01 V and 1.50 V versus Li<sup>+</sup>/Li at a scan rate of 0.1 mV s<sup>-1</sup> by an electrochemical workstation Im6ex (ZAHNER, Germany).

### 3. Results and Discussion

**3.1. Materials Characterization.** The strategy to design and fabricate the silicon-encapsulated hollow carbon nanofiber networks is schematically illustrated in Figure 1(a). Three simple yet critical steps are adopted in the present strategy. Firstly, the Si/PVA nanofibers to form Si-containing hollow tubular cavity were prepared using electrospinning and the morphology of them is present in Figure 1(b). It can be seen that Si/PVA nanofibers exhibit interconnected nonwoven nanofibrous structure. They have smooth, clean surfaces with diameters varying from tens to hundreds of nanometers and length of hundreds of microns. Such a high aspect ratio may provide considerable specific surface area for high mass uptake of resol deposits. Secondly, the Si/PVA-Resol composites were prepared by dip-coating a layer of resol onto the surface of Si/PVA nanofibers. To modulate the mass loading of resol deposits on the Si/PVA nanofibers surface, different concentrations of resol/ethanol solutions were undertaken to dip. As expected, it is clearly seen from Figure 1(c), by increasing the concentration of resol/ethanol solution, that the color of Si/PVA-Resol composites gets darker after solidification, indicating the increase of loading amount of resol. In addition, it is worthwhile to point out that, just after 5 seconds of dip-coating, there are large amounts of resol coated on the surface of Si/PVA nanofibers (inset of Figure 1(c)). The rapid and uniform formation of resol deposits on the Si/PVA nanofibers can be attributed to the high specific surface area (156 m<sup>2</sup> g<sup>-1</sup>) and turbostratic structure of Si/PVA nanofibers, which can provide more active sites for deposition. Raman spectrum shown in Figure 1(e) confirms the characteristic of amorphous structure of Si/PVA nanofibers, which show a relatively high intensity ratio of disorder induced band (D-peak) and graphite band (G-peak) ( $I_D/I_G = 1.77$ ). Finally, hollow Si/C composites were obtained by solidification and carbonization of Si/PVA-Resol composites. After the elaborate control of solidification and carbonization processes, original PVA located in core of

Si/PVA-Resol composites could be removed by decomposition, and solid resol shell will turn to tubular carbon and form triaxial interconnected hollow carbon nanofiber networks. This unique architecture can encapsulate Si nanoparticles into triaxial interconnected hollow carbon tubes and provide ample empty space around Si nanoparticles. Hence it can not only enhance electrical conductivity and stabilize solid electrolyte interface (SEI) but also allow for silicon expansion freely during electrochemical cycling, supporting a stable cycling of the entire electrode as well as high charge and discharge rates. The macrograph of the H-Si/C-3 was shown in Figure 1(c). Apparently, H-Si/C-3 has reserved the free-standing membrane macrostructure. As for microstructure of H-Si/C-3 (Figures 1(d) and 2(b)), it can be seen that H-Si/C-3 exhibits triaxial interconnected fiber networks morphology, with diameters ranging from tens to hundreds of nanometers. The Si nanoparticles with diameters around 50~100 nm were encapsulated in hollow carbon fibers and the wall thickness of hollow fibers is around 10~20 nm. Moreover, to ascertain the silicon in the hollow Si/C composites, X-ray diffractions (XRD) were performed. As shown in Figure 1(f), the broad peaks of all samples with  $2\theta$  around 23° demonstrate the existence of disordered amorphous carbon. Five obvious diffraction peaks with 28.4°, 47.3°, 56.1°, 69.1°, and 76.4° can be assigned to the pure crystalline silicon element, which represent (111), (220), (311), (400), and (311) planes of Si crystallites (JCPDS no. 27-1402), respectively. Furthermore, interestingly, for hollow Si/C composites, characteristic peaks at 26.5° appear which can be indexed to the (002) plane of graphite, and the intensity of diffraction peaks of it increases at higher concentration of dip solution, which exhibits the increase of carbon content in hollow Si/C composites [10].

Figures 2(a)–2(d) show the magnified SEM images of hollow Si/C composites. Triaxial interconnected nanofiber networks were obtained for all hollow Si/C composites. The concentration increase of dip solution definitely affected the morphology of the resultant nanofiber networks. In the case of H-Si/C-1, the tubular structure was broken and collapsed seriously on account of the lack of resol coating. With the increase of the dip solution concentration from 3% to 10% for H-Si/C-3, H-Si/C-5, and H-Si/C-10, it can be seen that the integrated nanofiber networks and the wall thickness of them become thicker. This phenomenon is also confirmed by TEM observation. In Figure 2(e), it is found that H-Si/C-1 was a solid Si/C nanofiber, and there was no residual space around the silicon nanoparticles. For H-Si/C-3, H-Si/C-5, and H-Si/C-10 (Figures 2(f)–2(h)), they have typical tubular morphology and wall thickness arises apparently from around 20 nm for H-Si/C-3 to around 100 nm for H-Si/C-10. Furthermore, it can be seen from inset of Figures 2(g) and 2(h) that well-stacked sheets along the in-plane direction as well as the random orientations in the wall are observed indicating a graphitic shell for H-Si/C-5 and H-Si/C-10. This is in good agreement with the XRD analysis.

The carbon yield and silicon content of the hollow Si/C composites were characterized by TGA. As shown in Figure 3(a), the final residual weight of the hollow Si/C composites at 600°C in Ar atmosphere increases with the increase of the concentration of dip solution. Figure 3(b)

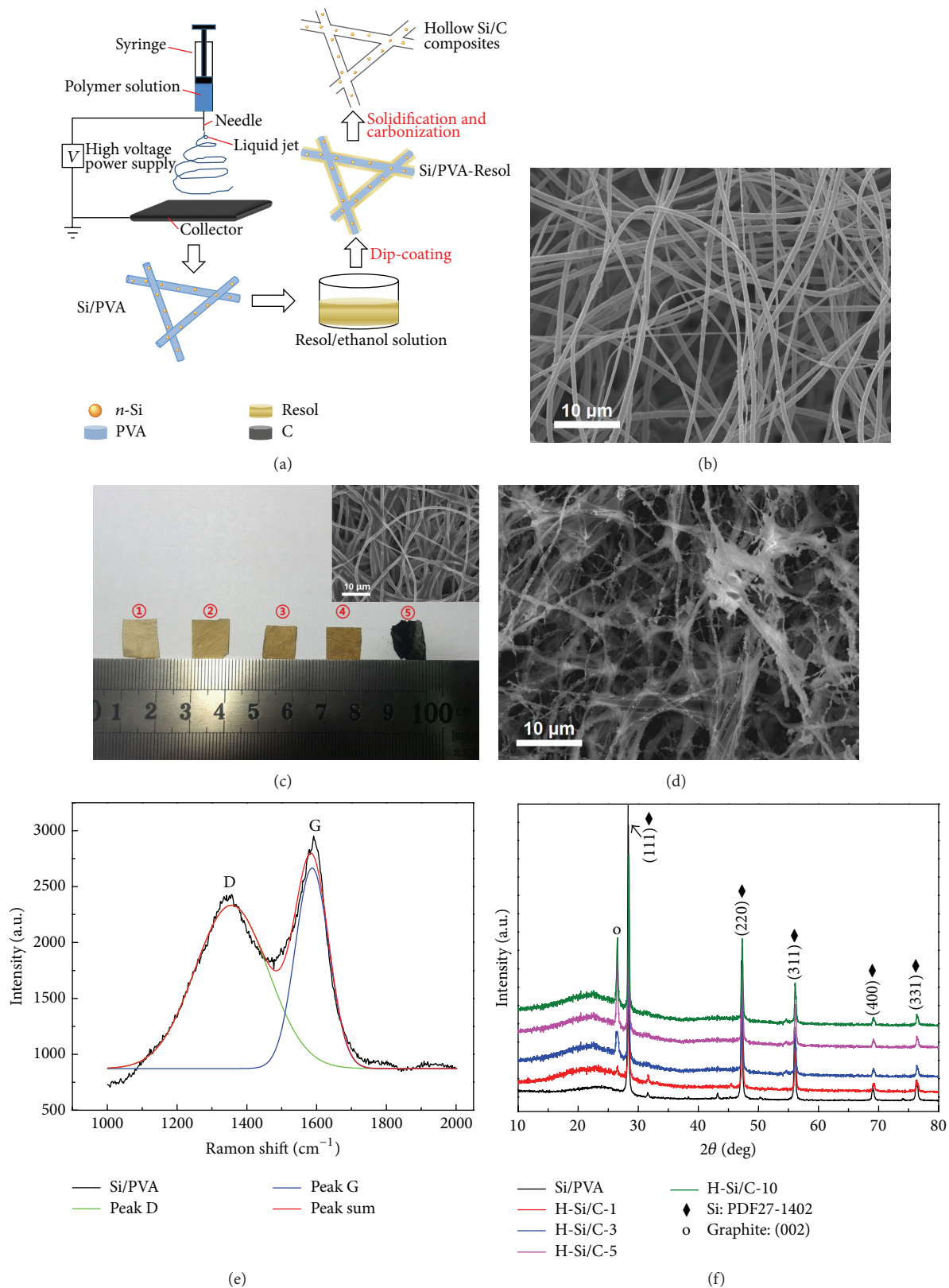


FIGURE 1: (a) Schematic illustration of the formation of the hollow Si/C nanofiber networks; (b) SEM image of Si/PVA nanofibers; (c) a macrograph of the Si/PVA-Resol composites after solidification and hollow Si/C composites (inset is SEM image of Si/PVA-Resol-3). ① is Si/PVA-Resol-1, ② is Si/PVA-Resol-3, ③ is Si/PVA-Resol-5, ④ is Si/PVA-Resol-10, and ⑤ is H-Si/C-3; (d) SEM image of H-Si/C-3; (e) Raman spectrum of the Si/PVA nanofibers; (f) XRD patterns of Si/PVA nanofibers and hollow Si/C composites.

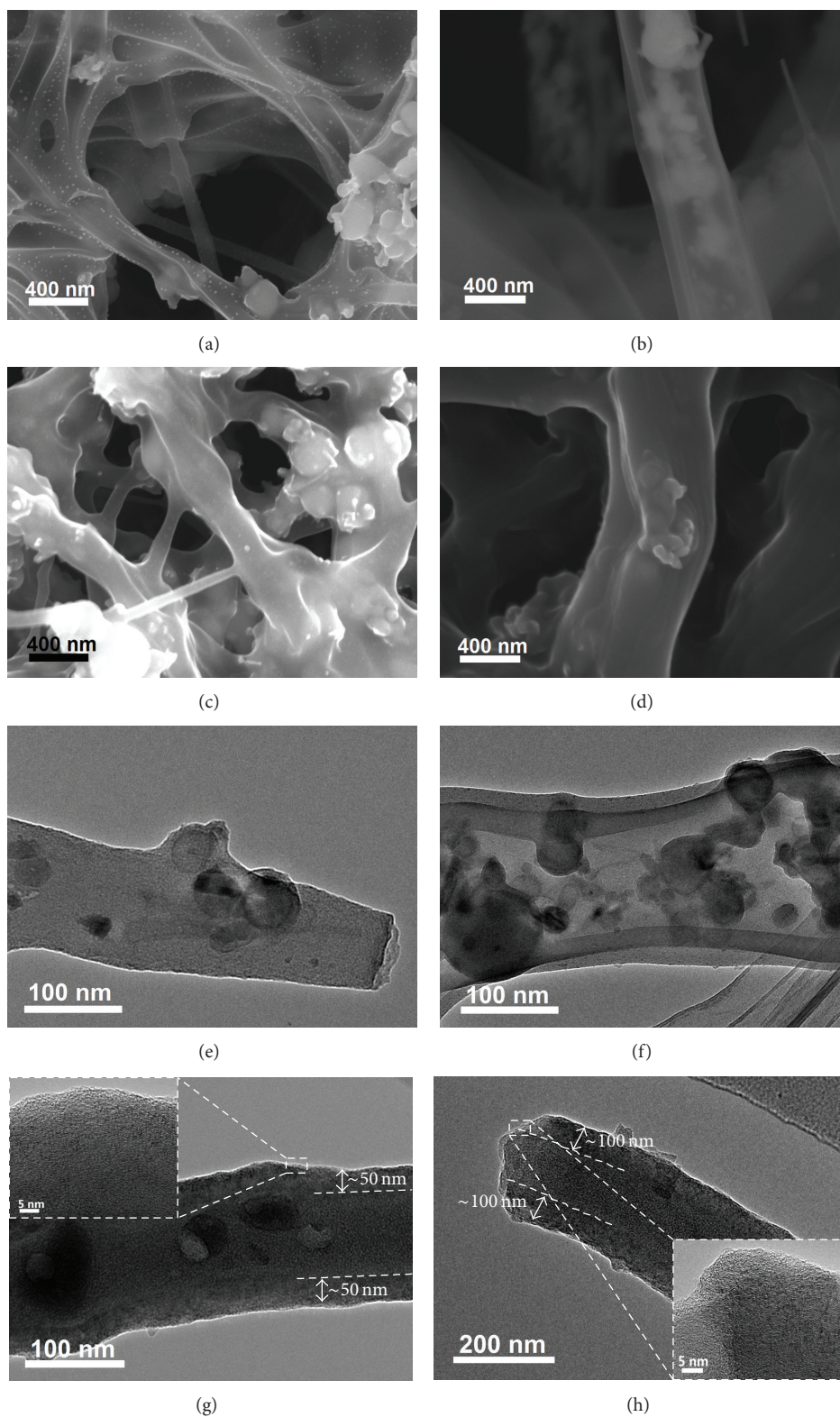


FIGURE 2: Magnified SEM images of hollow Si/C composites, (a) H-Si/C-1, (b) H-Si/C-3, (c) H-Si/C-5, and (d) H-Si/C-10. TEM images of hollow Si/C composites, (e) H-Si/C-1, (f) H-Si/C-3, (g) H-Si/C-5, and (h) H-Si/C-10 (insets in (g) and (h) are HRTEM images of H-Si/C-5 and H-Si/C-10, resp.).

TABLE 1: The physical and electrochemical properties of different hollow Si/C composite nanostructures.

Sample	Si content (%)	SSA <sup>a</sup> (m <sup>2</sup> g <sup>-1</sup> )	Theoretical capacity (mAh g <sup>-1</sup> )	1st cycle reversible capacity (mAh g <sup>-1</sup> )	1st cycle CE <sup>b</sup> (%)	50th cycle reversible capacity (mAh g <sup>-1</sup> )
H-Si/C-1	17.3	177.3	1181	913	48	567
H-Si/C-3	13.0	273.7	1025	841	58	745
H-Si/C-5	9.3	332.8	889	626	50	652
H-Si/C-10	8.0	274.8	842	579	54	493

<sup>a</sup>Specific surface area (SSA) was calculated by the Brunauer-Emmett-Teller (BET) method.

<sup>b</sup>The columbic efficiency (CE).

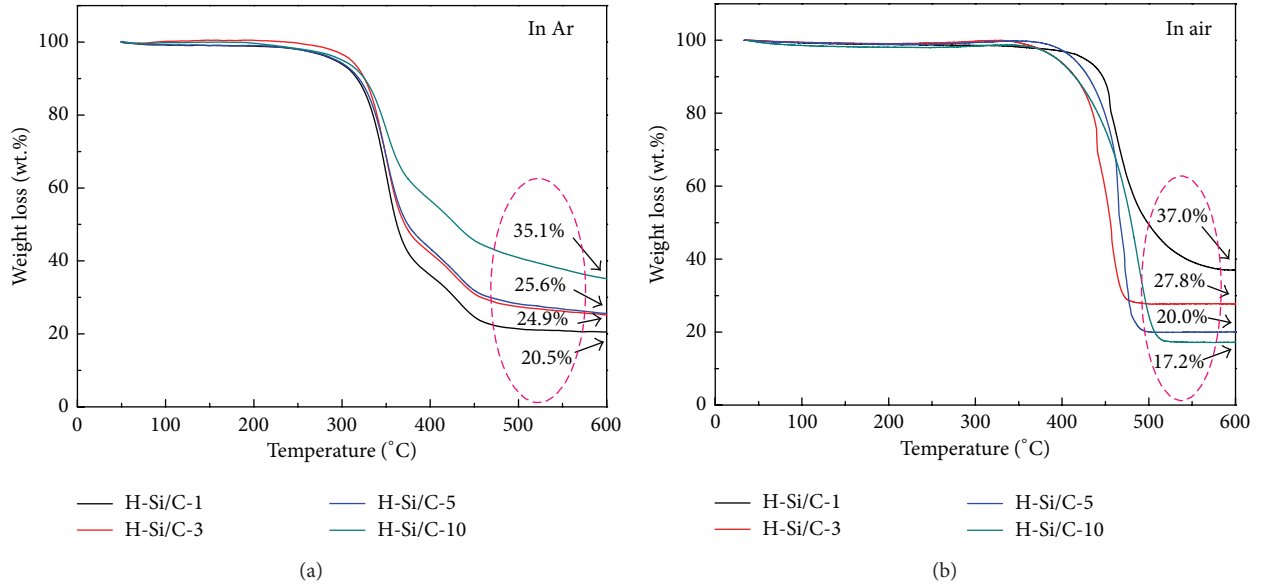


FIGURE 3: Thermogravimetric analysis (TGA) profiles of different hollow Si/C composites in (a) Ar and (b) air atmosphere.

presents the TGA results of the hollow Si/C composite from 25°C to 600°C under air atmosphere. In air atmosphere, above 400°C, the silicon can be oxidized to silica, while the carbon would be evolved to CO<sub>2</sub>. Thus the content of silicon can be calculated from the content of highly thermal stable SiO<sub>2</sub> [3, 26, 37]. The final results of silicon content were summarized in Table 1. Obviously, for increase of the relatively content of carbon, the content of silicon was decreased by increasing of the concentration of dip solution. These results suggested that we can effectively regulate the relatively content of carbon and silicon by changing the concentration of dip solution.

**3.2. Electrochemical Evaluations.** The electrochemical behaviors of hollow Si/C composites were evaluated using deep galvanostatic charge/discharge cycles and cyclic voltammetry (CV) from 0.01 to 1.50 V. The collected free-standing silicon-encapsulated hollow carbon nanofiber networks were directly used as anodes in LIBs, without using copper current collector and adding any other polymeric binders or conductive additives. It could remarkably facilitate the high-speed electron transport, hold great potential to enhance the electrochemical performance, simplify the preparation process of electrode, and reduce the cost. The cycling performance of

hollow Si/C composites at a charge/discharge current density of 100 mA g<sup>-1</sup> is illustrated in Figure 4(a). It is clear that H-Si/C-3 shows the largest capacity and good cycling stability superior to the H-Si/C-1, H-Si/C-5, and H-Si/C-10. And the first cycle reversible capacity was 841 mAh g<sup>-1</sup> based on all the Si and carbon mass, which is more than twice that of traditional graphitic anodes (372 mAh g<sup>-1</sup>). Furthermore, H-Si/C-3 showed an excellent cycling stability and discharge capacity retention of about 89% after 50 cycles, with 745 mAh g<sup>-1</sup> in the 50th cycle. In addition, as deduced from Figure 4(a), with the increase of concentration of dip solution, the hollow Si/C composites exhibit decreased first cycle reversible capacity. This can be attributed to the decrease of weight percentage of Si with the increase of concentration of dip solution. Based on the capacity from pure Si and carbon, the theoretical capacity ( $C_t$ ) of hollow Si/C composites was calculated according to the following equation and the results were summarized in Table 1:

$$C_t = C_{Si}W_{Si} + C_CW_C, \quad (1)$$

where  $C_{Si}$  and  $C_C$  denote the theoretical capacity of Si (4200 mAh g<sup>-1</sup>) and resol-derived carbon (550 mAh g<sup>-1</sup>) [43], respectively.  $W_{Si}$  and  $W_C$  are the weight percentages of Si

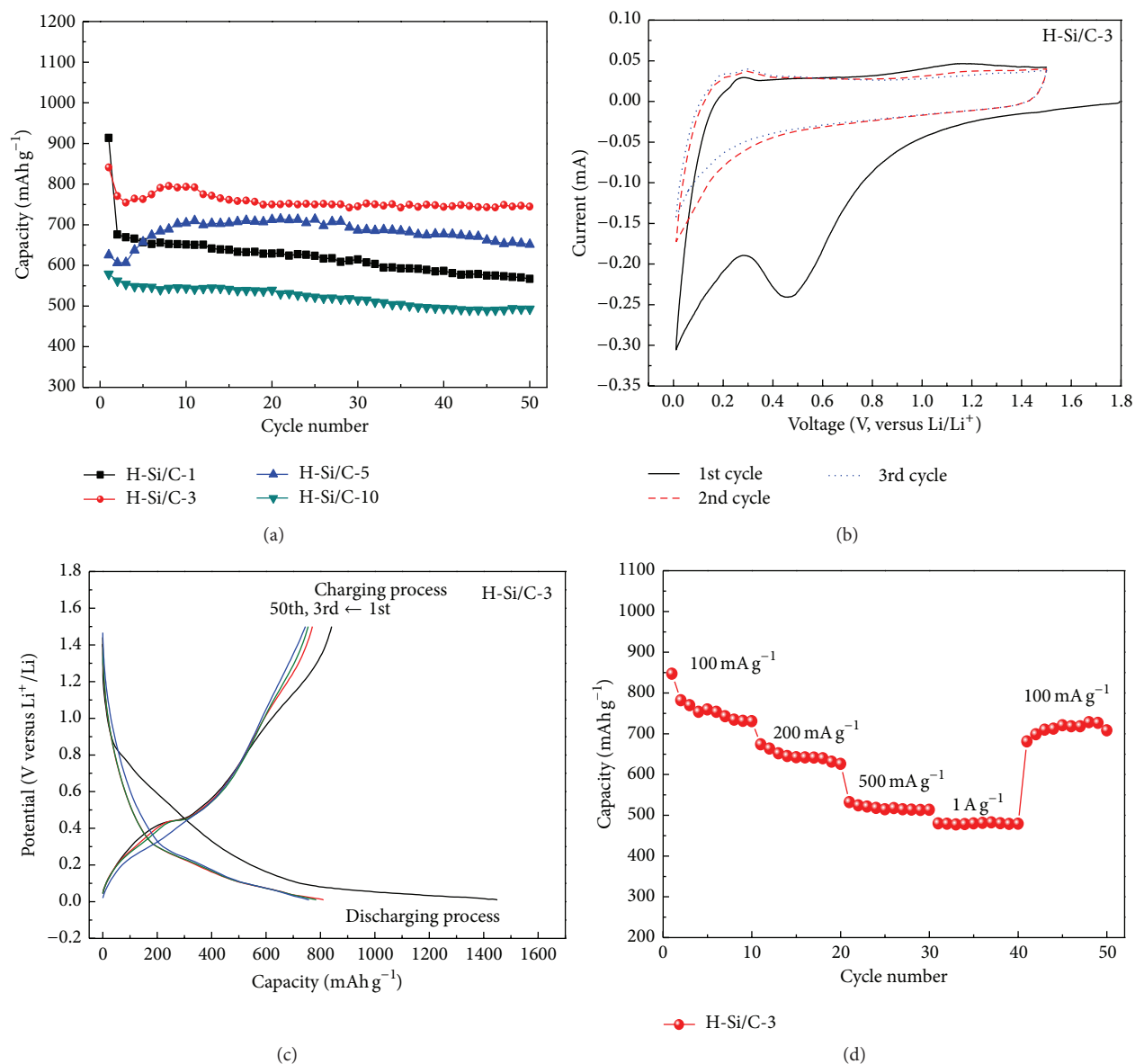


FIGURE 4: (a) Cycling performance of hollow Si/C composites; (b) cyclic voltammograms, (c) charge/discharge curves, and (d) rate performance of H-Si/C-3.

and carbon, respectively. The first cycle reversible capacity of H-Si/C-1, H-Si/C-3, H-Si/C-5, and H-Si/C-10 was about 77%, 82%, 70%, and 69% of their theoretical capacity, respectively.

These results indicate that hollow Si/C composites, especially H-Si/C-3, arouse the electrochemical potential of Si efficiently as well as improving the structural stability of the Si-containing anode materials. H-Si/C-1 shows the highest theoretical capacity and initial reversible capacity but a worse cycling performance than H-Si/C-3, H-Si/C-5, and H-Si/C-10. The 50th cycle discharge capacity of H-Si/C-1 was 567 mAh g<sup>-1</sup>, yielding capacity retention only about 62%. It is because the tubular nanostructure of H-Si/C-1 was crumpled up due to lack of resol, becoming solid Si/C nanofibers, thus no residual space around the silicon nanoparticles for

expansion during charge-discharge process. In a word, the concentration of dip solution has an optimum value for hollow Si/C composites. If the concentration of dip solution is too high, it will cause the decrease of Si weight percentage and the increase of the carbon wall thickness accordingly. On the contrary, the decrease of the dip solution concentration will lead to the collapse of the tubular nanostructure due to the lack of enough resol. Therefore, we can effectively coordinate the structure and Si content of hollow Si/C composites by merely varying the concentration of dip solution to obtain good electrochemical performance.

Figure 4(b) shows the CVs for the 1st, 2nd, and 3rd cycles of H-Si/C-3 electrode in lithium ion half cells, in which a lithium foil was used as the counter and reference

electrode. In the first cycle, a broad peak ranging from 0.3 to 0.8 V in the reduction process, which disappears at the second and third cycle, corresponds to SEI formation on the electrode surface due to electrolyte decomposition. The distinct peak around 0.1 V demonstrates the alloying process of Si nanoparticles with lithium ions. In the oxidation process, a broad oxidation peak which corresponds to the lithium extraction from H-Si/C-3 is located at 0.2–0.4 V and becomes more distinct after the first cycle [10]. Figure 4(c) shows the typical galvanostatic charge/discharge curves of H-Si/C-3 anode for the initial three cycles and 50th cycle at a current density of 100 mA g<sup>-1</sup>. The voltage has a sharp drop to a relatively potential plateau at 0.3–0.8 V in the first cycle, which is associated with the formation of solid electrolyte interphase (SEI) film on the electrode due to the decomposition of electrolyte [26, 36, 37]. The initial discharge capacity of H-Si/C-3 is as high as 1450 mAh g<sup>-1</sup> and yields 609 mAh g<sup>-1</sup> of irreversible charge capacity. The coulombic efficiency of it is 58%. The large initial irreversible capacity can be mainly ascribed to the formation of SEI layer at the surface of H-Si/C-3 and/or the irreversible side reactions with the electrolyte [36]. Nevertheless, the coulombic efficiency in the second cycle and thereafter increases over 95% and a stable capacity is achieved. The rate capability of H-Si/C-3 was further investigated. As depicted in Figure 4(d), H-Si/C-3 anode delivers a capacity of 847 mAh g<sup>-1</sup> at 100 mA g<sup>-1</sup>, 674 mAh g<sup>-1</sup> at 200 mA g<sup>-1</sup>, 532 mAh g<sup>-1</sup> at 500 mA g<sup>-1</sup>, and 480 mAh g<sup>-1</sup> at 1000 mA g<sup>-1</sup>. The capacity can be recovered to 681 mAh g<sup>-1</sup> when the current density is turned back to 100 mA g<sup>-1</sup>, indicating good cycling stability and rate capability.

The outstanding electrochemical properties of silicon-encapsulated hollow carbon nanofiber networks can be attributed to its unique 3D interconnected tubular hollow nanostructure encapsulated silicon nanoparticles with ambient empty space. Firstly, the hollow Si/C composites electrode contained plenty of void spaces around Si nanoparticle, which can effectively prevent damage of whole electrode by allowing Si nanoparticle to expand freely without mechanical constraint during lithiation process, enabling a stable electrochemical cycle performance and excellent rate performance. Secondly, the triaxial interconnected conducting nanofibrous networks constituted by carbon tubes and lack of insulating binders can remarkably enhance the conductivity of electrode, which will ensure a fast electron transfer for rapid Faradic reaction, and shorten the ionic transport length as well. Lastly, the encapsulation with hollow carbon nanofibers defends silicon nanoparticles against direct contact with the electrolyte; thus stable SEI can be obtained during cycling.

#### 4. Conclusions

Silicon-encapsulated hollow carbon nanofiber networks with plenty of space around the Si nanoparticles were successfully prepared by dip-coating resol on the surface of electrospinning Si/PVA nanofibers and the subsequent solidification and carbonization processes. By simply varying the concentration

of dip solution, we can effectively tune the structure and Si content of hollow Si/C composites and acquire prominent electrochemical performance. As binder-free anodes for LIBs, H-Si/C-3 shows a high capacity of 841 mAh g<sup>-1</sup> in the first cycle, prominent rate capability, and excellent cycling stability. The discharge capacity retention of H-Si/C-3 was ~90%, with 745 mAh g<sup>-1</sup> after 50 cycles. It demonstrates that the hollow Si/C composites are very promising as alternative anode candidates for high-performance LIBs. Furthermore, this study also provides a new insight that the triaxial interconnected tubular hollow nanostructure is a good solution for other LIBs electrodes that suffer from volume expansion or unstable interfacial properties with electrolytes, such as Sn and metal oxides anodes.

#### Conflict of Interests

The authors declare that there is no conflict of interests regarding the publication of this paper.

#### Acknowledgments

The authors thank the financial supports from the National Natural Science Foundation of China (no. 51232005) and 973 program of China (no. 2014CB932401). This work is also supported by Ministry of Science and Technology (MOST) of China under Grant 2010DFA72760, Collaboration on cutting-edge technology development of electric vehicle.

#### References

- [1] J. R. Szczech and S. Jin, "Nanostructured silicon for high capacity lithium battery anodes," *Energy and Environmental Science*, vol. 4, no. 1, pp. 56–72, 2011.
- [2] H. Wu, G. Zheng, N. Liu, T. J. Carney, Y. Yang, and Y. Cui, "Engineering empty space between Si nanoparticles for lithium-ion battery anodes," *Nano Letters*, vol. 12, no. 2, pp. 904–909, 2012.
- [3] T. H. Hwang, Y. M. Lee, B.-S. Kong, J.-S. Seo, and J. W. Choi, "Electrospun core-shell fibers for robust silicon nanoparticle-based lithium ion battery anodes," *Nano Letters*, vol. 12, no. 2, pp. 802–807, 2012.
- [4] H. Li, X. Huang, L. Chen, Z. Wu, and Y. Liang, "High capacity nano-Si composite anode material for lithium rechargeable batteries," *Electrochemical and Solid-State Letters*, vol. 2, no. 11, pp. 547–549, 1999.
- [5] N. Dimov, S. Kugino, and M. Yoshio, "Carbon-coated silicon as anode material for lithium ion batteries: advantages and limitations," *Electrochimica Acta*, vol. 48, no. 11, pp. 1579–1587, 2003.
- [6] G. X. Wang, J. H. Ahn, J. Yao, S. Bewlay, and H. K. Liu, "Nanostructured Si-C composite anodes for lithium-ion batteries," *Electrochemistry Communications*, vol. 6, no. 7, pp. 689–692, 2004.
- [7] S.-H. Ng, J. Wang, D. Wexler, K. Konstantinov, Z.-P. Guo, and H.-K. Liu, "Highly reversible lithium storage in spherical carbon-coated silicon nanocomposites as anodes for lithium-ion batteries," *Angewandte Chemie—International Edition*, vol. 45, no. 41, pp. 6896–6899, 2006.

- [8] H. Uono, B.-C. Kim, T. Fuse, M. Ue, and J.-I. Yamaki, "Optimized structure of silicon/carbon/graphite composites as an anode material for Li-ion batteries," *Journal of the Electrochemical Society*, vol. 153, no. 9, pp. A1708–A1713, 2006.
- [9] H. M. Jeong, S. Y. Lee, W. H. Shin et al., "Silicon@porous nitrogen-doped carbon spheres through a bottom-up approach are highly robust lithium-ion battery anodes," *RSC Advances*, vol. 2, no. 10, pp. 4311–4317, 2012.
- [10] Y. Yong and L.-Z. Fan, "Silicon/carbon nanocomposites used as anode materials for lithium-ion batteries," *Ionics*, vol. 19, no. 11, pp. 1545–1549, 2013.
- [11] H. Kim, B. Han, J. Choo, and J. Cho, "Three-dimensional porous silicon particles for use in high-performance lithium secondary batteries," *Angewandte Chemie—International Edition*, vol. 47, no. 52, pp. 10151–10154, 2008.
- [12] A. Magasinski, P. Dixon, B. Hertzberg, A. Kvit, J. Ayala, and G. Yushin, "High-performance lithium-ion anodes using a hierarchical bottom-up approach," *Nature Materials*, vol. 9, no. 4, pp. 353–358, 2010.
- [13] S. Bourderau, T. Brousse, and D. M. Schleich, "Amorphous silicon as a possible anode material for Li-ion batteries," *Journal of Power Sources*, vol. 81–82, pp. 233–236, 1999.
- [14] L. Y. Beaulieu, K. W. Eberman, R. L. Turner, L. J. Krause, and J. R. Dahna, "Colossal reversible volume changes in lithium alloys," *Electrochemical and Solid-State Letters*, vol. 4, no. 9, pp. A137–A140, 2001.
- [15] J. Graetz, C. C. Ahn, R. Yazami, and B. Fultz, "Highly reversible lithium storage in nanostructured silicon," *Electrochemical and Solid-State Letters*, vol. 6, no. 9, pp. A194–A197, 2003.
- [16] J. P. Maranchi, A. F. Hepp, and P. N. Kumta, "High capacity, reversible silicon thin-film anodes for lithium-ion batteries," *Electrochemical and Solid-State Letters*, vol. 6, no. 9, pp. A198–A201, 2003.
- [17] J. P. Maranchi, A. F. Hepp, A. G. Evans, N. T. Nuhfer, and P. N. Kumta, "Interfacial properties of the a-SiCu: active-inactive thin-film anode system for lithium-ion batteries," *Journal of the Electrochemical Society*, vol. 153, no. 6, pp. A1246–A1253, 2006.
- [18] A. A. Arie, J. O. Song, and J. K. Lee, "Structural and electrochemical properties of fullerene-coated silicon thin film as anode materials for lithium secondary batteries," *Materials Chemistry and Physics*, vol. 113, no. 1, pp. 249–254, 2009.
- [19] M.-H. Park, M. G. Kim, J. Joo et al., "Silicon nanotube battery anodes," *Nano Letters*, vol. 9, no. 11, pp. 3844–3847, 2009.
- [20] T. Song, J. Xia, J.-H. Lee et al., "Arrays of sealed silicon nanotubes as anodes for lithium ion batteries," *Nano Letters*, vol. 10, no. 5, pp. 1710–1716, 2010.
- [21] J.-K. Yoo, J. Kim, Y. S. Jung, and K. Kang, "Scalable fabrication of silicon nanotubes and their application to energy storage," *Advanced Materials*, vol. 24, no. 40, pp. 5452–5456, 2012.
- [22] C. K. Chan, H. Peng, G. Liu et al., "High-performance lithium battery anodes using silicon nanowires," *Nature Nanotechnology*, vol. 3, no. 1, pp. 31–35, 2008.
- [23] J. L. Gómez-Cámer, J. Morales, and L. Sánchez, "Anchoring Si nanoparticles to carbon nanofibers: an efficient procedure for improving Si performance in Li batteries," *Journal of Materials Chemistry*, vol. 21, no. 3, pp. 811–818, 2011.
- [24] T. Song, D. H. Lee, M. S. Kwon et al., "Silicon nanowires with a carbon nanofiber branch as lithium-ion anode material," *Journal of Materials Chemistry*, vol. 21, no. 34, pp. 12619–12621, 2011.
- [25] K. Fu, L. Xue, O. Yildiz et al., "Effect of CVD carbon coatings on Si@CNF composite as anode for lithium-ion batteries," *Nano Energy*, vol. 2, no. 5, pp. 976–986, 2013.
- [26] X. Fan, L. Zou, Y.-P. Zheng, F.-Y. Kang, and W.-C. Shen, "Electrospinning preparation of nanosilicon/disordered carbon composite as anode materials in li-ion battery," *Electrochemical and Solid-State Letters*, vol. 12, no. 10, pp. A199–A201, 2009.
- [27] L. Ji and X. Zhang, "Fabrication of porous carbon/Si composite nanofibers as high-capacity battery electrodes," *Electrochemistry Communications*, vol. 11, no. 6, pp. 1146–1149, 2009.
- [28] L. Ji, K.-H. Jung, A. J. Medford, and X. Zhang, "Electrospun polyacrylonitrile fibers with dispersed Si nanoparticles and their electrochemical behaviors after carbonization," *Journal of Materials Chemistry*, vol. 19, no. 28, pp. 4992–4997, 2009.
- [29] L. Ji and X. Zhang, "Electrospun carbon nanofibers containing silicon particles as an energy-storage medium," *Carbon*, vol. 47, no. 14, pp. 3219–3226, 2009.
- [30] L. Wang, C. X. Ding, L. C. Zhang et al., "A novel carbon-silicon composite nanofiber prepared via electrospinning as anode material for high energy-density lithium ion batteries," *Journal of Power Sources*, vol. 195, no. 15, pp. 5052–5056, 2010.
- [31] S. Y. Kim, B.-H. Kim, and K. S. Yang, "Preparation and electrochemical characteristics of a polyvinylpyrrolidone-stabilized Si/carbon composite nanofiber anode for a lithium ion battery," *Journal of Electroanalytical Chemistry*, vol. 705, pp. 52–56, 2013.
- [32] Y. Li, B. Guo, L. Ji et al., "Structure control and performance improvement of carbon nanofibers containing a dispersion of silicon nanoparticles for energy storage," *Carbon*, vol. 51, no. 1, pp. 185–194, 2013.
- [33] Y. Li, G. Xu, L. Xue et al., "Enhanced rate capability by employing carbon nanotube-loaded electrospun Si/C composite nanofibers as binder-free anodes," *Journal of the Electrochemical Society*, vol. 160, no. 3, pp. A528–A534, 2013.
- [34] L. Xue, K. Fu, Y. Li et al., "Si/C composite nanofibers with stable electric conductive network for use as durable lithium-ion battery anode," *Nano Energy*, vol. 2, no. 3, pp. 361–367, 2013.
- [35] H. Wu, G. Chan, J. W. Choi et al., "Stable cycling of double-walled silicon nanotube battery anodes through solid-electrolyte interphase control," *Nature Nanotechnology*, vol. 7, no. 5, pp. 309–314, 2012.
- [36] W. Jigging, Y. Yan, G. Lin, W. Chunlei, T. Kun, and J. Maier, "Highly reversible lithium storage in Si (core)-hollow carbon nanofibers (sheath) nanocomposites," *Nanoscale*, vol. 5, no. 7, pp. 2647–2650, 2013.
- [37] J. Kong, W. A. Yee, Y. Wei et al., "Silicon nanoparticles encapsulated in hollow graphitized carbon nanofibers for lithium ion battery anodes," *Nanoscale*, vol. 5, no. 7, pp. 2967–2973, 2013.
- [38] H. Kim and J. Cho, "Superior lithium electroactive mesoporous Si@Carbon core-shell nanowires for lithium battery anode material," *Nano Letters*, vol. 8, no. 11, pp. 3688–3691, 2008.
- [39] L.-F. Cui, R. Ruffo, C. K. Chan, H. Peng, and Y. Cui, "Crystalline-amorphous core-shell silicon nanowires for high capacity and high current battery electrodes," *Nano Letters*, vol. 9, no. 1, pp. 491–495, 2009.
- [40] L.-F. Cui, Y. Yang, C.-M. Hsu, and C. Yi, "Carbon-silicon Core-shell nanowires as high capacity electrode for lithium ion batteries," *Nano Letters*, vol. 9, no. 9, pp. 3370–3374, 2009.
- [41] G. K. Simon, B. Maruyama, M. F. Durstock, D. J. Burton, and T. Goswami, "Silicon-coated carbon nanofiber hierarchical nanostructures for improved lithium-ion battery anodes," *Journal of Power Sources*, vol. 196, no. 23, pp. 10254–10257, 2011.

- [42] B.-S. Lee, S.-B. Son, K.-M. Park et al., "Fabrication of Si core/C shell nanofibers and their electrochemical performances as a lithium-ion battery anode," *Journal of Power Sources*, vol. 206, pp. 267–273, 2012.
- [43] T. Zheng, Q. Zhong, and J. R. Dahn, "High-capacity carbons prepared from phenolic resin for anodes of lithium-ion batteries," *Journal of the Electrochemical Society*, vol. 142, no. 11, pp. L211–L214, 1995.

## Review Article

# An Overview on Structure and Field Emission Properties of Carbon Nitride Films

Qiong Wang<sup>1</sup> and Jinlong Jiang<sup>1,2</sup>

<sup>1</sup> Department of Physics, Lanzhou University of Technology, Lanzhou 730050, China

<sup>2</sup> State Key Laboratory of Solid Lubrication, Lanzhou Institute of Chemical Physics, Chinese Academy of Sciences, Lanzhou 730000, China

Correspondence should be addressed to Jinlong Jiang; jinlong@lut.cn

Received 26 February 2014; Revised 29 April 2014; Accepted 29 April 2014; Published 21 May 2014

Academic Editor: Jun Yang

Copyright © 2014 Q. Wang and J. Jiang. This is an open access article distributed under the Creative Commons Attribution License, which permits unrestricted use, distribution, and reproduction in any medium, provided the original work is properly cited.

Carbon nitride films have excellent properties and wide application prospects in the aspect of field emission properties. In this review structure characteristics and a variety of synthetic methods of carbon nitride film will be described. In the carbon nitrogen films, we mainly from the following three points:  $sp^2/sp^3$  ratio, surface morphology and N content to discuss the change of field emission properties. Appropriate  $sp^2/sp^3$  (about 1.0–1.25) ratio, N content (about 8 at.%–10 at.%), and rough surfaces will strengthen the field emission properties.

## 1. Introduction

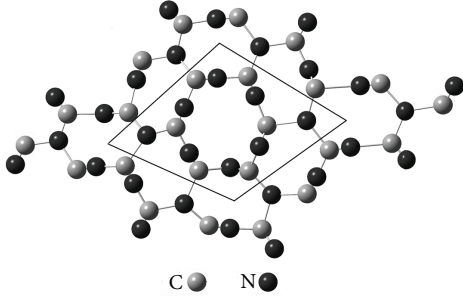
In the 1989, Liu and Cohen [1, 2] theoretically predicted the structure and physical properties of  $\beta$ - $C_3N_4$  whose bulk modulus and hardness, compared with diamond, are more outstanding. Although great effort has been made in synthesis of this material, in most cases amorphous carbon nitrogen (a- $CN_x$ ) films instead of crystalline  $C_3N_4$  were obtained. Either crystalline  $C_3N_4$  or a- $CN_x$  films have excellent performance. Studies have shown that carbon nitrogen ( $CN_x$ ) films have excellent properties in terms of high hardness [3], wear resistance [4], hydrogen storage performance [5], and excellent field emission properties [6]. In the past three decades, diamond-like carbon films incorporated with nitrogen or called  $CN_x$  films have been extensively studied owing to their potential application as cold cathode materials in field emission displays (FED). In the case of the previous reports, the threshold fields of the pure DLC film were usually 3–20 V/ $\mu m$  [7–9] and decreased to 1–12 V/ $\mu m$  after nitrogen incorporation [10–12]. In the past few years, there has been considerable interest in electron field emission from  $CN_x$  films. In addition, the structures and synthesis methods of  $CN_x$  films are diverse, so they have attracted much attention.

## 2. The Structures of $CN_x$ Films

**2.1. The Structures of Crystalline Phase  $CN_x$  Films.** Teter and Hemley through the theoretical calculation have predicted five kinds of crystalline phase structures of  $C_3N_4$ : alpha  $C_3N_4$  ( $\alpha$ - $C_3N_4$ ), beta  $C_3N_4$  ( $\beta$ - $C_3N_4$ ), cubic  $C_3N_4$  (c- $C_3N_4$ ), pseudo-cubic  $C_3N_4$  (pc- $C_3N_4$ ), and graphite  $C_3N_4$  (g- $C_3N_4$ ) [13]. In addition, these crystal structures have been found and reported in experiments [14–17]. The  $\alpha$ - $C_3N_4$  is earlier obtained by Yu et al. [18]. They used the calculation method of quantum mechanics clusters model and got  $\alpha$ - $C_3N_4$  by optimization crystal structure of simulative  $C_3N_4$ . The  $\alpha$ - $C_3N_4$  has crystal plane cascade order of crystal structure, by ABAB pattern to stack. In the structure of  $\alpha$ - $C_3N_4$ , C and N atoms connection by  $sp^3$  key formed a tetrahedron structure. Liu and Cohen [1] predicted the existence of  $\beta$ - $C_3N_4$  using band theory of first principles and prepared  $\beta$ - $C_3N_4$  based on  $\beta$ - $Si_3N_4$  crystal structure. They previewed that the structure of  $\beta$ - $C_3N_4$  is the hexagonal containing 14 atoms per unit cell. As a new kind of superhard material,  $\beta$ - $C_3N_4$  got more extensive research; its structure is shown in Figure 1. The c- $C_3N_4$  was first reported by Teter and Hemley [13]. They suggested the structure of c- $C_3N_4$  using the conjugate gradient method

TABLE 1: The structure parameters of crystal, bulk moduli  $B$ , and total energies  $E_0$  for five kinds of the predicted carbon nitride crystals.

	$\alpha$ -C <sub>3</sub> N <sub>4</sub>	$\beta$ -C <sub>3</sub> N <sub>4</sub>	Cubic-C <sub>3</sub> N <sub>4</sub>	Pseudocubic-C <sub>3</sub> N <sub>4</sub>	Graphite-C <sub>3</sub> N <sub>4</sub>
Space group	P31c(159)	P3(143)	$\bar{1}43d(220)$	$\bar{p}42m(111)$	$\bar{P}6m2(187)$
$Z$	4	2	4	1	2
$a$ (Å)	6.4665	6.4017	5.3973	3.4232	4.7420
$c$ (Å)	4.7097	2.4041			6.7205
$B_0$ (GPa)	425	451	496	448	
$E_0$ (eV/unit)	-1598.669	-1598.403	-1597.388	-1597.225	-1598.71

FIGURE 1: Schematic atomic structure of  $\beta$ -C<sub>3</sub>N<sub>4</sub>.

and found it has a similar structural characteristic with the Zn<sub>2</sub>SiO<sub>4</sub>. Liu and Wentzcovitch [19] proposed pc-C<sub>3</sub>N<sub>4</sub> crystal structure based on the structure of cubic ZnS removed a quarter of Zn atom. They found that pc-C<sub>3</sub>N<sub>4</sub> and  $\beta$ -C<sub>3</sub>N<sub>4</sub> have similar crystal structures. The g-C<sub>3</sub>N<sub>4</sub> has a variety of structures model. Liu and Wentzcovitch [19] proposed a rhombus g-C<sub>3</sub>N<sub>4</sub> crystal structure described as ABCABC... pattern to stack by calculation. However, Teter and Hemley [13] believed the mode of g-C<sub>3</sub>N<sub>4</sub> is hexagonal graphite structure in which the arrangement of atoms is along the C axis and crystal structures are based on the ABAB pattern to stack [20].

In those structures of C<sub>3</sub>N<sub>4</sub>, the g-C<sub>3</sub>N<sub>4</sub> has the most stable structure, but others have the superhard characteristics that it does not have. In the superhard structures of C<sub>3</sub>N<sub>4</sub>,  $\alpha$ -C<sub>3</sub>N<sub>4</sub> is the most stable structure. In a single cell, the volume of g-C<sub>3</sub>N<sub>4</sub>,  $\alpha$ -C<sub>3</sub>N<sub>4</sub>,  $\beta$ -C<sub>3</sub>N<sub>4</sub>, c-C<sub>3</sub>N<sub>4</sub>, and pc-C<sub>3</sub>N<sub>4</sub> subsequently decreases; however, their energy increases in turn. Table 1 shows the structure parameters of crystal, bulk modulus  $B$  and total energies  $E_0$  for five kinds of the predicted carbon nitride crystals. In order to prepare the C<sub>3</sub>N<sub>4</sub> crystalline, carbon and nitrogen ratio of precursors should be as close as possible to the theoretical value of 1.33. The researchers can also adopt appropriate methods to improve the reaction temperature, which can help the molecular fracture of the precursors.

**2.2. The Structures of Amorphous CN<sub>x</sub>.** Because carbon and nitrogen have the characteristic of various valence states forming bonding, therefore, in a-CN<sub>x</sub> films there are diverse of valence bond structures, as shown in Figure 2 [21]. In a-CN<sub>x</sub> films, N/C ratio depended on preparation methods of

the films and parameters of the technique. Studies have found that some C<sub>3</sub>N<sub>4</sub> defect structures and amorphous structures of CN<sub>x</sub> films are still the metastable structures, but with the increase of N vacancy, these two kinds of structure of CN<sub>x</sub> material reduce in bulk modulus. Researches show that the hardness of a-CN<sub>x</sub> films which be reached is 15 GPa–50 GPa. At the same time, a-CN<sub>x</sub> films have very excellent tribological properties. The structural characteristics, composition of materials, and crystallinity of CN<sub>x</sub> films can be characterized and analyzed by XRD, XPS, and Raman, techniques. From the current results, the superior mechanical properties, good heat conductivity properties, and excellent field emission properties make a-CN<sub>x</sub> films win a place in the new materials.

### 3. The Preparation Methods of CN<sub>x</sub> Films

The research on syntheses and properties of carbon nitride (CN<sub>x</sub>) films has aroused interest of scholars from different countries. CN<sub>x</sub> films with particular properties have been synthesized whose structures and characteristics were reviewed [22, 23]. The synthetic methods include physical vapor deposition (PVD), chemical vapor deposition (CVD), and so forth. These methods have led to amorphous CN<sub>x</sub> films or in some cases formed carbon nitride crystallites structure embedded in an amorphous CN<sub>x</sub> matrix.

**3.1. Physical Vapor Deposition (PVD).** Physical vapor deposition comprises magnetron sputtering, ion beam deposition (IBD), reaction sputtering, and pulsed laser deposition, and so forth. Reaction sputtering is the basic method for preparation of compound films. When used it to prepare CN<sub>x</sub> films, the mass fraction of nitrogen is generally lower than 40%. However, to form  $\beta$ -C<sub>3</sub>N<sub>4</sub>, system should include enough nitrogen and stoichiometric ratio should reach 57%. Niu et al. [24] obtained the CN<sub>x</sub> films on silicon substrate by using pulse laser evaporation C target, auxiliary deposition of atom nitrogen. Their studies found that N content reached 40% in the films and then C, N atoms combined with nonpolar covalent bond. Subsequently, Sharma et al. [25] and Zhang et al. [26] also obtained CN<sub>x</sub> films by a similar method. Mihailescu et al. [27] using ammonia instead of N<sub>2</sub> produced hard CN<sub>x</sub> films with carbon nitrogen single bond, double bond, and triple bond and then got that its optical band gap is 4.5 eV. Through analysis of the current study, people mostly get are mixture films which containing a various of crystal phases. Traditionally, these mixture films are called CN<sub>x</sub> films.

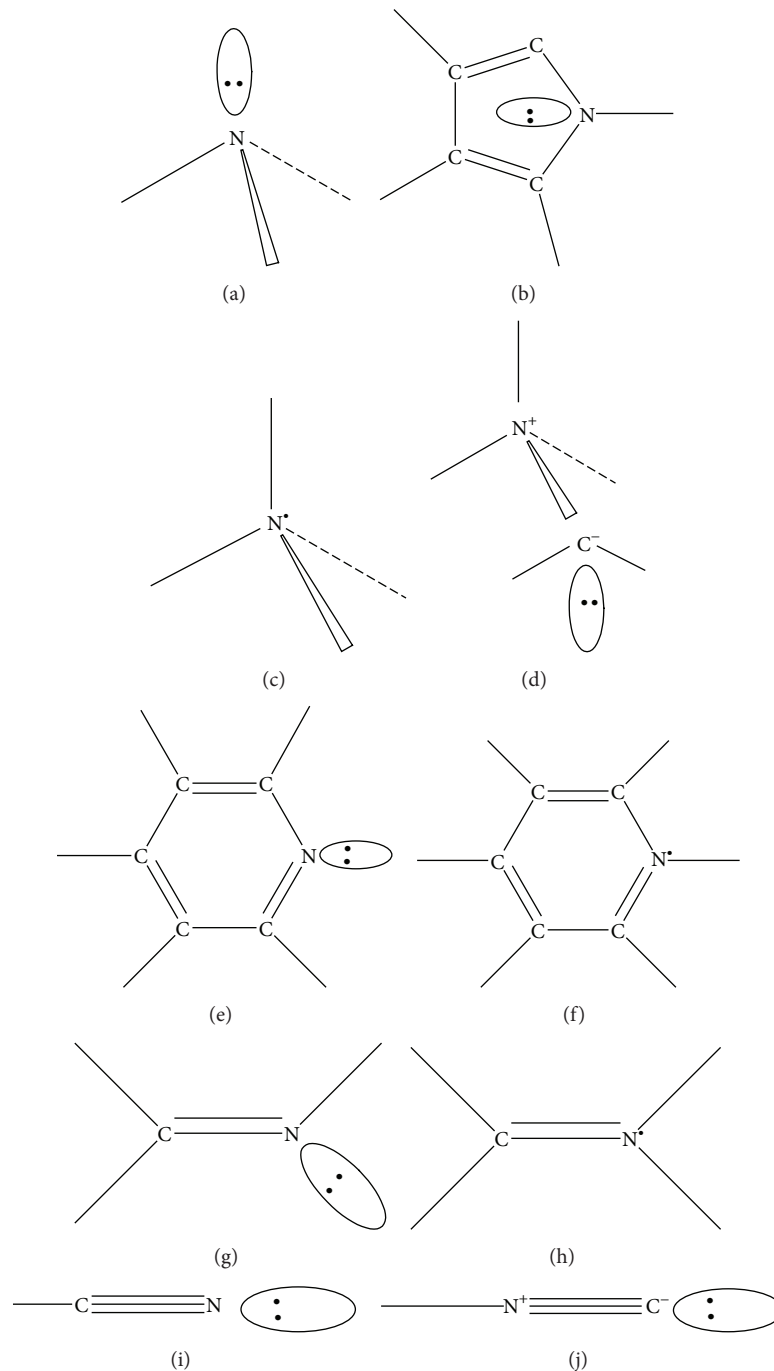


FIGURE 2: The possible bonding configuration in a-CN<sub>x</sub> films: (a)–(d) N sp<sup>3</sup> hybridization; (e)–(f) N atom in benzene; (g)–(h) N sp<sup>2</sup> hybridization (linear); (i) N sp<sup>1</sup> hybridization (nit rile); (j) N sp<sup>1</sup> hybridization (nitrile-like, autocompensation effect).

**3.2. Chemical Vapor Deposition (CVD).** Chemical vapor deposition achieved good results in the synthesis of carbon nitride films compared with other synthetic methods. CVD method is mainly used for one or more elements belonging to the film, so that these elements generate chemical reaction on the surface of the substrate and then generate films. CVD methods mainly include electron cyclotron resonance, hot filament assisted, DC glow discharge, radiofrequency discharge, and microwave plasma chemical vapor deposition.

Bias of auxiliary hot filament chemical vapor deposition (HFCVD) is one of the traditional devices used in the deposition of diamond films. Wang et al. [32, 33] got CN<sub>x</sub> films on Ni substrate by using HFCVD method firstly. Because preparation of the films is more likely to generate C–H and N–H bonds under the CVD conditions, so most of the CN<sub>x</sub> films are amorphous. Many researches are focused on the mechanical properties and field emission performance of the thin films. Based on previous researches, when CVD methods

TABLE 2: Optimal  $sp^2/sp^3$  ratio of amorphous carbon films which can be used as a reference of  $CN_x$  films.

	$sp^2/sp^3$ ratio	Preparation method	Turn-on electric field ( $F_T$ )	Highest current density	Reference
DLC films	0.85–1.0	Microwave plasma chemical vapor deposition (MPCVD)	10 V/ $\mu\text{m}$ (defined as the low-end electric field to emit electrons)	—	[28]
a-C	1.25	MPCVD	4.8 V/ $\mu\text{m}$ (0.28 mA/cm <sup>2</sup> )	—	[29]
Metal-DLC	1.0	Electrochemical deposition	6.5 V/ $\mu\text{m}$ (1 $\mu\text{A}/\text{cm}^2$ )	1.2 mA/cm <sup>2</sup> (23.5 V/ $\mu\text{m}$ )	[30]
Metal-DLC	1.2016	Electrochemical deposition	8.4 V/ $\mu\text{m}$ (1 $\mu\text{A}/\text{cm}^2$ )	163.89 $\mu\text{A}/\text{cm}^2$ (12.455 V/ $\mu\text{m}$ )	[31]

are used to prepare  $CN_x$  films, the choice of substrate materials is critical.

#### 4. Field Emission Properties of $CN_x$ Films

Field emission displays have high brightness, high resolution and vivid colors, fast response speed, and low energy consumption which can make true the advantages of flat displays and make it become the future direction of the display technology [34]. The preparation of cold cathode is the key factor in field emission display technology. Low-dimensional structure cold cathode materials with excellent field emission have broad application prospects in the vacuum microelectronic device. It is known that carbon-based materials such as diamond [28], diamond-like carbon, and carbon nanotubes [35, 36] are good cold cathode field emission materials. However, these materials still have many drawbacks [37–39], for DLC films are limited owing to its low total field emission current and high threshold fields, which have restricted the field emission properties. The incorporation of suitable amount of nitrogen into carbon films formed  $CN_x$  films which can enhance field emission properties of the materials. It is attributed to the weak donor activity of nitrogen that make the Fermi level rise [40], work function lower and formation of more  $sp^2$  clusters in films. The  $sp^2/sp^3$  ratio and surface morphology of  $CN_x$  films may also affect the field emission properties [41].

##### 4.1. The Influence of $sp^2/sp^3$ Ratio on Field Emission Properties.

From the results of studies, the  $sp^2/sp^3$  ratio in the DLC films increases with the increase of nitrogen doping [30, 42–44]. The  $sp^2$  clusters have high electrical conductivity that has better ability to provide high currents [45]. These  $sp^2$  clusters forming caused electron delocalization and/or improved electron hop between the clusters. Moreover, these clusters were likely to be overlapped, which also further accelerated electrons transportation between the connecting clusters [46, 47]. The electrons would be easily extracted from the film surface while the external electric field was applied, so high content of  $sp^2$  cluster plays a very important role in the field emission properties. These  $sp^2$  clusters with good connectivity act as a conductive channel in amorphous structures so that electrons can be launched into vacuum through this channel under the action of the outer electric field. With the increase of emission electron in films, the Fermi level rise, the work function, and surface potential barrier height of the

material are reduced, and then the electron emits from the surface more easily [48, 49]. In addition, the threshold field decreases when the  $sp^2$  clusters size increases [50]. However, Satyanarayana et al. [51–53] hold a different view with most researchers. They suggested that electron emission increases with the higher  $sp^3$  content and the field emission was not enhanced by an excessive amount of  $sp^2$ -bonded carbon. This is due to a serious graphitization of films at a higher level of  $sp^2$  content.

From Table 2, it can be concluded that an optimum  $sp^2/sp^3$  bonding ratio provides a high emission current density and a low turn-on electric field ( $F_T$ ) value. The  $sp^3$  bonding confers on  $CN_x$  film with low electron affinity and also a chemical and physical inertness that is invaluable for FED applications, with low electron affinity aid in electron emission to a vacuum. Shi et al. proposed a multiple step emission mechanism and the junction between  $sp^2$  and  $sp^3$  rich clusters provides an intermediate ladder for the electrons to climb up from the  $sp^2$  rich clusters to  $sp^3$  rich ones where they may have enough energy to overcome the small barrier to emit to vacuum [54]. As is shown in Table 3, the  $sp^2$  clusters size plays an important role in electron field emission properties [55]. Table 3 shows that the size of  $sp^2$  aromatic clusters is in the range of 1.8–2.4 nm, according to the Tuinstra-Koenig (TK) relationship [56, 57]. According to Tables 2 and 3 we suggest that in  $CN_x$  films what can effectively improve the field emission properties is the appropriate size and concentration ( $sp^2/sp^3$  ratio is about 1.0–1.25) of  $sp^2$  clusters [58]; the more conductive  $sp^2$  phase should be surrounded by insulating  $sp^3$  matrix to form a conductive channels, which at the same time can ensure that the electronic can easily be launched into the vacuum, which can effectively improve the field emission properties.

##### 4.2. The Influence of Surface Morphology on Field Emission Properties.

The electron emission is strongly related to the surface roughness: rougher surface means that there are more dense protrusions in the film surface. Protrusive structures could further increase the field enhancement factor which can geometrically promote the field emission [63, 64]. The  $CN_x$  films prepared by doping nitrogen into DLC films have a more rough surface morphology than DLC films [65, 66]. So these  $CN_x$  films have a higher geometric enhancement factor compared with DLC films and also have lower threshold field.

Some methods can be used to process the surface of films, such as ion etching which can create surface roughness to

TABLE 3: Appropriate size of  $sp^2$  clusters.

	Size of $sp^2$ clusters (nm)	Preparation method	Turn-on electric field ( $F_T$ )/threshold field ( $F_{th}$ )	Current density	Reference
Ta-C (annealed in nitrogen and acetylene ambient)	2	Filtered cathodic vacuum arc technique	4.8 V/ $\mu\text{m}$ (1 $\mu\text{A}/\text{cm}^2$ )	—	[50]
N-PPANI	2.2	Pyrolysis of polyaniline	1.7 V/ $\mu\text{m}$ (10 $\mu\text{A}/\text{cm}^2$ )	—	[59]
CN <sub>x</sub>	1.8–2.4	Magnetron sputtering of carbon target	4.0 V/ $\mu\text{m}$ (1 $\mu\text{A}/\text{cm}^2$ )	10 $\mu\text{A}/\text{cm}^2$ (11.0 V/ $\mu\text{m}$ )	[56]

TABLE 4: Nitrogen content of the CN<sub>x</sub> films.

	N content (at.%)	Preparation method	Turn-on electric field ( $F_T$ )/threshold field ( $F_{th}$ )	Current density	Reference
a-C:N films	8.0	Electron cyclotron resonance plasma	—	—	[60]
ta-C:N	10	A pulsed filtered vacuum arc deposition	4 V/ $\mu\text{m}$ ( $1 \times 10^{-6}$ A/ $\text{cm}^2$ )	—	[10]
DLC:N	10	Electrodeposition	11.8 V/ $\mu\text{m}$ (1 $\mu\text{A}/\text{mm}^2$ )	59.5 $\mu\text{A}/\text{mm}^2$ (24 V/ $\mu\text{m}$ )	[61]
ta-C:N	10.3	Filtered cathodic vacuum arc deposition	—	—	[62]

cause a field enhancement of the films. Songbo Wei et al. reported that, with increasing the bombarding energy, the film surface changed from smooth to a peak-and-valley structure, and the film surface became rougher. The root mean square (RMS) values of the CN<sub>x</sub> films increased from 0.27 nm to 0.78 nm in this process [67]. Hart et al. and Shi et al. believe that hydrogen treatment on the surface of films can create  $sp^2$  clusters which would induce a field enhancement of the surface [54, 68], while Robertson think that, after treating with hydrogen, some areas of the surface will adsorb hydrogen and form C–H dipole which would cause a nonuniform distribution of electric field and produce an electric field enhancement effect which is similar to the metal tip needle [37].

#### 4.3. The Influence of N Content on Field Emission Properties.

It was found that the field emission of CN<sub>x</sub> films depended on the N content and this effect dominated the effects of other parameters, such as  $sp^3$  content, band gap of the films, Fermi level position, and resistivity of the films. The effect is negative on field emission no matter too much or too little nitrogen doping into CN<sub>x</sub> films and only the appropriate nitrogen content can enhance field emission properties [69]. As shown in Table 4, which is based on previous experimental results, it can be seen that the CN<sub>x</sub> film containing 8 at.%–10 at.% nitrogen [10, 60–62, 70] possesses enhanced field emission properties. A minimum for threshold field and a maximum for emission current density at this suitable N content were found. High levels of nitrogen additions are found to reduce field emission properties; from the above

description we know that N incorporation into the DLC films favors formation of  $sp^2$  units and leads to serious graphitization of the CN<sub>x</sub> films [11, 53]. According to the proposal of Cutler et al.'s three-step field emission model, the emitted electrons are assumed to subject a three-step process. The first step is internal emission, the second step is electron transport, and the third step is vacuum emission [10, 54, 71]. The determinative within third step is the fraction of  $sp^3$  phase, since the  $sp^3$  phase carbon has a low electron affinity, and the  $sp^3$  phase is favorable for electron emission into vacuum [54]. So serious graphitization of the CN<sub>x</sub> films is not conducive to the field emission. Vacuum emission is a determinative for the whole emission process.

In the first step, the determinative for emission is the value of band gap and Fermi level position. However, in the second step, the injected electrons transport across the CN<sub>x</sub> films bulk, which is directly limited by the resistivity of the CN<sub>x</sub> films [10]. From Figure 3 it can be seen that as the N content increases, the optical band gap reduces and Fermi level increases of CN<sub>x</sub> films [10, 72]. When the N content keeping at an optimum range the resistivity of the films decreases remarkably [62]. However, when the N content becomes higher than the appropriate value, Fermi level and band gap width do not move any more, the resistivity approaches gradually to a saturation value [10, 73].

## 5. Conclusions

For several decades, a variety of techniques have been used for the synthesis of CN<sub>x</sub> films; in this paper PVD and CVD

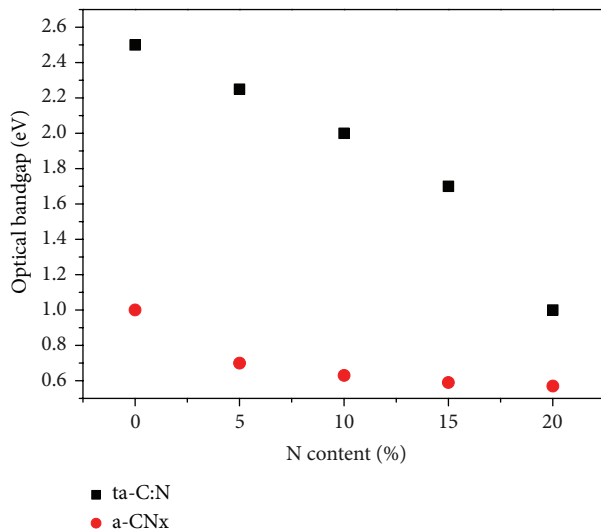


FIGURE 3: Optical band gap versus nitrogen content. Data from Zhang et al. [10] and Meškinis et al. [72].

methods have been introduced. The structures properties in crystalline and amorphous  $CN_x$  films have been elaborated in this paper.

The field emission properties of  $CN_x$  films are influenced by ratio of  $sp^2/sp^3$ , size of  $sp^2$  clusters, surface morphology, and N content of films. Appropriate  $sp^2/sp^3$  ratio (about 1.0–1.25) and N content (about 8 at.%–10 at.%) will strengthen the field emission properties. When N contents remain at an optimum range, the optical band gap and resistivity reduce and Fermi level of  $CN_x$  films increases, which are important for enhancing field emission properties. Appropriate size of  $sp^2$  clusters is about 1.8–2.4 nm. Doping nitrogen can enhance surface roughness of  $CN_x$  films; the  $CN_x$  films with rougher surface also have lower threshold field. So  $CN_x$  films with rough surface can improve the field emission properties.

## Conflict of Interests

The authors declare that there is no conflict of interests regarding the publication of this paper.

## References

- [1] A. Y. Liu and M. L. Cohen, "Prediction of new low compressibility solids," *Science*, vol. 245, no. 4920, pp. 841–842, 1989.
- [2] A. Y. Liu and M. L. Cohen, "Structural properties and electronic structure of low-compressibility materials: p-Si<sub>3</sub>N<sub>4</sub> and hypothetical p-C<sub>3</sub>N<sub>4</sub>," *Physical Review*, vol. 1341, pp. 10727–10734, 1990.
- [3] W. C. Chan, B. Zhou, Y. W. Chuang, C. S. Lee, and S. T. Lee, "Synthesis, composition, surface roughness and mechanical properties of thin nitrogenated carbon films," *Journal of Vacuum Science and Technology A*, vol. 16, no. 3, pp. 1907–1910, 1998.
- [4] C. J. Torng, J. M. Sivertsen, and J. H. Judy, "Structure and bonding studies of the C:N thin solid films produced by RF Sputtering method," *Journal of Materials Research*, vol. 5, no. 11, pp. 2490–2496, 1990.
- [5] Y. Ohkawara, S. Ohshio, T. Suzuki, K. Yatsui, H. Ito, and H. Saitoh, "Hydrogen storage in amorphous phase of hydrogenated carbon nitride," *Japanese Journal of Applied Physics*, vol. 41, no. 12, pp. 7508–7509, 2002.
- [6] J. J. Li, W. T. Zheng, L. Sun et al., "Field emission from amorphous carbon nitride films deposited on silicon tip arrays," *Chinese Physics Letters*, vol. 20, no. 6, pp. 944–946, 2003.
- [7] C. Wang, A. Garcia, D. C. Ingram, M. Lake, and M. E. Kordesch, "Cold field emission from CVD diamond films observed in emission electron microscopy," *Electronics Letters*, vol. 27, no. 16, pp. 1459–1461, 1991.
- [8] K. Okano, S. Koizumi, S. Ravi, P. Silva, and G. A. J. Amarantunga, "Low-threshold cold cathodes made of nitrogen-doped chemical-vapour-deposited diamond," *Nature*, vol. 381, pp. 140–141, 1996.
- [9] D. S. Mao, W. Li, X. Wang, and X. H. Liu, "Diamond-like carbon films prepared by filtered arc deposition for electron field emission application," *Surface and Coatings Technology*, vol. 137, no. 1, pp. 1–5, 2001.
- [10] X. W. Zhang, W. Y. Cheung, and S. P. Wong, "Field electron emission characteristics of nitrogenated tetrahedral amorphous carbon films," *Thin Solid Films*, vol. 429, no. 1-2, pp. 261–266, 2003.
- [11] B. S. Satyanarayana, A. Hart, W. I. Milne, and J. Robertson, "Field emission from tetrahedral amorphous carbon," *Diamond and Related Materials*, vol. 7, pp. 656–659, 1998.
- [12] E. Fogarassy, T. Szoreny, G. Pirio, J. Olivier, P. Legagneux, and P. Boher, "Field emission properties of a-CN<sub>x</sub> films prepared by pulsed laser deposition," *Applied Physics A*, vol. 76, no. 1, pp. 15–19, 2003.
- [13] D. M. Teter and R. J. Hemley, "Low-compressibility carbon nitrides," *Science*, vol. 271, no. 5245, pp. 53–55, 1996.
- [14] Y. Tian, J. Z. Wang, W. F. Yu, R. Cao, Y. Song, and X. Ning, "Effect of acetic acid on electrochemical deposition of carbon-nitride thin film," *Science in China, Series E: Technological Sciences*, vol. 52, no. 6, pp. 1698–1702, 2009.
- [15] Y. S. Gu, Z. J. Duan, H. G. Yi et al., "The preparation of crystalline  $\beta$ -C<sub>3</sub>N<sub>4</sub> film," *Physics*, vol. 26, no. 8, pp. 449–450, 1997.
- [16] C. Li, C. B. Cao, and H. S. Zhu, "Electrodeposition of graphite-like carbon nitride thin films," *Journal of Synthetic Crystals*, vol. 32, no. 3, pp. 252–256, 2003.
- [17] J. T. Zhang, C. B. Cao, and H. S. Zhu, "Preparation and photoelectrical properties of CN<sub>x</sub> films," *Chinese Journal of Materials Research*, vol. 17, no. 4, pp. 432–438, 2003.
- [18] K. M. Yu, M. L. Cohen, E. E. Haller, W. L. Hansen, A. Y. Liu, and I. C. Wu, "Observation of crystalline C<sub>3</sub>N<sub>4</sub>," *Physical Review B*, vol. 49, no. 7, pp. 5034–5037, 1994.
- [19] A. Y. Liu and R. M. Wentzcovitch, "Stability of carbon nitride solids," *Physical Review B*, vol. 50, no. 14, pp. 10362–10365, 1994.
- [20] D. L. Yu, *Research on synthesis methods and crystal structures of carbon nitrides [Ph.D. thesis]*, Yanshan University, Hebei, China, December, 2001.
- [21] B. Zheng, *Theoretical study for amorphous carbon, amorphous carbon nitride and nanodiamond [Ph.D. thesis]*, Jilin University, Jilin, China, May, 2006.
- [22] Z. B. Ma, "Progress in the synthesis and characterization of carbon nitride crystals," *New Carbon Materials*, vol. 21, no. 3, pp. 276–283, 2006.
- [23] X. R. Liang, Y. L. Jiang, L. Y. Kong et al., "The synthesis, application and research progress of carbon nitride (C<sub>3</sub>N<sub>4</sub>) materials," *The New Technology and New Process*, vol. 1, pp. 88–90, 2013.

- [24] C. Niu, Y. Z. Lu, and C. M. Lieber, "Experimental realization of the covalent solid carbon nitride," *Science*, vol. 261, no. 5119, pp. 334–337, 1993.
- [25] A. K. Sharma, P. Ayyub, M. S. Multani et al., "Synthesis of crystalline carbon nitride thin films by laser processing at a liquid-solid interface," *Applied Physics Letters*, vol. 69, no. 23, pp. 3489–3491, 1996.
- [26] Z. J. Zhang, S. S. Fan, J. L. Huang, and C. M. Lieber, "Diamond-like properties in a single phase carbon nitride solid," *Applied Physics Letters*, vol. 68, no. 19, pp. 2639–2641, 1996.
- [27] I. N. Mihailescu, E. Gyorgy, R. Alexandrescu et al., "Optical studies of carbon nitride thin films deposited by reactive pulsed laser ablation of a graphite target in low pressure ammonia," *Thin Solid Films*, vol. 323, no. 1-2, pp. 72–78, 1998.
- [28] Y. C. Chen, X. Y. Zhong, B. Kabius, J. M. Hiller, N. H. Tai, and I. N. Lin, "Improvement of field emission performance on nitrogen ion implanted ultrananocrystalline diamond films through visualization of structure modifications," *Diamond and Related Materials*, vol. 20, no. 2, pp. 238–241, 2011.
- [29] Z. L. Lu, B. L. Zhang, N. Yao, X. Y. Zhang, B. X. Ma, and Z. Q. Fan, "The effect of surface  $sp^2/sp^3$  bonding ratios of carbon films on the field emission property," in *Proceedings of the 5th International Vacuum Electron Sources Conference (IVESC '04)*, September 2004.
- [30] X. M. Ling, P. Z. Zhang, R. S. Li, D. W. Fan, and X. M. Yao, "Electron field emission of iron and cobalt-doped DLC films fabricated by electrochemical deposition," *Surface and Interface Analysis*, vol. 45, pp. 943–948, 2013.
- [31] Q. Wang, S. L. Li, and S. H. Wan, "Investigation of field emission characteristics and microstructure of nickel-doped DLC nanocomposite films by electrochemical deposition," *Physica E*, vol. 46, pp. 89–96, 2012.
- [32] E. G. Wang, Y. Chen, and L. P. Guo, "Preparation and structure of  $C_3N_4$ -specimens on Ni substrate," *Science in China A*, vol. 27, no. 2, pp. 154–157, 1997.
- [33] Y. Chen, L. P. Guo, and E. G. Wang, "Experimental evidence for alpha and beta -phases of pure crystalline  $C_3N_4$  in films deposited on nickel substrates," *Philosophical Magazine Letters*, vol. 75, no. 3, pp. 155–162, 1997.
- [34] R. Wang and B. Wang, "A critical review of field electron emission thin film materials," *Materials China*, vol. 28, no. 3, pp. 6–12, 2009.
- [35] B. Padya, D. Kalita, P. K. Jain, G. Padmanabham, M. Ravi, and K. S. Bhat, "Nitrogen incorporated highly aligned carbon nanotube arrays thin film grown from single feedstock for field emission," *Journal of Nanoelectronics and Optoelectronics*, vol. 8, no. 2, pp. 177–181, 2013.
- [36] B. B. Wang, Q. J. Cheng, X. Chen, and K. Ostrikov, "Enhancement of electron field emission of vertically aligned carbon nanotubes by nitrogen plasma treatment," *Journal of Alloys and Compounds*, vol. 509, no. 38, pp. 9329–9334, 2011.
- [37] T. Y. Tsai, N. H. Tai, and I. N. Lin, "Characteristics of carbon nanotube electron field emission devices prepared by LTCC process," *Diamond and Related Materials*, vol. 13, no. 4–8, pp. 982–986, 2004.
- [38] W. I. Milne, K. B. K. Teo, G. A. J. Amaratunga et al., "Aligned carbon nanotubes/fibers for applications in vacuum microwave devices," *Current Applied Physics*, vol. 4, no. 5, pp. 513–517, 2004.
- [39] S. R. P. Silva and J. D. Carey, "Enhancing the electrical conduction in amorphous carbon and prospects for device applications," *Diamond and Related Materials*, vol. 12, no. 2, pp. 151–158, 2003.
- [40] X. C. LeQuan, W. P. Kang, J. L. Davidson, M. Guo, and B. K. Choi, "Micro-Raman, SEM, XPS, and electron field emission characterizations of nitrogen-induced shallow defects on nanodiamond films fabricated with different growth parameters," *Diamond and Related Materials*, vol. 18, no. 2-3, pp. 191–195, 2009.
- [41] P. Z. Zhang, R. S. Li, H. Yang, Y. C. Feng, and E. Q. Xie, "Enhanced electron field emission from ZnO nanoparticles-embedded DLC films prepared by electrochemical deposition," *Solid State Sciences*, vol. 14, no. 6, pp. 715–718, 2012.
- [42] E. Fogarassy, T. Szorenyi, F. Antoni et al., "Influence of the nitrogen content on the field emission properties of a-CN<sub>x</sub> films prepared by pulsed laser deposition," *Applied Surface Science*, vol. 197–198, pp. 316–320, 2002.
- [43] X. Yan, T. Xu, G. Chen, S. Xu, and S. Yang, "Field-emission properties of diamond-like-carbon and nitrogen-doped diamond-like-carbon films prepared by electrochemical deposition," *Applied Physics A*, vol. 81, no. 1, pp. 41–46, 2005.
- [44] A. Majumdar, S. C. Das, R. Bogdanowicz, T. Shripathib, W. Langeld, and R. Hipplera, "Role of nitrogen in evolution of  $sp^2/sp^3$  bonding and optical band gap in hydrogenated carbon nitride," *Vibrational Spectroscopy*, vol. 66, pp. 63–68, 2013.
- [45] R. Wächter, A. Cordery, S. Proffitt, and J. S. Foord, "Influence of film deposition parameters on the field emission properties of diamond-like carbon films," *Diamond and Related Materials*, vol. 7, no. 2–5, pp. 687–691, 1998.
- [46] S. H. Wan, L. P. Wang, J. Y. Zhang, and Q. J. Xue, "Field emission properties of DLC and phosphorus-doped DLC films prepared by electrochemical deposition process," *Applied Surface Science*, vol. 255, no. 6, pp. 3817–3821, 2009.
- [47] J. J. Li, W. T. Zheng, Z. S. Jin et al., "Electron field emission of radio frequency magnetron sputtered CN<sub>x</sub> films annealed at different temperatures," *Journal of Vacuum Science and Technology B*, vol. 21, no. 6, pp. 2382–2387, 2003.
- [48] Y. Umehara, S. Murai, Y. Koide, and M. Murakami, "Effects of  $sp^2/sp^3$  bonding ratios on field emission properties of diamond-like carbon films grown by microwave plasma chemical vapor deposition," *Diamond and Related Materials*, vol. 11, no. 7, pp. 1429–1435, 2002.
- [49] J. J. Li, W. T. Zheng, and H. J. Bian, "The effect of annealing on the field emission properties of amorphous CN<sub>x</sub> films," *Acta Physica Sinica*, vol. 52, no. 07, pp. 1797–1801, 2003.
- [50] Y. B. Zhang, S. P. Lau, L. Huang, Z. Sun, and B. K. Tay, "Microstructure effect on field emission from tetrahedral amorphous carbon films annealed in nitrogen and acetylene ambient," *Diamond and Related Materials*, vol. 13, no. 1, pp. 133–138, 2004.
- [51] O. S. Panwar, M. A. Khan, M. Kumar et al., "Effect of high substrate bias and hydrogen and nitrogen incorporation on filtered cathodic vacuum arc deposited tetrahedral amorphous carbon films," *Thin Solid Films*, vol. 516, no. 8, pp. 2331–2340, 2008.
- [52] O. S. Panwar, M. A. Khan, B. S. Satyanarayana et al., "Effect of high substrate bias and hydrogen and nitrogen incorporation on density of states and field-emission threshold in tetrahedral amorphous carbon films," *Journal of Vacuum Science and Technology B*, vol. 28, no. 2, pp. 411–422, 2010.
- [53] B. S. Satyanarayana, A. Hart, W. I. Milne, and J. Robertson, "Field emission from tetrahedral amorphous carbon," *Applied Physics Letters*, vol. 71, no. 10, pp. 1430–1432, 1997.
- [54] X. Shi, L. K. Cheah, B. K. Tay, and S. R. P. Silva, "Electron field emission from surface treated tetrahedral amorphous carbon films," *Applied Physics Letters*, vol. 74, no. 6, pp. 833–835, 1999.

- [55] J. D. Carey, R. D. Forrest, R. U. A. Khan, and S. R. P. Silva, "Influence of  $sp^2$  clusters on the field emission properties of amorphous carbon thin films," *Applied Physics Letters*, vol. 77, no. 13, pp. 2006–2008, 2000.
- [56] B. Zhang, Y. L. Yu, Z. Wang, and J. Y. Zhang, "Structure evolution from nanocolumns to nanoporous of nitrogen doped amorphous carbon films deposited by magnetron sputtering," *Applied Surface Science*, vol. 256, no. 22, pp. 6506–6511, 2010.
- [57] F. Tuinstra and J. L. Koenig, "Raman spectrum of graphite," *The Journal of Chemical Physics*, vol. 53, no. 3, pp. 1126–1130, 1970.
- [58] R. Paul, S. Dalui, and A. K. Pal, "Modulation of field emission properties of DLC films with the incorporation of nanocrystalline silver nanoparticles by CVD technique," *Surface and Coatings Technology*, vol. 204, no. 24, pp. 4025–4033, 2010.
- [59] L. Lin, H. J. Niu, M. L. Zhang, W. Song, Z. Wang, and X. D. Bai, "Electron field emission from amorphous carbon with N-doped nanostructures pyrolyzed from polyaniline," *Applied Surface Science*, vol. 254, no. 22, pp. 7250–7254, 2008.
- [60] U. Hoffmann, A. Weber, C.-P. Klages, and T. Matth e, "Field emission of nitrogenated amorphous carbon films," *Carbon*, vol. 37, no. 5, pp. 753–757, 1999.
- [61] R. S. Li, E. Q. Xie, M. Zhou, Z. X. Zhang, T. Wang, and B. A. Lu, "Field emission properties of nitrogen incorporated DLC films prepared by electrodeposition," *Applied Surface Science*, vol. 255, no. 5, pp. 2787–2790, 2008.
- [62] R. McCann, S. S. Roy, P. Papakonstantinou et al., "NEXAFS study and electrical properties of nitrogen-incorporated tetrahedral amorphous carbon films," *Diamond and Related Materials*, vol. 14, no. 3–7, pp. 1057–1061, 2005.
- [63] J. J. Li, C. Z. Gu, P. Xu, Q. Wang, and W. T. Zheng, "Field emission enhancement of carbon nitride films by annealing with different durations," *Materials Science and Engineering B*, vol. 126, no. 1, pp. 74–79, 2006.
- [64] Y. J. Li, S. P. Lau, B. K. Tay et al., "Field emission from tetrahedral amorphous carbon films with various surface morphologies," *Diamond and Related Materials*, vol. 10, no. 8, pp. 1515–1522, 2001.
- [65] X. B. Yan, T. Xu, G. Chen, S. R. Yang, and H. W. Liu, "Study of structure, tribological properties and growth mechanism of DLC and nitrogen-doped DLC films deposited by Electrochemical technique," *Applied Surface Science*, vol. 236, no. 1, pp. 328–335, 2004.
- [66] G. Chen, X. B. Yan, H. W. Liu, and T. Xu, "The microstructure comparison of DLC and CN<sub>x</sub> films deposition by Electrochemical," *Journal of Chinese Electron Microscopy Society*, vol. 23, no. 4, p. 430, 2004.
- [67] S. B. Wei, T. M. Shao, and J. Xu, "Effect of bombarding energy of N ions on composition, hardness and surface free energy of carbon nitride films," *Surface and Coatings Technology*, vol. 206, no. 19–20, pp. 3944–3948, 2012.
- [68] A. Hart, B. S. Satyanarayana, W. I. Milne, and J. Robertson, "Field emission from tetrahedral amorphous carbon as a function of surface treatment and substrate material," *Applied Physics Letters*, vol. 74, no. 11, pp. 1594–1596, 1999.
- [69] H. Akasaka, T. Yamada, and N. Ohtake, "Effect of film structure on field emission properties of nitrogen doped hydrogenated amorphous carbon films," *Diamond and Related Materials*, vol. 18, no. 2–3, pp. 423–425, 2009.
- [70] D. S. Mao, J. Zhao, W. Li et al., "Electron field emission from nitrogen-containing diamond-like carbon films deposited by filtered arc deposition," *Materials Letters*, vol. 41, no. 3, pp. 117–121, 1999.
- [71] P. H. Cutler, N. M. Miskovsky, P. B. Lerner, and M. S. Chung, "The use of internal field emission to inject electronic charge carriers into the conduction band of diamond films: a review," *Applied Surface Science*, vol. 146, no. 1–4, pp. 126–133, 1999.
- [72] Š. Meškinis, R. Gudaitis, V. Kopustinskas, S. Tamulevičius, and K. Šlapika-Piezoresistive, "Optical and electrical properties of diamond like carbon and carbon nitride films," *Diamond and Related Materials*, vol. 19, no. 10, pp. 1249–1253, 2010.
- [73] J. Schwan, V. Batori, S. Ulrich, H. Ehrhardt, and S. R. P. Silva, "Nitrogen doping of amorphous carbon thin films," *Journal of Applied Physics*, vol. 84, no. 4, pp. 2071–2081, 1998.

## Research Article

# Study on the Microstructure and Electrical Properties of Boron and Sulfur Codoped Diamond Films Deposited Using Chemical Vapor Deposition

Zhang Jing,<sup>1,2</sup> Li Rongbin,<sup>2</sup> Wang Xianghu,<sup>2</sup> and Wei Xicheng<sup>1</sup>

<sup>1</sup> School of Materials Science and Engineering, Shanghai University, Shanghai 200072, China

<sup>2</sup> School of Mechanical Engineering, Shanghai Dianji University, 1201 Jiang Chuan Road, Shanghai 200245, China

Correspondence should be addressed to Li Rongbin; [lirb@sdju.edu.cn](mailto:lirb@sdju.edu.cn)

Received 23 January 2014; Revised 13 April 2014; Accepted 15 April 2014; Published 21 May 2014

Academic Editor: Jinlong Jiang

Copyright © 2014 Zhang Jing et al. This is an open access article distributed under the Creative Commons Attribution License, which permits unrestricted use, distribution, and reproduction in any medium, provided the original work is properly cited.

The atomic-scale microstructure and electron emission properties of boron and sulfur (denoted as B-S) codoped diamond films grown on high-temperature and high-pressure (HTHP) diamond and Si substrates were investigated using atom force microscopy (AFM), scanning tunneling microscopy (STM), secondary ion mass spectroscopy (SIMS), and current imaging tunneling spectroscopy (CITS) measurement techniques. The films grown on Si consisted of large grains with secondary nucleation, whereas those on HTHP diamond are composed of well-developed polycrystalline facets with an average size of 10–50 nm. SIMS analyses confirmed that sulfur was successfully introduced into diamond films, and a small amount of boron facilitated sulfur incorporation into diamond. Large tunneling currents were observed at some grain boundaries, and the emission character was better at the grain boundaries than that at the center of the crystal. The films grown on HTHP diamond substrates were much more perfect with higher quality than the films deposited on Si substrates. The local  $I$ - $V$  characteristics for films deposited on Si or HTHP diamond substrates indicate n-type conduction.

## 1. Introduction

Diamond is a semiconductor material with many excellent physical properties, such as a wide bandgap, a high saturation velocity of carriers, and other remarkable electronic properties. These properties make diamond a promising material for applications in high-power, high-temperature, high-frequency electronics, detectors, and electron emitter devices. The ability to produce large-area diamond wafers by chemical vapor deposition (CVD) techniques has aroused intensive interest in the use of the commercial material for active electronics. However, progress in this area has been severely hindered by the polycrystalline nature of such films and the difficulty in efficiently incorporating suitable dopant species [1]. Although homoepitaxial growth of diamond has been widely demonstrated, substrate cost and dopant incorporation limit commercial applications.

Identifying the best donor dopant for diamond is one of the fundamental issues for the development of diamond-based devices. Phosphorus (P) is expected to be a promising n-type dopant candidate for diamond. Katagiri reported that n-type conductivity of homoepitaxial diamond with a Hall mobility of  $410 \text{ cm}^2 \text{ V}^{-1} \text{ s}^{-1}$  at room temperature [2]. Sally et al. reported on the n-type conductivity of sulfur-doped polycrystalline samples on silicon [3]. However, the distribution of sulfur between grain boundaries and the bulk has still not been reported. Sakaguchi et al. reported an activation energy of 0.38 eV and a Hall mobility of  $597 \text{ cm}^2 \text{ V}^{-1} \text{ s}^{-1}$  at room temperature for sulfur-doped n-type diamond grown on (100) substrates [4]. Katayama-Yoshida et al. examined the theoretical aspects of codoping for wide-bandgap semiconductors [5]. Codoping has been proved as an effective way to incorporate donor dopants. However, up to now, doped films with such high Hall mobility have not been reported. This may be due to the compensation of donors by

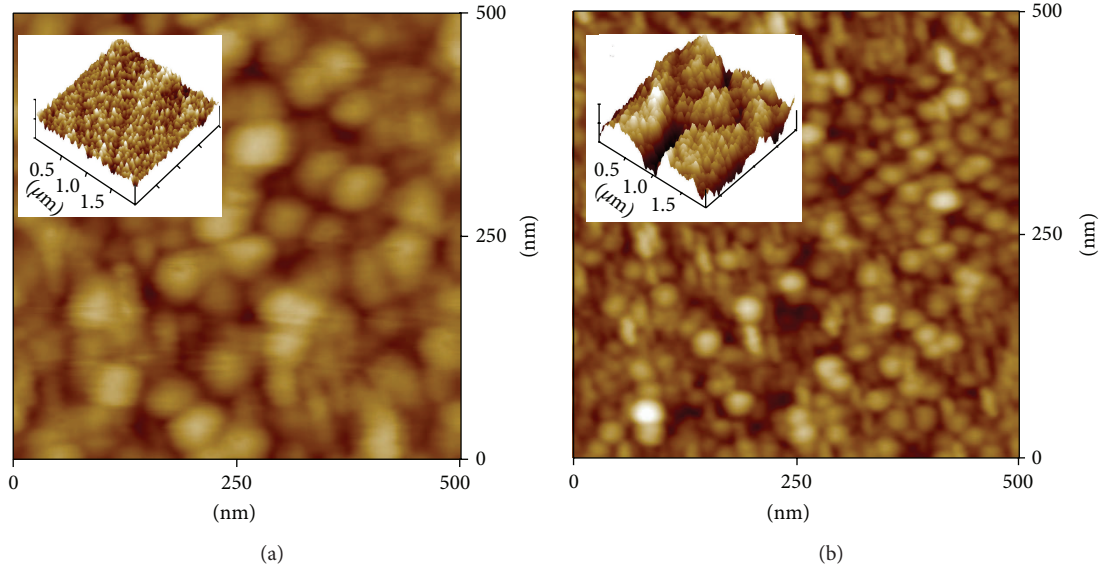


FIGURE 1: AFM image of the film on an HTHP diamond substrate with B-S codoping. The inset is a three-dimensional image. (a)  $S/C = 0.001$ ,  $B/S = 0.01$ ; (b)  $S/C = 0.005$ ,  $B/S = 0.02$ .

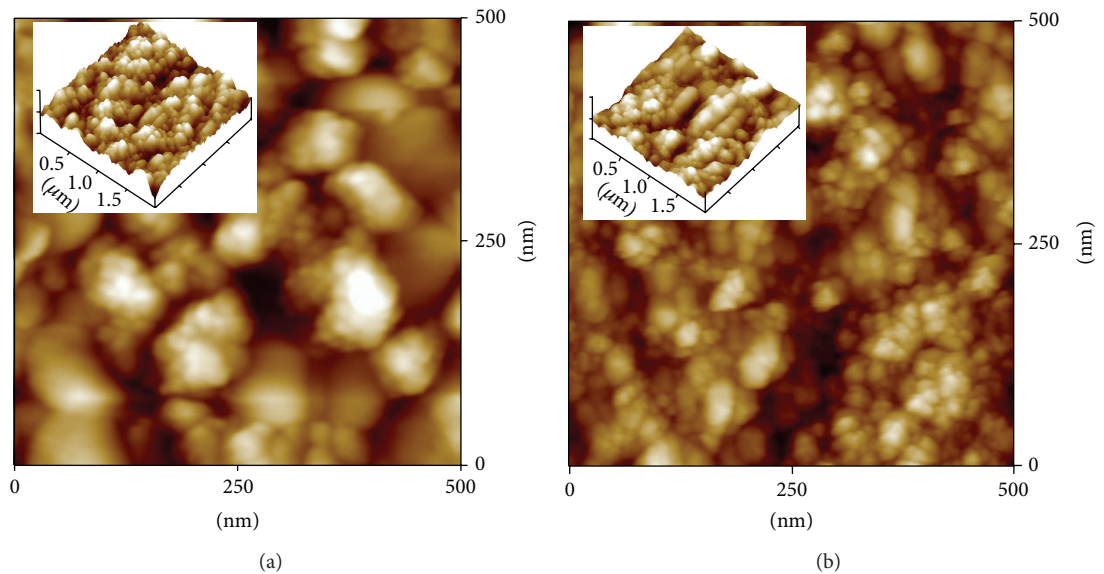


FIGURE 2: AFM image of the film deposited on a Si substrate with B-S codoping. The inset is a three-dimensional image. (a)  $S/C = 0.001$ ,  $B/S = 0.01$ ; (b)  $S/C = 0.005$ ,  $B/S = 0.02$ .

defects or residual acceptor impurities. The improvement in electrical properties is strongly related to the improvement of crystalline perfection, surface microstructure characteristics, and the electron surface states.

## 2. Methods

In our previous studies, the growth of boron and sulfur codoped diamond films on p-type (100) silicon substrates (heteroepitaxy) and HTHP diamond substrates (homoepitaxy) by microwave plasma-assisted chemical vapor deposition (MPCVD) is demonstrated. The diamond films were

grown in a microwave reactor using dimethyl disulfide as the sulfur source. Acetone and hydrogen were used as the main reactant gases. The acetone concentration was 0.5%; the  $S/C$  atomic ratio in the gas sources was from 0.001 to 0.005, with a  $B/S$  ratio of 0.01-0.02; and the total gas pressure and the substrate temperature were 25 Torr and  $750^{\circ}\text{C}$ , respectively.

In previous research, microstructures and electrical properties of CVD diamond films that were investigated by atomic force microscopy (AFM) and scanning tunneling microscopy (STM) were studied [6, 7]. Current imaging tunneling spectroscopy (CITS) [8] was used to compare the structures and electrical properties of the doped diamond

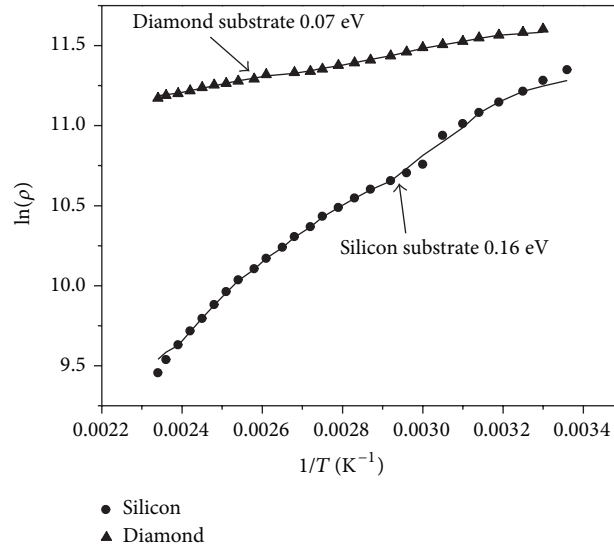


FIGURE 3: The temperature dependence of the resistance of B-S codoped diamond films grown under the different substrates.

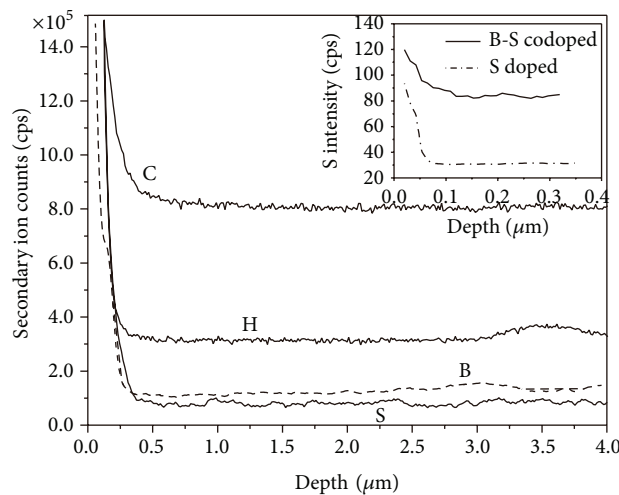


FIGURE 4: SIMS depth profile of various elements of doped diamond thin films. The inset showed the concentration of sulfur of B-S codoped and S lone doped films.

films on Si and HTHP diamond substrates. The study of the local conductivity characteristics is expected to provide essential information for the development of a controlled process and the improvement of crystalline perfection. STM measurements were carried out with air-based AFM under a tip bias of 1-2 V with a tip current of 0.1-1 nA. The surface of the diamond was connected to ground with silver paint.

### 3. Results and Discussion

Figures 1 and 2 show AFM images of films on HTHP diamond and Si substrates with B-S codoping ((a) S/C = 0.001, B/S = 0.01; (b) S/C = 0.005, B/S = 0.02). Figure 1(a) shows well-developed, randomly oriented polycrystalline facets with an average crystal size of 10-50 nm grown on

HTHP diamond substrates. The film was flat with a roughness of approximately 1.8 nm. As shown in Figure 1(b), the grain size of this film was about 5-20 nm, and the roughness of this film was approximately 1.6 nm. Figure 2(a) shows that the film grown on the Si substrate consisted of large grains with a high fraction of grain boundaries. The grain size of this film was about 100 nm. The roughness of this film was approximately 18.5 nm, which was due to the successive secondary nucleation. Figure 2(b) shows that the film has relatively small grains with about 50 nm, and the roughness of this film was approximately 16 nm. The comparison of (a) in Figures 1 and 2 and (b) in Figures 1 and 2 shows that the addition of sulfur and boron can decrease the grain size. The increase of boron content can improve the crystal quality and the surface morphology significantly.

Figure 3 showed the temperature dependency of the resistivity of B-S codoped diamond films deposited on different

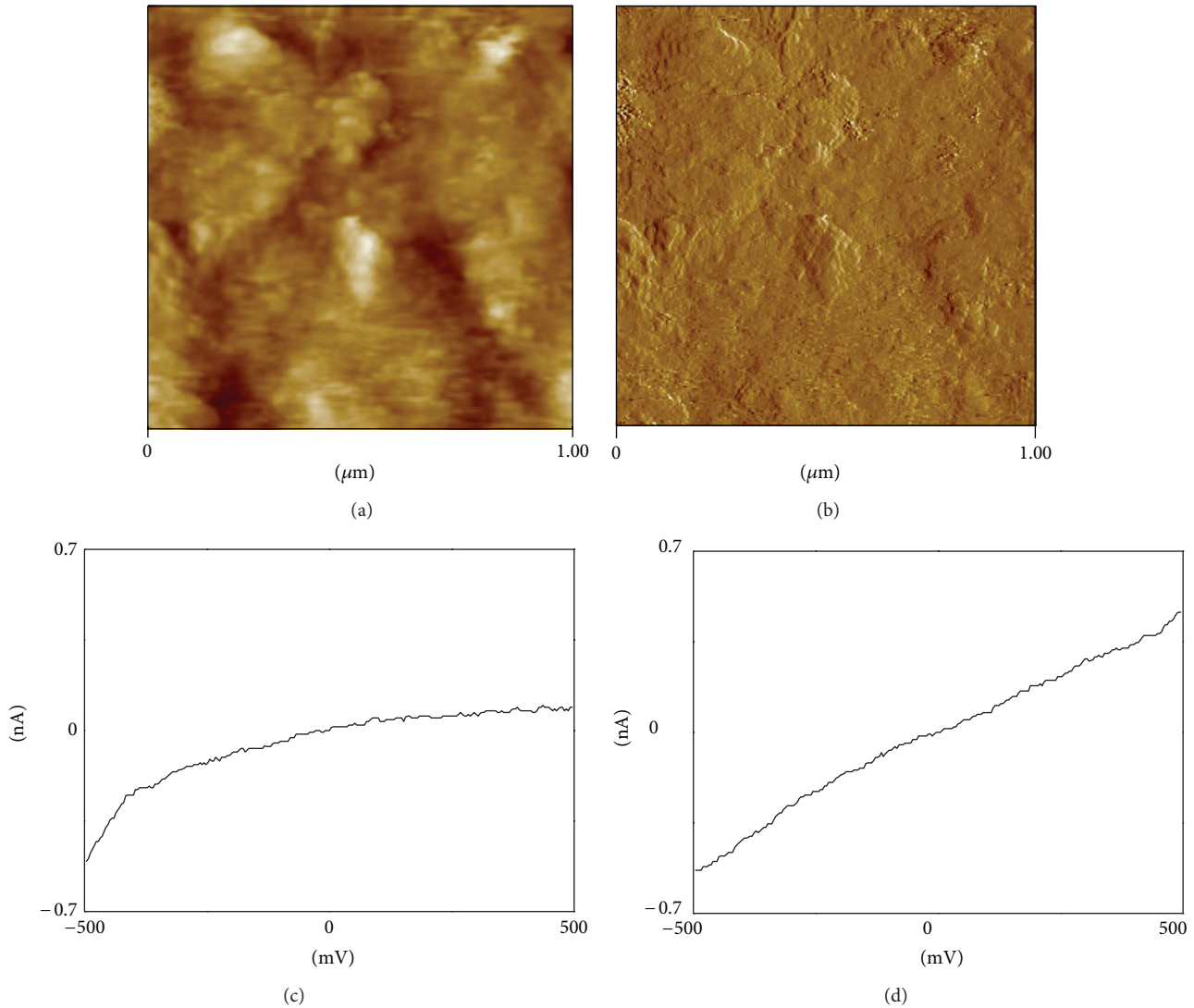


FIGURE 5: (a) STM and (b) CITS images for B-S codoped diamond on a Si substrate with S/C = 0.001 and B/S = 0.01. The  $I-V$  characteristics were obtained at low (c) and high (d) emission points.

substrate with a temperature range of 300–650 K. As shown in Figure 3, the linear relationship between  $\ln(\rho)$  and the inverse temperature indicated that the conductivity of the films was thermally activated. For the films deposited on silicon substrate, the activated energies of conductivity were determined to be 0.16 eV. But for the films deposited on diamond substrate, the activated energies of conductivity decreased to 0.07 eV. This indicated that conductivity of homoepitaxial films is better than that of heteroepitaxial films.

SIMS analyses confirmed that the sulfur was successfully introduced into diamond lattice. Figure 4 showed the SIMS spectrum from codoped sample with a B/S ratio of 0.01 and the surface of the film consisting of sulfur atoms, boron atoms, and hydrogen atoms. From the inset shown in Figure 4, the sulfur concentration of B-S codoped diamond films can increase by almost one order of magnitude of S doped diamond films. This indicated that the addition of boron facilitated sulfur incorporation into diamond.

Figure 5 shows the STM and CITS images for diamond films on a silicon substrate with B-S codoping (S/C = 0.001, B/S = 0.01). This image was taken with a sample bias and a tunneling current of 1.61 V and 0.10 nA, respectively. Small secondary grains or cluster grains with an average size less than 10 nm were observed in Figure 5(a). These small grains were observed in all crystalline facets and indicated continuous secondary nucleation during CVD processing. Figure 5(b) shows the corresponding CITS image of the sample shown in Figure 5(a). The white regions indicate the relatively high current area, and the black regions indicate low emission. High electron emission was observed only at some grain boundaries. These results are in agreement with the results of Frolov et al. [9]. The local  $I-V$  characteristics at high and low electron emission positions are also shown in Figures 5(c) and 5(d). It can be seen that the tunneling current at grain boundaries is larger than the current at specific facets. The result shows that the emission efficiency at the grain

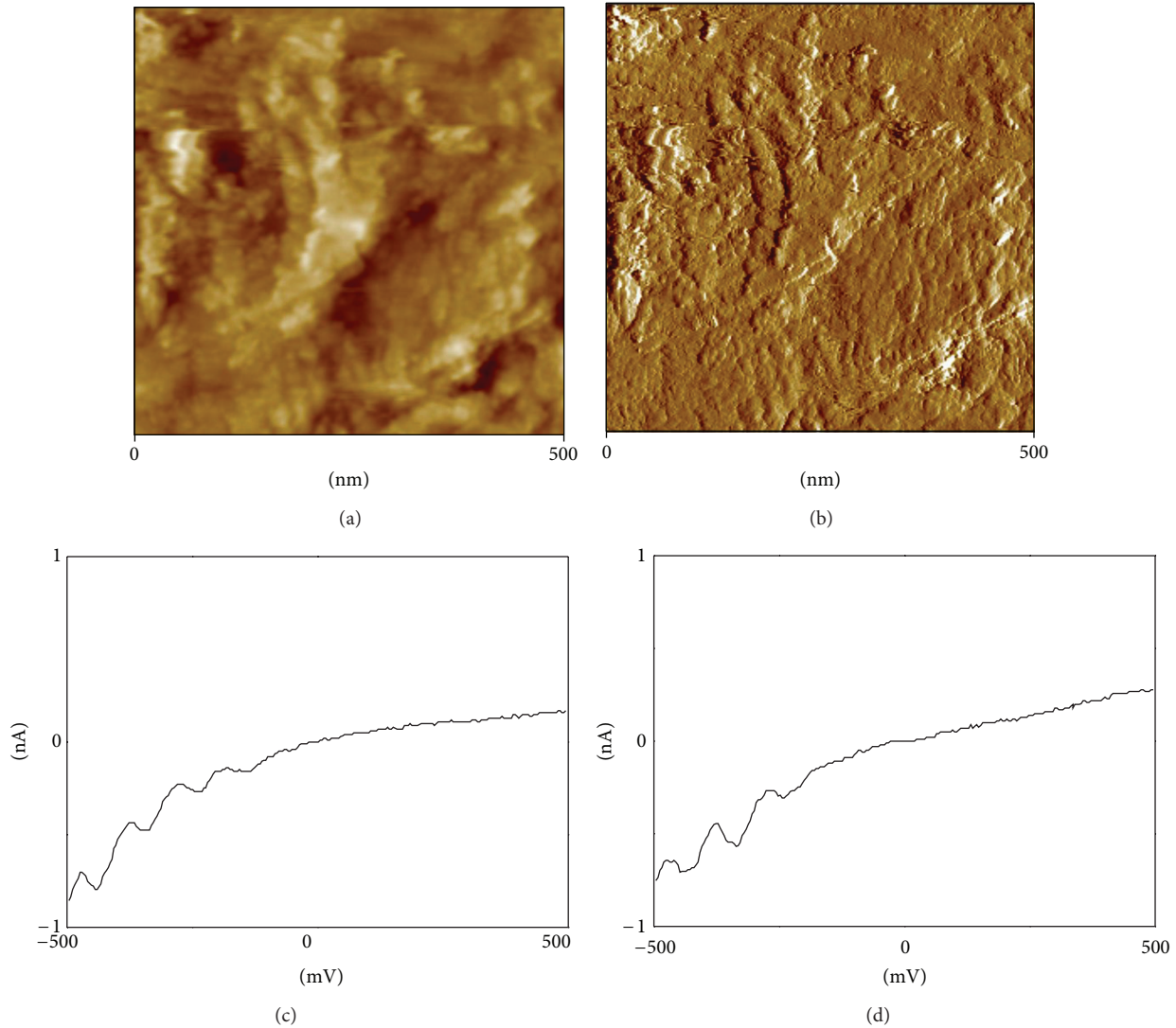


FIGURE 6: (a) STM and (b) CITS images for B-S codoped diamond on a Si substrate with S/C = 0.005 and B/S = 0.02. The  $I$ - $V$  characteristics were obtained at different points ((c) and (d)).

boundary is higher than the efficiency in the grain facet. This is probably due to the heterogeneity in the composition or defects at the grain boundary. Both results show the typical nonlinear behavior for the tunneling current. Figure 6 shows the STM and CITS images for diamond films on a silicon substrate with B-S codoping (S/C = 0.005, B/S = 0.02). Small grains with an average size less than 5 nm were observed in Figure 6(a). The local  $I$ - $V$  characteristics are also shown in Figures 6(c) and 6(d). In these figures, it can be seen that the electrical conductivity of the diamond film increases with the increase of the boron-doping concentration. The tunneling current at a negative voltage applied to the sample is larger than the current at a positive voltage, which indicates that the diamond film has n-type conductivity [10, 11].

The STM and CITS images of boron-sulfur codoped diamond deposited on an HTHP diamond substrate are shown in Figure 7. Those images were taken with a sample bias and a tunneling current of 2.15 V and 0.11 nA,

respectively. It is noted that the average size of grain deposited on HTHP diamond was approximately 40–70 nm. Figure 7(b) shows the corresponding CITS image of the sample in Figure 7(a). No significant difference in the emission efficiency was observed between the crystalline facets and the grain boundaries. Therefore, it indicates that the growth of homoepitaxial diamond film could improve the crystal quality and the crystal perfection. The local  $I$ - $V$  characteristics are also shown in Figures 7(c) and 7(d). In these figures, it can be seen that the tunneling current at a negative voltage is also larger than that at a positive voltage, which indicates that the diamond film has an n-type electronic conductivity.

#### 4. Conclusions

The structure and the electron field emission properties of boron-sulfur codoped diamond films on HTHP diamond

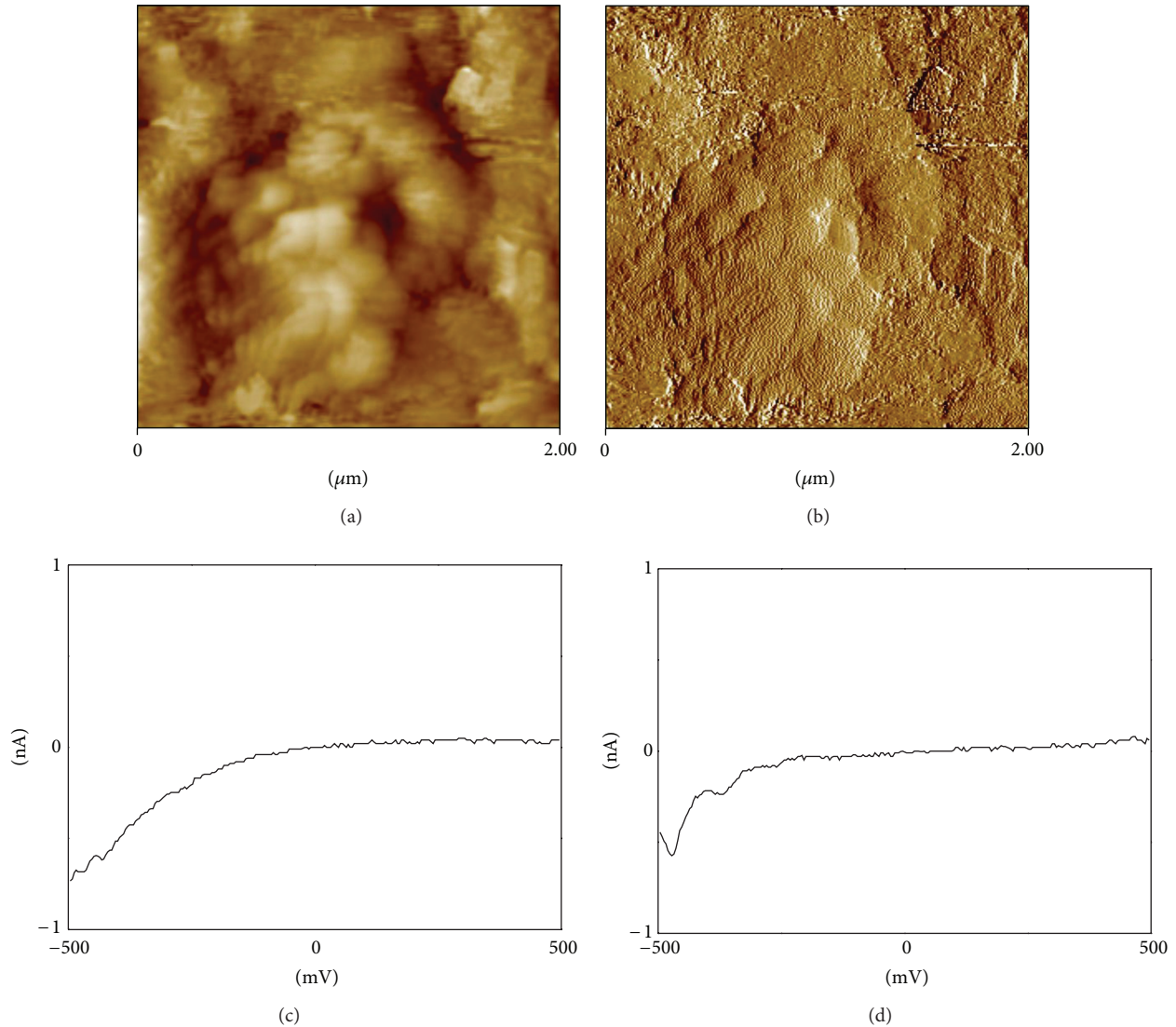


FIGURE 7: (a) STM and (b) CITS images of B-S codoped diamond film on HTHP diamond substrate under the condition of  $S/C = 0.001$  and  $B/S = 0.01$ . The  $I-V$  characteristics were obtained at different points ((c) and (d)).

substrates and Si substrates were investigated. It shows that the crystal grain size and the surface roughness of homoepitaxial diamond films were much smaller than those of heteroepitaxial diamond films, and films deposited on Si substrates had more grain boundaries than those deposited on HTHP diamond substrates. The electronic field emission efficiency at the grain boundaries is larger than that in the crystalline facets. The electronic structure was identified as an n-type electronic structure at the surface of films grown with sulfur and limited amount of boron.

### Conflict of Interests

The authors declare that there is no conflict of interests regarding the publication of this paper.

### Acknowledgments

This work was supported by the National Natural Science Foundation of China (Grant nos. 51072113 and 10804071) and the Shanghai Outstanding Academic Leaders Project Funding (12XD1420700) and the Innovation Program of Shanghai Municipal Education Commission (13ZZ143).

### References

- [1] F. Brunt, P. Germi, M. Pernet, A. Deneuve, E. Gheeraert, and J. Mambou, "Effect of boron incorporation on the structure of polycrystalline diamond films," *Diamond and Related Materials*, vol. 6, no. 5–7, pp. 774–777, 1997.
- [2] M. S. Katagiri, J. Isoya, S. Koizumi, and H. Kanda, "Lightly phosphorus-doped homoepitaxial diamond films grown by

- chemical vapor deposition,” *Applied Physics Letters*, vol. 85, no. 26, pp. 6365–6367, 2004.
- [3] C. E. Sally, B. A. Alfred, C. A. John, E. E. Yulia, and V. P. Yuri, “Diamond growth in the presence of boron and sulfur,” *Diamond and Related Materials*, vol. 12, no. 10-11, pp. 1627–1632, 2003.
- [4] I. Sakaguchi, M. Nishitani-Gamo, Y. Kukuchi et al., “Sulfur: a donor dopant for n-type diamond semiconductors,” *Physical Review B*, vol. 60, no. 4, pp. R2139–R2141, 1999.
- [5] H. Katayama-Yoshida, T. Nishimatsu, T. Yamamoto, and N. Orita, “Codoping method for the fabrication of low-resistivity wide band-gap semiconductors in p-type GaN, p-type AlN and n-type diamond: prediction versus experiment,” *Journal of Physics Condensed Matter*, vol. 13, no. 40, pp. 8901–8914, 2001.
- [6] M. Cannaearts, M. Nesladek, Z. Reme, and L. M. Stals, “Scanning tunneling microscopy and spectroscopy of non-doped, hydrogen terminated CVD diamond,” *Physica Status Solidi A*, vol. 181, no. 1, pp. 77–81, 2000.
- [7] S. Y. Chen, M. Y. Lee, C. S. Chen, and J. T. Lue, “The mechanism of field emission for diamond films studied by scanning tunneling microscopy,” *Physics Letters A*, vol. 313, no. 5, pp. 436–441, 2003.
- [8] H.-F. Cheng, Y.-C. Lee, S.-J. Lin, Y.-P. Chou, T. T. Chen, and I.-N. Lin, “Current image tunneling spectroscopy of boron-doped nanodiamonds,” *Journal of Applied Physics*, vol. 97, no. 4, Article ID 044312, 2005.
- [9] V. D. Frolov, A. V. Karabutov, V. I. Konov, S. M. Pimenov, and A. M. Prokhorov, “Scanning tunnelling microscopy: application to field electron emission studies,” *Journal of Physics D: Applied Physics*, vol. 32, no. 7, pp. 815–819, 1999.
- [10] W. Kaiser, L. Bell, M. Hecht, and F. Grunthner, “Scanning tunneling microscopy characterization of the geometric and electronic structure of hydrogen-terminated silicon surfaces,” *Journal of Vacuum Science & Technology A*, vol. 6, pp. 519–523, 1988.
- [11] M. Ito, K. Murato, K. Aiso, M. Hori, T. Goto, and M. Hiramatsu, “Scanning tunneling microscopic and spectroscopic characterization of diamond film prepared by capacitively coupled radio frequency CH<sub>3</sub>OH plasma with OH radical injection,” *Applied Physics Letters*, vol. 70, no. 16, pp. 2141–2143, 1997.

## Research Article

# Microstructure Changes of Ti-Al-C Films Deposited by Filtered Cathodic Vacuum Arc

Xianjuan Pang,<sup>1,2,3</sup> Xiaoqiang Liu,<sup>2</sup> and Bo Jin<sup>2</sup>

<sup>1</sup> School of Chemical Engineering and Pharmaceutics, Henan University of Science and Technology, No. 263 Kaiyuan Road, Luoyang 471023, China

<sup>2</sup> State Key Laboratory of Solid Lubrication, Lanzhou Institute of Chemical Physics, Chinese Academy of Sciences, Lanzhou 730000, China

<sup>3</sup> Henan Key Laboratory of Materials Tribology, Luoyang 471003, China

Correspondence should be addressed to Xianjuan Pang; xjpang2001@haust.edu.cn

Received 5 March 2014; Accepted 2 April 2014; Published 24 April 2014

Academic Editor: Jinlong Jiang

Copyright © 2014 Xianjuan Pang et al. This is an open access article distributed under the Creative Commons Attribution License, which permits unrestricted use, distribution, and reproduction in any medium, provided the original work is properly cited.

Nanocomposite Ti-Al-C films were deposited by filtered cathodic vacuum arc (FCVA) at different CH<sub>4</sub> flows. The deposited films were characterized in terms of elemental and phase compositions, chemical bonds, and texture as a function of CH<sub>4</sub> flow rate by XRD, XPS, HRTEM, Raman spectroscopy, and IR spectroscopy. The results show that the TiC grain size decreases from 4.2 to 2.9 nm as the CH<sub>4</sub> flow rate increases from 30 to 80 sccm. The analysis of XPS, HRTEM, and Raman spectroscopy shows that the microstructure of deposited films turns from a TiC dominant TiC-C film to a carbon network dominant TiAl-doped a-C film structure as the CH<sub>4</sub> flow increases from 30 sccm to 80 sccm. IR spectroscopy shows that most of the hydrogen atoms in the deposited films are bonded to the sp<sup>3</sup>-hybridized C atoms. All the composition and microstructure change can be explained by considering the plasma conditions and the effect of CH<sub>4</sub> flow.

## 1. Introduction

Advanced methods in surface technologies, providing new thin film materials with multifunctional properties, are demanded with progress in future engineering applications in tribology, machining, and manufacturing processes. For example, applications in tribology or machining of steels and alloys require coatings combining low friction coefficient, high hardness, and chemical and high temperature stability. These requirements of multifunctionality of the surface of components and/or tools could be met by applying improved coating concepts like metastable, multilayer, gradient, and nanocomposite PVD coatings [1]. In particular, nanostructured coatings, which consist of hard and solid lubricant phases, have attracted increasing interest because of the possibilities of synthesizing materials with unique mechanical and physical properties [2].

Graphite is one of typical solid lubricants of great technological interests. Carbon thin film deposition technology has reached an advanced status on its way from first laboratory

results to commercially available products from soft graphite-like to hard amorphous and super hard diamond-like films. Diamond-like carbon coatings offer outstanding physico-chemical properties such as relatively high hardness, chemical inertness, high wear resistance, and low friction coefficient [3]. However, there are still several problems, such as low toughness and high internal stress, which limits a-C:H films being used in a wide range of industrial applications [3–6]. Many studies have demonstrated that mono- and/or codoping some metal and nonmetal elements into a-C:H films can effectively reduce internal stress and improve mechanical and tribological properties [1, 6–8].

Filtered cathodic vacuum arc (FCVA) deposition is a promising technique for the production of high quality hard thin films, the main feature of which is to employ a curved magnetic field to guide the plasma generated from the cathodic vacuum arc to deposit on an out-of-sight substrate. Through this special magnetic filter, most of the unwanted macroparticles and neutral atoms will be removed. Only ions within a defined energy range can reach the substrate, thus

TABLE 1: Summary of the films deposition conditions.

Item	Parameter
CH <sub>4</sub> gas flow rate (sccm)	30, 40, 50, 60, 70, 80
Ar gas flow rate (sccm)	120
Deposition pressure (Pa)	0.54~0.70
Thickness ( $\mu\text{m}$ )	1.5
Arc current (A)	80

producing films with good controllability and reproducibility [9–11].

In this paper, Ti-Al-C ternary nanocomposite films were deposited by FCVA, TiAl target being used as cathode at the methane and argon atmosphere. The investigations were mainly focused on the change of microstructure in the deposited films as a function of CH<sub>4</sub> flow rate.

## 2. Experiment

The Ti-Al-C films were deposited by the FCVA technique. It employs a 90° curved filter to remove the macroparticles. Titanium aluminum cylindrical composite target (TiAl (70/30 at.)) was used to generate plasma with 65 mm in diameter. A rotated substrate holder was placed normal to the arc plasma beam at a distance of 10 cm from the exit of the FCVA source. The deposition conditions are detailed in Table 1. The vacuum chamber with 900 mm in diameter was evacuated to the base pressure less than  $3.2 \times 10^{-3}$  Pa, which was then backfilled with methane and argon at a pressure of ~0.6 Pa for depositing the films. A Si *n*(100) wafer was used for the substrate. Prior to deposition, the silicon substrates were sputtered by an Ar ion beam for 10 min at a pulsed substrate negative bias voltage of -700 V, to remove some adhering impurities and the native oxide layer on substrates. Subsequently, the films were deposited at a pulsed substrate negative bias voltage of -100 V and varied the CH<sub>4</sub> flow.

The microstructure and grain size are determined by X-ray diffraction (XRD) with a Philips X'pert diffractometer operated with Cu K $\alpha$  radiation in a glancing incident configuration ( $\theta = 1^\circ$ ). After ruling out influence of instrumental broadening the average grain size (*D*) of film is calculated from the full width at half maximum (FWHM) of the TiC(111) peak using Scherrer's formula [12]:

$$D = \frac{k\lambda}{B \cos \theta}, \quad (1)$$

where constant  $k = 0.89$ , *B* is the FWHM (degree),  $\lambda$  is the wavelength (nm), and  $\theta$  is the diffraction angle (degree).

High-resolution transmission electron microscopy (HRTEM) investigations and selected area diffraction (SAD) were performed on a JEM 2010 transmission electron microscope operated at 200 kV. About 20 nm thick films were produced on single crystals of NaCl for HRTEM investigations. Plan-view samples were made by floating off the films in distilled water and placing them on Cu grids.

The chemical composition of the films was determined by X-ray photoelectron spectroscopy analysis using a PHI-5702 X-ray photoelectron spectroscope (XPS) operating with

monochromatized Al K $\alpha$  radiation. After the removal of adventitious contamination corresponding to about 2 nm of carbon by ion sputter cleaning (4 KeV Ar<sup>+</sup>), the elemental composition was measured from the peak areas of Ti2*p*, Cls, and Alls. Using the built-in sensitivity factors, the concentrations were determined from the respective areas. Analysis of the peak shapes using curve fitting on the Ti2*p*<sub>3/2</sub> and Cls peaks with carefully chosen profiles allowed the separation of TiC and a-C:H phases at different methane flow for details.

Raman spectra were performed on a Horiba Jobin Yvon HR800 spectrometer at room temperature using the 532 nm line of an Ar laser as the excitation source. Moreover, the Raman spectra were recorded in the range of 200–2000 cm<sup>-1</sup> and special care was taken to avoid sample damage during measurements. Fourier transformation infrared (FTIR) spectra of deposited films were recorded on an IFS 66v/s spectrometer so as to detect the changes of the hydrogen bonding in the films.

## 3. Results and Discussion

**3.1. Composition.** Table 2 plots the variation of the Ti, Al, and C atomic ratios versus the applied methane flow during the deposition. It can be found that the content of Al changes slightly while the Ti concentration shows a decrease from 25.32 at.% to 11.92 at.% with increasing CH<sub>4</sub> flow rate from 30 sccm to 80 sccm. This is attributed to the poisoning effect; namely, with increasing CH<sub>4</sub> flow, the Ti cathode was poisoned and a compound layer of TiC was formed on the target surface. Meanwhile, Al belongs to weaker-carbide-forming metal, which is relatively difficult to form Al-C on the target surface. TiC has a significantly higher melting point (3150°C) comparing with the TiAl cathode (melting point of Ti 1660°C), which affects the plasma emission from the arc spots, resulting in reduction in the concentration of Ti and the slight change of Al concentration in deposited films. By contrast, the carbon concentration increased with an increase in the flow rate, a clear evidence of the poisoning effect. Meanwhile, an increasing CH<sub>4</sub> flow enhances deposition of carbon; therefore, the C concentration increases from 58.75 at.% to 68.80 at.% with increasing CH<sub>4</sub> flow from 40 sccm to 50 sccm. After that, with CH<sub>4</sub> flow further increasing the C concentration changed slightly, which is due to the balance of plasma [2].

**3.2. Structure of Deposited Films.** XRD experiment is performed to identify the microstructure of deposited films and the results are presented in Figure 1(a). The peak around 55° is from the Si (100) substrate underneath the film. Peaks at 35.4, 41.0, and 59.6° are attributed to (111), (200), and (220) diffraction planes of TiC [1, 13–16]. All these patterns exhibit relatively broad peaks.

The grain size of the nanocrystalline component is essential for the understanding of the nanostructure and hence of the properties of nanocomposite hard films. It was routinely evaluated from the XRD peak broadening taking the full width at half maximum (FWHM) of the TiC (111) peak in the Scherrer formula. The data were corrected for instrumental

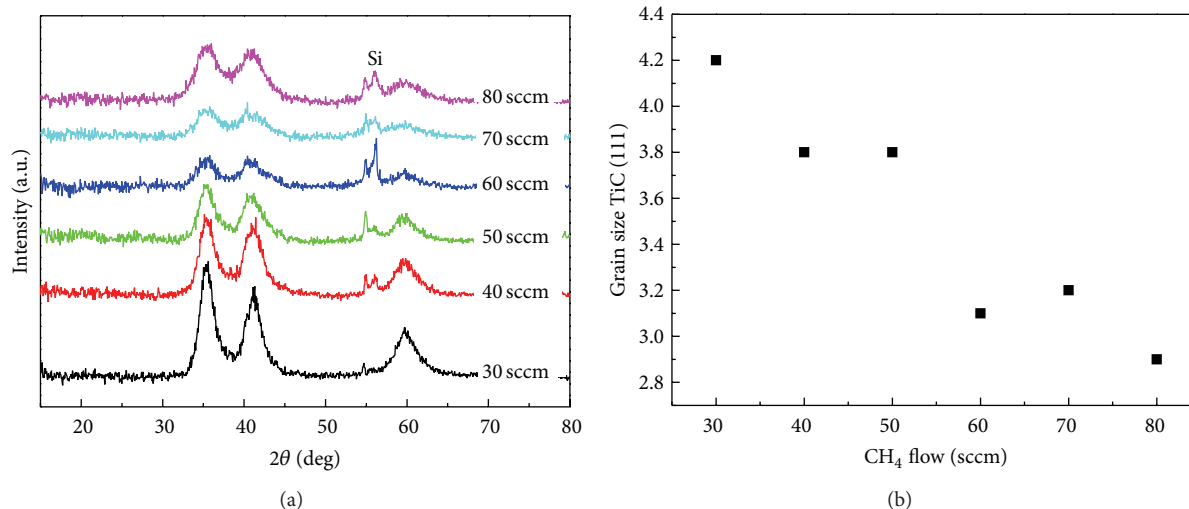


FIGURE 1: (a) The XRD spectra of the films prepared at different CH<sub>4</sub> flow; (b) the grain size of deposited films as a function of the CH<sub>4</sub> flow.

TABLE 2: Chemical composition: Ti/Al, Al/(Ti + Al), and C/(Ti + Al) atomic concentration ratios of deposited Ti-Al-C films.

	Elemental composition (at.%)				Ti/Al	Al/(Ti + Al)	C/(Ti + Al)
	Ti	Al	C				
30 sccm	25.32	15.89	58.79	1.59	0.39	1.43	
40 sccm	21.95	19.29	58.75	1.14	0.47	1.42	
50 sccm	14.16	17.04	68.80	0.83	0.41	2.21	
60 sccm	14.86	15.83	69.31	0.94	0.52	2.26	
70 sccm	13.01	15.93	71.07	0.82	0.55	2.46	
80 sccm	11.92	17.81	70.26	0.67	0.58	2.36	

broadening. The evolution of the grain size with CH<sub>4</sub> flow, obtained from this method, is displayed in Figure 1(b). It can be found that the grain size decreases from 4.2 to 2.9 nm as the CH<sub>4</sub> flow rate increases from 30 to 80 sccm.

A comparison of these values with data obtained from HRTEM shows that the values obtained from XRD agree reasonably well. This is illustrated in Figure 2 showing the HRTEM and SAED micrographs of the films. Indexing the lattice fringes and also the circular selected area diffraction patterns confirms the formation of TiC nanocrystalline phases.

The interplanar spacing of TiC (311) plane is about 0.13 nm, shown in Figure 2(a). The diffraction rings shown in Figure 2(b) are attributed to (111), (200), and (220) planes of TiC. In Figure 2, it shows fine-grained TiC crystals of about 5 nm in the case of films deposited at 30 sccm of CH<sub>4</sub> flow rate and a reduced quantity and grain size smaller than 5 nm in the case of films deposited at 50 sccm of CH<sub>4</sub> flow rate. It also clearly shows, on the one hand, many small TiC crystallites represented by the lattice fringes of TiC and, on the other hand, some areas not contributing to the imaging in the electron microscope. These areas could be interpreted to be an amorphous carbon phase, as is expected from the chemical composition of the coatings. It can be inferred that nanocomposite coatings have a two-phase microstructure, built of a nanocrystalline TiC phase and an amorphous

carbon phase. However, the microstructure of the films changes from TiC-based structure to C-based structure in which the nanocrystalline TiC particles are homogeneously embedded in the a-C:H matrix, as the CH<sub>4</sub> flow rate increases from 30 sccm to 50 sccm.

**3.3. Raman Spectroscopy and XPS Analysis.** The application of Raman spectroscopy enables the interpretation of the bonding in the deposited films. Figure 3 shows the Raman spectra of all the films deposited at different CH<sub>4</sub> flows. It reveals two important facts. (1) In all measured films vibrational modes in the range of 450–750 cm<sup>-1</sup> indicative of titanium carbide were detected [17]. (2) C–C bonds observable as a typical camel-like shape with humps at 1360 and 1590 cm<sup>-1</sup> so-called D and G peak were detected [5–7]. The structural changes can also be seen as the CH<sub>4</sub> flow increases from 30 sccm to 80 sccm.

Further complementary information on the constitution and microstructure of these deposited films is available from XPS. The chemical states of C, Ti, Al, and O in the deposited films are analyzed by XPS as shown in Figure 4. It can be initially referred that the Cls spectra show discrimination of these two components at the binding energies of 281.6 and 284.5 eV, respectively, both of which are responding to TiC and a-C:H phases. However, the Cls spectra are different. At low CH<sub>4</sub> flow, the TiC phase is dominant,

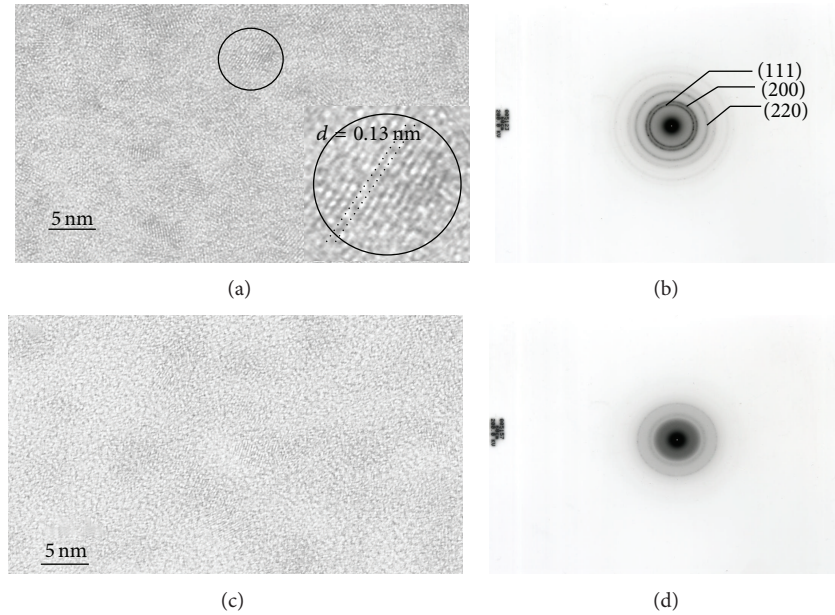


FIGURE 2: HR-TEM and SAED images of films deposited at different  $\text{CH}_4$  flow (a) and (b): 30 sccm and (c) and (d): 50 sccm.

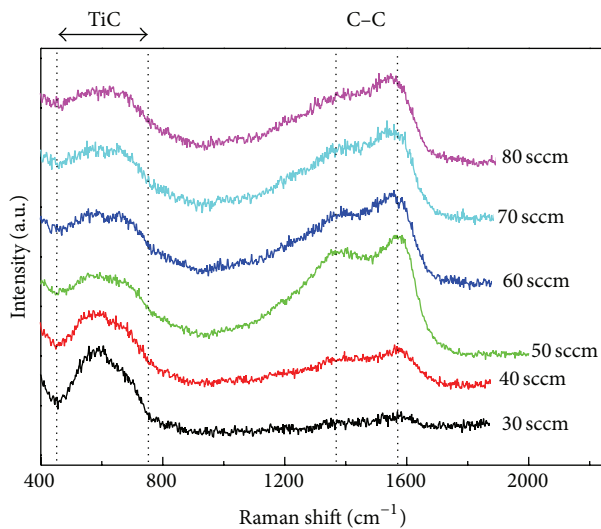


FIGURE 3: Raman spectra of the films prepared at different  $\text{CH}_4$  flow.

while the a-C:H phase changes to be dominant at higher  $\text{CH}_4$  flow, which demonstrates the structural change with increasing the  $\text{CH}_4$  flow. The same concentration profile is obtained using the  $\text{Ti}2p_{3/2}$  peak and performing curve-fitting procedures to separate the contributions from metallic and carbidic titanium. However, the difference in position of the carbide and metallic titanium is only 1.1 eV and the respective binding energies are 454.9 eV and 453.8 eV and hence the determination is less accurate than from Cls. The Cls peak can be fitted into five components around 281.6 eV, 282.6 eV,  $284.1 \pm 0.1$  eV,  $285.0 \pm 0.1$  eV, and  $286.7 \pm 0.1$  eV, in which the peaks at  $284.1 \pm 0.1$  eV and  $285.0 \pm 0.1$  eV correspond to  $\text{sp}^2$  and  $\text{sp}^3$  C-C bonds [1, 5–7], and the peak with much smaller

intensity near  $286.7 \pm 0.1$  eV is assigned to the Cls in the C–O bond. The peak at around 281.6 indicates the presence of TiC, and the peak at 282.6 eV assigned to  $\text{TiC}^*$  compared to TiC suggests additional carbon atoms in the vicinity of TiC [1, 18]. This is the case for C knocked into TiC during sputtering and at the interface of TiC and carbon phase. Combining the results of Raman, XRD, and XPS spectrum, it proves the microstructural change of the deposited films as the  $\text{CH}_4$  flow increases from 30 sccm to 80 sccm. The structure of films deposited at 30 and 40 sccm  $\text{CH}_4$  flows is TiC dominant TiC-C film, which changes to a carbon network dominant TiAl-doped a-C film as the  $\text{CH}_4$  flows up to 80 sccm.

**3.4. IR Analysis.** In order to get more structural details, IR spectroscopy is used in this sense to characterize the C–H bonding in deposited hydrogenated carbonaceous films. Figure 5 shows the IR absorption spectra of the films deposited at different  $\text{CH}_4$  flows. It can be found that the C–H absorption peaks are centered at  $2920 \text{ cm}^{-1}$ , which is associated with the asymmetric stretching mode of the hydrogen bonds in the form of  $\text{sp}^3\text{-CH}$  and  $\text{sp}^3\text{-CH}_2$ , while the two smaller shoulder peaks at  $2955 \text{ cm}^{-1}$  and  $2855 \text{ cm}^{-1}$  correspond to  $\text{sp}^3\text{-CH}_3$  asymmetric stretching mode and  $\text{sp}^3\text{-CH}_3$  symmetric model, respectively [19, 20]. This suggests that most of the hydrogen atoms in the deposited films are bonded to the  $\text{sp}^3$ -hybridized C atoms.

## 4. Conclusion

Nanocomposite Ti-Al-C films were deposited by FCVA at different  $\text{CH}_4$  flows. Two groups of deposited films can be distinguished depending on the composition and microstructure. At low  $\text{CH}_4$  flow of 30 sccm, the microstructure of the films is TiC dominant TiC-C film structure. While the  $\text{CH}_4$  flow

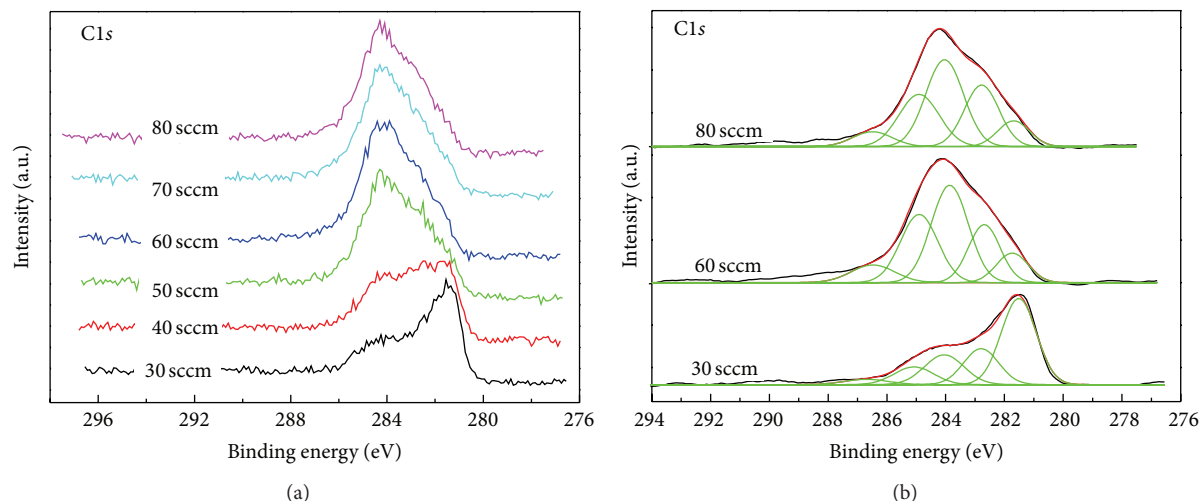


FIGURE 4: XPS C1s spectra of the films prepared at different  $\text{CH}_4$  flow.

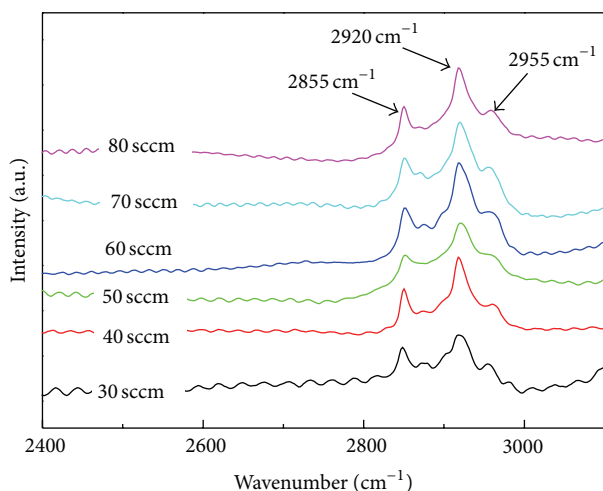


FIGURE 5: IR spectra of the films deposited at different methane flows.

increases to 80 sccm, the microstructure of deposited films changes to carbon network dominant TiAl-doped a-C film structure. The XPS and Raman results show the structural change at the  $\text{CH}_4$  flow increasing up to 50 sccm and higher flows. All the composition and microstructure change can be explained by considering the plasma conditions and the effect of  $\text{CH}_4$  flow. During the films deposition, as the  $\text{CH}_4$  flow increased, there is poisoning effect. When the poisoning effect and the plasma emission from the arc spots approach equilibrium, the arc plasma beam will be stable and the composition of the films will change slightly.

### Conflict of Interests

The authors declare that they have no competing interests regarding the publication of this paper.

### Acknowledgments

The authors gratefully acknowledge the Natural Science Foundation of China (Grant no. 50902133), the Project of the Education Department of Henan Province (14A430009), the Open Fund of State Key Laboratory of Solid Lubrication (1201), and the Fund of Henan University of Science and Technology (2013QN001).

### References

- [1] M. Stüber, H. Leiste, S. Ulrich, H. Holleck, and D. Schild, "Microstructure and properties of low friction TiC-C nanocomposite coatings deposited by magnetron sputtering," *Surface and Coatings Technology*, vol. 150, no. 2-3, pp. 218–226, 2002.
- [2] B. Yang, Z. H. Huang, H. T. Gao, X. J. Fan, and D. J. Fu, "Droplet-free TiC nanocrystal-containing diamond-like carbon coatings deposited by combined cathodic arc MF magnetron sputtering," *Surface and Coatings Technology*, vol. 201, no. 15, pp. 6808–6811, 2007.
- [3] J. Robertson, "Diamond-like amorphous carbon," *Materials Science and Engineering R: Reports*, vol. 37, no. 4–6, pp. 129–281, 2002.
- [4] I. Ahmad, S. S. Roy, M. A. Rahman, T. I. T. Okpalugo, P. D. Maguire, and J. A. McLaughlin, "Substrate effects on the microstructure of hydrogenated amorphous carbon films," *Current Applied Physics*, vol. 9, no. 5, pp. 937–942, 2009.
- [5] X. Pang, L. Shi, P. Wang, Y. Xia, and W. Liu, "Effects of Al incorporation on the mechanical and tribological properties of Ti-doped a-C:H films deposited by magnetron sputtering," *Current Applied Physics*, vol. 11, no. 3, pp. 771–775, 2011.
- [6] J. L. Jiang, Q. Wang, H. Huang, Y. B. Wang, X. Zhang, and J. Y. Hao, "Microstructure and property changes induced by substrate rotation in titanium/silicon dual-doped a-C:H films deposited by mid-frequency magnetron sputtering," *Surface and Coatings Technology*, vol. 240, pp. 419–424, 2014.
- [7] J. L. Jiang, H. Huang, Q. Wang, W. J. Zhu, J. Y. Hao, and W. M. Liu, "Comparative study on structure and properties of titanium/silicon mono- and co-doped amorphous carbon films

- deposited by mid-frequency magnetron sputtering,” *Surface and Interface Analysis*, vol. 46, no. 3, pp. 139–144, 2014.
- [8] A.-Y. Wang, K.-R. Lee, J.-P. Ahn, and J. H. Han, “Structure and mechanical properties of W incorporated diamond-like carbon films prepared by a hybrid ion beam deposition technique,” *Carbon*, vol. 44, no. 9, pp. 1826–1832, 2006.
- [9] X.-Z. Ding, B. K. Tay, H. S. Tan, S. P. Lau, W. Y. Cheung, and S. P. Wong, “Preferential orientation of titanium carbide films deposited by a filtered cathodic vacuum arc technique,” *Surface and Coatings Technology*, vol. 138, no. 2-3, pp. 301–306, 2001.
- [10] Y. H. Cheng, B. K. Tay, S. P. Lau, and X. Shi, “Influence of substrate bias on the structure and mechanical properties of ta-C: W films deposited by filtered cathodic vacuum arc,” *Surface and Coatings Technology*, vol. 146-147, pp. 398–404, 2001.
- [11] Y. H. Wang, X. Zhang, X. Y. Wu, H. Zhang, and X. Zhang, “Compositional, structural and mechanical characteristics of nc-TiC/a-C:H nanocomposite films,” *Applied Surface Science*, vol. 255, no. 5, pp. 1801–1805, 2008.
- [12] Y. H. Wang, X. Zhang, X. Y. Wu, H. Zhang, and X. Zhang, “Effect of filter coil current on properties of nc-TiC/a-C:H nanocomposite film prepared by dual plasma technique,” *Surface Review and Letters*, vol. 14, no. 6, pp. 1143–1148, 2007.
- [13] H. L. Wang, S. Zhang, Y. B. Li, and D. Sun, “Bias effect on microstructure and mechanical properties of magnetron sputtered nanocrystalline titanium carbide thin films,” *Thin Solid Films*, vol. 516, no. 16, pp. 5419–5423, 2008.
- [14] E. Lewin, E. Olsson, B. André et al., “Industrialisation study of nanocomposite ncTiC/a-C coatings for electrical contact applications,” *Plasma Processes and Polymers*, vol. 6, no. 1, pp. S928–S934, 2009.
- [15] H.-X. Liu, X.-F. Wang, L.-P. Wang, and B.-Y. Tang, “Rolling contact fatigue and mechanical properties of titanium carbide film synthesized on bearing steel surface,” *Surface and Coatings Technology*, vol. 201, no. 15, pp. 6606–6610, 2007.
- [16] C. Corbella, E. Pascual, G. Oncins, C. Canal, J. L. Andújar, and E. Bertran, “Composition and morphology of metal-containing diamond-like carbon films obtained by reactive magnetron sputtering,” *Thin Solid Films*, vol. 482, no. 1-2, pp. 293–298, 2005.
- [17] J. Soldán and J. Musil, “Structure and mechanical properties of DC magnetron sputtered TiC/Cu films,” *Vacuum*, vol. 81, no. 4, pp. 531–538, 2006.
- [18] D. E. Wolfe and J. Singh, “Titanium carbide coatings deposited by reactive ion beam-assisted, electron beam-physical vapor deposition,” *Surface and Coatings Technology*, vol. 124, no. 2-3, pp. 142–153, 2000.
- [19] H. X. Li, T. Xu, J. M. Chen, H. Zhou, and H. Liu, “Preparation and characterization of hydrogenated diamond-like carbon films in a dual DC-RF plasma system,” *Journal of Physics D: Applied Physics*, vol. 36, no. 24, pp. 3183–3190, 2003.
- [20] P. Wang, X. Wang, Y. M. Chen, G. Zhang, W. Liu, and J. Zhang, “The effect of applied negative bias voltage on the structure of Ti-doped a-C:H films deposited by FCVA,” *Applied Surface Science*, vol. 253, no. 7, pp. 3722–3726, 2007.

## Research Article

# Nanopolycrystalline Diamond Sintered from Onion-Like Carbon

**Qin Zou, Ming-Zhi Wang, Wen Gong, Qiang-Hua Yu, Yan-Guo Li, and Yu-Cheng Zhao**

*State Key Laboratory of Metastable Materials Science and Technology, College of Mechanical Engineering, Yanshan University, Qinhuangdao Hebei 066004, China*

Correspondence should be addressed to Ming-Zhi Wang; [zq@ysu.edu.cn](mailto:zq@ysu.edu.cn)

Received 17 December 2013; Revised 15 March 2014; Accepted 16 March 2014; Published 24 April 2014

Academic Editor: Jinlong Jiang

Copyright © 2014 Qin Zou et al. This is an open access article distributed under the Creative Commons Attribution License, which permits unrestricted use, distribution, and reproduction in any medium, provided the original work is properly cited.

The onion-like carbons (OLCs) annealed at 900–1400°C were used as raw materials to synthesize additive-free D-D type nanopolycrystalline diamond (nPCD) compacts in the industrial sintering conditions of 5.5 GPa, 1200°C, and 15 min. The results showed that the OLCs were transformed into additive-free D-D type nPCD compacts in industrial sintering conditions. The nPCD compacts contained a large number of nanotwins. The purities and performances of nPCD compacts were homogeneous in three dimensions. The purity and physical and mechanical performances of the nPCD compact (denoted as nPCD<sub>11</sub>) sintered from the OLCs annealed at 1100°C were the highest. The average Vickers hardness, density, and nanodiamond grain size of nPCD<sub>11</sub> were 32 GPa, 2.7 g/cm<sup>3</sup>, and 12 nm. During sintering process, the graphite layers of OLCs ruptured from inside toward outside forming larger nanodiamond particles. At the same time, the OLCs bonded adjacent to OLCs forming additive-free D-D type nPCD compacts.

## 1. Introduction

Presently, polycrystalline diamond (PCD) compacts are mainly fabricated using microdiamond as the starting material. Furthermore, catalysts are must be added in the starting material [1]. For example, the forming carbide element catalysts of Si and Ti [2] or catalytic metals of Co and Ni [3, 4] are generally used. In this case, the sintering pressures and temperatures of the PCD compacts usually reach 5.0–6.5 GPa and 1400–1600°C. Recently, some researchers [5, 6] also have successfully fabricated PCD compacts using nonmetal catalysts, such as FeTiO<sub>3</sub>, Fe<sub>2</sub>SiO<sub>4</sub>, Y<sub>3</sub>Fe<sub>5</sub>O<sub>12</sub>, and CaCO<sub>3</sub>. In this case, the sintering pressure and temperatures of the PCD compacts commonly reach 7.5–8.5 GPa and 1800–2300°C. However, catalysts are easy to remain in PCD compact. And Si and Ti catalysts are easy to form carbide of SiC and TiC [7–10]. The physical and mechanical performances of these catalysts and carbide are not as good as those of diamond, resulting in the existence of weak phase in PCD compacts, which further influences their performances and processing abilities [11, 12].

Synthesis of additive-free diamond-diamond (D-D) type PCD compact is a fundamental way to solve the above problem. Some researchers [13] have tried to fabricate additive-free PCD compacts using graphite, microdiamond, or nanodiamond as the starting materials. Even though additive-free PCD compacts have been successfully fabricated, the sintering pressure and temperatures usually reach 12–25 GPa and 1800–2500°C, which are very difficult to be achieved for the current industrial sintering apparatus. Scientists in this field have been working on finding new raw materials for sintering additive-free PCD compact in industrial conditions. The discovery of onion-like carbon (OLC) makes this research possible. OLC is one member of the fullerene family. Its exterior shape is polyhedral and its interior structure is similar to that of onion. Its interlayer distance is usually 0.34 nm, which is close to that of graphite. The innermost diameter of OLC is about 0.7 nm, which is close to that of C<sub>60</sub> [14]. OLC composes of both sp<sup>3</sup> diamond structure and sp<sup>2</sup> graphite structure, which can be transformed into each other under certain conditions.

In [15], Tomita et al. obtained diamond film by annealing OLC at the temperature of 500°C in the air. The OLC was fabricated by annealing detonation nanodiamond (average grain size was about 5 nm) at 1700°C. This research proves that diamond can be synthesized using OLC as starting material without any catalysts in conditions of very low temperature of 500°C and atmospheric pressure. However, in Tomita's work, only diamond film is prepared because there is no three-dimensional pressure applied during the transformation process of diamond from OLC, that is, there is no pressure for diamond growth in three dimensions. If a three-dimensional pressure is applied during the transformation process, OLC can be transformed into diamond and form diamond compact.

In this work, additive-free D-D type nanopolycrystalline diamond (nPCD) compacts were sintered from onion-like carbons (OLCs) annealed at 900–1400°C and 1 Pa in industrial conditions of 5.5 GPa, 1200°C, and 15 min. The microstructures, purities, and performances of the nPCD compacts were characterized. Based on the results, the formation mechanisms of the additive-free D-D type nPCD compacts sintered from OLCs in industrial conditions were discussed.

## 2. Experimental Details

The nanodiamond (average grain size was approximated to be 5 nm) used in this work was fabricated by means of detonation [16–18]. OLCs were prepared in volume by annealing the detonation nanodiamond at the temperatures and pressure of 900–1400°C and 1 Pa, which had been reported detailedly in our previous papers [19–23].

The sintering experiments of additive-free D-D type nPCD compacts from OLCs were carried out in a CS-1B type hexahedron anvils press. The nominal pressure of the press was 8000 kN (single-cylinder). Its slave cylinder diameter was 320 mm. Its working pressure reached high pressure of 10 GPa and ultra-high pressure of 100 GPa. Its largest piston path of slave cylinder was 60 mm. Its supercharging ratio was 10.8 : 1. The electric heating power was 30–40 kVA. The main motor power was 11 kN. Its external dimension (width \* height \* length) was 2150 \* 2150 \* 2430 mm. Its total weight was 15.5 t.

The main sintering procedures of additive-free nPCD compacts from OLCs were as follows. Firstly, OLCs were put into a graphite canister and prepressed with a 02000048 type press until the OLCs were densely and fully filled in the graphite canister. The external and internal heights of the graphite canister were 7.0 mm and 5.5 mm. The external and internal diameters of the graphite canister were 12.0 mm and 9.0 mm. The jamb wall and bottom thicknesses of the graphite canister were 1.5 mm, respectively. The inner cap diameter and thickness of the graphite canister were 9.0 mm and 1.5 mm. Secondly, the graphite canisters fully filled with OLCs were baked at 120°C for 10 h in a ZT-25-20 type vacuum carbon tube furnace. Thirdly, the sintering samples were assembled as shown in Figure 1. The conductive steel cap, pyrophyllite, and graphite sheet were used. Finally, the samples were put into the hexahedron anvils press for

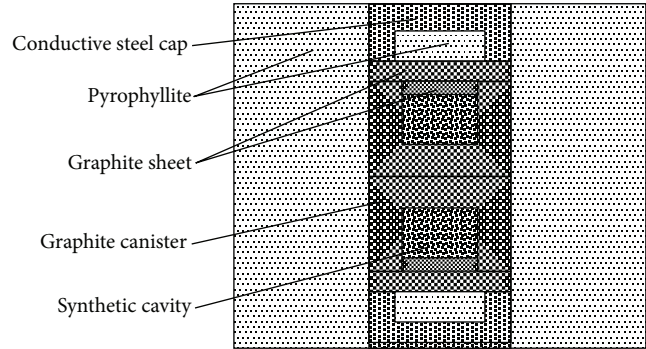


FIGURE 1: Assembling diagram of sintering sample.

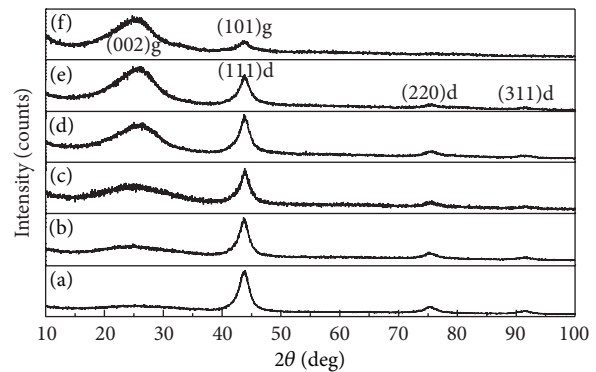


FIGURE 2: XRD patterns of OLCs annealed at (a) 900°C; (b) 1000°C; (c) 1100°C; (d) 1200°C; (e) 1300°C; (f) 1400°C.

sintering. The sintering pressure, temperature, and time were 5.5 GPa, 1200°C, and 15 min.

The end surfaces of nPCD compacts were polished with diamond powder (grain size was about 0.5 μm). In order to confirm its purity, microstructure, and density homogenization in three dimensions, various parts of nPCD compacts were cut into slices for characterizing, respectively. The phase analysis of nPCD compacts was carried out using a D-MAX-2500/P type X-ray diffractometer (XRD, Rigaku, Cu Kα, Japan). The microstructures of nPCD compacts were observed using a JEM-2010 type high-resolution transmission electron microscope (HRTEM, Japan). The densities of nPCD compacts were measured using Archimedes principle. A FM-700 type microscopic Vickers hardness tester (Future-Tech, Japan) was used to measure the microhardnesses of nPCD compacts. A pyramid diamond indenter was applied. The surface angle and the relative edge angle of the diamond indenter were 136°(± 30') and 148.7°(± 23'). The load and the loading time were 4.9 N and 10 s. In order to confirm its physical and mechanical homogenization, the microhardnesses of nPCD compacts were measured 10 times in different areas.

## 3. Results and Discussion

Figure 2 shows the XRD patterns of the OLCs annealed at 900°C, 1000°C, 1100°C, 1200°C, 1300°C, and 1400°C. As shown in Figures 2(a)–2(e), the patterns consisted of four

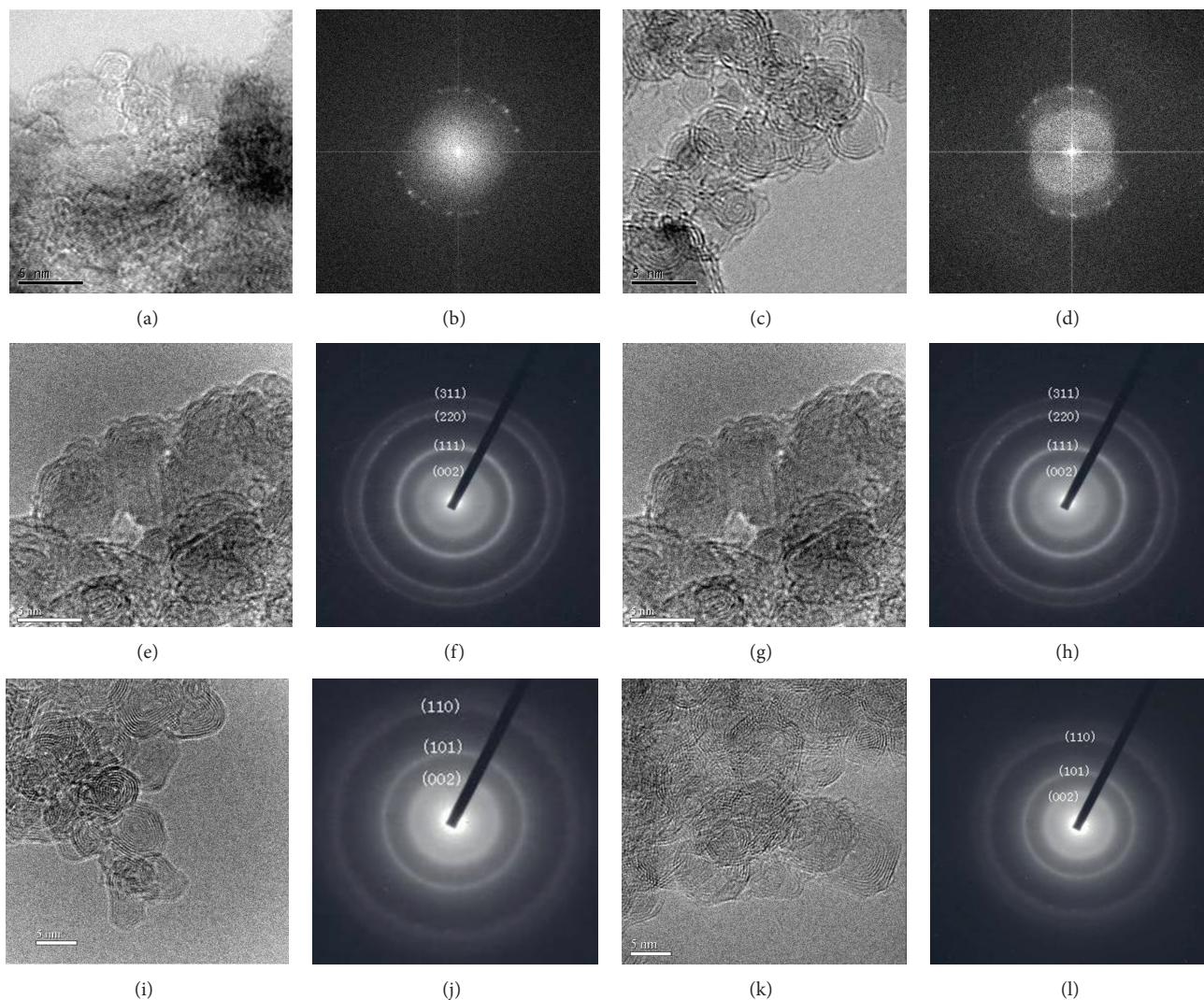


FIGURE 3: (a), (c), (e), (g), (i), and (k) are HRTEM images and (b), (d), (f), (h), (j), and (l) are SAD of OLCs annealed at 900°C, 1000°C, 1100°C, 1200°C, 1300°C, and 1400°C.

seriously broadened diffraction peaks locating at 44°, 75°, and 91°. The peak locating at 26° corresponded to the diffraction of graphite (002) crystal plane. The seriously broadened diffraction peak of graphite (002) crystal plane came from OLC [24]. The peaks locating at 44°, 75°, and 91° corresponded to the diffractions of diamond (111), (220), and (311) crystal planes. The relative diffraction intensity of graphite (002) crystal plane strengthened gradually with annealing temperature increase, while the relative diffraction intensity of each diamond crystal plane decreased. This illuminated that nanodiamond was transformed gradually into OLC with annealing temperature increase. At the annealing temperature of 1400°C as shown in Figure 2(f), the diffraction peaks locating at 26° and 44° and corresponding to the graphite (002) and (101) crystal planes appeared. The diffraction peaks locating at 75° and 91° and corresponding to the diamond (220) and (311) crystal planes disappeared. These indicated that nanodiamond had been transformed completely into OLC annealed at 1400°C. The XRD patterns

in Figure 2 showed strong background, which demonstrated that OLCs contained a certain amount of amorphous carbon. The broadness of diffraction peak might be derived from the stress and strain, nanometer small size, interior lattice distortion, and high density defect of grain.

Table 1 shows the grain sizes of the OLCs annealed at 900–1400°C, which were calculated according to the XRD patterns shown in Figure 2 and Scherrer formula. From the data we could see that the grain sizes of OLCs annealed at 900°C, 1000°C, 1100°C, 1200°C, 1300°C, and 1400°C were 3.4 nm, 3.8 nm, 4.0 nm, 4.2 nm, 4.6 nm, and 6.4 nm. The OLC grain sizes increased gradually with annealing temperature increase.

Figure 3 shows the HRTEM and select-area diffraction (SAD) images of the OLCs annealed at 900°C, 1000°C, 1100°C, 1200°C, 1300°C, and 1400°C. As shown in Figures 3(a) and 3(b), the nanodiamond particle edges had been converted into lamellar graphite when annealed at 900°C. Moreover, the quantity of OLC was very few because the

TABLE 1: Grain sizes of OLCs annealed at 900–1400°C.

Annealing temperature (°C)	900	1000	1100	1200	1300	1400
Grain size (nm)	3.4	3.8	4.0	4.2	4.6	6.4

temperature of 900°C was too low. As seen from Figures 3(c) and 3(d), the nanodiamond particle edges had been transformed into layer-structural OLC. There was nanodiamond untransformed and coexisted in the center of OLC. The content of OLC increased. From the images shown in Figures 3(e)–3(j), most of OLCs were ellipsoid and a small portion was spherical. The outer of OLC was curved graphite layer. Its core had lattice fringe structure. The interlayer distance of the OLC layers was about 0.344 nm, which was close to that of graphite. The lattice fringe distance of the OLC interior lattice fringe structure was approximate to be 0.21 nm, which corresponded to the diamond (111) crystal planes. These demonstrated that the OLCs annealed at 1100–1300°C were encapsulated untransformed nanodiamond in the core. The OLC axes were parallel to those of diamond (111) crystal planes, showing that the OLC graphitization was initiated from the diamond (111) crystal planes. As shown in the SAD graphs of the OLCs, there was one inner amorphous ring. The outer had three diamond rings. Through calculation, the interlayer distances were about 0.3341 nm, 0.2064 nm, 0.1261 nm, and 0.1074 nm, which corresponded to the graphite (002) and diamond (111), (220), and (311) crystal planes. Demonstrating that, nanodiamond had not been transformed completely into OLC annealed at 1100–1300°C, which was in conformity with the results of XRD patterns and HRTEM image shown in Figures 2(a)–2(e). As seen from the images shown in Figures 3(k) and 3(l), there were no diamond lattice fringe structures existing in the OLC center. Indicating that, nanodiamond had been transformed completely into OLC annealed at 1400°C. The interlayer distance was about 0.345 nm, which was close to that of graphite. The innermost diameter of the OLCs was about 0.69 nm, which was close to that of C<sub>60</sub>.

The graphite layer number, the maximum, the minimum, and the average particle sizes of the OLCs annealed at 900–1400°C are shown in Table 2. From the data we can see that the OLC particle sizes and the graphite layer number increased gradually with annealing temperature increase. The average particle sizes of OLCs annealed at 900°C, 1000°C, 1100°C, 1200°C, 1300°C, and 1400°C were 5.7 nm, 5.9 nm, 6.1 nm, 6.5 nm, 7.5 nm, and 8 nm, whose average graphite layer numbers were 3, 4, 6, 8, and 12.

Figure 4 shows the XRD patterns of the nPCD compacts sintered for 15 min at 5.5 GPa and 1200°C using the OLCs annealed at 900°C, 1000°C, 1100°C, 1200°C, 1300°C, and 1400°C as the starting materials. There were four seriously broadened diffraction peaks locating at 26°, 44°, 75°, and 91° and corresponding to the graphite (002), diamond (111), (220), and (311) crystal planes. This indicated that the nPCD compacts contained diamond and graphite. The existence of

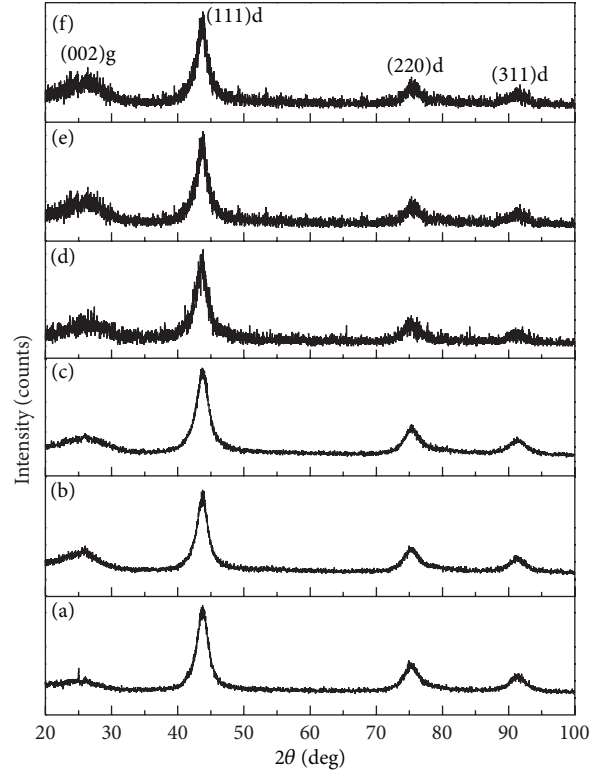


FIGURE 4: XRD patterns of nPCD compacts sintered for 15 min at 5.5 GPa and 1200°C from OLCs annealed at (a) 900°C; (b) 1000°C; (c) 1100°C; (d) 1200°C; (e) 1300°C; (f) 1400°C.

TABLE 2: Parameters of OLCs annealed at 1100–1400°C.

Annealing temperature (°C)	Average graphite layer number	Maximum particle size (nm)	Minimum particle size (nm)	Average particle size (nm)
900	Lamellar structure	8.0	5.0	5.7
1000	3	8.3	5.1	5.9
1100	4	8.5	5.3	6.1
1200	6	9	5.5	6.5
1300	8	9.5	5.7	7.5
1400	12	9.8	5.2	8

background showed that nPCD compacts contained a certain amount of amorphous carbon. Compared with each pattern, the nPCD compact sintered from the OLC annealed at 1100°C contained the least graphite and amorphous carbon in the same sintering conditions, showing that the purity of the nPCD compacts sintered from the OLC annealed at 1100°C was the highest.

Figure 5 shows the HRTEM images of the nPCD compact sintered for 15 min at 5.5 GPa and 1200°C using the OLC annealed at 1100°C as the starting material. In Figures 5(a) and 5(b), the lattice fringe structure could be seen clearly. The lattice distance was about 0.2065 nm through Fourier transform, which was very close to 0.2060 nm of diamond (111)

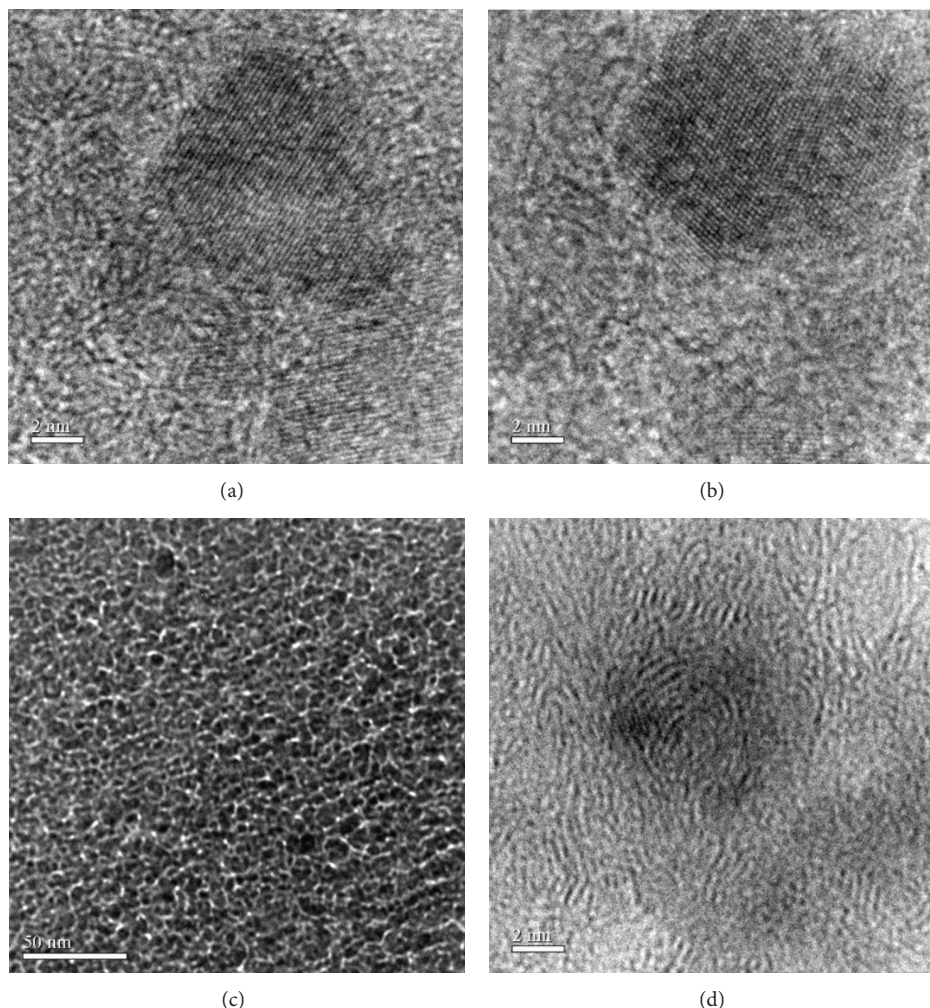


FIGURE 5: HRTEM images of the nPCD compact sintered for 15 min at 5.5 GPa and 1200°C from the OLC annealed at 1100°C: (a), (b), (d) high-resolution, and (c) low-resolution.

crystal plane. Thus this was the diamond (111) crystal plane. Therefore, the particles with lattice fringe structure were diamond. Interestingly, there were numerous nanotwins existing in the nPCD compact. In Figure 5(c), well-defined diamond particles could be observed. The majority of them were irregular. A bit of them were spherical or elliptic. The maximum and the minimum particle sizes of diamond particle in nPCD compact were 14 and 10 nm. The average particle size of diamond was about 12 nm through statistical analysis. As seen in Figure 5(d), there were completely transformed OLCs occurring in the nPCD compact, which composed of 10–12 graphite layers. Describing that, a small portion OLCs had completely transformed into OLC during the sintering process.

Figure 6 is the SAD of the nPCD compact sintered for 15 min at 5.5 GPa and 1200°C using the OLC annealed at 1100°C as the starting material. There were three polycrystalline diffraction rings and one amorphous ring. Through calculating, the interplanar distances

were 0.3445 nm, 0.2064 nm, 0.1261 nm, and 0.1074 nm, corresponding to the graphite (002) and diamond (111), (220), and (311) crystal planes. This showed that the nPCD compact contained diamond, a certain amount of graphite, and amorphous carbon, which conformed to the analysis results of XRD and HRTEM shown in Figures 4 and 5.

Figure 7 shows the fitting lines of Vickers hardness, density, and average diamond grain size of the nPCD compacts sintered for 15 min at 5.5 GPa and 1200°C using the OLCs annealed at 900°C, 1000°C, 1100°C, 1200°C, 1300°C, and 1400°C as the starting material. The Vickers hardness, density, and average diamond grain size (calculated according to the XRD patterns shown in Figure 4 and Scherrer formula) of the nPCD compacts sintered from the OLC annealed at 1100°C were the highest and largest, which were 32 GPa, 2.70 g/cm<sup>3</sup>, and 10.7 nm.

Through the above results and analysis, encapsulated nanodiamond (annealed at 900–1300°C) or empty (annealed at 1400°C) OLCs are transformed into additive-free D-D

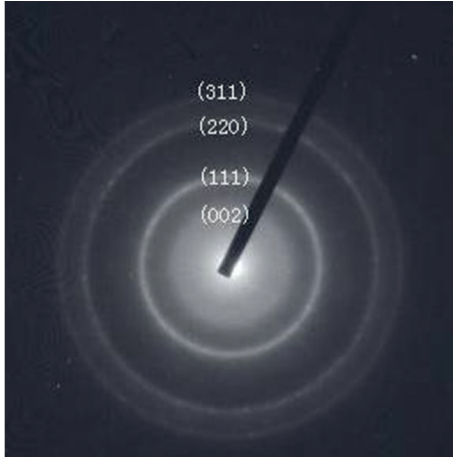


FIGURE 6: SAD of nPCD compact sintered for 15 min at 5.5 GPa and 1200°C using OLC annealed at 1100°C.

type nPCD compacts in the industrial sintering conditions of 5.5 GPa, 1200°C, and 15 min. The OLC particles are in nanometer size and there are  $sp^3$  structures in it. The  $sp^3$  sites can be the crystal seeds for diamond formation. Thus the transformation of diamond from OLC is easier than that of graphite. So the sintering pressure and temperatures of the nPCD compacts from OLCs are much lower than those of graphite and other raw materials. This work makes it possible for synthesizing additive-free D-D type nPCD compacts in industry conditions. Furthermore because there are no weak phases existing in the nPCD compacts, the performances and processing abilities of them can be improved greatly.

During sintering process, great energies and pressure are generated. The external graphite layers of OLC particles rupture at first under the effects of the pressure and energy, then the graphite layers of OLC rupture from inside towards its outside. In this way, the graphite layers of OLC break gradually, so that the  $sp^2$  graphite structure in OLC is transformed into  $sp^3$  diamond structure forming nanodiamond particles. Furthermore, the nanodiamond particles grow during the transformation process from OLC forming larger nanodiamond particles and bond adjacent nanodiamond particles through dangling bonds forming additive-free D-D type nPCD compacts.

The purity, diamond grain size, Vickers hardness, and density of the additive-free nPCD compacts sintered from the OLCs annealed at 1100°C are the largest and the highest, as shown in Figure 7. The average Vickers hardness and density of the nPCD compacts sintered from the OLCs annealed at 1100°C reach 32 GPa and 2.7 g/cm<sup>3</sup>. The average grain size of nanodiamond in the additive-free nPCD compact sintered from the OLC annealed at 1100°C grows up to 10.8 nm, which increases by 170% compared with 4.0 nm (as shown in Figure 2 and Table 1) of the OLC average grain size annealed at 1100°C. There is untransformed nanodiamond encapsulated in the OLC core annealed at 1100°C, which can be used as crystal seed for nanodiamond transformation from OLC. At the same time, the outer graphite layer structure of

the OLC annealed at 1100°C is the most suitable for transforming into nanodiamond. Although the OLCs annealed at 900°C, 1000°C, 1200°C, and 1300°C encapsulate untransformed nanodiamonds in the cores, the outer graphite layers of the OLCs have lamellar or unstable structures, which is not suitable for nanodiamond transformation from the OLCs. The OLCs annealed at 1400°C is transformed completely from nanodiamond, there is no untransformed nanodiamond in the core; in other words, there is no crystal seed for nanodiamond transformation from OLC during the sintering process of additive-free D-D type nPCD compacts. Thus the nanodiamond transformation from the OLC annealed at 1100°C forming additive-free D-D type nPCD compacts is the most complete transformation and the average grain size of nanodiamond is the largest. The purity of the nPCD compact sintered from the OLC annealed at 1100°C is the highest, which results in the highest physical and mechanical performances. Meanwhile, the nanotwins existing in the nPCD compacts also contribute to its high performances.

The above results are measured at different points of nPCD compacts. It is found that the purity and physical and mechanical performances of nPCD compacts are homogeneous in three dimensions. The reasons are as follows. Through three-pair hexahedron anvils of CS-1B type hexahedron anvils press, a three-dimensional isostatic pressure can be applied and controlled during the transformation process of diamond from OLCs. For sintering, the conductive steel cap, pyrophyllite, and graphite sheet (as shown in Figure 1) are used, which can make sure that the samples received three-dimensional isostatic pressure and homogeneous current during the nanodiamond transformation process from OLCs. Moreover, the sintering time is adapted 15 min. In such a short time, the pressure and current can be rapidly and evenly passed to every point of the samples, which further ensures that the samples received three-dimensional isostatic pressure and homogeneous current during the sintering process. Thus the purity and physical and mechanical performances of nPCD compacts are homogeneous in three dimensional directions.

#### 4. Conclusions

OLCs were fabricated by annealing detonation nanodiamond at the temperatures of 900–1400°C and the pressure of 1 Pa. The OLCs annealed at 900–1300°C encapsulated untransformed nanodiamond in the core. The OLCs annealed at 1400°C were transformed completely. The grain sizes of OLCs annealed at 900°C, 1000°C, 1100°C, 1200°C, 1300°C, and 1400°C were 3.4 nm, 3.8 nm, 4.0 nm, 4.2 nm, 4.6 nm, and 6.4 nm. The OLC grain size increased gradually with the annealing temperature increase. The average number of OLC graphite layers annealed at 900°C, 1000°C, 1100°C, 1200°C, 1300°C, and 1400°C were 3, 4, 6, 8, and 12.

In the industrial sintering conditions of 5.5 GPa, 1200°C, and 15 min, OLCs annealed at 900–1400°C could be transformed into additive-free D-D type nPCD compacts. The purity and physical and mechanical performances of the nPCD compacts were homogeneous. The purity and physical

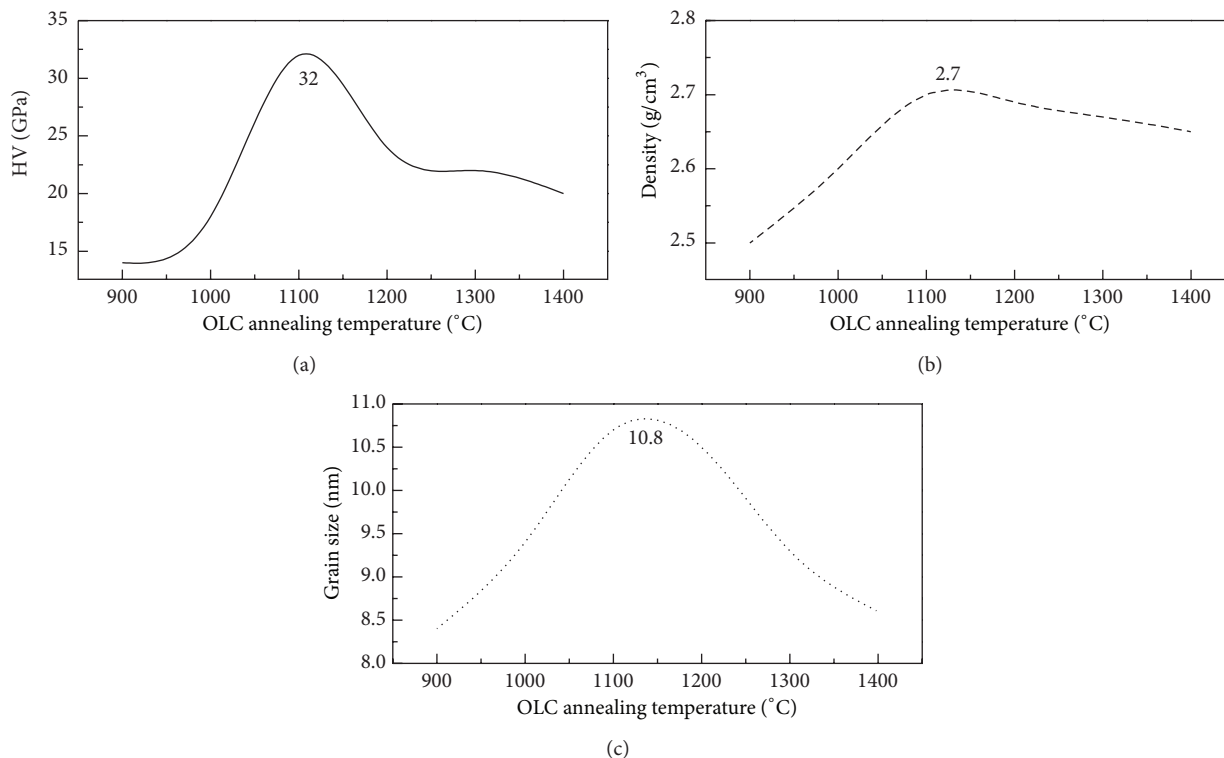


FIGURE 7: Properties of nPCD sintered from OLCs annealed at 900–1400°C: (a) Vickers hardness; (b) density; (c) grain size.

and mechanical performances of the nPCD compacts sintered from the OLCs annealed at 1100°C were the highest. Moreover, the Vickers hardness, density, and nanodiamond grain size were 32 GPa, 2.7 g/cm<sup>3</sup>, and 10.8 nm.

In the sintering process, the OLC graphite layers ruptured from inside towards outside. At the same time, the OLC particles bonded with adjacent OLCs forming larger nanodiamond particles, which further formed additive-free D-D type nPCD compacts. The results of this research show that it is feasible to sinter additive-free D-D type nPCD compacts from OLCs in industrial sintering conditions.

### Conflict of Interests

The authors declare that there is no conflict of interests regarding the publication of this paper.

### Acknowledgments

This work was supported by the National Nature Science Foundation of China (Grant no. 51102205), the Youth Foundation of Hebei Educational Committee (Grant no. QN20131092), and the first batch of young talent support plan in Hebei province.

### References

- [1] L. Ding, J. Chen, and X. Wei, "The change of metal inclusions and its influence on the strength of synthetic diamond," *Chinese Journal of High Pressure Physics*, vol. 4, no. 2, pp. 96–104, 1990.
- [2] Y. H. Wang, M. Z. Wang, and B. Y. Li, "The influence of high temperature and ultra high pressure on structure and wear resistance of Si bond polycrystalline diamond (PCD)," *Journal of Composite Materials*, vol. 11, pp. 57–62, 1994.
- [3] R. H. Wentorf, R. C. Devries, and F. P. Bundy, "Sintered superhard materials," *Science*, vol. 208, no. 4446, pp. 873–880, 1980.
- [4] H. Jia, H. Ma, and X. Jia, "Research on polycrystalline diamond compact (PDC) with low residual stress prepared using nickel-based additive," *International Journal of Refractory Metals and Hard Materials*, vol. 29, no. 1, pp. 64–67, 2011.
- [5] H. Sumiya and S. Satoh, "Synthesis of polycrystalline diamond with new non-metallic catalyst under high pressure and high temperature," *International Journal of Refractory Metals and Hard Materials*, vol. 17, no. 5, pp. 345–350, 1999.
- [6] J. E. Westraadt, N. Dubrovinskaia, J. H. Neethling, and I. Sigalas, "Thermally stable polycrystalline diamond sintered with calcium carbonate," *Diamond and Related Materials*, vol. 16, no. 11, pp. 1929–1935, 2007.
- [7] A. D. Krawitz, R. A. Winholtz, E. F. Drake, and N. D. Griffin, "Residual stresses in polycrystalline diamond compacts," *International Journal of Refractory Metals and Hard Materials*, vol. 17, no. 1, pp. 117–122, 1999.
- [8] T.-P. Lin, M. Hood, G. A. Cooper, and R. H. Smith, "Residual stresses in polycrystalline diamond compacts," *Journal of the American Ceramic Society*, vol. 77, no. 6, pp. 1562–1568, 1994.
- [9] T.-P. Lin, M. Hood, G. A. Cooper, and X. Li, "Wear and failure mechanisms of polycrystalline diamond compact bits," *Wear*, vol. 156, no. 1, pp. 133–150, 1992.

- [10] D. Miess and G. Rai, "Fracture toughness and thermal resistance of polycrystalline diamond compacts," *Materials Science and Engineering A*, vol. 209, no. 1-2, pp. 270-276, 1996.
- [11] F. Nabhani, "Wear mechanisms of ultra-hard cutting tools materials," *Journal of Materials Processing Technology*, vol. 115, no. 3, pp. 402-412, 2001.
- [12] S. Miklaszewski, M. Zurek, P. Beer, and A. Sokolowska, "Micromechanism of polycrystalline cemented diamond tool wear during milling of wood-based materials," *Diamond and Related Materials*, vol. 9, no. 3-6, pp. 1125-1128, 2000.
- [13] J. Hu and Z. L. Dou, "Synthesis of pure polycrystalline diamond transformed directly from graphite under high temperature and high pressure," *Superhard Material Engineering*, vol. 5, pp. 48-52, 2006.
- [14] M. G. de Azevedo, A. Potemkin, A. L. D. Skury, and R. N. de Azevedo Faria Jr., "The high temperature-high pressure sintering of diamond-Cu-Si-B composite," *Diamond and Related Materials*, vol. 10, no. 9-10, pp. 1607-1611, 2001.
- [15] S. Tomita, M. Fujii, S. Hayashi, and K. Yamamoto, "Transformation of carbon onions to diamond by low-temperature heat treatment in air," *Diamond and Related Materials*, vol. 9, no. 3-6, pp. 856-860, 2000.
- [16] Q. Zou, M. Z. Wang, and Y. G. Li, "Analysis of the nanodiamond particle fabricated by detonation," *Journal of Experimental Nanoscience*, vol. 5, no. 4, pp. 319-328, 2010.
- [17] Q. Zou, Y. G. Li, L. H. Zou, and M. Z. Wang, "Characterization of structures and surface states of the nanodiamond synthesized by detonation," *Materials Characterization*, vol. 60, no. 11, pp. 1257-1262, 2009.
- [18] Q. Zou, M. Z. Wang, Y. G. Li, L. H. Zou, H. Yu, and Y. C. Zhao, "Analysis of structures and surface states of the nanodiamond particle synthesised by detonation," *Micro and Nano Letters*, vol. 4, no. 3, pp. 133-141, 2009.
- [19] Q. Zou, M. Z. Wang, and Y. G. Li, "Onion-like carbon synthesis by annealing nanodiamond at lower temperature and vacuum," *Journal of Experimental Nanoscience*, vol. 5, no. 5, pp. 375-382, 2010.
- [20] Q. Zou, Y. G. Li, M. Z. Wang, L. H. Zou, and Y. C. Zhao, "Characterisation of onion-like carbon fabricated by annealing nanodiamond," *Materials Research Innovations*, vol. 14, no. 4, pp. 285-288, 2010.
- [21] Q. Zou, Y. G. Li, B. Lv, M. Z. Wang, L. H. Zou, and Y. C. Zhao, "Transformation of onion-like carbon from nanodiamond by annealing," *Inorganic Materials*, vol. 46, no. 2, pp. 127-131, 2010.
- [22] Q. Zou, M. Z. Wang, Y. G. Li, Y. C. Zhao, and L. H. Zou, "Fabrication of onion-like carbon from nanodiamond by annealing," *Science in China E: Technological Sciences*, vol. 52, no. 12, pp. 3683-3689, 2009.
- [23] Q. Zou, M. Z. Wang, Y. G. Li, and B. Lu, "High-resolution transmission-electron microscope characterization of onion-like carbon transformed from nanodiamond," *Journal of Vacuum Science and Technology B: Microelectronics and Nanometer Structures*, vol. 28, no. 5, pp. 935-939, 2010.
- [24] S. Tomita, A. Burian, C. Dorec, D. LeBollochd, M. Fujii, and S. J. Hayashi, "Diamond nanoparticles to carbon onions transformation: X-ray diffraction studies," *Carbon*, vol. 40, no. 9, pp. 1469-1474, 2002.

## Research Article

# Tribological Performance and Lubrication Mechanism of Alkylimidazolium Dialkyl Phosphates Ionic Liquids as Lubricants for $\text{Si}_3\text{N}_4$ - $\text{Ti}_3\text{SiC}_2$ Contacts

Hai-zhong Wang,<sup>1,2</sup> Dan Qiao,<sup>1,2</sup> Song-wei Zhang,<sup>1,2</sup> Da-peng Feng,<sup>1</sup> and Jin-jun Lu<sup>3</sup>

<sup>1</sup> State Key Laboratory of Solid Lubrication, Lanzhou Institute of Chemical Physics, Chinese Academy of Sciences, Lanzhou 730000, China

<sup>2</sup> University of Chinese Academy of Sciences, Beijing 100049, China

<sup>3</sup> College of Chemistry and Materials Science, Northwest University, Xi'an 710069, China

Correspondence should be addressed to Da-peng Feng; [dpfeng@licp.cas.cn](mailto:dpfeng@licp.cas.cn) and Jin-jun Lu; [jjlu@lzb.ac.cn](mailto:jjlu@lzb.ac.cn)

Received 14 February 2014; Accepted 21 March 2014; Published 16 April 2014

Academic Editor: Jinlong Jiang

Copyright © 2014 Hai-zhong Wang et al. This is an open access article distributed under the Creative Commons Attribution License, which permits unrestricted use, distribution, and reproduction in any medium, provided the original work is properly cited.

The tribological performance of  $\text{Si}_3\text{N}_4$ - $\text{Ti}_3\text{SiC}_2$  contacts lubricated by alkylimidazolium dialkyl phosphates ionic liquids (ILs) was investigated using an Optimol SRV-IV oscillating reciprocating friction and wear tester at room temperature (25°C) and 100°C. Glycerol and tributyl phosphate (TBP) were also selected as lubricants for  $\text{Si}_3\text{N}_4$ - $\text{Ti}_3\text{SiC}_2$  contacts to study the tribological properties under the same experimental conditions for comparison. Results show that the alkylimidazolium dialkyl phosphates ILs were effective in reducing the friction and wear for  $\text{Si}_3\text{N}_4$ - $\text{Ti}_3\text{SiC}_2$  contacts, and their performance is superior to that of glycerol and TBP. The SEM/EDS and XPS results reveal that the excellent tribological endurance of alkylimidazolium dialkyl phosphates ILs is mainly attributed to the high load-carrying capacity of the ILs and the formation of surface protective films consisting of  $\text{TiO}_2$ ,  $\text{SiO}_x$ , titanium phosphate, amines, and nitrogen oxides by the tribochemical reactions.

## 1. Introduction

It is known that  $\text{Ti}_3\text{SiC}_2$  is the most studied material in the system of  $M_{n+1}AX_n$  ( $n = 1-3$ ) phases, which has a layered crystal structure and possesses the properties of both metals and ceramics. The unique properties of  $\text{Ti}_3\text{SiC}_2$  include high strength and modulus, good damage tolerance at room temperature (RT), excellent thermal shock resistance, good electrical and thermal conductivities, easy machinability, good oxidation resistance, and low density. These unusual combinations of the properties render it a candidate structural material for high temperature applications [1-5].

Interestingly, all these unique properties of  $\text{Ti}_3\text{SiC}_2$  are attributed to its layered structure, which is similar to that of graphite and  $\text{MoS}_2$ . Thus, it is proposed that  $\text{Ti}_3\text{SiC}_2$  is a self-lubricating material and possesses low friction coefficient [6, 7], and the related research about  $\text{Ti}_3\text{SiC}_2$  has been

reported with the measurement of its mechanical properties [8, 9]. However, limited work has been carried out to evaluate the tribological behavior of  $\text{Ti}_3\text{SiC}_2$  with liquid lubricants, which mainly focuses on the liquid lubricants of water and alcohol [10-16]. Hibi reveals that both the friction and wear of  $\text{Ti}_3\text{SiC}_2$ -SiC composite are much lower with the lubrication of ethanol than that of water, even under dry condition [14]. Unfortunately, water and alcohol could not be used under extreme conditions, such as wide temperature changes and high load.

Recently, a program has been started to illustrate the tribochemical reactions of  $\text{Ti}_3\text{SiC}_2$  lubricating by several liquid lubricants which could be used under extreme conditions. Ionic liquids (ILs) as a unique member in the family of liquid lubricants have received increasing attention in the academic and industrial tribology fields owing to their intrinsic characteristics, such as negligible volatility, nonflammability, high

thermal stability, and low melting point. An explosive growth of researches on ILs has been conducted in the past few years [17–22].

Research shows that the phosphates can be used to improve the antiwear and load-carrying capacity of liquid lubricant for ceramic materials [23]. Wei and Xue found that tributyl phosphate (TBP) has a little antiwear function for lubrication of ceramic because of their physical adsorption on the rubbing surfaces [24]. ILs with functional group of phosphate also can perform good tribological properties, especially at a moderate temperature [25].

Bearing this in mind, the alkylimidazolium dialkyl phosphates ILs were synthesized and evaluated as lubricants for  $\text{Si}_3\text{N}_4$ - $\text{Ti}_3\text{SiC}_2$  contacts. Glycerol and TBP were also investigated under the same conditions for comparison. The details of the wear mechanism have been studied using scanning electron microscope with a Kevex energy dispersive X-ray analyzer attachment (SEM) and X-ray photoelectron spectrometer (XPS).

## 2. Experimental Details

**2.1. Materials Preparation.** The bulk  $\text{Ti}_3\text{SiC}_2$  sample was prepared using an in situ hot pressing/solid-liquid reaction process starting from Ti, Si, and graphite powders and Al powder (3.1 mol%) as a sintering additive [15, 26]. Three kinds of powders with stoichiometric quantities were weighed, ball-milled, and then hot-pressed at  $1450^\circ\text{C}$ , 25 MPa in a graphite die. The home-made  $\text{Ti}_3\text{SiC}_2$  has the relative density of 96.4%, hardness of 4.66 GPa, and surface roughness ( $R_a$ ) of  $0.24\ \mu\text{m}$ . The composition of  $\text{Ti}_3\text{SiC}_2$  was determined by D/Max-2400 (Japan) X-ray diffraction (XRD). The XRD spectrum of  $\text{Ti}_3\text{SiC}_2$  sample is shown in Figure 1, and it can be seen that the structure of sample is polycrystalline with a small amount (less than 3 wt.%) of TiC impurity.

The alkylimidazolium dialkyl phosphates ILs were synthesized according to the references [27, 28], and the synthesized route and molecular structures of them are shown in Figure 2. Glycerol and TBP were selected with the analytical reagent.

Several typical physical properties of the lubricants are shown in Table 1. The kinematic viscosities of the lubricants were measured using an SYP1003-III kinematic viscosity of petroleum-product measuring apparatus at  $40^\circ\text{C}$  and  $100^\circ\text{C}$ . Thermogravimetric analysis (TGA) was performed on a Perkin-Elmer TGA-7 conducted in nitrogen atmosphere from  $20^\circ\text{C}$  to  $600^\circ\text{C}$  at a rate of  $10^\circ\text{C}/\text{min}$ . The volatilization losses of all used lubricants were tested at  $100^\circ\text{C}$  for 24 h according to the standard method of ASTM D972.

**2.2. Friction and Wear Tests.** Friction and wear tests were conducted on an Optimol SRV-IV oscillating reciprocating friction and wear tester with a ball-on-disc configuration at RT ( $25^\circ\text{C}$ ) and at  $100^\circ\text{C}$ . The upper ball was made of  $\text{Si}_3\text{N}_4$  (G5 according to ANSI/AFBMA Std 10-1989 with surface roughness  $R_a$  of  $0.02\ \mu\text{m}$ ) with a diameter of 10 mm. The surface roughness ( $R_a$ ) of the  $\text{Ti}_3\text{SiC}_2$  disc is  $0.04\ \mu\text{m}$ . Both the balls and discs were cleaned ultrasonically in ethanol for

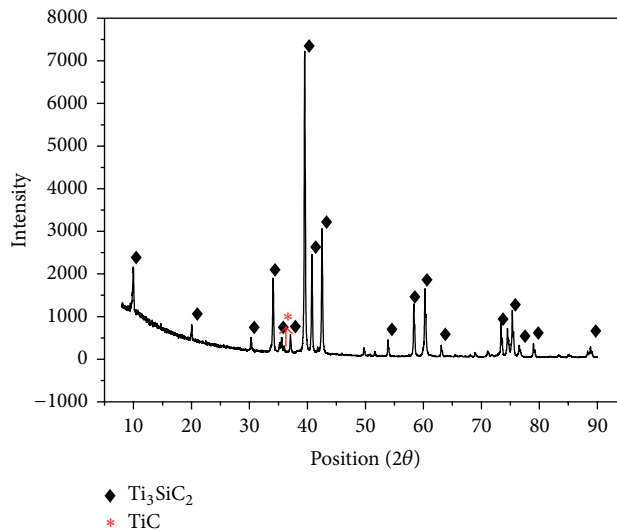


FIGURE 1: XRD spectrum of  $\text{Ti}_3\text{SiC}_2$ .

30 min and allowed to dry before testing. The contact between frictional pairs was achieved by pressing the upper running ball against the lower stationary disc. The upper running ball was reciprocated at a constant frequency and stroke.

All the SRV tests were conducted under the following condition: load of 100 N, frequency of 25 Hz, amplitude of 1 mm, duration of 30 min, and a relative humidity of 20–50%. Before the tests, 0.2 mL liquid lubricants were dropped onto the ball-disc contact area. The corresponding friction curves were recorded automatically with a charter attached to the SRV test rig. The wear volumes of lower discs were measured using a MicroXAM-3D noncontact surface mapping microscope profilometer. Three repetitive measurements were carried out under each test condition, and the average values are reported in this paper.

**2.3. Measurements and Analysis.** The morphologies of worn surfaces were observed by JSM-5600LV scanning electron microscopy (SEM). The X-ray photoelectron spectrometer (XPS) analysis was carried out on a PHI-5702 multifunctional XPS, using Al-K $\alpha$  radiation as the exciting source. The binding energies of the target elements were determined at pass energy of 29.35 eV, and the resolution is about  $\pm 0.3\ \text{eV}$  with the binding energy of contaminated carbon (C 1s: 284.8 eV) as reference.

## 3. Results and Discussion

**3.1. Physical Properties of ILs.** Table 1 shows the physical properties of the alkylimidazolium dialkyl phosphates ILs. It can be seen that all the ILs compounds have a good viscosity index as well as a high decomposition temperature compared with glycerol and TBP. When the alkyl chains of anions increased, the viscosity of ILs became higher. And the order of the viscosity for these lubricants at  $100^\circ\text{C}$  is as follows: TBP < Glycerol < PEE < PBE < POE and the details were shown in

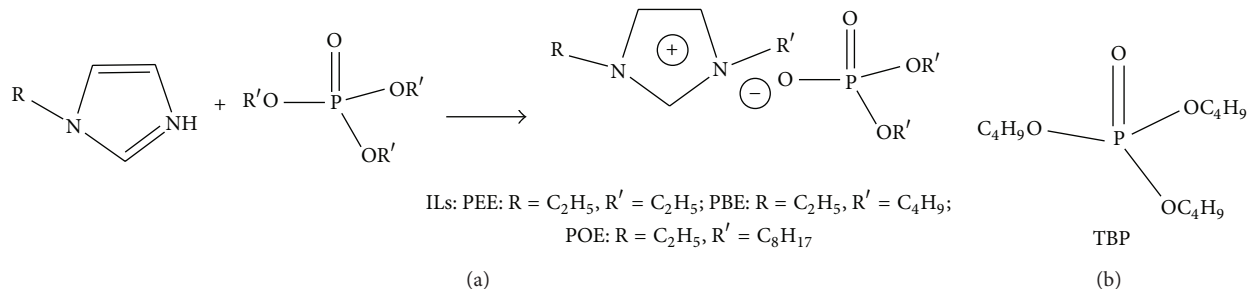


FIGURE 2: Synthesized route of the ILs of alkyimidazolium dialkyl phosphates (a) and molecular structures of TBP (b).

TABLE 1: Physical properties of the alkyimidazolium dialkyl phosphates ILs.

Lubricants	Properties				
	Kinetic viscosity/ $\text{mm}^2\cdot\text{s}^{-1}$			Density/ $\text{Kg}\cdot\text{m}^{-3}$	TGA/ $^{\circ}\text{C}$ (onset decomposition temperature)
	40 $^{\circ}\text{C}$	100 $^{\circ}\text{C}$	VI		
PEE	138	17.1	129	1125	275
PBE	231	23.9	115	1038	281
POE	267	28.4	117	1016	274
Glycerol	246	13.7	4.9	1258	156
TBP	3.0	1.1	—	979	118

“—” Could not be calculated.

Table 1. And it is indicated that the alkyimidazolium dialkyl phosphates ILs were superior to the glycerol and TBP as lubricants for ceramic materials which can be used under wide temperature conditions.

The volatilization losses results of these lubricants are listed in Table 2. It can be seen that the PEE IL has the least weight loss (0.54%) among the alkyimidazolium dialkyl phosphates ILs. TBP has the worst thermal stability with a weight loss of 53.4% and the glycerol exhibits the thermal stability with a weight loss of 8.49%. These results illustrate that the alkyimidazolium dialkyl phosphates ILs possess better thermal stability and are more suitable to be used as high-temperature lubricants compared to glycerol and TBP.

### 3.2. Tribological Behavior

**3.2.1. Tribological Behavior of ILs.** Figures 3 and 4 exhibited the evolution of friction coefficients for  $\text{Si}_3\text{N}_4\text{-Ti}_3\text{SiC}_2$  contacts and wear volumes of  $\text{Ti}_3\text{SiC}_2$  discs lubricated by different ILs at 25 $^{\circ}\text{C}$  and 100 $^{\circ}\text{C}$  under the load of 100 N. It can be seen from Figure 3 that POE performed the highest friction coefficient among the three kinds of ILs, and the other two ILs showed the similar evolution of friction coefficients at RT. However, the lowest wear loss of ILs was obtained by the lubrication of POE, while PEE showed the highest wear loss. When the test temperature increased to 100 $^{\circ}\text{C}$ , it could be found from Figure 4 that the friction coefficient decreased remarkably as the viscosity decreased. However, the higher viscosity is benefit to improve the antiwear performance of the lubricants. Moreover, POE still exhibited the highest friction coefficient and the lowest wear loss within the three kinds of ILs. It can also be seen that PEE showed lower

TABLE 2: Volatilization losses of the lubricants (100 $^{\circ}\text{C}$ , 24 hours).

Lubricants	PEE	PBE	POE	TBP	Glycerol
Mass loss (%)	0.54	0.97	2.9	53.4	8.49

friction coefficient and lower wear loss compared to the other two kinds of ILs at 100 $^{\circ}\text{C}$ .

In our previous work [29], it is found that anions in ILs are always involved in the tribochemical reactions, and the presence of reaction products on the worn surface makes the ILs to be good lubricants. Liu et al. also found that the structure of alkyimidazolium cation had an important effect on the tribological properties of ILs [30]. In this study, based on the aforementioned results, a conjecture can be drawn which describes that the anion with shorter alkyl chain shows higher reactivity than the anion with longer alkyl chain in the molecular structure of ILs. It also shows that lower viscosity would produce lower friction coefficient and higher wear loss under the tested conditions. Accordingly, the anion with longer alkyl chain in the molecular structure of ILs would show higher friction coefficient and the lower wear loss. In addition, ILs with longer alkyl chains in cations show the higher viscosity, which might cause higher friction coefficient and lower wear loss. Moreover, it can be seen that ILs with higher viscosity would show stronger load-carrying capacity under boundary lubrication condition from the above tribological results, which means reduction in friction coefficient depended on lower viscosity of ILs and ILs with higher viscosity showed good antiwear performance. Thus, it can also be found that the above mentioned two effects, high

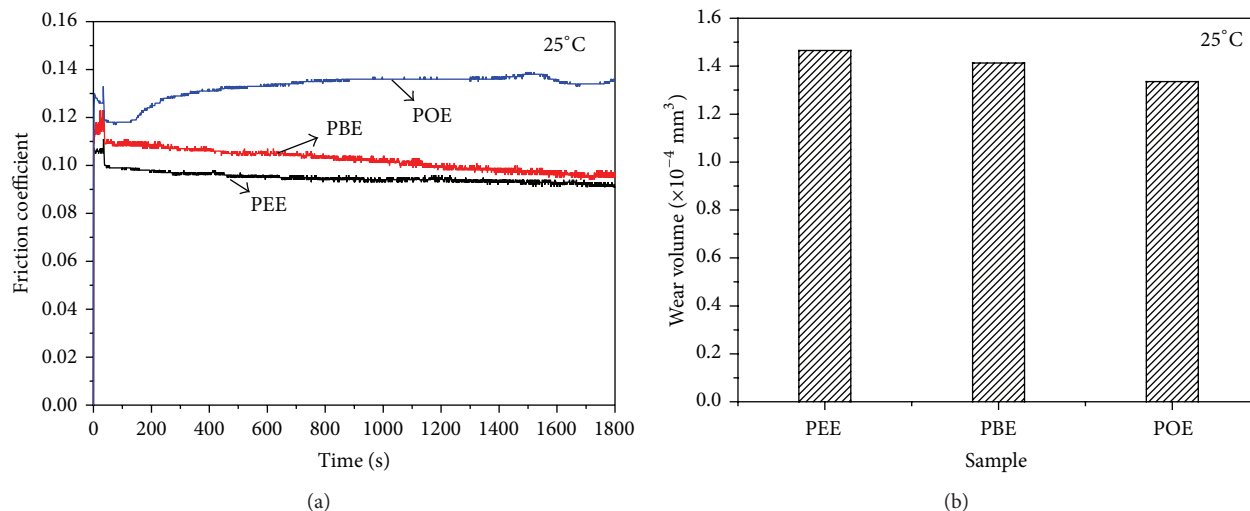


FIGURE 3: Evolution of friction coefficients (a) and wear volumes (b) of  $\text{Ti}_3\text{SiC}_2$  discs lubricated by different ILs at 25°C under 100 N.

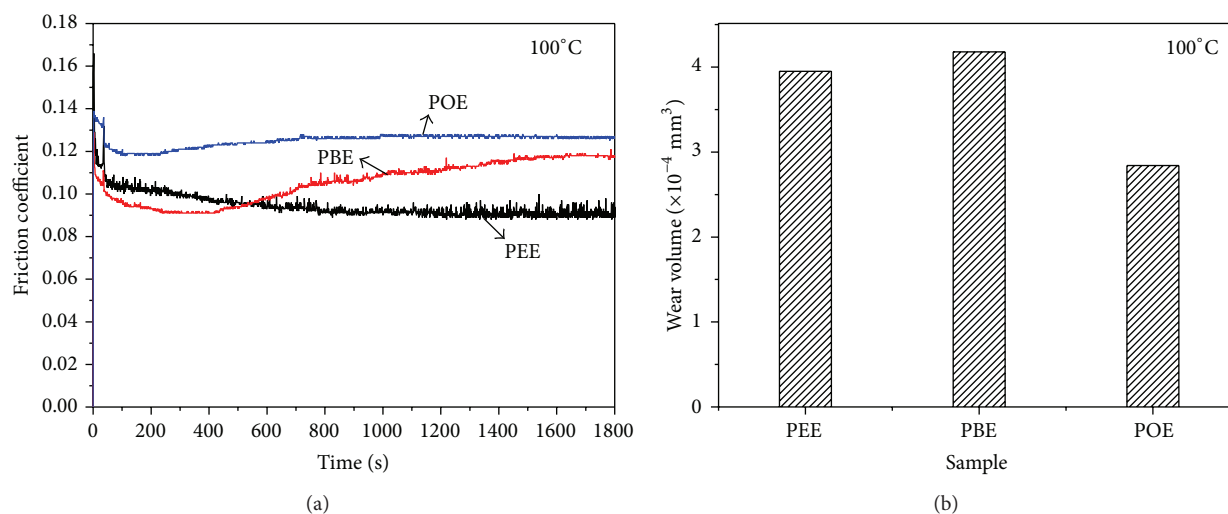


FIGURE 4: Evolution of friction coefficients (a) and wear volumes (b) of  $\text{Ti}_3\text{SiC}_2$  discs lubricated by different ILs at 100°C under 100 N.

reactivity and high viscosity, have exhibited more obviously synergistic effects while the temperature increased.

**3.2.2. Comparison of Tribological Behavior with Glycerol and TBP.** To verify the hypothesis that is mentioned above, the tribological experiments of TBP were also done under the same conditions, and the molecular structure of TBP is similar to the part of anion in ILs of PBE. Glycerol, which was an extensively investigated lubricant for  $\text{Ti}_3\text{SiC}_2$ , was also tested as a comparison with ILs. The compared results of the two kinds of lubricants with PBE were summarized in Figures 5 and 6. It can be found that TBP showed much higher friction coefficient and higher wear loss both at 25°C and at 100°C, which is attributed to the simple molecular structure and poor load-carrying capacity of TBP compared to that

of PBE. The results were consistent to the above hypothesis that ILs with longer alkyl chains in cations would show greater load-carrying capacity under boundary lubrication condition, which means reduction in friction coefficient and wear loss. Compared with glycerol, it could be found from Figures 5 and 6 that PBE exhibited more steady friction coefficient and lower wear loss.

As a result, the high thermal stability and excellent tribological property of alkyylimidazolium dialkyl phosphates ILs made it an attractive alternative to liquid lubricants for  $\text{Si}_3\text{N}_4\text{-Ti}_3\text{SiC}_2$  contacts.

**3.3. Surface Analysis.** SEM and three-dimensional (3D) non-contact surface measurement were employed to examine the morphologies of the wear tracks on the  $\text{Ti}_3\text{SiC}_2$  discs. Figure 7

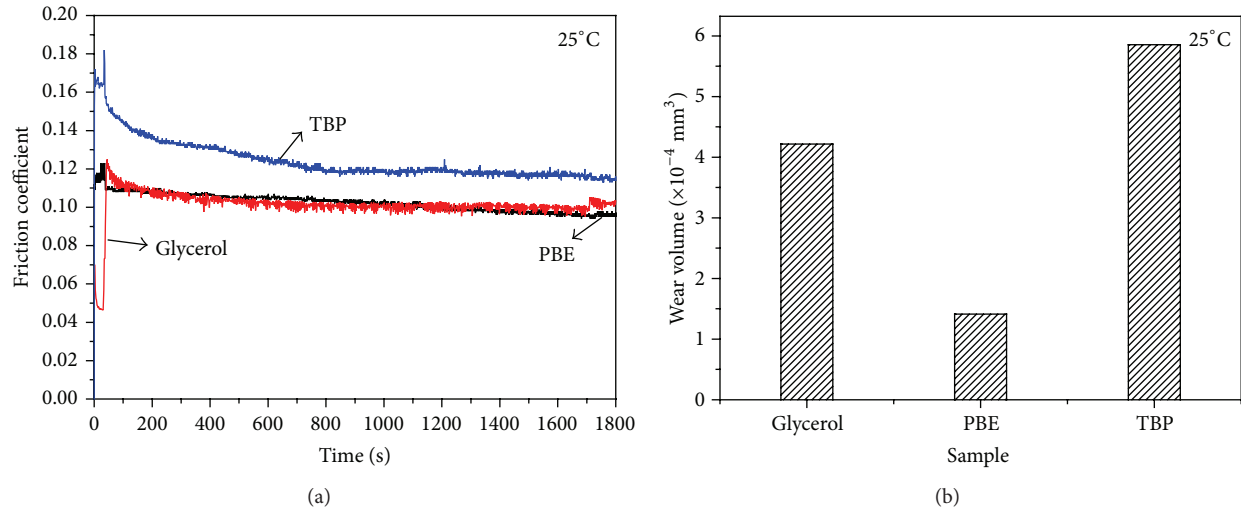


FIGURE 5: Evolution of friction coefficients (a) and wear volumes (b) of  $\text{Ti}_3\text{SiC}_2$  discs lubricated by PBE, TBP, and glycerol at 25°C under 100 N.

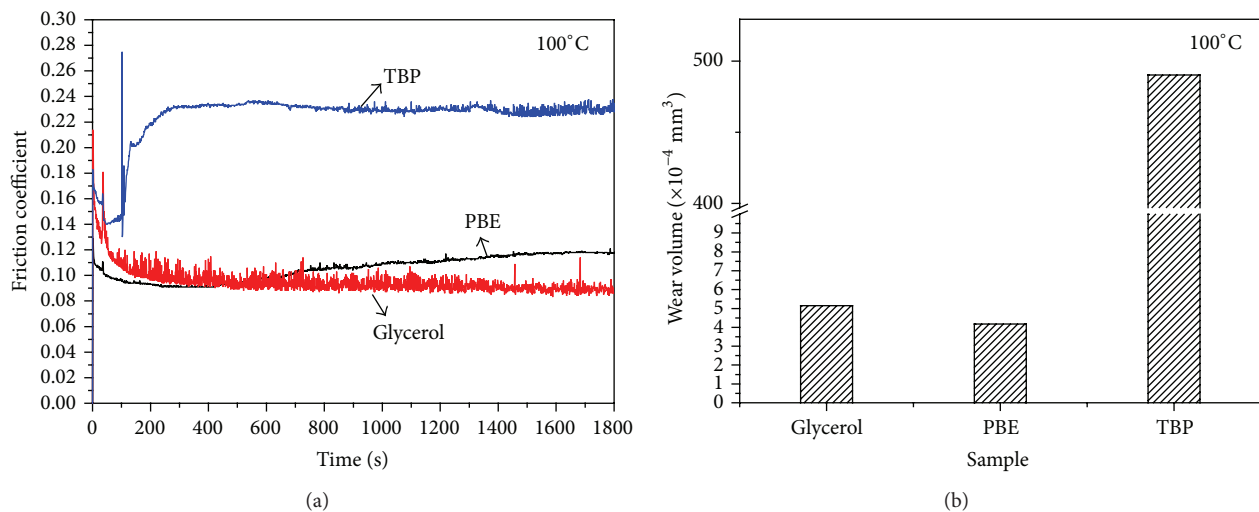


FIGURE 6: Evolution of friction coefficients (a) and wear volumes (b) of  $\text{Ti}_3\text{SiC}_2$  discs lubricated by PBE, TBP, and glycerol at 100°C under 100 N.

shows the SEM and 3D optical microscopic images of the worn surfaces lubricated by POE and glycerol under a load of 100 N at 100°C. It can be seen that the worn surfaces under the lubrication of glycerol presented severe fracture and oxidation wear, whereas the worn surfaces lubricated by POE exhibited slight wear. These results highly agreed with those of high-temperature experimental results and further indicated that POE could effectively improve the wear-resistance ability for  $\text{Si}_3\text{N}_4$ - $\text{Ti}_3\text{SiC}_2$  contacts. Figures 7(c) and 7(f) show the 3D optical microscopic images of the corresponding wear scars, which could clearly observe the wear scenario under the lubrication of different lubricants. The worn surfaces lubricated by glycerol (Figure 7(f)) exhibited considerably wider wear scars; however, the wear scar that is lubricated

by POE (Figure 7(c)) was narrow and deeper. This result further confirms the excellent antiwear properties of POE, corresponding with the results of SEM.

To gain further insights into the complex tribochemistry of the  $\text{Si}_3\text{N}_4$ -ILs- $\text{Ti}_3\text{SiC}_2$  interface, the worn surfaces of the  $\text{Ti}_3\text{SiC}_2$  disc lubricated with ILs were analyzed by XPS (Figure 8). The XPS analyses of P2p and N1s for neat POE were conducted before the tribo-tests (A), and the XPS spectra of Ti2p, Si2p, P2p, and N1s for POE were obtained after the tribo-tests (B). It can be seen that the XPS spectra of Ti2p peak at 454.50 eV correspond to  $\text{Ti}_3\text{SiC}_2$ , and the binding energy of Ti2p at 458.00 eV and 464.10 eV would be ascribed to  $\text{TiO}_2$  [16]. In addition, titanium phosphate (458.80 eV) [31] could be generated on the worn surface

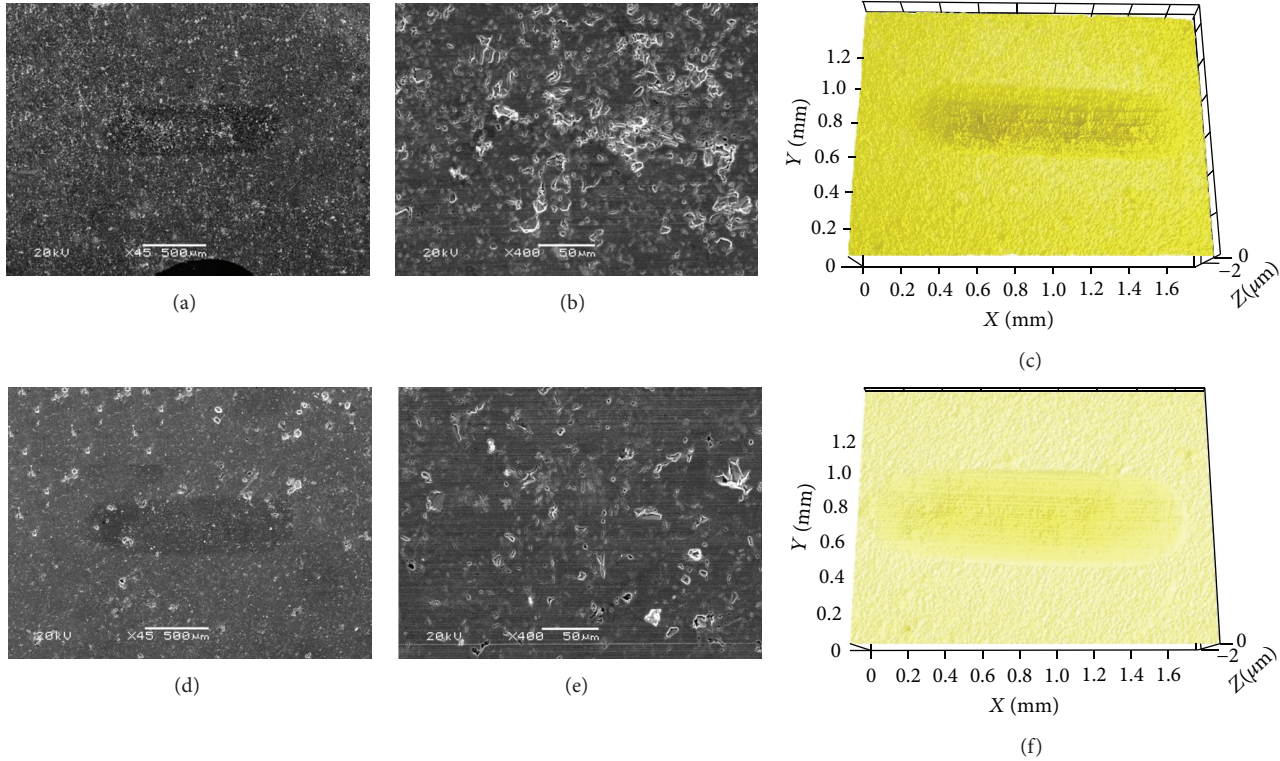


FIGURE 7: SEM and 3D morphologies of worn surfaces lubricated by POE and glycerol (SRV: 100 N, 100°C).

during the friction process because of the interaction between the substrate and the IL lubricant.

However, a decrease for the main binding energy of the Si2p peaks occurs after the friction tests, which is obtained from the comparison with the previous reported result [16]. It can be seen that the peak at 99.50 eV corresponds to  $\text{SiO}_2$ , and the peak at 100.60 eV is referred to  $\text{Si}_3\text{N}_4$ . There is also  $\text{SiO}_x$  present on the worn surface.

The binding energies of N1s undergo some changes compared with neat phosphate IL (the binding energy of N1s for POE appears at 401.20 eV). The appearance of N1s peaks at 398.70 eV after friction can be ascribed to  $\text{Si}_3\text{N}_4$ , which is in agreement with the Si2p peak at 100.60 eV. Amines and nitrogen oxides (400.90 eV) [32] are produced because of the high reactivity of cation moiety. However, there is little difference for the main binding energy of the P2p peaks of phosphate IL which occurred after the friction tests. Based on the binding energy of P2p at 133.25 eV, we can infer that phosphate anions are capable of reacting with Ti to form  $\text{Ti}_3(\text{PO}_4)_4$ .

Based on the above analysis, it can be concluded that ILs are easily adsorbed on the sliding surface of frictional pairs to form strongly ordered adsorbed films. Tribochemical reactions occur during the friction process, thus forming effective boundary-lubricating films which consisted of  $\text{TiO}_2$ ,  $\text{SiO}_x$ , titanium phosphate, amines, and nitrogen oxides. Hence, the friction and wear of  $\text{Ti}_3\text{SiC}_2$  materials are reduced.

## 4. Conclusions

Sliding friction experiments were carried out with the lubrication of alkyimidazolium dialkyl phosphates ILs. Based on the above experimental results, the following conclusions are drawn.

- (1) The alkyimidazolium dialkyl phosphates ILs were effective for  $\text{Si}_3\text{N}_4$ - $\text{Ti}_3\text{SiC}_2$  contacts lubrication and are superior to the glycerol and TBP both at 25°C and 100°C; the high thermal stability and excellent tribological properties of alkyimidazolium dialkyl phosphates ILs made it an attractive alternative to liquid lubricants for  $\text{Si}_3\text{N}_4$ - $\text{Ti}_3\text{SiC}_2$  contacts.
- (2) The friction coefficient and wear loss for  $\text{Si}_3\text{N}_4$ - $\text{Ti}_3\text{SiC}_2$  contacts decreased, which is attributed to the shorter alkyl chains of anion and the longer alkyl chains of cation in alkyimidazolium dialkyl phosphate ILs.
- (3) The tribological mechanisms of alkyimidazolium dialkyl phosphates ILs were mainly attributed to the load-carrying capacity of the ILs and the formation of surface protective films which consisted of  $\text{TiO}_2$ ,  $\text{SiO}_x$ , titanium phosphate, amines, and nitrogen oxides by the tribochemical reactions.

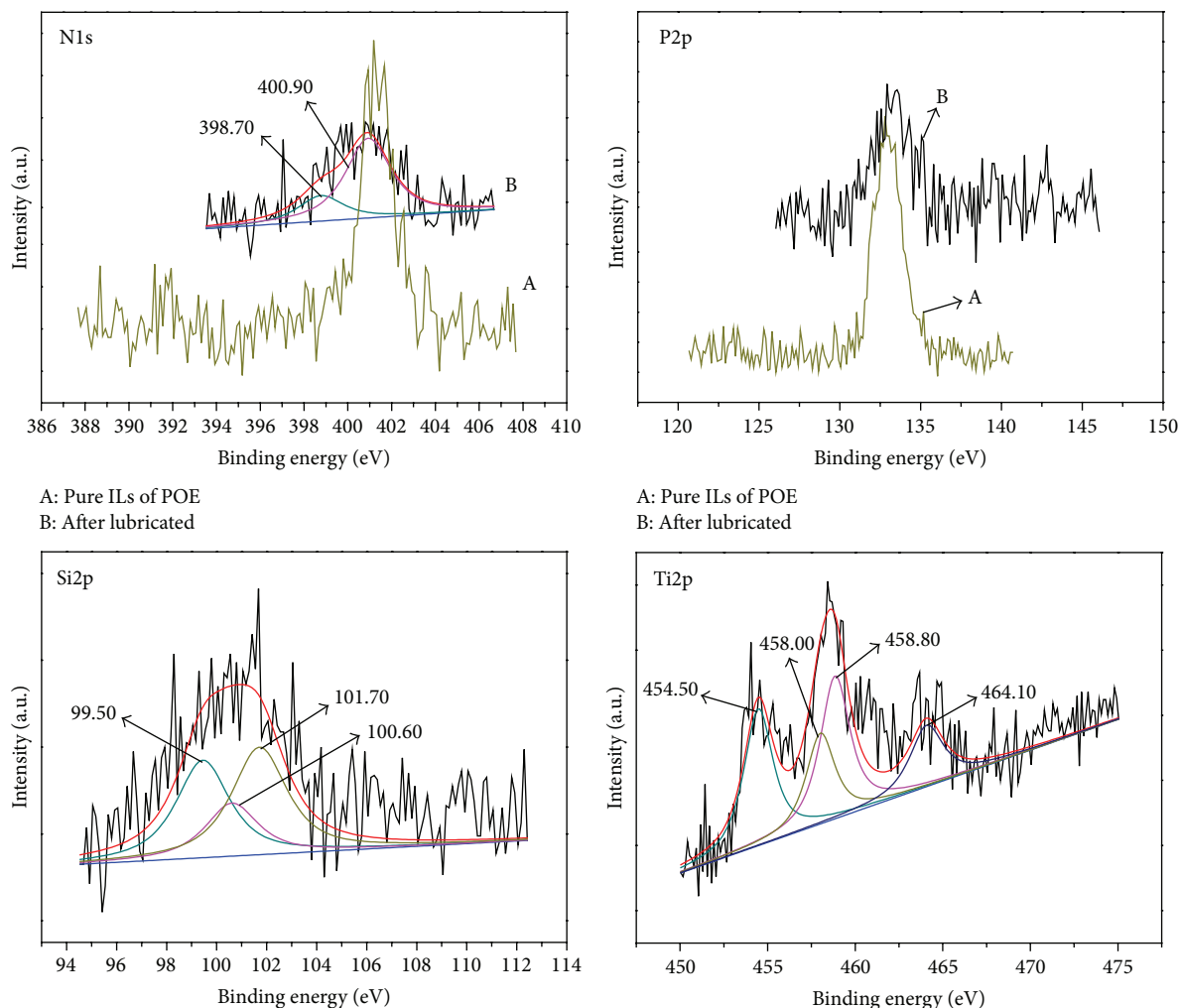


FIGURE 8: XPS spectra of the worn  $\text{Ti}_3\text{SiC}_2$  surfaces lubricated by POE under 100 N and  $100^\circ\text{C}$  (SRV: 100 N,  $100^\circ\text{C}$ ).

## Conflict of Interests

The authors declare that there is no conflict of interests regarding the publication of this paper.

## Acknowledgments

The authors acknowledge financial support from the National Key Basic Research Program of China (973) (2013CB632301) and the National Natural Science Foundation of China (51175492).

## References

- [1] M. W. Barsoum and T. El-Raghy, "Synthesis and characterization of a remarkable ceramic:  $\text{Ti}_3\text{SiC}_2$ ," *Journal of the American Ceramic Society*, vol. 79, no. 7, pp. 1953–1956, 1996.
- [2] S. Myhra, J. W. B. Summers, and E. H. Kisi, " $\text{Ti}_3\text{SiC}_2$ —a layered ceramic exhibiting ultra-low friction," *Materials Letters*, vol. 39, no. 1, pp. 6–11, 1999.
- [3] M. W. Barsoum, " $\text{M}_{N+1}\text{AX}_N$  phases: a new class of solids; thermodynamically stable nanolaminates," *Progress in Solid State Chemistry*, vol. 28, no. 1–4, pp. 201–281, 2000.
- [4] A. Souchet, J. Fontaine, M. Belin, T. Le Mogne, J.-L. Loubet, and M. W. Barsoum, "Tribological duality of  $\text{Ti}_3\text{SiC}_2$ ," *Tribology Letters*, vol. 18, no. 3, pp. 341–352, 2005.
- [5] J. L. Zeng, S. F. Ren, and J. J. Lu, "Phase evolution of  $\text{Ti}_3\text{SiC}_2$  annealing in vacuum at elevated temperatures," *International Journal of Applied Ceramic Technology*, vol. 10, pp. 527–539, 2013.
- [6] Y. Zhang, G. P. Ding, Y. C. Zhou, and B. C. Cai, " $\text{Ti}_3\text{SiC}_2$  self-lubricating ceramic," *Materials Letters*, vol. 55, pp. 285–289, 2002.
- [7] D. Sarkar, B. Basu, S. J. Cho, M. C. Chu, S. S. Hwang, and S. W. Park, "Tribological properties of  $\text{Ti}_3\text{SiC}_2$ ," *Journal of the American Ceramic Society*, vol. 88, no. 11, pp. 3245–3248, 2005.
- [8] T. El-Raghy, A. Zavaliangos, M. W. Barsoum, and S. R. Kalidindi, "Damage mechanisms around hardness indentations in  $\text{Ti}_3\text{SiC}_2$ ," *Journal of the American Ceramic Society*, vol. 80, no. 2, pp. 513–516, 1997.
- [9] M. Radovic, M. W. Barsoum, T. El-Raghy, J. Seidensticker, and S. Wiederhorn, "Tensile properties of  $\text{Ti}_3\text{SiC}_2$  in the 25– $1300^\circ\text{C}$

- temperature range," *Acta Materialia*, vol. 48, no. 2, pp. 453–459, 2000.
- [10] M. W. Barsoum and T. El-Raghy, "Synthesis and characterization of a remarkable ceramic:  $\text{Ti}_3\text{SiC}_2$ ," *Journal of the American Ceramic Society*, vol. 79, no. 7, pp. 1953–1956, 1996.
- [11] A. Crossley, E. H. Kisi, J. W. B. Summers, and S. Myhra, "Ultra-low friction for a layered carbide-derived ceramic,  $\text{Ti}_3\text{SiC}_2$ , investigated by lateral force microscopy (LFM)," *Journal of Physics D: Applied Physics*, vol. 32, no. 6, pp. 632–638, 1999.
- [12] Z. Sun, Y. Zhou, and S. Li, "Tribological behavior of  $\text{Ti}_3\text{SiC}_2$ -based material," *Journal of Materials Science and Technology*, vol. 18, no. 2, pp. 142–145, 2002.
- [13] A. Souchet, J. Fontaine, M. Belin, T. L. Mogne, J.-L. Loubet, and M. W. Barsoum, "Tribological duality of  $\text{Ti}_3\text{SiC}_2$ ," *Tribology Letters*, vol. 18, no. 3, pp. 341–352, 2005.
- [14] Y. Hibi, K. Miyake, T. Murakami, and S. Sasaki, "Tribological behavior of SiC-reinforced  $\text{Ti}_3\text{SiC}_2$ -based composites under dry condition and under lubricated condition with water and ethanol," *Journal of the American Ceramic Society*, vol. 89, no. 9, pp. 2983–2985, 2006.
- [15] Z.-K. Du, S.-F. Ren, J.-B. Wang, J.-H. Meng, and J.-J. Lu, "Tribological properties of  $\text{Ti}_3\text{SiC}_2$ - $\text{Al}_2\text{O}_3$  composite in different liquid," *Tribology*, vol. 30, no. 3, pp. 223–228, 2010 (Chinese).
- [16] W. X. Hai, J. L. Zeng, S. F. Ren, J. H. Meng, and J. J. Lu, "Tribological behavior and tribochemistry of self-mated  $\text{Ti}_3\text{SiC}_2$  in ethanol," *Tribology Letter*, vol. 50, pp. 449–455, 2013.
- [17] M. D. Bermúdez, A. E. Jiménez, J. Sanes, and F. J. Carrión, "Ionic liquids as advanced lubricant fluids," *Molecules*, vol. 14, no. 8, pp. 2888–2908, 2009.
- [18] I. Minami, "Ionic liquids in tribology," *Molecules*, vol. 14, no. 6, pp. 2286–2305, 2009.
- [19] F. Zhou, Y. M. Liang, and W. M. Liu, "Ionic liquid lubricants: designed chemistry for engineering applications," *Chemical Society Reviews*, vol. 38, no. 9, pp. 2590–2599, 2009.
- [20] C. A. Angell, Y. Ansari, and Z. Zhao, "Ionic Liquids: past, present and future," *Faraday Discussions*, vol. 154, pp. 9–27, 2012.
- [21] A. E. Somers, P. C. Howlett, D. R. MacFarlane, and M. Forsyth, "A review of Ionic liquid lubricants," *Lubricants*, vol. 1, pp. 3–21, 2013.
- [22] Z. G. Mu, F. Zhou, S. X. Zhang, Y. M. Liang, and W. M. Liu, "Effect of the functional groups in ionic liquid molecules on the friction and wear behavior of aluminum alloy in lubricated aluminum-on-steel contact," *Tribology International*, vol. 38, no. 8, pp. 725–731, 2005.
- [23] K. Demizu, H. Ishigaki, H. Kakutani, and F. Kobayashi, "The effect of trialkyl phosphites and other oil additives on the boundary lubrication of ceramics: friction of silicon-based ceramics," *Journal of Tribology*, vol. 114, no. 4, pp. 653–658, 1992.
- [24] J. J. Wei and Q. J. Xue, "Tribochemical mechanisms of  $\text{Si}_3\text{N}_4$  with additives," *Wear B*, vol. 162–164, pp. 1068–1072, 1993.
- [25] L. Zhang, D. P. Feng, and B. Xu, "Tribological characteristics of alkylimidazolium diethyl phosphates ionic liquids as lubricants for steel-steel contact," *Tribology Letters*, vol. 34, no. 2, pp. 95–101, 2009.
- [26] S. F. Ren, J. H. Meng, J. Lu, and S. Yang, "Tribological behavior of  $\text{Ti}_3\text{SiC}_2$  sliding against Ni-based alloys at elevated temperatures," *Tribology Letters*, vol. 31, no. 2, pp. 129–137, 2008.
- [27] X.-C. Jiang, C.-Y. Yu, J. Feng, C.-X. Li, and Z.-H. Wang, "Synthesis and application of ionic liquid 1-butyl-3-methylimidazolium dibutyl phosphate," *Journal of Beijing University of Chemical Technology*, vol. 33, no. 1, pp. 5–7, 2006.
- [28] Z.-G. Mu, F. Zhou, S.-X. Zhang, Y.-M. Liang, and W.-M. Liu, "Preparation and characterization of new phosphonyl-substituted imidazolium ionic liquids," *Helvetica Chimica Acta*, vol. 87, no. 10, pp. 2549–2555, 2004.
- [29] S. W. Zhang, L. T. Hu, D. Qiao, D. P. Feng, and H. Z. Wang, "Vacuum tribological performance of phosphonium-based ionic liquids as lubricants and lubricant additives of multialkylated cyclopentanes," *Tribology International*, vol. 66, pp. 289–295, 2013.
- [30] X. Q. Liu, F. Zhou, Y. M. Liang, and W. M. Liu, "Tribological performance of phosphonium based ionic liquids for an aluminum-on-steel system and opinions on lubrication mechanism," *Wear*, vol. 261, no. 10, pp. 1174–1179, 2006.
- [31] <http://srdata.nist.gov/xps/>.
- [32] M. R. Cai, Y. M. Liang, M. H. Yao, Y. Q. Xia, F. Zhou, and W. M. Liu, "Imidazolium ionic liquids as antiwear and antioxidant additive in poly(ethylene glycol) for steel/steel contacts," *ACS Applied Materials and Interfaces*, vol. 2, no. 3, pp. 870–876, 2010.

## Research Article

# Tribological Performance of Silahydrocarbons Used as Steel-Steel Lubricants under Vacuum and Atmospheric Pressure

Hai-Zhong Wang,<sup>1,2</sup> Song-Wei Zhang,<sup>1,2</sup> Dan Qiao,<sup>1,2</sup> Da-Peng Feng,<sup>1</sup> and Wei-Min Liu<sup>1</sup>

<sup>1</sup> State Key Laboratory of Solid Lubrication, Lanzhou Institute of Chemical Physics, Chinese Academy of Sciences, Lanzhou 730000, China

<sup>2</sup> Graduate University of the Chinese Academy of Sciences, Beijing 100049, China

Correspondence should be addressed to Da-Peng Feng; dpfeng@licp.cas.cn and Wei-Min Liu; wmliu@licp.cas.cn

Received 6 March 2014; Accepted 2 April 2014; Published 16 April 2014

Academic Editor: Jun Yang

Copyright © 2014 Hai-Zhong Wang et al. This is an open access article distributed under the Creative Commons Attribution License, which permits unrestricted use, distribution, and reproduction in any medium, provided the original work is properly cited.

The silahydrocarbons of tetraalkylsilanes with different substituted alkyl groups (named as SiCH) were synthesized and evaluated as lubricants for steel-steel contacts by a home-made vacuum four-ball tribometer (VFBT-4000) under atmospheric pressure and under vacuum pressure ( $5 \times 10^{-4}$  Pa). The SiCH oils possess better thermal stability, low temperature fluidity, and lower saturated vapor pressure than those of multialkylatedcyclopentanes (MACs). The tribological performances of the SiCH oils are also superior to those of MACs and PFPE-Z25 in terms of friction-reduction ability and antiwear capacity under sliding friction at vacuum. The SEM/EDS and XPS results reveal that the boundary lubricating film consisting of  $(-O-Si-R-)_n$  compounds is formed by tribochemical reactions and serious adhesion wear under atmospheric pressure and the film consisting of  $(-Si-R-Si-)_n$  compounds is formed on the worn surface under vacuum pressure.

## 1. Introduction

The use of space satellites for communication, navigation, and defense is becoming more and more important. High costs for both construction and launch satellites are driving the need to extend the service life of these satellites from the current 5 to 8 years to 10 years and even for a longer period. According to NASA, many mechanical failures in spacecraft were caused by tribological problems [1–6]. Thus, the improvement of lubrication and antiwear performance for the mechanical systems is the key to extend the service life of satellites and spacecrafts. The synthetic liquid lubricants have been very commonly used in aerospace equipment for many years. And low vapor pressure, low pour point, good thermal stability, and good lubrication properties, particularly, good boundary lubrication performance and low wear formation rates, are crucial physicochemical and tribological properties which is to be ensured for aerospace devices [7, 8]. The majority of current aerospace applications use mineral oils, perfluoropolyalkylethers (PFPEs), or synthetic hydrocarbons, such

as multialkylatedcyclopentanes (MACs) and polyalphaolefins (PAO) [9, 10]. PFPEs are the mostly used liquid lubricants for aerospace mechanisms but suffer from poor boundary lubrication capability, the incompatibility with conventional additives, the catalytic degradation, and so forth [11, 12]. MACs and PAO are of limited use at low temperature and in vacuum.

Recently, a relatively new type of space lubricants (i.e., silahydrocarbons) has been developed. These lubricants contain only silicon carbon and hydrogen [8]. Early studies [13–16] have shown that silahydrocarbons have significantly lower melting points compared to corresponding hydrocarbons. Silahydrocarbons are superior to mineral oils and synthetic hydrocarbons in both thermal and oxidative stabilities as well as viscosity-temperature behaviour. They possess unique friction-reducing and antiwear properties while retaining the ability to solubilize conventional additive, which is an attractive future lubrication requirement for aircraft and aerospace mechanisms, particularly for low temperature and high vacuum applications use in space.

The aim of this work was to study the physical properties of silahydrocarbons of tetraalkylsilanes with different substituted alkyl groups (named as SiCH) and evaluate the tribological performance of SiCH as liquid lubricants for steel-steel contacts by a vacuum four-ball tribometer under atmospheric pressure and under vacuum pressure. For comparison, the tribological properties of two aerospace lubricants, namely, PFPE-Z25 (under the trade name "Z25") and MACs, were also investigated under the same circumstances.

## 2. Experimental

The SiCH oils and MACs were synthesized according to the references in laboratory [17–19], and the molecular structures of the SiCH oils were characterized by an intensity fluctuation spectroscopy 66 v/s Fourier transformation infrared (FTIR) spectroscopy and 400 MHz Bruker-400 FT nuclear magnetic resonance spectroscopy (NMR) spectrometers. PFPE-Z25 is commercially provided by Fomblin Inc., in the US, which is used in the aviation and military industries.

The molecular structures of the SiCH oils and MACs are shown in Figure 1; several typical physical properties of the SiCH oils and MACs are shown in Table 1. The kinematic viscosities of the lubricants were measured using an SVM3000 Stabinger viscometer at different temperatures according to ASTM D445 designation. The saturated vapor pressure of the lubricants was evaluated on a home-made vacuum grease saturated vapor pressure tribometer by the method of evaporation. Thermogravimetric analysis (TGA) was performed on a Perkin-Elmer TGA-7 conducted in nitrogen atmosphere from 20°C to 600°C at a heating speed of 10°C/min. The evaporation weight loss of the lubricants was evaluated in a vacuum oven under approximately  $5 \times 10^{-3}$  Pa at 125°C (the results were shown in Table 2).

In order to test the anticorrosion properties of the SiCH oil to metal substrates in the presence of water, the corrosion tests were carried out in an environmental chamber under the hot and humid condition according to standard method of ASTM D130-94. The polished GCr15 bearing steel (SAE52100) block was used as the substrate, and the testing conditions are as follows: test temperature of 100°C, 80% relative humidity, and duration of 24 h.

The tribological performances of the SiCH oils, MACs, and PFPE-Z25 as lubricants for steel-steel contacts were evaluated on a home-made vacuum four-ball tribometer (VFBT-4000) under atmospheric pressure and under vacuum pressure ( $5 \times 10^{-4}$  Pa). The vacuum four-ball tribometer which was designed and manufactured by the State Key Laboratory of Solid Lubrication, Lanzhou Institute of Chemical Physics, Chinese Academy of Sciences, based on the configuration of a traditional four-ball tribometer, was employed. As shown schematically in Figure 2, the vacuum chamber was evacuated by using a series of a turbomolecular pump and a mechanical pump. The tribological characteristics of liquid lubricants for aerospace applications were evaluated by this tribometer under the pressures of  $5 \times 10^{-4}$  Pa. It can also be run at lower vacuum (about 10 Pa) and at atmospheric pressure with air or nitrogen.

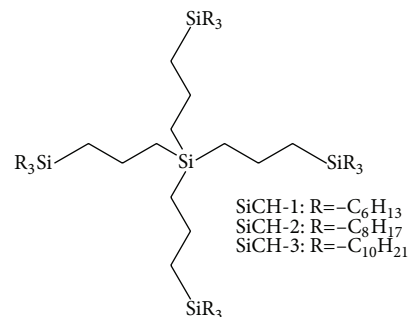


FIGURE 1: Molecular structures of the prepared SiCH oils.

All tribological performance tests were performed under the load of 392 N with a rotating speed of 1450 rpm at 25°C for 30 min. The steel balls (diameter 12.7 mm, hardness HRC 59 to 61) were made of GCr15 bearing steel (SAE 52100). Before and after each test, test specimens were ultrasonically cleaned in petroleum ether (normal alkane with a boiling point of 60~90°C). For each sample, three tests were conducted to minimize data scattering. At the end of each test, the wear scar diameters of the three lower balls were measured with an optical microscope with an accuracy of 0.01 mm, and then the average wear scar diameter of the three identical tests was calculated as the wear scar diameter (WSD) in this paper. The friction coefficients were recorded automatically with a computer equipped with a four-ball tribometer.

Experiments using a scanning electron microscope with a Kevex energy dispersive X-ray analyzer attachment (SEM/EDS) and an X-ray photoelectron spectrometer (XPS) were conducted to examine the morphology and chemical composition of the wear scars and the possible tribochemical changes involved in the sliding process. The SEM/EDS analysis was performed on a JSM-5600LV SEM. The XPS analysis was carried out on a PHI-5702 multifunctional X-ray photoelectron spectroscope, with Al-K $\alpha$  radiation as the exciting source. The binding energies of the target elements were determined at a pass energy of 29.35 eV with resolution of approximately  $\pm 0.3$  eV, with the binding energy of carbon (C1s: 284.8 eV) as the reference.

## 3. Results and Discussion

**3.1. Physical Properties of Silahydrocarbon Lubricants.** The molecular structures of SiCH are shown in Figure 1 and are analyzed by infrared spectroscopy (IR) and proton nuclear magnetic resonance ( $^1\text{H-NMR}$ ). It can be seen that the molecular structure of SiCH resembles branched macromolecules (tree-like structure); the substituted alkyl ( $-\text{R}$ ) in the molecular structures was selected as hexyl( $-\text{C}_6\text{H}_{13}$ ), octyl( $-\text{C}_8\text{H}_{17}$ ), and decyl( $-\text{C}_{10}\text{H}_{21}$ ), named as SiCH-1, SiCH-2, and SiCH-3, respectively.

As an example, the findings of SiCH-3 are shown as follows [IR (KBr film),  $\nu_{\text{max}}/\text{cm}^{-1}$ , Figure 3(a)]: C–H stretching vibration bands appear at  $2956\text{ cm}^{-1}$ ,  $2921\text{ cm}^{-1}$ , and  $2853\text{ cm}^{-1}$ ; C–H band modes at  $1466\text{ cm}^{-1}$  and  $1378\text{ cm}^{-1}$ , and the band at  $720\text{ cm}^{-1}$  is the  $-(\text{CH}_2)_7-$ rocking vibration; Si–C

TABLE 1: Physical properties of these liquid lubricants.

Lubricants	Saturated vapor pressure/Torr, 25°C	Kinematic viscosity ( $\text{mm}^2\cdot\text{s}^{-1}$ )				Properties		
		-20°C	40°C	100°C	VI	Density/ $\text{kg}\cdot\text{m}^{-3}$	TGA (onset decomposition temperature/°C)	Pour point/°C
SiCH-1	$3.4 \times 10^{-9}$	2180	73.8	13.2	184	843.2	362	<-55
SiCH-2	$6.2 \times 10^{-10}$	2621	86.6	15.4	189	851.0	387	<-55
SiCH-3	$2.0 \times 10^{-10}$	3025	97.2	17.2	194	857.4	394	<-55
MACs	$1.7 \times 10^{-8}$	2550	58.1	8.8	140	8471	385	-55
PFPE-Z25	$2.9 \times 10^{-12}$	—	160.5	48.4	350	1850.8	383	-73

TABLE 2: Evaporation weight loss of the SiCH oils, MACs, and PFPE-Z25 under vacuum pressure (24 h at 125°C,  $5 \times 10^{-3}$  Pa).

Lubricants	Evaporation weight loss (wt.%)
SiCH-1	0.91
SiCH-2	0.63
SiCH-3	0.28
MACs	2.32
PFPE-Z25	0.23

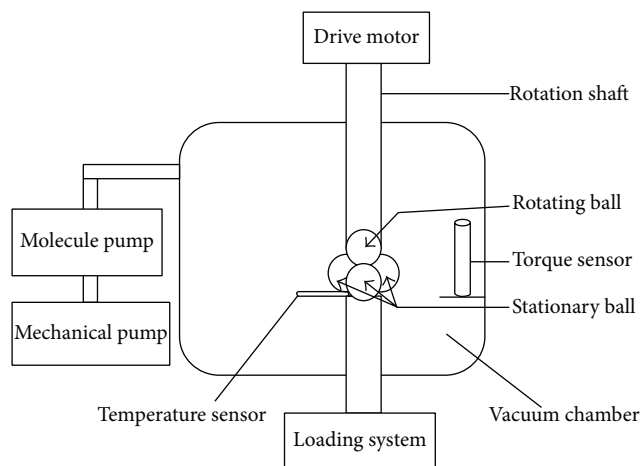


FIGURE 2: Schematic illustration of the vacuum four-ball tribometer.

stretching vibration bands at  $1411\text{ cm}^{-1}$ ,  $1176\text{ cm}^{-1}$ ,  $1139\text{ cm}^{-1}$ , and  $895\text{ cm}^{-1}$ .  $^1\text{H-NMR}$  (chloroform-d, Figure 3(b)) is as follows: 1.29 [b, 152 H], 0.91 to 0.89 [b, 36 H], and 0.76 to 0.50 [m, 40 H]. Both of the IR and  $^1\text{H NMR}$  results proved that the synthetic compound has the designed molecular structure.

Table 1 shows several physical properties of SiCH, MACs, and PFPE-Z25 oils. It can be seen that the three kinds of SiCH oils have lower saturated vapor pressure compared with MACs, but higher than that of PFPE-Z25 oil. The viscosity indices (named as VI) of the three SiCH oils are similar. The kinetic viscosity increases with the carbon number increase of the substituted alkyl groups within the SiCH molecular structures; the viscosity of SiCH-1 is the smallest among the three SiCH oils at  $-20^\circ\text{C}$ , which are also superior to MACs.

Table 1 reveals that the three SiCH oils also exhibit better low temperature fluidity, with their pour points lower than  $-55^\circ\text{C}$ . By contrast, MACs could not flow under  $-55^\circ\text{C}$ . These results indicate that the SiCH synthetic oils can be used in a wide temperature range and especially exhibit good fluidity under low temperature conditions.

Table 1 also presents the thermal stability results of these oils. SiCH-3 exhibits the highest thermal decomposition temperature among all the liquid lubricants in this study. Moreover, the thermal stability of the SiCH oils increases with an increase in the chain length of the substituted alkyl within the molecular structures.

Meanwhile, the evaporation weight loss results of these oils at  $125^\circ\text{C}$  with 24 hours under vacuum pressure (nearly  $5 \times 10^{-3}$  Pa) are listed in Table 2. The vacuum evaporation weight loss of SiCH-3 is the smallest among the oils in this study, which is close to that of the PFPE-Z25 oil; it is also indicated that the lubricant with longer chain length structure would show lower volatility. The results show that all of the SiCH oils are superior to the synthetic oil of MACs in the evaporation weight loss, which is due to the tree-like molecular structure of SiCH.

The corrosion results of SiCH-3 with steel were selected to describe the anticorrosion property in Figure 4 because the SiCH oils possess the similar anticorrosion properties. It can be seen that there is no corrosion on bearing steel with the oils under the hot and humidity conditions, and no corrosion could be produced during the friction process.

**3.2. Tribological Performance.** Figures 5 and 6 present the curves of friction coefficient (Figures 5(a) and 5(b)) and the average friction coefficient (Figure 6) lubricated with the SiCH oils, MACs, and PFPE-Z25 by a vacuum four-ball tribometer under atmospheric pressure and under vacuum pressure, respectively. The wear scar diameters of these lubricants by this experiment are shown in Figure 7.

It can be seen from Figures 5(a) and 6 that MACs show the steadiest friction curves and the lowest average friction coefficient (approximately 0.08) compared with the SiCH oils and PFPE-Z25 under atmospheric pressure. It is also seen that SiCH oils with different chain of the substituted alkyl groups exhibit different tribological behavior. The friction coefficient decreases along with the increase of carbon number in the alkyl chain under this tested condition. The curves of friction

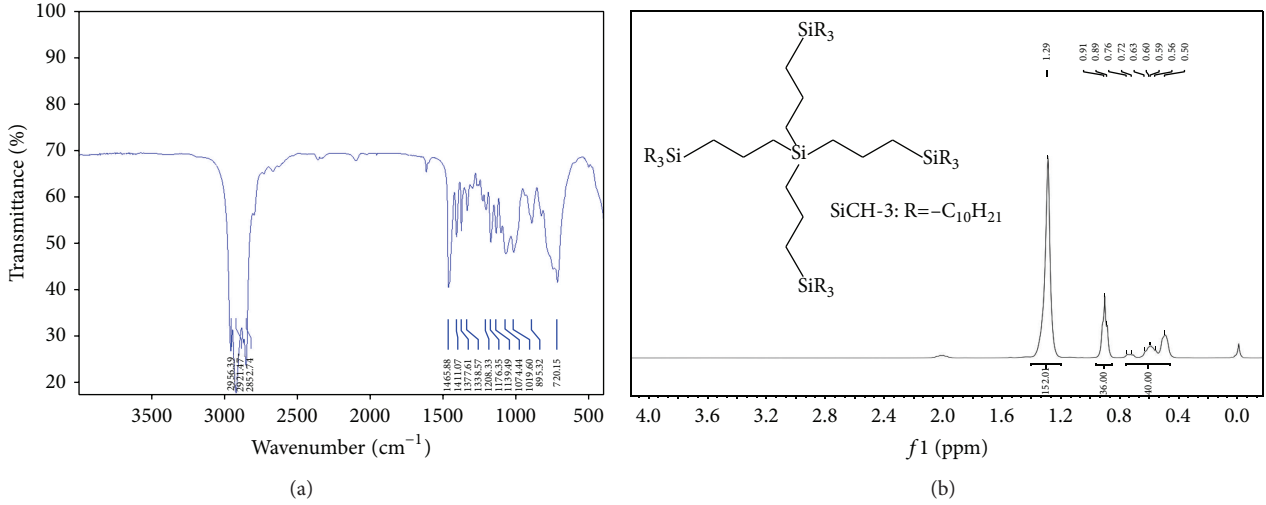


FIGURE 3: FTIR spectrum (a) and <sup>1</sup>H-NMR spectrum (b) of the SiCH-3 oil.

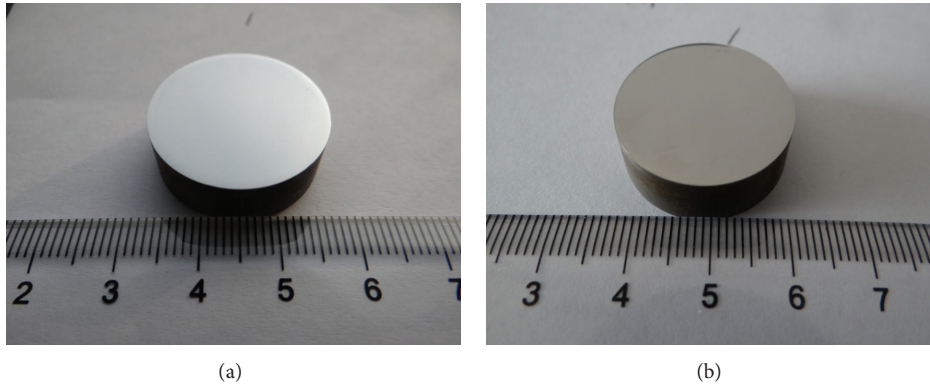


FIGURE 4: The corrosion capability test of SiCH-3 oils on steel SAE 52100 ((a) before corrosion test; (b) after corrosion test) (100°C, 24 h, and relative humidity 80%).

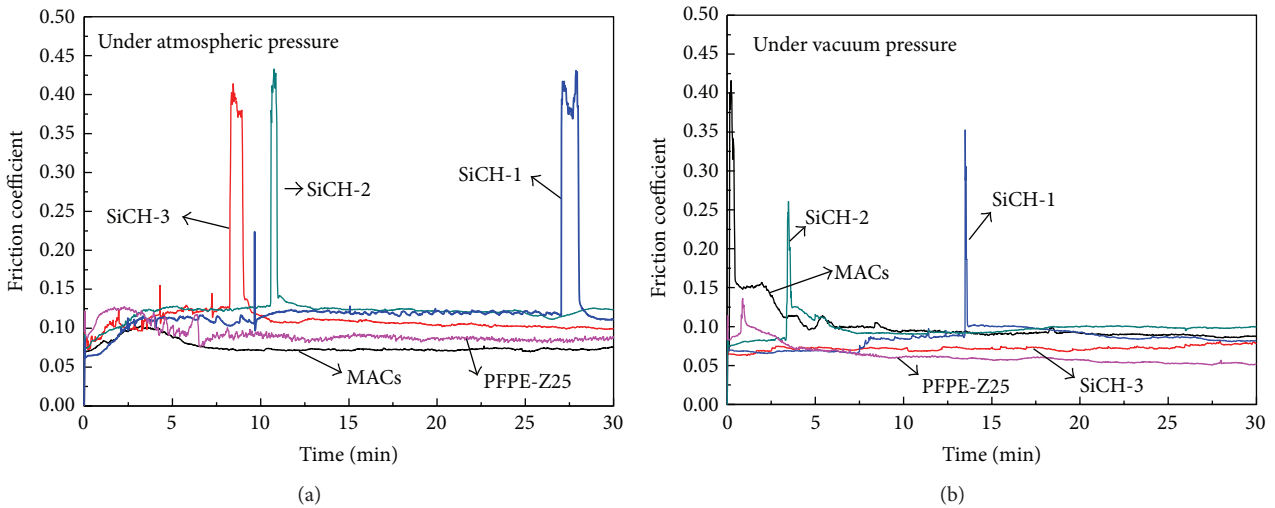


FIGURE 5: The friction coefficient curves of the lubricants for steel-steel contacts under atmospheric pressure (a) and under vacuum pressure (b) (392 N, 30 min 1450 rpm, and four-ball tribometer).

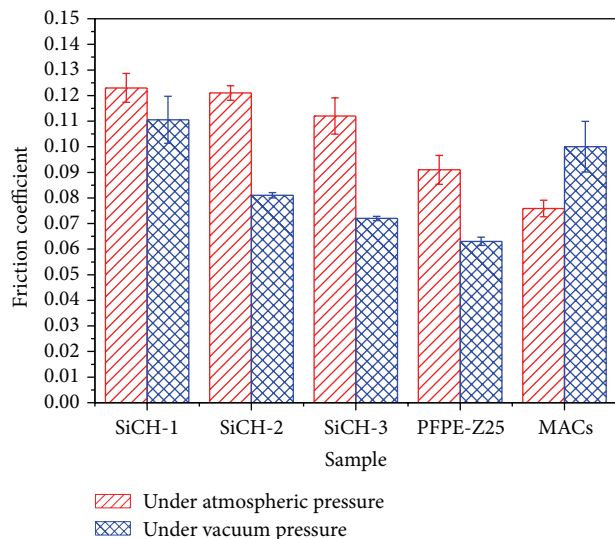


FIGURE 6: The average friction coefficients of lubricants for steel-steel contacts under atmospheric pressure and under vacuum pressure (392 N, 30 min, 1450 rpm, and four-ball tribometer).

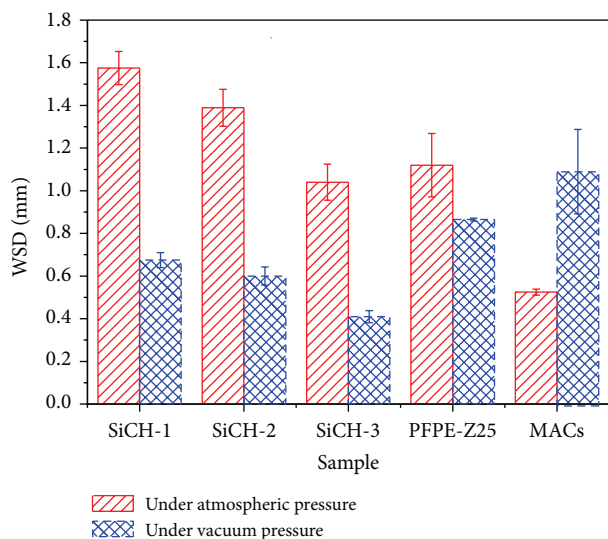


FIGURE 7: Wear scar diameters of SiCH oils for steel-steel contacts under atmospheric pressure and under vacuum pressure (392 N, 30 min, 1450 rpm, and four-ball tribometer).

coefficient of the SiCH oils are all instable and show transient seizure-like high friction [20–22] and transient dry friction or abrasive wear occurred on the worn surface. This result should be explained as that some compounds, for example,  $\text{SiO}_x$ , might be produced on the steel surfaces lubricated by the SiCH oils during the high friction period, which facilitate returning to a low-friction period. Meanwhile, comparing the antiwear performances of these lubricants under atmospheric pressure as seen in Figure 7, MACs exhibit the smallest WSD. In addition, the antiwear property of SiCH-3 is superior to that of PFPE-Z25 and the WSD lubricated by SiCH-3 is the smallest among the three SiCH oils. This finding

indicates that the tribological properties of the SiCH oils would improve with an increase in the chain length of the substituted alkyl in case this tendency continues.

The curves of friction coefficient results of these lubricants under vacuum pressure are shown in Figure 5(b). SiCH-3 exhibits the steadiest curves of friction coefficient, and did not show transient seizure-like high friction during the entire sliding process under vacuum pressure. The MACs show higher average friction under vacuum pressure than that under atmospheric pressure, which is contrary to the results of other lubricants. It can be seen from Figure 7 that SiCH-3 also shows the smallest wear scar diameter as lubricant for steel-steel contacts among the three SiCH oils, which is benefited from the longer chain in the molecular structure, which indicating that the antiwear property of SiCH-3 is superior to that of PFPE-Z25 and MACs under vacuum pressure. It is noticeable that the average friction coefficient and WSD of MACs are the maximum under vacuum pressure, which is contrary to the results obtained under atmospheric pressure. The tribochemical reactions of the SiCH oils with the steel surface are different under atmospheric pressure and the vacuum pressure; thus, different boundary films might be formed during the sliding friction under different conditions.

**3.3. Surface Analysis.** Since SEM/EDS and XPS analyses of the worn scars lubricated by SiCH oils with different substituted alkyl groups show similar results, we describe here the emphasis of the results of SiCH-3. Figure 8 shows the typical SEM images and elemental distributions of silicon on the wear scar surfaces lubricated by SiCH-3 under atmospheric pressure and under vacuum pressure, respectively. The wear scar (Figure 8(d)) that was lubricated by SiCH-3 under vacuum pressure is smaller and the worn surface is smooth along with mild scuffing. However, wider wear scar is shown in Figure 8(a) after the lubrication by SiCH-3 under the atmospheric pressure with serious adhesion wear (Figure 8(b)). The results of wear scar morphologies on the worn surfaces (Figures 8(b) and 8(e)) are consistent with those of the elemental distributions of silicon (Figures 8(c) and 8(f)), implying that silicon is enriched on the wear track and the concentration of silicon is clearly higher on the worn surface lubricated under vacuum friction condition than that under atmospheric friction condition.

The SEM/EDS analysis shows that the elemental distribution of silicon on the worn surface lubricated under vacuum friction condition is different from that under atmospheric friction condition, which explains the different tribological performances of the oils under atmospheric pressure and under vacuum pressure.

XPS analysis is used to further clarify the chemical states of the typical elements on the wear scar surfaces lubricated by the SiCH oils. XPS results indicate that complicated tribochemical reaction occurred during friction. Figure 9 shows the XPS spectra of typical elements of O and Si on the worn surfaces lubricated by SiCH-3 under atmospheric pressure and under vacuum pressure. Under atmospheric pressure, it can be seen that the binding energy of  $\text{Si}2p$  appears at 102.3 eV, combining with the binding energy of  $\text{O}1s$  at 531.3 eV, which

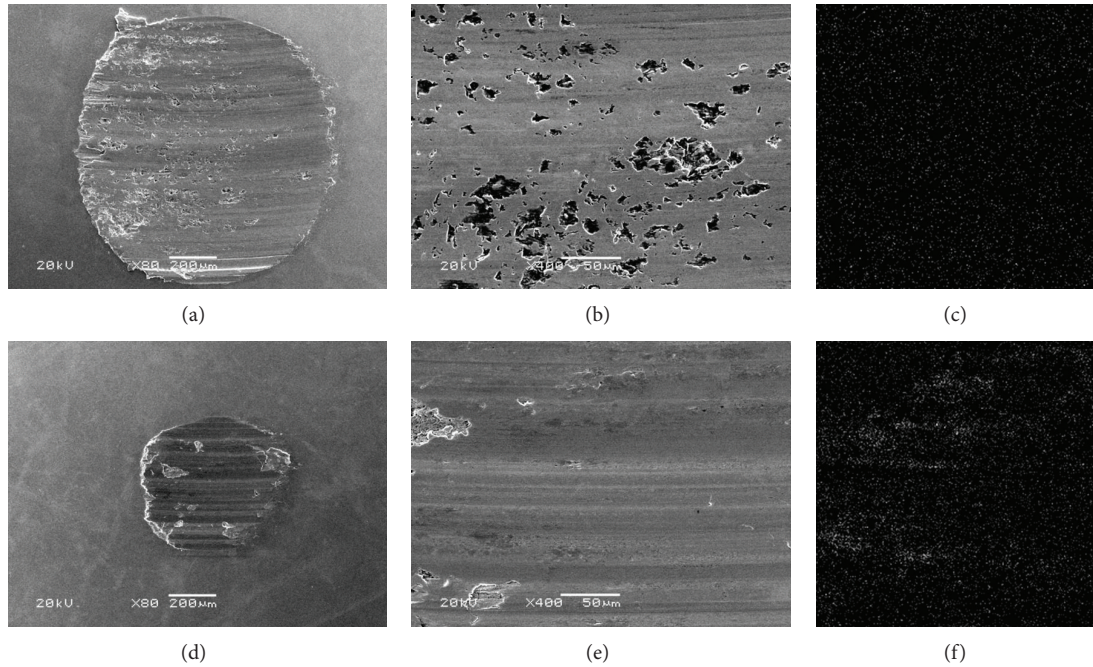


FIGURE 8: SEM images ((a), (b), (d), and (e)) and elemental distribution of Si ((c) and (f)) on the worn surface of the steel ball lubricated by SiCH-3 under atmospheric pressure ((a), (b), and (c)) and under vacuum pressure ((d), (e), and (f)).

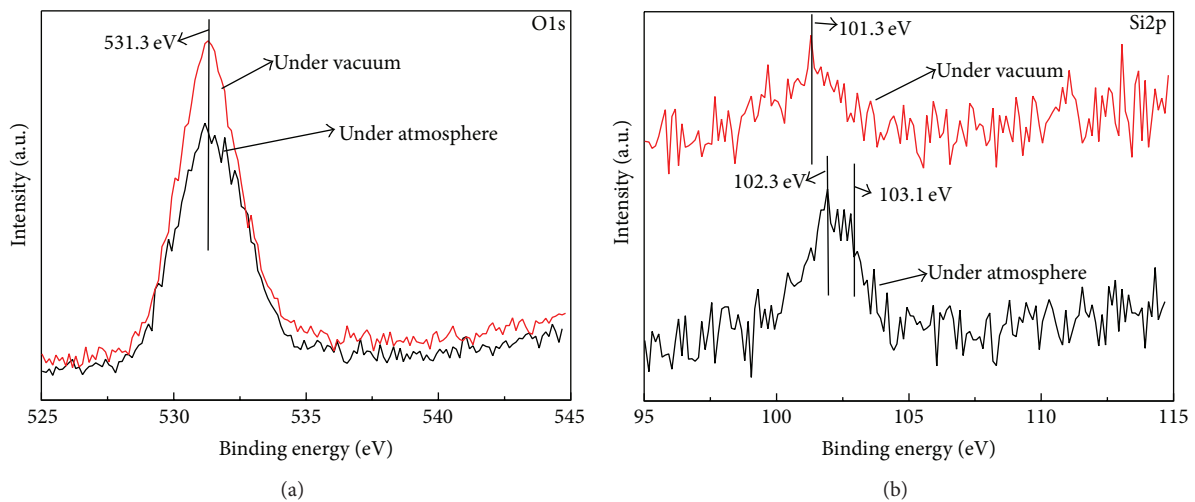


FIGURE 9: XPS spectra of O1s (a) and Si2p (b) of the worn surface lubricated by SiCH-3 under atmospheric pressure and under vacuum pressure.

is corresponding to the compound of  $(-\text{O}-\text{Si}-\text{R}-)_n$  [23]. Moreover, the Si2p peak at 103.1 eV is ascribed to  $\text{SiO}_2$ . Lubricating with SiCH oil under atmospheric condition, much oxygen dissolving in the oil participated in the tribochemical reaction to produce some oxidative compounds.

However, the main binding energy of Si2p (101.7 eV) under vacuum pressure is different with respect to that of Si2p (102.3 eV) under atmospheric pressure, which is characterized by the compound of  $(-\text{Si}-\text{R}-\text{Si})_n$  with lack of

oxygen. And abrasive wear is observed on the worn surface under vacuum pressure during the friction process, which can be seen from the SEM images (Figures 8(d) and 8(e)). There is few flaking on the worn track, which presents that SiCH performs excellent lubricating properties under vacuum pressure.

On the basis of the above results, it illustrates that different tribochemical reactions occurred on the worn surface lubricated by the SiCH oils when the sliding friction experiments

were carried out under different conditions. The boundary film consisted of the compound  $(-O-Si-R-)_n$  and  $SiO_2$  is formed by the tribochemical reaction and serious adhesion wear under atmospheric pressure, whereas the compound of  $(-Si-R-Si)_n$  is formed on the worn surface by abrasive wear under vacuum pressure during the sliding friction with the SiCH oils.

#### 4. Conclusions

Sliding friction experiments of SiCH synthetic oils as lubricants for steel-steel contacts were carried out on a vacuum four-ball tribometer under different atmospheric pressure. Based on the above experimental results, the following conclusions are drawn.

- (i) The SiCH synthetic oils were prepared and they possess good thermal stability, low temperature fluidity, and lower saturated vapor pressure, denoting that they are superior to that of MACs as aerospace lubricants.
- (ii) The SiCH with decyl group substituted shows the best tribological behaviour among the three SiCH synthetic oils for steel-steel contacts under vacuum pressure and is superior to those of MACs and PFPE-Z25 in terms of friction-reduction ability and antiwear capacity.
- (iii) The SEM/EDS and XPS results reveal that the tribochemical reactions of SiCH oils with the steel surface are different under atmospheric pressure and under vacuum pressure during the sliding friction. The boundary lubricating film that consisted of the compound of  $(-O-Si-R-)_n$  and  $SiO_2$  is formed by the tribochemical reaction and serious adhesion wear under atmospheric pressure, whereas the compound of  $(-Si-R-Si)_n$  is formed on the worn surface by abrasive wear under vacuum pressure.

#### Conflict of Interests

The authors declare that there is no conflict of interests regarding the publication of this paper.

#### Acknowledgments

The authors acknowledge financial support from the National Key Basic Research Program of China (973) (2013CB632301) and the National Natural Science Foundation of China (51175492).

#### References

- [1] T. Krantz and F. Oswald, "Wear of spur gears having a dithering motion and lubricated with a perfluorinated polyether grease," NASA Technical Memorandum 215008, 2007.
- [2] L. J. Gschwender, C. E. Snyder Jr., M. Massey, and S. Peterangelo, "Improved liquid/grease lubricants for space mechanism," *Lubrication Engineering*, vol. 56, no. 12, pp. 25–31, 2000.
- [3] W. J. Bartz, "Synthetic hydraulic fluids for high performance applications," *Lubrication Engineering*, vol. 56, no. 10, pp. 42–53, 2000.
- [4] R. Fusaro, "Preventing spacecraft failures due to tribological problems," NASA Technical Memorandum 210806, 2001.
- [5] D. N. Baker, "Effects of the Sun on the Earth's environment," *Journal of Atmospheric and Solar-Terrestrial Physics*, vol. 62, no. 17–18, pp. 1669–1681, 2000.
- [6] D. N. Baker, "What is space weather?" *Advances in Space Research*, vol. 22, no. 1, pp. 7–16, 1998.
- [7] E. V. Zaretsky, "Liquid lubrication in space," *Tribology International*, vol. 23, no. 2, pp. 75–93, 1990.
- [8] W. R. Jones, B. A. Shogrin, and M. J. Jansen, "Research on liquid lubricants for space mechanisms," *Journal of Synthetic Lubrication*, vol. 17, no. 2, pp. 109–122, 2000.
- [9] S. S. Hirsch and W. J. Bailey, "Base-catalyzed alkylation of cyclopentadiene rings with alcohols and amines," *Journal of Organic Chemistry*, vol. 43, no. 21, pp. 4090–4094, 1978.
- [10] J. Sicre, P. Vergne, P. Prat, and M. Pochard, "New consideration on fluid lubricants for spacecraft applications," in *Proceedings of the 6th European Space Mechanism and Tribology Symposium*, pp. 169–176, Zurich, Switzerland, 1995.
- [11] E. Cosmacini and V. Veronesi, "A study of the tribological behaviour of perfluoro-polyethers," *Wear*, vol. 108, no. 3, pp. 269–283, 1986.
- [12] M. Masuko, I. Fujinami, and H. Okabe, "Lubrication performance of perfluoropolyalkylethers under high vacuum," *Wear*, vol. 159, no. 2, pp. 249–256, 1992.
- [13] C. Tamborski, G. J. Chen, D. R. Anderson, and C. E. Snyder Jr., "Synthesis and properties of silahydrocarbons, a class of thermally stable, wide liquid range fluids," *Industrial and Engineering Chemistry Product Research and Development*, vol. 22, no. 2, pp. 172–178, 1983.
- [14] C. E. Snyder Jr, L. J. Gschwender, B. B. Randolph et al., "Research and development of low-volatility long life silahydrocarbon-based liquid lubricants for space," *Lubrication Engineering*, vol. 48, pp. 325–328, 1992.
- [15] K. J. L. Paciorek, J. G. Shih, R. H. Kratzer, B. B. Randolph, and C. E. Snyder Jr., "Polysilahydrocarbon synthetic fluids. 1. Synthesis and characterization of trisilahydrocarbons," *Industrial and Engineering Chemistry Research*, vol. 29, no. 9, pp. 1855–1858, 1990.
- [16] P. A. Bessette, "Advanced lubricants based on multiply alkylated cyclopentane, polyphenyl ether and silahydrocarbon," *NLGI Spokesman*, vol. 66, no. 11, pp. 20–24, 2003.
- [17] L. P. Kazimiera, R. E. Pratt, and K. J. L. Paciorek, "Trisilahydrocarbon lubricants," United States patent 4788312, 1988.
- [18] K. J. L. Paciorek, J. G. Shih, R. H. Kratzer, B. B. Randolph, and C. E. Snyder Jr., "Polysilahydrocarbon synthetic fluids. 2. Synthesis and characterization of tetrasilahydrocarbons," *Industrial & Engineering Chemistry Research*, vol. 30, no. 9, pp. 2191–2194, 1991.
- [19] C. G. Venier and E. W. Casserly, "Multiply-alkylated cyclopentanes (MACs). A new class of synthesized hydrocarbon fluids," *Lubrication Engineering*, vol. 47, no. 7, pp. 586–591, 1991.
- [20] S. W. Zhang, L. T. Hu, D. P. Feng, and H. Z. Wang, "Anti-wear and friction-reduction mechanism of Sn and Fe nanoparticles as additives of multialkylated cyclopentanes under vacuum condition," *Vacuum*, vol. 87, pp. 75–80, 2013.
- [21] M. Masuko, H. Mizuno, A. Suzuki, S. Obara, and A. Sasaki, "Lubrication performance of multialkylated cyclopentane oils

for sliding friction of steel under vacuum condition,” *Journal of Synthetic Lubrication*, vol. 24, no. 4, pp. 217–226, 2007.

- [22] S. W. Zhang, L. T. Hu, H. Z. Wang, and D. P. Feng, “The anti-seizure effect of Ag nanoparticles additive in multialkylatedcyclopentanes oil under vacuum condition,” *Tribology International*, vol. 55, pp. 1–6, 2012.
- [23] <http://srdata.nist.gov/xps/>.

## Research Article

# The Long-Term Fate and Toxicity of PEG-Modified Single-Walled Carbon Nanotube Isoliquiritigenin Delivery Vehicles in Rats

Bo Han,<sup>1,2</sup> Mingming Zhang,<sup>1</sup> Ting Tang,<sup>3</sup> Qiusheng Zheng,<sup>1,2</sup>  
Keyu Wang,<sup>1</sup> Le Li,<sup>1,2</sup> and Wen Chen<sup>1,2</sup>

<sup>1</sup> Pharmacy School of Shihezi University, Shihezi 832002, China

<sup>2</sup> Key Laboratory of Xinjiang Phytomedicine Resources, Shihezi 832002, China

<sup>3</sup> The Ankang Hospital of Xinjiang P&C Corps, Shihezi 832002, China

Correspondence should be addressed to Wen Chen; chen-wen2000@126.com

Received 28 October 2013; Revised 11 December 2013; Accepted 12 December 2013; Published 16 March 2014

Academic Editor: Jinlong Jiang

Copyright © 2014 Bo Han et al. This is an open access article distributed under the Creative Commons Attribution License, which permits unrestricted use, distribution, and reproduction in any medium, provided the original work is properly cited.

Oxidized single-walled carbon nanotubes (o-SWNTs) was modified by covalently and noncovalently linking PEG to the o-SWNTs. The influence of oxidation time, PEG molecular weight, and type of PEG linkage on the blood clearance time of PEG-modified single-walled carbon nanotubes (SWNTs) was investigated. The toxicity profile of SWNTs covalently linked to PEG (c-PEG-o-SWNTs) in rats has also been determined. The pharmacokinetics of c-PEG-o-SWNTs in rats and their distribution in vital organs were monitored by Raman spectroscopy, and the blood clearance of homogenate isoliquiritigenin (ISL) was determined by HPLC. Photos of tissue and tissue sections were taken to evaluate the toxicity of c-PEG-o-SWNTs. We found that SWNTs which were covalently modified with PEG and have a molecular weight of 3500 had the longest blood clearance half-lives. However, SWNTs were toxic to the kidneys and the hearts. The high renal clearance of long-term fate SWNTs may occur because of impaired kidney filtration function. Therefore, we assume that while researchers study the long-term fate of SWNTs, the toxicity of SWNTs also needs to be taken into account.

## 1. Introduction

The root of *Glycyrrhiza uralensis* Fischer is widely used as a harmonizing ingredient in traditional herbal formulations in oriental medicine; it is used in more formulations than any other herb. One of the most notable ingredients in *Glycyrrhiza uralensis* Fischer is isoliquiritigenin (ISL), a simple chalcone-type flavonoid that has antioxidative effect [1, 2], antiplatelet aggregation effect [3], anti-ischemia effect [4], anti-inflammatory property [5, 6], antispasmodic effect [7], and estrogenic property [8]. In the past seven years, our group has expanded the study of ISL drug performance [9–11] and has made progress in ISL tumor pharmacology [12], natural product chemistry [11], and *in vivo* analysis [13]. In this study, we aim to improve the target performance of ISL by delivering the compound with the help of SWNTs.

SWNTs have been heavily studied because of their unique physicochemical properties and potential applications [14]. Encouraged by the success of using carbon nanotubes (CNTs) for *in vitro* sensing, drug delivery, and imaging, researchers in this field have moved to *in vivo* investigations in animals [15].

*In vivo* biodistribution and pharmacokinetic studies have been carried out by a number of groups using different CNT materials. Many of these studies confirmed the poor biocompatibility of original carbon nanotube formulations [16]. Purified SWNTs implanted in mice via intratracheal instillation resulted in epithelioid granulomas and interstitial inflammation in a 90-day study [17]. Lam et al. found that undoped multiwalled CNTs (MWCNTs) can induce severe granulomatous inflammatory responses compared with nitrogen-doped MWCNTs when administered intratracheally in mice [18]. Original MWCNTs inhaled by mice

for 6 h were found throughout the lungs and significant pulmonary toxicity was observed [19].

SWNTs used for drug delivery are usually functionalized with polyethylene glycol (PEG). PEG provides a desirable coating for nanotubes and nanoparticles, because it reduces their immunogenicity and reduces their chance of being nonspecifically taken up by cells of the reticuloendothelial system. Consequently, the phagocytosis of nanoparticles is diminished and their clearance time is prolonged when modified with PEG [20].

The purpose of our study is to investigate the influence of SWNTs' oxidation time, PEG molecular weight, and PEG linkage type on the clearance time of SWNTs. After the best long-term fate single-walled carbon nanotubes (LTFS) were synthesized, the blood clearance time changes between ISL and ISL loaded with LTFS were investigated. The toxicity of LTFS in rats was also studied. While there are many researchers concern about the toxicity of carbon nanotube as well as its long-term fate, there is little work focusing on the relationship between the toxicity and the long-term fate of CNTs.

## 2. Materials and Methods

### 2.1. Reagents, Instruments, and Test Animals

**2.1.1. Reagents.** SWNTs were obtained from Nanjing Jicang Technology Co., Ltd (purity  $\geq 90\%$ ); ISL was purchased from Tianye Chemical Co., Ltd. (purity  $\geq 98\%$ ); N-Hydroxysuccinimide (NHS) and carbodiimide-HCl (EDC · HCl, purity  $\geq 98.5\%$ ) were obtained from GL Biochem (Shanghai), Ltd.;  $\text{NH}_2$ -PEG- $\text{NH}_2$  (MWs of 2000, 3500, and 5000) were purchased from Beijing Kaizheng Biotech Development Co., Ltd. Heparin sodium injection was purchased from Tianjin Biochemical Co., Ltd.; mixed phosphate buffer solution (PBS) was purchased from Sigma-Aldrich; and nitric acid, sulfuric acid, ethyl acetate, dimethyl sulfoxide, and anhydrous ethanol (A.R.) were purchased from Sinopharm Chemical Reagent Co., Ltd.

**2.1.2. Instruments.** An STA409PC composite thermal analyzer and  $\text{Al}_2\text{O}_3$  crucible were used in this study (NETZSCH Scientific Instrument Trading (Shanghai) Co., Ltd.). An H-600 transmission electron microscope (Japan Electronics Co., Ltd.); a Raman spectrometer (Bruker 70), a dialysis bag (MWCO 7000–14000; Hainan Nanjing Science and Technology Development Co., Ltd.), an LC-20A high-performance liquid chromatograph (Shimadzu); and a chromatographic column (Symmetry 300,  $\text{C}_{18}$ ,  $5\ \mu\text{m}$ ,  $\Phi\ 4.6 \times 150\ \text{mm}$ ) were also used.

**2.1.3. Test Animals.** Six-week-old Wistar rats with body weight of  $200 \pm 20\ \text{g}$  and production certificate number of SCXK (Xin)-2003-0001 (Animal Center of Xinjiang Medical University) were used in this study.

**2.2. Preparation of PEGylated Nanotubes.** One hundred mg of HiPco SWNTs were added to 50 mL of a 1:1  $\text{HNO}_3$ - $\text{H}_2\text{SO}_4$

solution. The mixture was refluxed for 15 min, 30 min, or 45 min at  $140^\circ\text{C}$ , respectively, and then cooled. The mixture was diluted with 250 mL of deionized water and filtered through a microporous membrane. The filter film containing oxidized SWNTs (o-SWNTs) was then washed with deionized water. The carboxyl groups present on o-SWNTs surfaces provide the binding sites required for attaching PEG.

Covalently linked PEG to o-SWNTs (c-PEG-o-SWNTs) was prepared according to the following steps. 50 mg of o-SWNTs was combined with 50.00 mL of phosphate buffer (pH 6.8) under sonication to achieve an evenly dispersed solution. 200 mg carbodiimide (EDC) and 250 mg NHS were added into the dispersed solution and then the mixture was sonicated for 30 min. After that, 50 mg  $\text{NH}_2$ -PEG- $\text{NH}_2$  (MW of 2000, 3500, or 5000) was added and the mixture was magnetically stirred at room temperature for 24 h. Distilled water was added to achieve a final volume 3 times larger than initial volume. The diluted mixture was centrifuged at 22 000 g for 1 h. The supernatant was placed in a dialysis bag dialysed to neutral pH [21]. The amount of grafted PEG was determined by the thermal gravimetric analysis method (TG) [22].

Noncovalently linked PEG to o-SWNTs (n-PEG-o-SWNTs) was prepared according to the following steps. 50 mg of o-SWNTs was combined with 50.00 mL of pH 6.8 phosphate buffer solution and then sonicated for 30 min. The solution obtained was combined with 50 mg  $\text{NH}_2$ -PEG- $\text{NH}_2$  (MW 2000) and stirred evenly at room temperature for 24 h to get n-PEG-o-SWNTs [21]. The amount of grafted PEG was determined by TG [22].

**2.3. Preparation of ISL and Functionalization of SWNTs Complexes.** In order to attach ISL onto c-PEG-o-SWNTs noncovalently, 12 mg of ISL was dissolved in a mixture of DMSO, PEG400, and saline (1:2:9) to make a 1 mg/mL ISL solution. 60 mg of c-PEG-o-SWNTs was added to the ISL solution and the mixture was stirred for 6 h in a  $25^\circ\text{C}$  water bath to obtain SWNT-ISL complexes (c-PEG-o-SWNTs-ISL). The prepared products were resuspended and stored at  $4^\circ\text{C}$ .

**2.4. Animal Experiments.** Twenty-four hours after injecting 200  $\mu\text{L}$  of the c-PEG-o-SWNTs-ISL test solution into rats' tail veins, 0.5 mL of blood was obtained through orbital veins and placed into heparin sodium treated centrifuge tubes. After centrifuging the blood for 10 min at 5000 rpm, 200  $\mu\text{L}$  plasma was collected for future use. Then rats were killed by cervical dislocation, and their hearts, livers, spleens, lungs, kidneys, and brains were collected and weighed. The various tissues and organs were placed in 4 mL centrifuge tubes containing 2 mL of normal saline and homogenized. Two portions of homogenate (7.5 mL) were taken. One portion was used to determine the ISL content by HPLC. The other portion was combined with 0.75 mL of CMC-Na solution and then homogenized by vortex oscillation for 5 min. This portion was reserved for Raman spectroscopy.

**2.5. Raman Measurement of PEG-SWNT Solutions.** Various concentrations of SWNT solutions were drawn into capillary glass tubes (Fisher) and measured using a Bruker 70 Raman spectrometer (laser excitation wavelength was 1024 nm; 30 min; 850 times). Four spectra were measured for each sample to obtain an average spectrum. For a given concentration of SWNTs, the Raman intensity was obtained by integrating the PEG-o-SWNT G-band peak area from  $1570\text{ cm}^{-1}$  to  $1620\text{ cm}^{-1}$ . The Raman G-band peak areas were used to calculate PEG-o-SWNT concentrations in the blood. The percentage of injected dose per gram (%ID/g) of blood was calculated using the following equation:

$$\%ID/g = \frac{[SWNTs]_{\text{blood lysate}} \times V_{\text{blood lysate}}}{[SWNTs]_{\text{injected}} \times V_{\text{injected}} \times \text{tissue weight}} \times 100\%. \quad (1)$$

**2.6. Determination of Isoliquiritigenin Content in the Tissue Homogenate with HPLC.** The mobile phase consisted of a mixture of acetonitrile and double distilled water (1:1 (v/v)), the flow rate was 10 mL/min, and the column temperature was  $40^\circ\text{C}$ . A sample volume of  $20\ \mu\text{L}$  was injected into the HPLC. The ISL detection wavelength was 368 nm and the operating time was 9 min.

**2.7. Statistical Analysis.** The pharmacokinetic parameters were performed by DAS (ver1.0) program and compared by statistical analysis. One-way ANOVA was used for parametric data, when differences were statistically significant ( $P < 0.05$ ).

### 3. Results and Discussion

**3.1. Characterization of PEG-Modified SWNTs.** The structure of c-PEG-o-SWNTs after synthesized by EDC is shown in Figure 1. SWNTs covalently functionalized by PEG can form stable solution in water [23]. Centrifugation was used to remove big bundles and impurities, leaving short individual and small bundles of tubes in solution. Strong resonance Raman scattering is an intrinsic optical property of SWNTs, with sharp peaks and low background in the spectra. The tangential graphite-like phonon mode (G band), which is the strongest peak in the SWNTs Raman spectrum, was used to detect nanotubes in blood and tissue lysates.

**3.2. Determination of c-PEG-o-SWNTs In Vivo by Raman Spectroscopy.** SWNTs have a unique crystal structure, which produces unique Raman scattering at a wavelength of about 1590 nm. SWNTs retain the feature of Raman scattering after covalent or noncovalent modification with PEG. Figure 2 shows the Raman spectra of different concentrations of c-PEG-o-SWNTs in plasma solutions. The G bands of SWNTs were absorbed, and the absorption strength increased as the c-PEG-o-SWNT concentration in solution increased. With the above positive correlation, c-PEG-o-SWNTs in the blood and tissue fluid were quantified by using the peak area of the

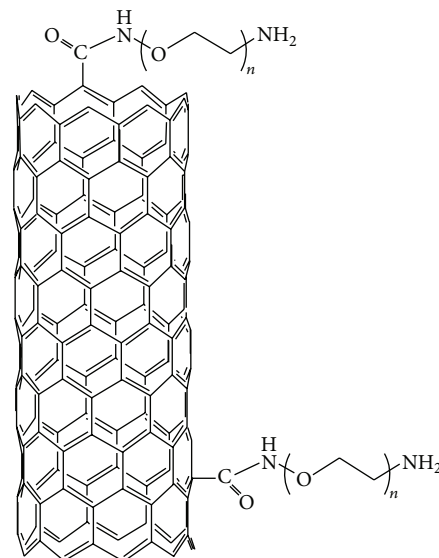


FIGURE 1: The structure of c-PEG-o-SWNTs.

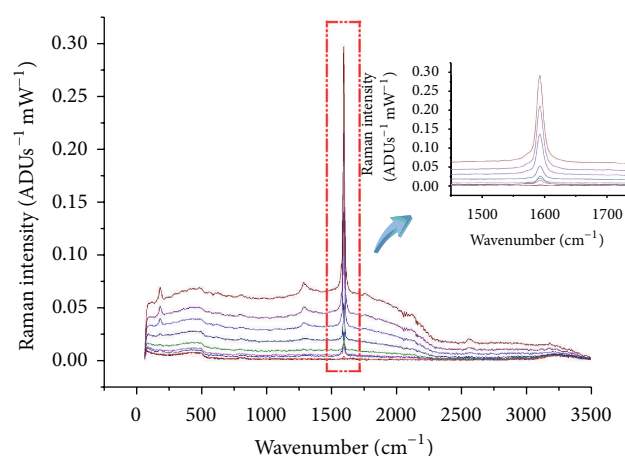


FIGURE 2: The Raman spectra of different concentrations of c-PEG-o-SWNTs in blood samples.

G band. The data were fitted by the nonlinear standard curve  $y = 0.0164X - 2.123 \times 10^{-5}X^2 - 0.07973$  ( $R = 0.9935$ ) using Origin 7.5 software. The results of the sampling recovery test, precision test, and durability test showed that the amount of c-PEG-o-SWNTs in the animals' tissues and blood were accurately determined by using this method.

**3.3. Determination of Isoliquiritigenin Content in Rat Tissues by HPLC.** The ultraviolet absorption spectrum of ISL with a maximum absorption wavelength of 368 nm. ISL was eluted at 5.1 min under the HPLC conditions employed in this work, while blank plasma revealed no peak at or around 5.1 min under the same conditions, suggesting the good specificity of determining ISL by HPLC. The results of the sampling recovery test, precision test, and durability test displayed that the ISL content in the animals' tissues and blood were accurately assayed by this method [11].

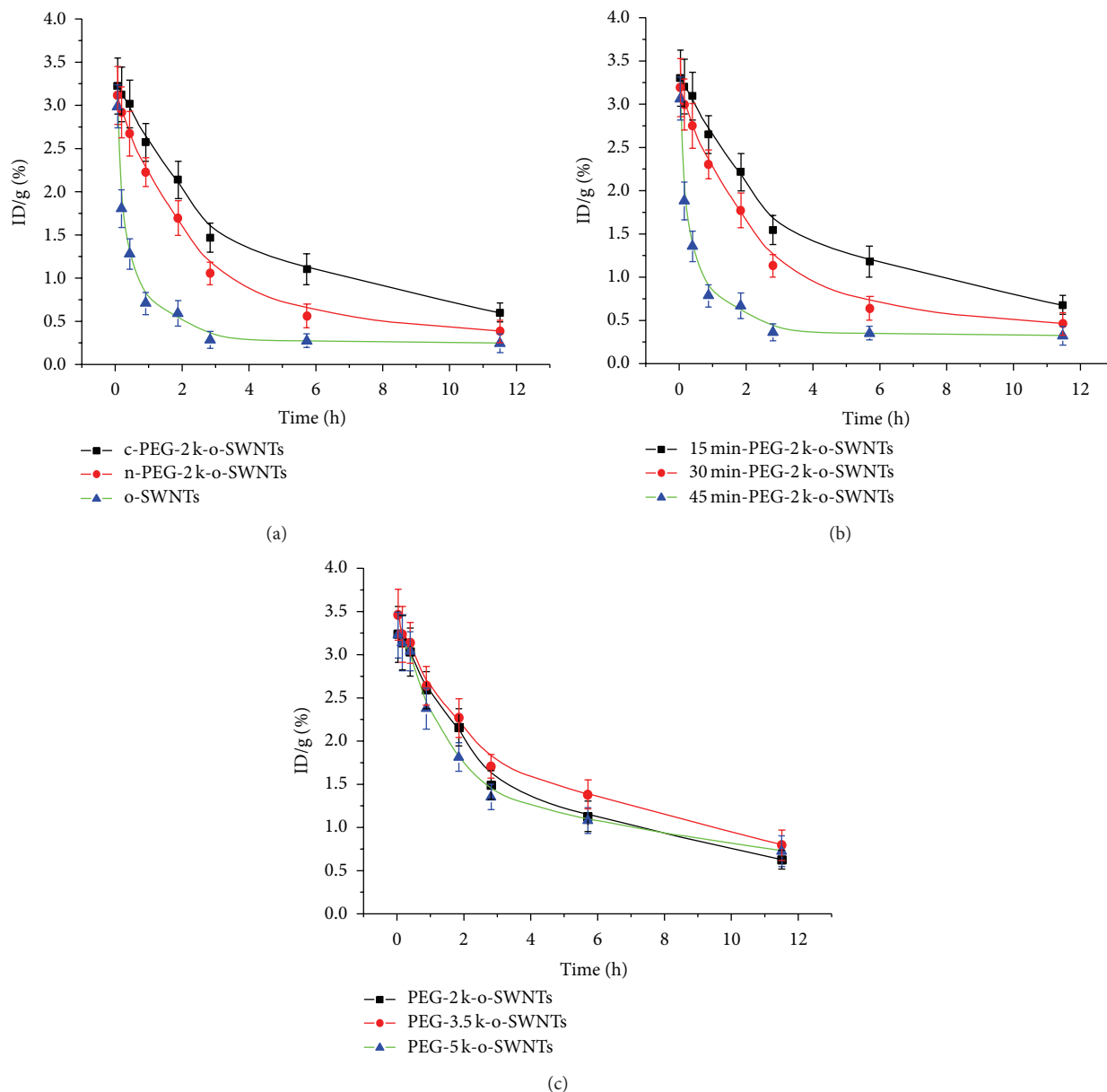


FIGURE 3: The investigation of the influence of different types of PEG modification factors (a), different degrees of oxidation on SWNT clearance time (b), and the influence modifying SWNTs with different PEG molecular weights (c) on the SWNT clearance time *in vivo*.

**3.4. Investigation on Factors That Influence the Blood Clearance Time of SWNTs.** Figure 3(a) shows the influence of different types of PEG modification (covalent, noncovalent, or no PEG modification) on the blood clearance time of SWNTs. The half-lives of SWNTs were  $t_{1/2(o-SWNTs)} = 0.24$  h,  $t_{1/2(c-PEG-2k-o-SWNTs)} = 2.35$  h, and  $t_{1/2(n-PEG-2k-o-SWNTs)} = 1.75$  h. Covalently linking  $NH_2$ -PEG- $NH_2$  (MW 2000) significantly prolonged the clearance time of SWNTs, but non-covalently linking  $NH_2$ -PEG- $NH_2$  (MW 2000) to SWNTs did not. These results imply that noncovalent modification of SWNTs using  $NH_2$ -PEG- $NH_2$  (MW 2000) may not protect SWNTs from clearance by the reticuloendothelial system. In contrast, covalently linking  $NH_2$ -PEG- $NH_2$  (MW 2000) increases the blood clearance time of SWNTs.

Figure 3(b) shows the influence of different degrees of oxidation on SWNT clearance time. Using TG calculation, the carboxyl contents were found to be 9.44%, 13.18%, and 15.32% at 15 min, 30 min, and 45 min of oxidation, respectively. Through the DAS 1.0 pharmacokinetic software calculation, we found that CNTs covalently linked to  $NH_2$ -PEG- $NH_2$  (MW 2000) caused blood clearance half-lives of 1.57 h, 2.35 h, and 1.61 h according to oxidation time of 15 min, 30 min, and 45 min, respectively. These results suggest that 30 min of mixed acid oxidation results in SWNTs that have the longest blood clearance time. Oxidation time longer than 30 min did not extend the clearance time of SWNTs.

Figure 3(c) shows the influence of modifying SWNTs with different PEG molecular weights on the SWNT

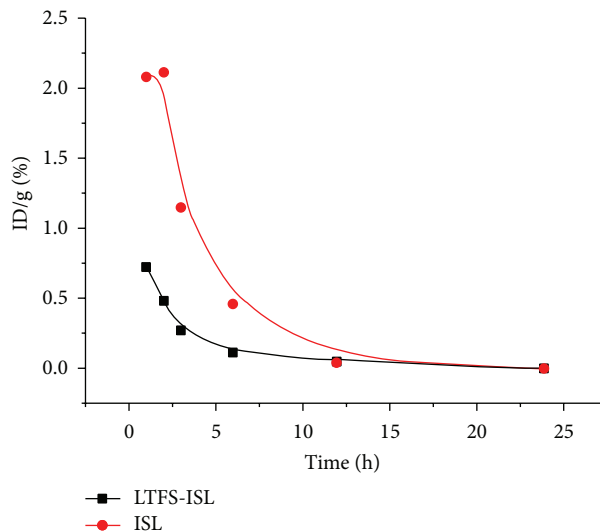


FIGURE 4: The blood concentration of ISL with and without LTFS. The y-axis represents injected dose per gram (%ID/g).

clearance time. Through calculation, the half-lives were  $t_{1/2(c\text{-PEG-}2\text{ k-o-SWNTs})} = 2.35$  h,  $t_{1/2(c\text{-PEG-}3.5\text{ k-o-SWNTs})} = 2.77$  h, and  $t_{1/2(c\text{-PEG-}5\text{ k-o-SWNTs})} = 2.41$  h. Although PEG modification on the surface of SWNTs prolonged their blood clearance time, the molecular weight of  $\text{NH}_2\text{-PEG-NH}_2$  that can prolong blood clearance time to the highest level remains unclear.

In summary, these results suggest that 30 min of mixed acid oxidation of SWNTs followed by covalently linking  $\text{NH}_2\text{-PEG-NH}_2$  (MW 3500) resulted in SWNTs with the longest blood clearance time. After the formulation of the best LTFS was obtained, ISL was incorporated into the LTFS (LTFS-ISL), and the pharmacokinetic profile and the toxicity of LTFS-ISL on rats were determined.

The research group led by Dai et al. at Stanford University found that ultrasonic dispersion of multiwalled carbon nanotubes with a molecular weight of 7000 for 1 h resulted in a long-term fate of one day after tail vein injection [16]. However, the Hudson group at the University of New Mexico has contended that one hour of ultrasonic dispersion will break the long chain of PEG and thereby reduce the actual molecular weight of the PEG on the carbon nanotubes [24]. In this work, we did not use ultrasonic-assisted dispersion of  $c\text{-PEG-o-SWNTs}$ , and our results suggest that SWNTs covalently linked to PEG with a molecular weight of 3500 display the longest blood clearance half-life.

**3.5. Influence of LTFS on ISL Blood Clearance Time and Distribution.** Figure 4 shows the concentration of ISL in blood with or without the SWNT carriers. Using the DAS 1.0 pharmacokinetic software, we determined that  $t_{1/2\text{ ISL}} = 2.51$  h and  $t_{1/2(\text{LTFS-ISL})} = 0.95$  h, demonstrating that the existence of carriers reduces the half-life of ISL in the blood.

Interestingly, as shown in Figure 4, the existence of carriers significantly reduces the concentration of ISL in blood. Thirty minutes after LTFS-ISL was injected through tail veins, the rats developed gross hematuria and black

discharge in the urine, raising the possibility that LTFS-ISL may cause renal toxicity and that carbon nanotubes were discharged through the urine.

**3.6. Appearance Changes in the Heart and Kidneys after the Injection of LTFS-ISL.** We compared the hearts, livers, spleens, lungs, and kidneys of rats injected with ISL and LTFS-ISL. The results showed that the hearts and kidneys of rats in the LTFS-ISL group were blacker and larger than those of rats in the ISL group, suggesting that the carbon nanotubes remained in the hearts and kidneys, as shown in Figure 5.

**3.7. Tissue Distribution of  $c\text{-PEG-}3.5\text{ k-o-SWNTs-}30$  min.** We determined the content of carbon nanotubes in the tissues (hearts, livers, spleens, and kidneys) and in the urine of rats injected with LTFS using Raman spectroscopy. Figure 6 shows the content of LTFS in the tissues and urine. It was discovered that the content of LTFS in the urine, liver, spleen, and kidney was higher than that in other organs. The results suggest that, like most nanosubstances, macrophages readily consume LTFS in the liver, spleen, and other organs through phagocytosis.

It should be noted that the discharged urine contained a large amount of carbon nanotubes, which is consistent with reports by Singh et al. [25] and Lacerda et al. [26], indicating that most carbon nanotubes are removed through kidney. From our experimental results and the work presented by Singh and Lacerda, we speculate that ISL can be adsorbed onto the surface of LTFS. Therefore, after LTFS are removed by kidney and the reticuloendothelial system, the concentration of ISL in blood significantly decreases.

**3.8. Histopathology Changes after Injecting LTFS-ISL in the Heart and Kidney Tissues.** We examined the heart and kidney tissue sections after H&E staining. As illustrated in Figure 7, the myocardial cell cytoplasm of LTFS-ISL-treated rats changed into granules and vacuoles in some

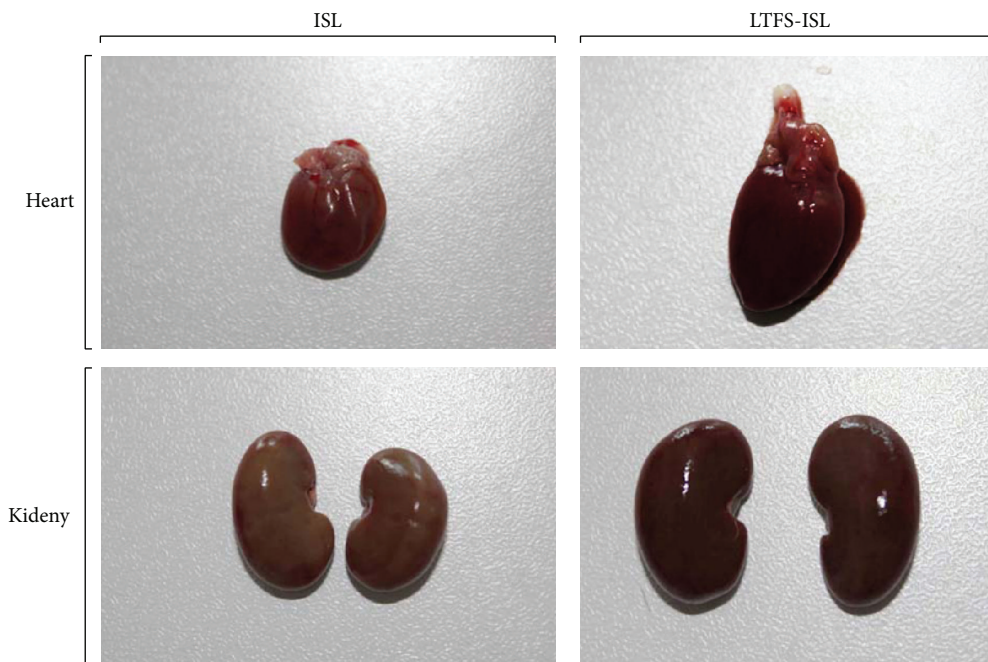


FIGURE 5: The influence of ISL and LTFS-ISL on the appearance of various organs.

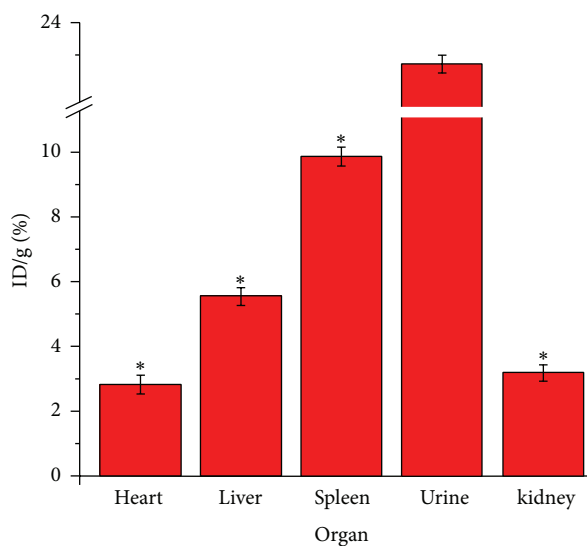


FIGURE 6: The distribution of LTFS ( $n = 6$ ) in the tissues and urine. “\*” indicates the differences were statistically significant compared with urine bar ( $P < 0.05$ ).

regions, and the color of the myocardial fibers faded and the nuclei of myocytes shrank. In addition, there were vacuolar deformations and particulate deformations in kidney tubules after LTFS-ISL administration. The above results suggest that LTFS-ISL may cause heart and kidney toxicity. The large discharge of LTFS-ISL in urine may be attributed to glomerular damage caused by LTFS-ISL.

#### 4. Conclusions

We speculate that LTFS-ISL is toxic to kidney and heart. The results of our study showed that the longest half-life

of PEG-o-SWNTs was obtained after SWNTs underwent reflux oxidation for 30 min and were covalently linked with  $\text{NH}_2\text{-PEG-NH}_2$  (MW 3500). These results indicate that surface modification of SWNTs with  $\text{NH}_2\text{-PEG-NH}_2$  indeed prolongs their clearance time, and c-PEG-o-SWNT carriers reduce the blood clearance half-life of ISL. The black and red discharge in urine and postmortem tissue sections infer that LTFS are likely to cause liver and kidney toxicity. The increased renal clearance of LTFS may occur owing to impaired kidney filtration function. This discovery provides a new way to explain of long-term fate SWNTs' high renal clearance in rats.

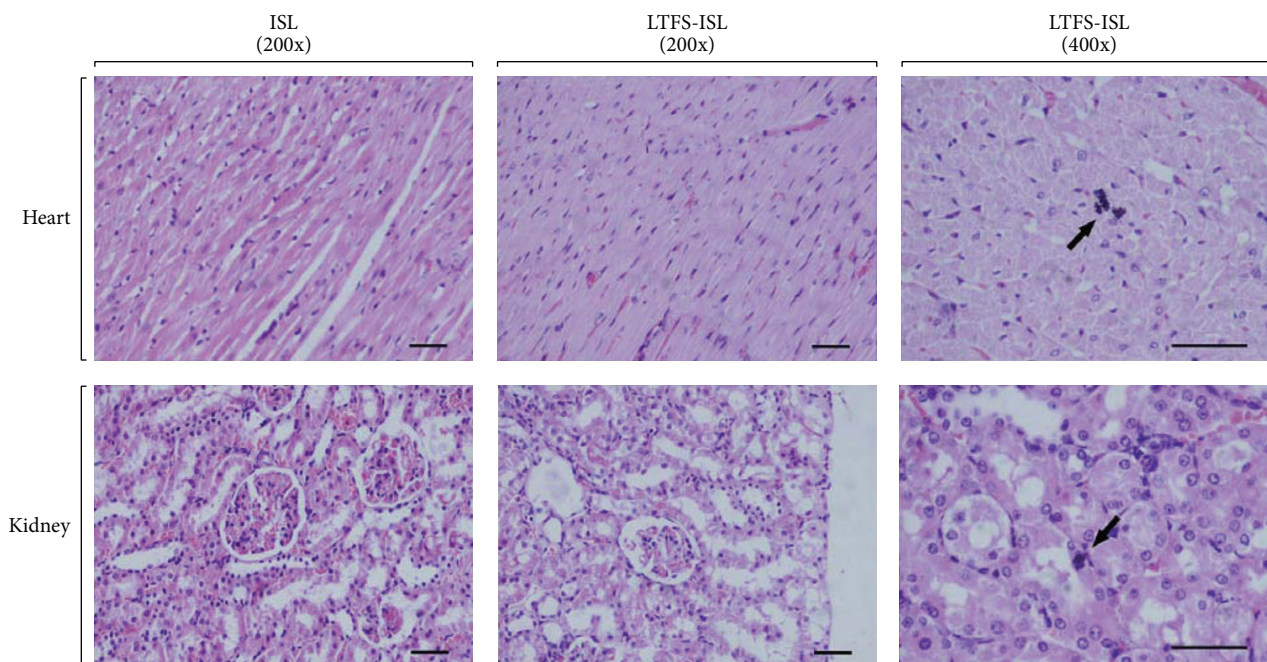


FIGURE 7: The effect of LTFs-ISL on the heart and kidneys. The arrows indicate that the carbon nanotubes remained in some organs. The scale bar is 100  $\mu\text{m}$ .

## Conflict of Interests

The authors declare that they have no conflict of interests.

## Acknowledgment

This work was supported by the National Natural Science Foundation of China (nos. 30960515 and 81260487), the Doctor Foundation of Xinjiang Bingtuan (no. 2012BB020) and the Foundation from Shihezi University (ZRKXYB-13, YX07010, RCZX201115).

## References

- [1] T. Umemura, R. Kitaguchi, K. Inagaki, and H. Haraguchi, "Direct injection determination of theophylline and caffeine in blood serum by high-performance liquid chromatography using an ODS column coated with a zwitterionic bile acid derivative," *Analyst*, vol. 123, no. 8, pp. 1767–1770, 1998.
- [2] H.-X. Liu, W.-H. Lin, X.-L. Wang, and J.-S. Yang, "Flavonoids from preparation of traditional Chinese medicines named Sini-Tang," *Journal of Asian Natural Products Research*, vol. 7, no. 2, pp. 139–143, 2005.
- [3] M. Tawata, K. Aida, T. Noguchi et al., "Anti-platelet action of isoliquiritigenin, an aldose reductase inhibitor in licorice," *European Journal of Pharmacology*, vol. 212, no. 1, pp. 87–92, 1992.
- [4] C. Zhan and J. Yang, "Protective effects of isoliquiritigenin in transient middle cerebral artery occlusion-induced focal cerebral ischemia in rats," *Pharmacological Research*, vol. 53, no. 3, pp. 303–309, 2006.
- [5] J.-Y. Kim, S. J. Park, K.-J. Yun, Y.-W. Cho, H.-J. Park, and K.-T. Lee, "Isoliquiritigenin isolated from the roots of *Glycyrrhiza ularensis* inhibits LPS-induced iNOS and COX-2 expression via the attenuation of NF- $\kappa$ B in RAW 264.7 macrophages," *European Journal of Pharmacology*, vol. 584, no. 1, pp. 175–184, 2008.
- [6] D.-C. Kim, S.-Y. Choi, S.-H. Kim et al., "Isoliquiritigenin selectively inhibits H<sub>2</sub> histamine receptor signaling," *Molecular Pharmacology*, vol. 70, no. 2, pp. 493–500, 2006.
- [7] Y. Sato, J.-X. He, H. Nagai, T. Tani, and T. Akao, "Isoliquiritigenin, one of the antispasmodic principles of *Glycyrrhiza ularensis* roots, acts in the lower part of intestine," *Biological and Pharmaceutical Bulletin*, vol. 30, no. 1, pp. 145–149, 2007.
- [8] S. Tamir, M. Eizenberg, D. Somjen, S. Izrael, and J. Vaya, "Estrogen-like activity of glabrene and other constituents isolated from licorice root," *Journal of Steroid Biochemistry and Molecular Biology*, vol. 78, no. 3, pp. 291–298, 2001.
- [9] B. Han, Q.-N. Li, S.-W. Wu, J.-G. Li, W. Chen, and W.-X. Li, "Selective adsorption of multi-walled carbon nanotubes with liquiritin and isoliquiritin," *Yao Xue Xue Bao*, vol. 42, no. 11, pp. 1222–1226, 2007.
- [10] B. Han, W. Chen, W.-J. Jin, and S.-P. Liu, "Evaluation of AB-8 macroporous adsorption resin for adsorption of total flavones in liquorice," *Nan Fang Yi Ke Da Xue Xue Bao*, vol. 27, no. 3, pp. 265–267, 2007.
- [11] B. Han, Q. -s. Zheng, W. Chen, X. Wang, Q. Wang, and L. Li, "A novel process for extraction of isoliquiritigenin from licorice (*Glycyrrhiza glabra*) roots by facile convert," *Chemistry of Nature Compounds*, vol. 46, no. 4, pp. 523–527, 2010.
- [12] D. Li, Z. Wang, H. Chen et al., "Isoliquiritigenin induces monocytic differentiation of HL-60 cells," *Free Radical Biology and Medicine*, vol. 46, no. 6, pp. 731–736, 2009.
- [13] B. Han, W. Chen, Q. Zheng et al., "Determination of isoliquiritigenin and its distribution in mice by synchronous fluorescence spectrometry," *Analytical Sciences*, vol. 27, no. 11, pp. 1115–1119, 2011.

- [14] S. A. Hodge, M. K. Bayazit, K. S. Coleman, and M. S. Shaffer, "Unweaving the rainbow: a review of the relationship between single-walled carbon nanotube molecular structures and their chemical reactivity," *Chemical Society Reviews*, vol. 41, no. 12, pp. 4409–4429, 2012.
- [15] H. Ali-Boucetta and K. Kostarelos, "Carbon nanotubes in medicine and biology: therapy and diagnostics," *Advanced Drug Delivery Reviews*, vol. 65, no. 15, pp. 1897–1898, 2013.
- [16] Z. Liu, S. Tabakman, K. Welsher, and H. Dai, "Carbon nanotubes in biology and medicine: In vitro and in vivo detection, imaging and drug delivery," *Nano Research*, vol. 2, no. 2, pp. 85–120, 2009.
- [17] C.-W. Lam, J. T. James, R. McCluskey, and R. L. Hunter, "Pulmonary toxicity of single-wall carbon nanotubes in mice 7 and 90 days after intratracheal instillation," *Toxicological Sciences*, vol. 77, no. 1, pp. 126–134, 2004.
- [18] J. C. Carrero-Sánchez, A. L. Elías, R. Mancilla et al., "Biocompatibility and toxicological studies of carbon nanotubes doped with nitrogen," *Nano Letters*, vol. 6, no. 8, pp. 1609–1616, 2006.
- [19] K. Donaldson and C. A. Poland, "Nanotoxicology: new insights into nanotubes," *Nature Nanotechnology*, vol. 4, no. 11, pp. 708–710, 2009.
- [20] S. M. Ryan, G. Mantovani, X. Wang, D. M. Haddleton, and D. J. Brayden, "Advances in PEGylation of important biotech molecules: delivery aspects," *Expert Opinion on Drug Delivery*, vol. 5, no. 4, pp. 371–383, 2008.
- [21] B. Zhao, H. Hu, A. Yu, D. Perea, and R. C. Haddon, "Synthesis and characterization of water soluble single-walled carbon nanotube graft copolymers," *Journal of the American Chemical Society*, vol. 127, no. 22, pp. 8197–8203, 2005.
- [22] A. Sarafraz-Yazdi, A. Amiri, G. Rounaghi, and H. E. Hosseini, "A novel solid-phase microextraction using coated fiber based sol-gel technique using poly(ethylene glycol) grafted multi-walled carbon nanotubes for determination of benzene, toluene, ethylbenzene and o-xylene in water samples with gas chromatography-flam ionization detector," *Journal of Chromatography A*, vol. 1218, no. 34, pp. 5757–5764, 2011.
- [23] B. Han, S. Ma, H. A. Aisa, X. C. Wang, and W. Chen, "Characterization and biocompatibility of pegylated single walled carbon nanotubes," *Chinese Journal of Hospital Pharmacy*, vol. 32, no. 18, pp. 1415–1419, 2012.
- [24] R. Zeineldin, M. Al-Haik, and L. G. Hudson, "Role of polyethylene glycol integrity in specific receptor targeting of carbon nanotubes to cancer cells," *Nano Letters*, vol. 9, no. 2, pp. 751–757, 2009.
- [25] R. Singh, D. Pantarotto, L. Lacerda et al., "Tissue biodistribution and blood clearance rates of intravenously administered carbon nanotube radiotracers," *Proceedings of the National Academy of Sciences of the United States of America*, vol. 103, no. 9, pp. 3357–3362, 2006.
- [26] L. Lacerda, A. Soundararajan, R. Singh et al., "Dynamic imaging of functionalized multi-walled carbon nanotube systemic circulation and urinary excretion," *Advanced Materials*, vol. 20, no. 2, pp. 225–230, 2008.

## Research Article

# Asymmetric Electrodes Constructed with PAN-Based Activated Carbon Fiber in Capacitive Deionization

Mingzhe Li, Yingzhi Chen, Zheng-Hong Huang, and Feiyu Kang

Key Laboratory of Advanced Materials (MOE), School of Materials Science and Engineering, Tsinghua University, Beijing 100084, China

Correspondence should be addressed to Zheng-Hong Huang; zhhuang@mail.tsinghua.edu.cn

Received 4 December 2013; Accepted 8 February 2014; Published 11 March 2014

Academic Editor: Jian Lin

Copyright © 2014 Mingzhe Li et al. This is an open access article distributed under the Creative Commons Attribution License, which permits unrestricted use, distribution, and reproduction in any medium, provided the original work is properly cited.

Capacitive deionization (CDI) method has drawn much attention for its low energy consumption, low pollution, and convenient manipulation. Activated carbon fibers (ACFs) possess high adsorption ability and can be used as CDI electrode material. Herein, two kinds of PAN-based ACFs with different specific surface area (SSA) were used for the CDI electrodes. The CDI performance was investigated; especially asymmetric electrodes' effect was evaluated. The results demonstrated that PAN-based ACFs showed a high electrosorption rate (complete electrosorption in less than half an hour) and moderate electrosorption capacity (up to 0.2 mmol/g). CDI experiments with asymmetric electrodes displayed a variation in electrosorption capacity between forward voltage and reverse voltage. It can be attributed to the electrical double layer (EDL) overlap effect and inner pore potential; thus the ions with smaller hydrated ionic radius can be adsorbed more easily.

## 1. Introduction

Water scarcity has become an increasing concern on the earth. Fresh water accounts for only 0.007% of the global water resources. Yet, such a small amount of water has been unconscionably exploited and overused by continuously increasing population [1]. On the other hand, sea water and brackish water constitute nearly 97% of the water resources, but these kinds of water cannot be used directly. Therefore water desalination plays a significant role in reduction or even elimination of water crisis [2]. Capacitive deionization (CDI) is a promising method of water desalination. The concept was first brought forward by Caudle from America in the 1960s [3]. Then, Johnson made great contribution on electrosorption and electrolysis adsorption. In the late twentieth century, a brand new method: Flow-Through Capacitor (FTC) for electrosorption deionization using the capacitive character theory was proposed. CDI has the advantages of convenience, low energy consumption, and absence of secondary pollutant [4]. The mechanism of CDI involves application of an electric field between two electrodes to force ionic species toward oppositely charged electrodes. The ions are held within the electrical double layer (EDL)

formed near the electrode surfaces [5, 6]. A part of these ions belongs to nonelectrosorption, namely, the physisorption or chemisorption; the other part belongs to electroadsorption, which is reversible. When the adsorption has reached an equilibrium condition, electrodes can be regenerated with ease by reversing the power supply or to short the circuit while adsorbed ions are released.

CDI's performance relies on its adsorbing efficiency [7], which is mainly influenced by electrode materials, apart from external conditions such as solution's concentration. If CDI's efficiency can reach 85% or more, then CDI could be a real rival for reverse osmosis and distillation. In fact, scientists have successfully made carbon electrode with cyclic efficiency of over 90% [8]. Many kinds of carbon materials have been used and tested as CDI's electrode, and the high CDI performance usually depends on the physical and structural properties of the electrode materials such as specific surface, conductivity, and pore size distribution. Relatively high specific surface area (SSA) and better conductivity contribute to a better adsorption capacity [9, 10]. Graphene or carbon nanotubes (CNT) [11–13] have to be attached to other supporting materials with the assistance of additives [14–16]. While self-supporting materials like carbon aerogel

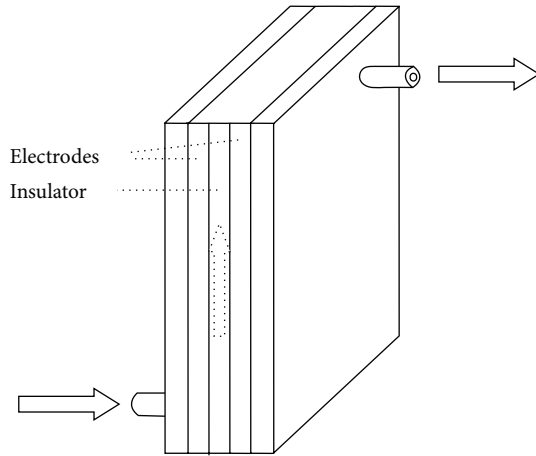


FIGURE 1: Schematic of CDI cell with PAN-based ACFs electrodes.

[17, 18] and activated carbon fiber (ACF) [19] encourage better CDI behavior by avoiding the complex fabrication [20]. Apart from the material type of the electrodes, the geometric dimensioning could also affect CDI performance. Recently, Porada et al. [21] reported the effect of electrode thickness variation on CDI, in which they used different layers of anode and cathode made of chemically unmodified porous carbon particles. By doubling and tripling one electrode but not the other, they obtained increasing salt adsorption. Their work revealed that EDL structure is independent of the sign of the electronic charge.

In the present work, we exploited activated carbon fibers (ACFs) electrodes with different specific surfaces and studied the influence of electrodes asymmetry's on CDI performance. Electrodes with size asymmetry and material asymmetry were used in CDI process and electroadsorption performances were analyzed. Different from Porada's research, we used electrodes with various geometric sizes other than thickness and evaluated the CDI performance.

## 2. Experiment

**2.1. Material.** The PAN-based ACFs used in the experiments were kindly provided by Professor Tse-Hao Ko from Feng Chia University, Taiwan. The ACFs were produced by the process of stabilization, precarbonization, carbonization, and surface treatment [22, 23]. The ACF samples were designated as P7 and P10 according to their Brunauer-Emmett-Teller (BET) surface areas of 700 and 1000 m<sup>2</sup>/g.

**2.2. Characterization.** The morphologies of the PAN-based ACFs were measured by a LEO-1530 scanning electron microscopy (SEM). The Brunauer-Emmett-Teller (BET) surface areas and pore structure parameters were characterized by N<sub>2</sub> sorption method at 77 k.

**2.3. CDI Configuration.** A typical configuration (Figure 1) of the flow-through CDI cell usually comprises two parallel electrodes with an in-between insulating spacer of 5.5 \* 5 cm<sup>2</sup>,

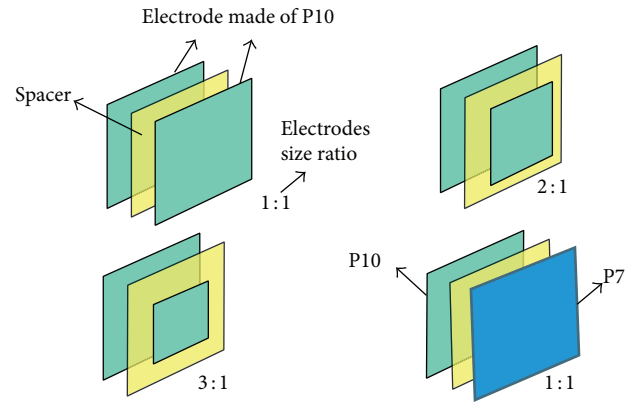


FIGURE 2: Schematic of asymmetric electrodes.

just as depicted in our previous work [3]. The electrode was made up of PAN-based ACFs cloth. In the CDI process, a NaCl aqueous solution was continuously pumped into CDI cell at a rate of 6 mL/min from a peristaltic pump. All the experiments were operated in a thermostatic chamber under 20°C with a cell voltage of 1.2 V, just a little lower than the water electrolysis potential. The ion adsorption behavior is reflected by the change of solution's conductivity, which was monitored online by a conductivity meter (type 308 A, Leici Co.) with 10 s interval.

**2.4. CDI Performance Evaluation.** To study the influence of electrode symmetry on CDI performance, asymmetric electrodes (Figure 2) were designed to treat NaCl aqueous solution.

- (1) Size asymmetry: both P10 electrodes with a tailored geometric proportion of 1:1, 2:1 and 3:1 were constructed to study the CDI behavior, with one electrode remaining the same size while the other is smaller and smaller.
- (2) Material asymmetry: two same sized electrodes with different material of P7 and P10 were constructed to study the CDI behavior.

## 3. Results and Discussion

**3.1. Structural Analysis.** The SEM image of the two PAN-based ACFs (Figure 3) shows that the P7 and P10 cloth have smooth, cross-linked fibers with diameter of 8 and 5 μm, respectively. N<sub>2</sub> adsorption results (Figure 4) indicate that both ACFs are microporous materials. Detailed pore parameters are listed in Table 1. P10 demonstrates higher SSA and bigger average pore width and volume than P7.

**3.2. Capacitive Deionization Performance with Symmetric Electrodes.** To evaluate the PAN-based ACFs' CDI performances, NaCl aqueous solutions with different concentration were fed into the CDI cell with P7 and P10 symmetrical electrodes, respectively. Before each experiment, electrodes

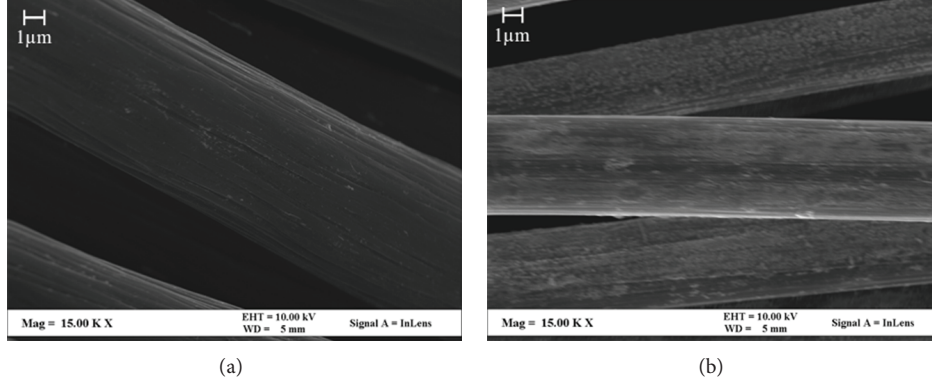
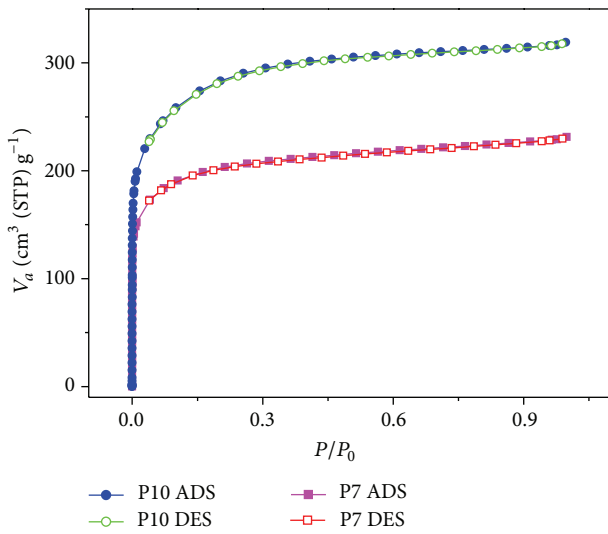


FIGURE 3: SEM image of P7 (a) and P10 (b).

FIGURE 4: N<sub>2</sub> adsorption/desorption isotherms of P7 and P10.

were washed by pure water until no salt remained and then dried with nitrogen.

Total adsorption of ions consists of two parts, non-electrosorption and electrosorption. At first when the NaCl aqueous solution was input into the CDI cell, solution's concentration dropped because of physical adsorption or chemical adsorption. Nonelectrosorption is irreversible. After the nonelectrosorption reached equilibrium, electric field was applied, and the electrosorption process started (Figure 5). Here, electrosorption is reversible. After electrosorption reached an equilibrium state, electric field was reversed manually and ions' desorption proceeded, in which the electrodes were regenerated. If the reversed electric field was applied continually, electrodes would begin to adsorb ions in solution again, thus beginning a new cycle. It can also be seen that PAN-based ACFs electrodes had a quite fast adsorption rate. It only takes less than half an hour for PAN-based ACFs to complete most of the electrosorption process, which would take more than an hour for CNT sponges (100 min) [3], pitch-based ACF (65 min) [24], mesoporous activated carbon (100 min) [9], and some other carbon

TABLE 1: PAN-based ACFs' pore structure parameters.

Sample	BET SSA (m <sup>2</sup> /g)	Pore volume (cc/g)	Average pore width (nm)
P7	754	0.36	1.9
P10	1000	0.49	2.0

materials under the same conditions. This high adsorption rate contributes to a high adsorption efficiency of PAN-based ACFs. However, it is shown that PAN-based ACF possesses a lower electrosorption capacity in comparison with pitch-based ACF [24] because its higher nonelectrosorption has a negative effect.

The electrosorption isotherms of PAN-based ACFs were obtained by altering the feeding concentration (Figure 6). It shows that P10 has a higher adsorption capacity at higher equilibrium concentration. This is because under low solution concentration, only a few ions contact and impact pores of electrodes' surface, so adsorption and desorption reach equilibrium state at low electrosorption capacity; while under high solution concentration, more ions contact and interact with surface's pores and more surface area is effective in electrosorption, so electrosorption reach equilibrium at higher capacity. We can correlate the experiments data fit with the Langmuir model and Freundlich model, shown in (1) [25]

$$Q = \frac{Q_m K_L C_e}{1 + K_L C_e}, \quad (1)$$

$$Q = k_f \cdot C_e^{1/n}.$$

$Q_m$  is the maximum adsorption capacity (mmol/g).  $C_e$  is the equilibrium concentration (mmol/L).  $Q$  is the specific adsorption capacity (mmol/g) while solution's concentration is  $C_e$ .  $K_L$  is Langmuir constant,  $k_f$  and  $n$  are Freundlich constants.

Both Langmuir model and Freundlich model fit the data well with P7's correlation coefficient being around 0.99 and P10's being around 0.83. This suggests a monolayer adsorption of ions on the electrodes' surface under the experimental concentrations [26]. The theoretic capability to adsorb NaCl,  $Q_m$ , presents an adsorption capacity of over

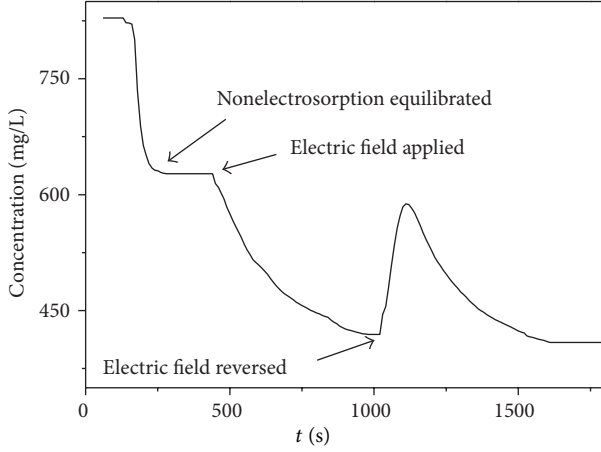


FIGURE 5: PAN-based ACFs' CDI dynamic adsorption curve.

0.2 mmol/g of P10, and nearly 0.15 mmol/g of P7. P10 has a higher electrosorption capacity of CDI. This result shows ACFs with bigger pore width and pore volume and higher SSA (if not too high SSA); thus electrosorption capacity is higher.

**3.3. CDI Configuration with Asymmetry Electrodes.** We used two kinds of asymmetric electrodes in CDI described in the experiment. For convenience, when we connected the positive pole of power supply to the small-sized electrode, with the negative to the other, the voltage direction is regarded as forward voltage. On the other hand, when the positive pole power supply was connected to the big-sized electrode, the voltage direction is regarded as reverse voltage. It is interestingly found that asymmetric electrodes showed a different adsorption CDI capacity between forward voltage and reverse voltage. Under the condition of forward voltage, the electrodes adsorb more sodium chloride ions. Moreover, the electrosorption capacity increases with increasing the electrode ratio. The CDI data were compiled in Table 2. For the smaller anode electrode, it gave a smaller divisor and thus led to a higher electrosorption capacity. Porada et al. [21] had similar results with varied electrode ratio.

The reason for such difference could not be found in the EDL model [5]. In (2) of EDL model,  $\sigma$  is electric charge density of the EDL,  $\sigma_0$  is charge density around electrode surface in tight layer,  $e^{(ze\varphi_s+\delta)/kT}$  is the Boltzmann factor,  $N_s$  is the mole concentration of solution,  $n_0$  is the positive or negative charge density in a far enough distance,  $\epsilon_0$  is vacuum permittivity, and  $\epsilon_r$  is relative permittivity.

$$\sigma = \frac{\sigma_0}{1 + 1/N_s e^{-(ze\varphi_0)/kT}} + \sqrt{8n_0\epsilon_0\epsilon_r kT} \sinh \frac{ze\varphi_\delta}{2kT}. \quad (2)$$

The forward or reverse voltage condition did not change the factors in (2), which should lead to equal electrosorption capacity. The EDL theory was based on the hypothesis that electrodes are flat, without pores and microtopography. To explain the difference in electrosorption amount, the pore structure and microtopography of the electrode material

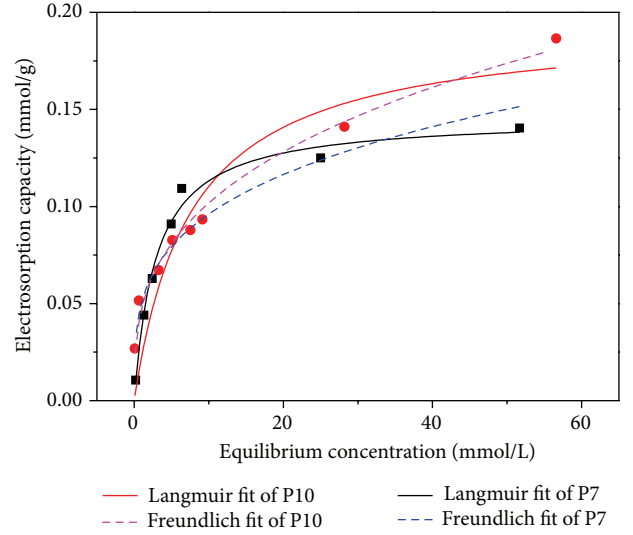


FIGURE 6: Electrosorption isotherms of NaCl and their fitting curves.

TABLE 2: Influence of asymmetric electrodes on CDI adsorption.

Initial concentration of NaCl	100 mg/L			200 mg/L		
Proportion of electrodes' size	1:1	2:1	3:1	1:1	2:1	3:1
Electrosorption capacity of reverse voltage (mg/g)	1.07	1.82	2.79	3.02	3.51	5.26
Electrosorption capacity of forward voltage (mg/g)	1.07	2.38	3.45	3.03	5.05	6.25

have to be taken into account. In addition, the EDL overlap effect and the increase of inner-pore potential cannot be neglected. PAN-based ACFs are microporous materials; thus the EDL overlap effect and the inner-pore potential are fairly significant. These factors made ions with smaller hydrated ionic radius liable to enter into the micropores. The hydrated ionic radius of  $\text{Na}^+$  (3.58 Å) is bigger than  $\text{Cl}^-$  (3.32 Å) [27], so  $\text{Cl}^-$  can be adsorbed more easily. When the size of electrodes differed, smaller electrode reached adsorption equilibrium more quickly. To guarantee the electric neutrality of the outflow solution, the big electrode would not adsorb more ions even if it has more adsorption sites. Under the reverse voltage,  $\text{Na}^+$  was adsorbed by small electrode, which was harder than  $\text{Cl}^-$  under the forward voltage. Thereby, only a smaller number of  $\text{Na}^+$  was adsorbed, which accordingly led to a low adsorption of chloride on the bigger electrode. Hence, the electrosorption capacity under reverse voltage was less than that under forward voltage.

To confirm that the difference in electrosorption capacity is caused by pore structure but not geometric changes, a comparison experiment was designed by using two same sized electrodes with different pore characteristics. One electrode was made of P7 with an average pore width of 1.9 nm, and the other electrode was made of P10 with an average pore width of 2.0 nm. When applying negative voltage on P10, the electrosorption amount was higher than the reversed condition. That is to say, when the larger pore material was

used as negative electrode to adsorb  $\text{Na}^+$  and the smaller pore material adsorbed  $\text{Cl}^-$ , electrosorption capacity was higher. These results verify our explanation of the micromechanism adsorption.

#### 4. Conclusions

PAN-based activated carbon fibers were used as CDI electrodes, which demonstrated a moderate electrosorption capacity. ACFs electrodes with higher specific surface area (as in the case of P10) and under higher solution concentration have higher electrosorption capacity. Because of the EDL overlap effect and inner-pore potential, ions with smaller hydrated ionic radius could be adsorbed in the electrode materials more easily. This could be proved by applying asymmetric electrodes in CDI experiments, which shows variation in electrosorption capacity between forward voltage and reverse voltage.

#### Conflict of Interests

The authors declare that they have no conflict of interests regarding the publication of this paper.

#### Acknowledgments

The authors are grateful for the financial support from the National Natural Science Foundation of China (Grant no. 51072091) and the cooperative Project JST-MOST (no. 2011DFA50430).

#### References

- [1] C. J. Vörösmarty, P. Green, J. Salisbury, and R. B. Lammers, "Global water resources: vulnerability from climate change and population growth," *Science*, vol. 289, no. 5477, pp. 284–288, 2000.
- [2] P. H. Gleick, "The changing water paradigm a look at twenty-first century water resources development," *Water International*, vol. 25, no. 1, pp. 127–138, 2000.
- [3] L. Wang, M. Wang, Z.-H. Huang et al., "Capacitive deionization of NaCl solutions using carbon nanotube sponge electrodes," *Journal of Materials Chemistry*, vol. 21, no. 45, pp. 18295–18299, 2011.
- [4] M. Mossad and L. Zou, "A study of the capacitive deionisation performance under various operational conditions," *Journal of Hazardous Materials*, vol. 213–214, pp. 491–497, 2012.
- [5] M. A. Anderson, A. L. Cudero, and J. Palma, "Capacitive deionization as an electrochemical means of saving energy and delivering clean water. Comparison to present desalination practices: will it compete?" *Electrochimica Acta*, vol. 55, no. 12, pp. 3845–3856, 2010.
- [6] Y. Oren, "Capacitive deionization (CDI) for desalination and water treatment—past, present and future (a review)," *Desalination*, vol. 228, no. 1–3, pp. 10–29, 2008.
- [7] J. Yang, L. Zou, and N. R. Choudhury, "Ion-selective carbon nanotube electrodes in capacitive deionisation," *Electrochimica Acta*, vol. 91, pp. 11–19, 2013.
- [8] M. Inagaki, H. Konno, and O. Tanaike, "Carbon materials for electrochemical capacitors," *Journal of Power Sources*, vol. 195, no. 24, pp. 7880–7903, 2010.
- [9] G. Wang, B. Qian, Q. Dong, J. Yang, Z. Zhao, and J. Qiu, "Highly mesoporous activated carbon electrode for capacitive deionization," *Separation and Purification Technology*, vol. 103, pp. 216–221, 2013.
- [10] H. Li, L. Zou, L. Pan, and Z. Sun, "Novel graphene-like electrodes for capacitive deionization," *Environmental Science and Technology*, vol. 44, no. 22, pp. 8692–8697, 2010.
- [11] P. S. Goh, A. F. Ismail, and B. C. Ng, "Carbon nanotubes for desalination: performance evaluation and current hurdles," *Desalination*, vol. 308, pp. 2–14, 2013.
- [12] L. Pan, X. Wang, Y. Gao, Y. Zhang, Y. Chen, and Z. Sun, "Electrosorption of anions with carbon nanotube and nanofiber composite film electrodes," *Desalination*, vol. 244, no. 1–3, pp. 139–143, 2009.
- [13] H. Li, T. Lu, L. Pan, Y. Zhang, and Z. Sun, "Electrosorption behavior of graphene in NaCl solutions," *Journal of Materials Chemistry*, vol. 19, no. 37, pp. 6773–6779, 2009.
- [14] D. Zhang, X. Wen, L. Shi, T. Yan, and J. Zhang, "Enhanced capacitive deionization of graphene/mesoporous carbon composites," *Nanoscale*, vol. 4, pp. 5440–5446, 2012.
- [15] Z. Wang, B. Doua, L. Zhengb, G. Zhangb, and Z. Liub, "Effective desalination by capacitive deionization with functional graphene nanocomposite as novel electrode material," *Desalination*, vol. 299, pp. 96–102, 2012.
- [16] J. C. Farmer, D. V. Fix, G. V. Mack, R. W. Pekala, and J. F. Poco, "Capacitive deionization of NaCl and  $\text{NaNO}_3$  solutions with carbon aerogel electrodes," *Journal of the Electrochemical Society*, vol. 143, no. 1, pp. 159–169, 1996.
- [17] K.-L. Yang, T.-Y. Ying, S. Yiacoumi, C. Tsouris, and E. S. Vittoratos, "Electrosorption of ions from aqueous solutions by carbon aerogel: an electrical double-layer model," *Langmuir*, vol. 17, no. 6, pp. 1961–1969, 2001.
- [18] G. Wang, C. Pan, L. Wang et al., "Activated carbon nanofiber webs made by electrospinning for capacitive deionization," *Electrochimica Acta*, vol. 69, pp. 65–70, 2012.
- [19] M.-W. Ryoo and G. Seo, "Improvement in capacitive deionization function of activated carbon cloth by titania modification," *Water Research*, vol. 37, no. 7, pp. 1527–1534, 2003.
- [20] L. Wang, Z.-H. Huang, M. Yueb, M. Lia, M. Wanga, and F. Kanga, "Preparation of flexible phenolic resin-based porous carbon fabrics by electrospinning," *Chemical Engineering Journal*, vol. 218, pp. 232–237, 2013.
- [21] S. Porada, M. Bryjak, A. van der Wal, and P. M. Biesheuvel, "Effect of electrode thickness variation on operation of capacitive deionization," *Electrochimica Acta*, vol. 75, pp. 148–156, 2012.
- [22] T.-H. Ko, P. Chiranairadul, and C.-H. Lin, "The influence of continuous stabilization on the properties of stabilized fibers and the final activated carbon fibers. Part I," *Polymer Engineering & Science*, vol. 31, pp. 1618–1626, 1991.
- [23] T.-H. Ko and C.-H. Li, "Influence of pre-carbonization on the properties of PAN-based carbon fibers developed by two-stage continuous carbonization and air oxidation," *Polymer Composites*, vol. 16, no. 3, pp. 224–232, 1995.
- [24] Z.-H. Huang, M. Wang, L. Wang, and F. Kang, "Relation between the charge efficiency of activated carbon fiber and its desalination performance," *Langmuir*, vol. 28, no. 11, pp. 5079–5084, 2012.

- [25] Z. Aksu, "Determination of the equilibrium, kinetic and thermodynamic parameters of the batch biosorption of nickel(II) ions onto *Chlorella vulgaris*," *Process Biochemistry*, vol. 38, no. 1, pp. 89–99, 2002.
- [26] B. Özkaya, "Adsorption and desorption of phenol on activated carbon and a comparison of isotherm models," *Journal of Hazardous Materials*, vol. 129, no. 1–3, pp. 158–163, 2006.
- [27] E. R. Nightingale Jr., "Phenomenological theory of ion solvation. Effective radii of hydrated ions," *Journal of Physical Chemistry*, vol. 63, no. 9, pp. 1381–1387, 1959.

## Research Article

# Carbon Nanofibers from Carbon Nanotubes by 1.2 keV Ar<sup>+</sup> Sputtering at Room Temperature

Shuang-Xi Xue, Qin-Tao Li, Xian-Rui Zhao, Qin-Yi Shi, Zhi-Gang Li, and Yan-Ping Liu

*Department of Physics and Electronic Engineering, Taizhou University, Taizhou, 318000, China*

Correspondence should be addressed to Qin-Tao Li; [liqintao@tzc.edu.cn](mailto:liqintao@tzc.edu.cn)

Received 6 December 2013; Accepted 14 January 2014; Published 20 February 2014

Academic Editor: S. C. Wang

Copyright © 2014 Shuang-Xi Xue et al. This is an open access article distributed under the Creative Commons Attribution License, which permits unrestricted use, distribution, and reproduction in any medium, provided the original work is properly cited.

Multi-walled carbon nanotubes (MWCNTs) were irradiated by 1.2 keV Ar ion beams for 15–60 min at room temperature with current density of  $60 \mu\text{A}/\text{cm}^2$ . The morphology and microstructure are investigated by scanning electron microscopy, transmission electron microscopy and Raman spectroscopy. The results show that carbon nanofibers are achieved after 60 min ion irradiation and the formation of carbon nanofibers proceeds through four periods, carbon nanotubes—amorphous carbon nanowires—carbon nanoparticles along the tube axis—conical protrusions on the nanoparticles surface—carbon nanofibers from the conical protrusions.

## 1. Introduction

Since their discovery by Iijima in 1991 [1], carbon nanotubes (CNTs) have attracted considerable attention due to their high electrical conductivity, high aspect ratio “whisker-like” shape for optimum geometrical field enhancement, and remarkable thermal stability, which makes it possible to use CNTs as conduction wires and building blocks of a variety of nanoscale electronic and optoelectronic devices [2]. The realization of nanoscale devices and interconnections among building blocks with CNTs requires fully exploiting the CNTs potentials and effective methods to tailor CNTs with desired aims. Furthermore, since the devices are often used in an electromagnetic and/or high-energy particle radiation environment, the investigations on structural modification through irradiating CNTs are of great importance for providing insights into interactions between energetic particles and CNTs, for controllably fabricating multifunctional nanodevices, and for controllably protecting and producing radiation damages.

The interactions between high energy particles and CNTs have been extensively studied during the last several years [3–13]. Structural evolution of CNTs irradiated by in situ electron beam performed by Banhart et al. showed that basal planes of CNTs appeared as rupture, tilting, and bending under the

irradiation [3, 4]. Other researchers found structural transformations from CNTs to carbon onions [5] or to diamond [6] by electron beam. Wei et al. tailored CNTs that could be tailored by using 30 or 50 keV Ga ion beam of different doses [7]. The transformation of CNTs proceeds from highly ordered pillbox-like nanocompartments and the formation of amorphous rod with hollow structure, without destroying the tubular shape of CNTs after the irradiation-induced amorphization to homogenous amorphous rods. CNTs irradiated by 4 MeV Cl ion beam have been investigated by Kim et al. [8]. They found that morphological transformation from CNTs to nanocompartments with bamboo-like structure inside the tubes was formed at the dose of  $3 \times 10^{16}$  ions/cm<sup>2</sup> and concluded that the nanocompartments with bamboo-like structure were originated from folding of the inner walls. In our previous work [9–11], the interaction between the CNTs and Si ion beam with the energy of 40 keV has been investigated. The result shows that with the increment of ion dose, the CNTs are transformed into semisolid amorphous carbon nanowire with hollow structure, solid amorphous carbon nanowire, and carbon nanowire junctions by the defects assisted the bridging of carbon nanowire. Therefore, CNTs should transform into other carbon nanostructure such as onion, diamond, and amorphous wire by high energy ion sputtering. However, the investigation of the interactions

between CNTs and ion beam with energy that ranged from several ten eV to several keV has not been attention.

Recently, the interaction between the carbon material and ion beam with energy of several keV has been studied, such as diamond [12], graphite and graphite paste [13, 14], glassy carbon [15, 16], and flexible plastic substrate [17–19]. These results show that the carbon nanofiber could form by ion sputtering and carbon nanofiber only grow on the tip of cone. Hence, it is believed that the carbon nanofiber could be formed by ion sputtering carbon nanotube with low energy of several keV. In this paper, carbon nanotubes are irradiated by Ar ion beam with energy of 1.2 keV at room temperature and the structural transformation is investigated.

## 2. Experimental Details

Multiwalled carbon nanotubes (MWCNTs), synthesized by chemical vapor deposition (CVD), were dispersed in alcohol by ultrasonic waves and dropped onto Si substrates as the samples. Then, the samples were placed in the chamber of Kaufman low energy gas ion source and were irradiated by Ar ion beam at room temperature with energy of 1.2 keV and current intensity of  $60 \mu\text{A}/\text{cm}^2$ . The irradiation time was from 15 min to 60 min. The morphology evolution of samples before and after the low energy ion treatment was observed through Scanning electron microscopy (SEM, LEO 1530VP). The characteristic of structural changing of CNTs was investigated by transmission electron microscope (TEM, JEOL 2010F) operated at 200 kV and micro-Raman spectroscopy (Dilor LabRam-1B) at room temperature.

## 3. Results and Discussion

Figure 1 shows the SEM images and TEM images of the as-grown CNTs and the inset is the high-resolution TEM (HRTEM) images. The diameters of as-grown CNTs are 18–35 nm. TEM and high-resolution TEM (HRTEM) images show that the as-grown CNTs are well-ordered graphitic sheets in [002] orientation (average plane spacing  $\sim 0.34$  nm).

Figure 2 shows the SEM images of CNTs irradiated by 1.2 keV Ar ions for 15–60 min. The inset images in Figures 2(b) and 2(d) are the corresponding TEM images and high-resolution SEM images, respectively. After 15 min sputtering, the tube shapes of CNTs are almost intact and the diameters of CNTs are 4–35 nm, and only a few CNTs are broken into several parts along the tube axis; the inset TEM images of typical CNTs show that the CNTs are transformed into amorphous carbon nanowires, consistent with the results of our previous work [9–11]. After 30 min irradiation, the CNTs are separated into some particles with the size from 20–30 nm to 300–400 nm along the tube axis and the surfaces of particles are smooth with no conical protrusion. After 45 min sputtering, the all tube morphology of CNTs on the top layer of CNTs stacks is broken and the tube morphology of CNTs at the bottom of CNTs stacks is almost intact; some protrusions can be observed on the coarse aggregated nanoparticles surface. With 60 min sputtering, all CNTs are broken, and some nanofibers can be observed: the lengths of

nanofibers are ranged from several ten nm to several  $\mu\text{m}$ . The high-resolution SEM images of typical nanofiber show that the nanofiber grows on the tip of protrusion.

Typical micro-Raman spectra of the as-grown CNTs and CNTs by Ar ion irradiation from 15 min to 60 min are shown in Figure 3. There are two bands between 1000 and 2000  $\text{cm}^{-1}$  corresponding to the typical Raman peaks of carbonaceous materials [20, 21]. The peak at 1580  $\text{cm}^{-1}$  (*G* band) corresponds to an  $E_{2g}$  mode of graphite and the peak at 1330  $\text{cm}^{-1}$  (*D* band) is associated with the vibration of carbon atoms with turbostratic carbon. The Raman spectrum is considered to depend on clustering of the  $\text{sp}^2$  phase, bond disorder, presence of  $\text{sp}^2$  rings or chains, and the  $\text{sp}^2/\text{sp}^3$  ratio. The intensity ratio of the *D* to *G* band models ( $I_D/I_G$ ) represents the amorphous phase content or the degree of crystallinity of the carbonaceous materials. With increasing the sputtering time, the  $I_D/I_G$  increases from 0.61 to 0.94 and the *G* position moves from 1580.9 to 1566.1  $\text{cm}^{-1}$ , consistent with that of from carbon nanoparticle of graphene stacks to amorphous carbon provided by Ferrari and Robertson [21].

Based on the investigation of SEM, TEM, and Raman spectroscopy, it is speculated that the formation of carbon nanofiber has four processes: the CNTs are transformed into the amorphous carbon nanowire, the amorphous carbon nanowires are broken into some particles with smooth surface along the tube axis, some protrusions are formed on the particles, and the carbon nanofibers grow from the tip of the protrusions. It is known that the ion-induced surface morphology is accounted for two competitive effects, the roughening process and the smoothing process. The roughening process is caused by the different sputtering yield depending on the curvature of the surface. For a rough surface, the sputtering yield at the trough is higher than that on the crest, which should enlarge the amplitude rapidly. The smoothing process is caused by the thermal or ion-induced diffusion driven by surface energy minimization. In general, the ripple-like or periodic structure [22] is formed on solid surface by the off-normal ion beam irradiation. Habenicht et al. [23] have investigated the topography of graphite surface eroded by a 5 keV  $\text{Xe}^+$  ion beam. The investigation result shows that the periodic ripple morphology evolved with the ion fluences of  $5 \times 10^{16}$  ions/ $\text{cm}^2$  at the incident angle of  $60^\circ$ , and then large perturbations of the surface topography occurred for rising ion fluences to  $2 \times 10^{18}$  ions/ $\text{cm}^2$ ; even the periodic structure was damaged by the larger perturbations of the surface topography at the ion fluences of  $5 \times 10^{18}$  ions/ $\text{cm}^2$ . Floro et al. [24] have investigated the formation of cones on graphite by 1 keV  $\text{Ar}^+$  bombardment with current density of 2 mA/ $\text{cm}^2$ . They found that very fine whiskers or leaders became visible after 5 min of bombardment (the ion fluences was  $\sim 3.8 \times 10^{18}$  ions/ $\text{cm}^2$ ). The first 25 min of whisker formation were characterized by a rapid growth process in which whiskers grew to some critical length and radius. Subsequent to the initial growth spurt, length and radius increased slowly with time. The investigations of carbon material (such as glass amorphous carbon, graphite, and diamond) irradiated by  $\text{Ar}^+$  with energy of several keV show that the cone or protrusions could form by several ten min sputtering [12–19]. Hence,

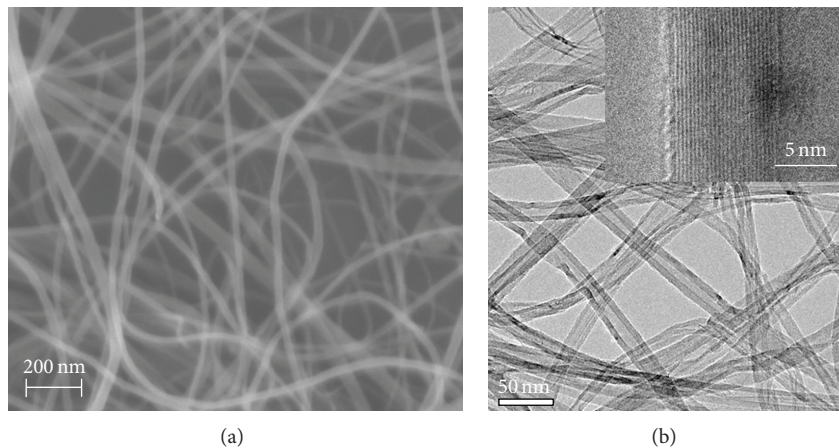


FIGURE 1: Morphology and structure observations of the as-grown CNTs. (a) A typical SEM image; (b) typical TEM image and HRTEM image (the inset).

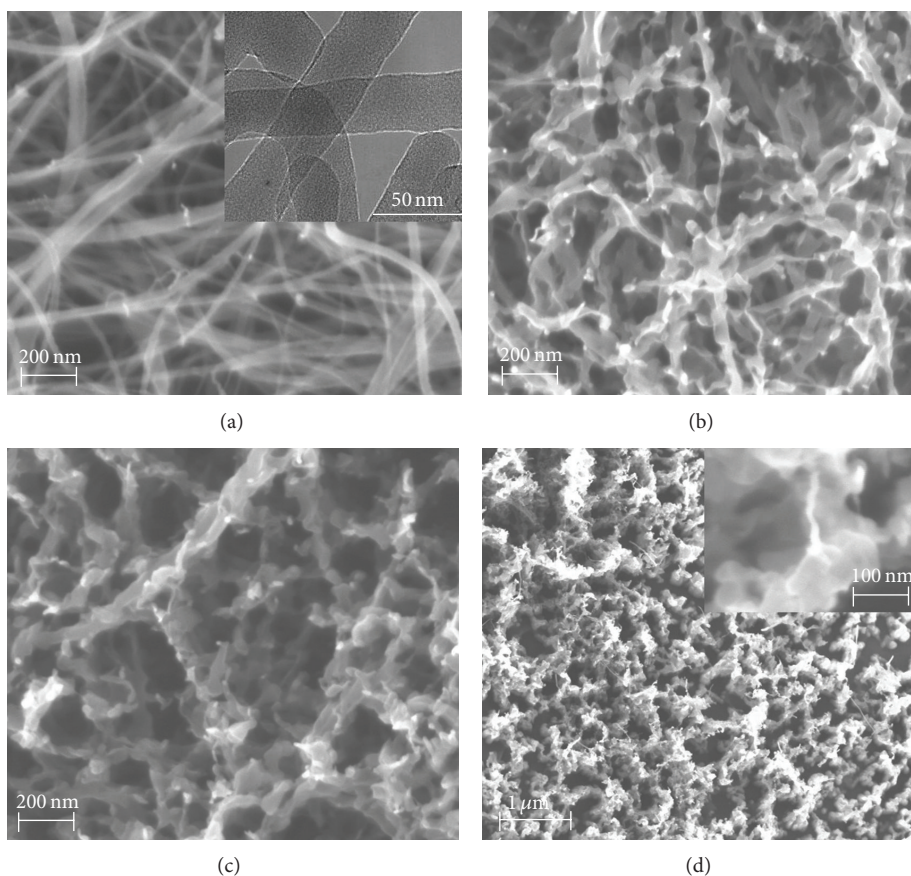


FIGURE 2: SEM images of CNTs irradiated by 1.2 keV Ar ions for 15–60 min. (a) 15 min; (b) 30 min; the inset was the typical TEM images of CNTs; (c) 45 min; (d) 60 min; the inset was the high-resolution SEM images.

it is believed that the formation of cone or conical carbon protrusions is contributed to the competitive effects of the roughening process and the smoothing process. This is the formation reason of carbon protrusions in our experiment. The investigations of carbon material irradiated by  $Ar^+$  with energy of several keV also show that carbon nanofibers grow only on the tip of cone or protrusion, the cone or protrusion

formation is a prerequisite for carbon nanofiber growth, and the redeposited massive carbon atoms diffuse toward the cone tips, resulting in carbon nanofiber formation. It is also the reason of carbon nanofiber growth in our experiment.

Therefore, the formation process of carbon nanofibers by  $Ar^+$  sputtering CNTs could be speculated. At first, the CNTs are subjected to structural changes due to displacement

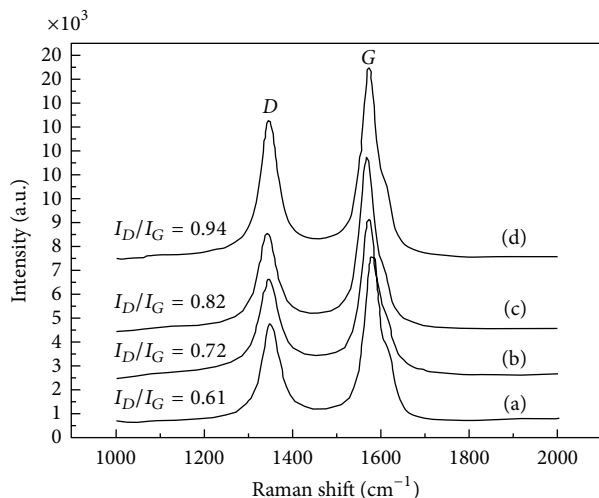


FIGURE 3: Typical micro-Raman spectra of the as-grown CNTs (a) and CNTs by Ar ion irradiation from 15 min to 60 min; (b) 15 min; (c) 30 min; (d) 60 min.

collisions and collision cascade effect, which generate large quantities of defects (vacancies and interstitials) on the tube walls and between the walls. The concentration of higher defects results in the increment of degree of disorder. With the further generation of defects, the CNTs could even collapse and form amorphous nanowires. Then, due to the different sputtering yield dependent on the curvature of the amorphous nanowire surface, carbon atom on some area are sputtered quickly, CNTs are broken, and some particles are formed along the tube axis. Subsequently, the protrusions are formed due to the competitive effects of the roughening process and the smoothing process. At last, the migration of mass redeposition atom toward the tip leads to the growth of carbon nanofibers on the protrusion.

#### 4. Conclusions

In conclusion, the carbon nanotubes are irradiated by Ar ion beam with energy of 1.2 keV at room temperature with current density of  $60 \mu\text{A}/\text{cm}^2$  and the samples are investigated by SEM, TEM, and Raman spectroscopy. The structural evolution of CNTs by ion beam bombardment shows that the formation of carbon nanofibers proceeds through four periods: carbon nanotubes, amorphous carbon nanowires; carbon nanoparticles aligned along the tube axis; conical protrusions on the nanoparticles surface; and carbon nanofibers from the conical protrusions. The formation of carbon nanofibers is accounted for the competitive effects between the roughening process and the smoothing process.

#### Conflict of Interests

The authors declare that they have no conflict of interests regarding the publication of this paper.

#### Acknowledgments

The authors gratefully acknowledge the financial support of the project by the National Natural Science Foundation of China (Grant nos. 51001078 and 51202155).

#### References

- [1] S. Iijima, "Helical microtubules of graphitic carbon," *Nature*, vol. 354, no. 6348, pp. 56–58, 1991.
- [2] C. Dekker, "Carbon nanotubes as molecular quantum wires," *Physics Today*, vol. 52, no. 5, pp. 22–28, 1999.
- [3] F. Banhart, "Irradiation effects in carbon nanostructures," *Reports on Progress in Physics*, vol. 62, no. 8, pp. 1181–1221, 1999.
- [4] F. Banhart, "The formation of a connection between carbon nanotubes in an electron beam," *Nano Letters*, vol. 1, no. 6, pp. 329–332, 2001.
- [5] F. Banhart, T. Füller, P. Redlich, and P. M. Ajayan, "The formation, annealing and self-compression of carbon onions under electron irradiation," *Chemical Physics Letters*, vol. 269, no. 3-4, pp. 349–355, 1997.
- [6] B. Wei, J. Zhang, J. Liang, and D. Wu, "The mechanism of phase transformation from carbon nanotube to diamond," *Carbon*, vol. 36, no. 7-8, pp. 997–1001, 1998.
- [7] B. Q. Wei, J. D'Arcy-Gall, P. M. Ajayan, and G. Ramanath, "Tailoring structure and electrical properties of carbon nanotubes using kilo-electron-volt ions," *Applied Physics Letters*, vol. 83, no. 17, pp. 3581–3583, 2003.
- [8] H. M. Kim, H. S. Kim, S. K. Park, J. Joo, T. J. Lee, and C. J. Lee, "Morphological change of multiwalled carbon nanotubes through high-energy (MeV) ion irradiation," *Journal of Applied Physics*, vol. 97, no. 2, Article ID 026103, 2005.
- [9] Z. Ni, Q. Li, J. Gong, D. Zhu, and Z. Zhu, "Structural change of carbon nanotubes produced by Si ion beam irradiation," *Nuclear Instruments and Methods in Physics Research B*, vol. 260, no. 2, pp. 542–546, 2007.
- [10] Z. Ni, Q. Li, D. Zhu, and J. Gong, "Fabrication of carbon nanowire networks by Si ion beam irradiation," *Applied Physics Letters*, vol. 89, no. 5, Article ID 053107, 2006.
- [11] Z. Ni, Q. Li, L. Yan, J. Gong, and D. Zhu, "Large-scale fabrication of carbon nanowire networks using kilo-electron-volt ion beam," *Diamond and Related Materials*, vol. 17, no. 3, pp. 365–371, 2008.
- [12] Q. Li, S. Xue, Z. Li, J. Gong, and D. Zhu, "Carbon nanofibres from diamond film using Ar-ion bombardment and their field emission property," *Micro and Nano Letters*, vol. 4, no. 1, pp. 1–4, 2009.
- [13] X. L. Liu, R. Z. Zhang, and Z. M. Zhang, "Near-field thermal radiation between hyperbolic metamaterials: graphite and carbon nanotubes," *Applied Physics Letters*, vol. 103, no. 21, Article ID 203102, 2013.
- [14] Y. B. Chen, Y. Hu, M. X. Liu et al., "Chiral structure determination of aligned single-walled carbon nanotubes on graphite surface," *Nano Letters*, vol. 13, no. 11, pp. 5666–5671, 2013.
- [15] M. Tanemura, T. Okita, J. Tanaka et al., "Room-temperature growth of carbon nanofibers induced by  $\text{Ar}^+$  ion bombardment," *European Physical Journal D*, vol. 34, no. 1-3, pp. 283–286, 2005.
- [16] M. Tanemura, T. Okita, H. Yamauchi, S. Tanemura, and R. Morishima, "Room-temperature growth of a carbon nanofiber

- on the tip of conical carbon protrusions," *Applied Physics Letters*, vol. 84, no. 19, pp. 3831–3833, 2004.
- [17] M. Tanemura, H. Hatano, M. Kitazawa et al., "Room-temperature growth of carbon nanofibers on plastic substrates," *Surface Science*, vol. 600, no. 18, pp. 3663–3667, 2006.
- [18] T. T. Tan, H. S. Sim, S. P. Lau, H. Y. Yang, M. Tanemura, and J. Tanaka, "X-ray generation using carbon-nanofiber-based flexible field emitters," *Applied Physics Letters*, vol. 88, no. 10, Article ID 103105, 2006.
- [19] H. S. Sim, S. P. Lau, H. Y. Yang, L. K. Ang, M. Tanemura, and K. Yamaguchi, "Reliable and flexible carbon-nanofiber-based all-plastic field emission devices," *Applied Physics Letters*, vol. 90, no. 14, Article ID 143103, 2007.
- [20] F. Tuinstra and J. L. Koenig, "Raman spectrum of graphite," *The Journal of Chemical Physics*, vol. 53, no. 3, pp. 1126–1130, 1970.
- [21] A. C. Ferrari and J. Robertson, "Interpretation of raman spectra of disordered and amorphous carbon," *Physical Review B*, vol. 61, no. 20, pp. 14095–14107, 2000.
- [22] R. M. Bradley and J. M. Harper, "Theory of ripple topography induced by ion bombardment," *Journal of Vacuum Science and Technology A*, vol. 6, no. 4, pp. 2390–2239, 1988.
- [23] S. Habenicht, W. Bolse, K. P. Lieb, K. Reimann, and U. Geyer, "Nanometer ripple formation and self-affine roughening of ion-beam-eroded graphite surfaces," *Physical Review B*, vol. 60, no. 4, pp. R2200–R2203, 1999.
- [24] J. A. Floro, S. M. Rossmagel, and R. S. Robinson, "Ion-bombardment-induced whisker formation on graphite," *Journal of Vacuum Science and Technology A*, vol. 1, no. 3, pp. 1398–1402, 1983.

## Research Article

# Synthesis, Characterization, and Tribological Behavior of Oleic Acid Capped Graphene Oxide

Tiedan Chen,<sup>1,2,3</sup> Yanqiu Xia,<sup>1</sup> Zhengfeng Jia,<sup>1,4,5</sup> Zhilu Liu,<sup>1</sup> and Haobo Zhang<sup>6</sup>

<sup>1</sup> State Key Laboratory of Solid Lubrication, Lanzhou Institute of Chemical Physics, Chinese Academy of Sciences, Lanzhou 730000, China

<sup>2</sup> Huaibei Normal University, School of Chemistry and Materials Science, Huaibei 235000, China

<sup>3</sup> Graduate School of Chinese Academy of Sciences, Beijing 100039, China

<sup>4</sup> College of Materials Science and Engineering, Liaocheng University, Liaocheng 252059, China

<sup>5</sup> School of Materials Science and Engineering, Central South University, Changsha 410083, China

<sup>6</sup> Gansu University of Traditional Chinese Medicine, Lanzhou 730000, China

Correspondence should be addressed to Yanqiu Xia; [xiayq@licp.cas.cn](mailto:xiayq@licp.cas.cn)

Received 4 November 2013; Revised 17 December 2013; Accepted 24 December 2013; Published 3 February 2014

Academic Editor: Jinlong Jiang

Copyright © 2014 Tiedan Chen et al. This is an open access article distributed under the Creative Commons Attribution License, which permits unrestricted use, distribution, and reproduction in any medium, provided the original work is properly cited.

Graphene oxide (GO) nanosheets were prepared by modified Hummers and Offeman methods. Furthermore, oleic acid (OA) capped graphene oxide (OACGO) nanosheets were prepared and characterized by means of Fourier transform-infrared spectroscopy (FT-IR), transmission electron microscopy (TEM), and X-ray diffraction (XRD). At the same time, the friction and wear properties of OA capped graphite powder (OACG), OACGO, and oleic acid capped precipitate of graphite (OACPG) as additives in poly-alpha-olefin (PAO) were compared using four-ball tester and SRV-1 reciprocating ball-on-disc friction and wear tester. By the addition of OACGO to PAO, the antiwear ability was improved and the friction coefficient was decreased. Also, the tribological mechanism of the GO was investigated.

## 1. Introduction

Graphene has recently attracted extensive attention because of its excellent properties, such as high thermal conductivity, high young's modulus, large specific surface area, and outstanding tribological properties [1–4]. These excellent properties have opened new pathways for developing a wide range of novel functional materials, for example, solar cells, field-effect device, nanocomposites, antiwear materials, and so forth [5–8]. It is well known that graphene is one-atom layer thick carbon sheet. Graphene possesses excellent tribological properties because of its small size and extremely thin laminated structure. The graphene platelets easily enter the contact area during sliding, preventing the rough surfaces from coming into direct contact. Lin et al. [9] synthesized stearic acid and oil acid modified graphene using chemical methods. The modified graphene was dispersed into 350SN base oil as additives. The four-ball test exhibited that the wear resistance and load-carrying capacity of the lubricating

oil were greatly improved with the addition of the modified graphene. Huang et al. [10] synthesized graphite nanosheets with average diameter of 500 nm and thickness of about 15 nm by stirring ball milling. The tribological behavior of the graphite nanosheets as additive in paraffin oil was also investigated using a four-ball and a pin-on-disk friction and wear tester. The results showed that load-carrying capacity and antiwear ability of the lubricating oil were improved and the friction coefficient of the base oil was decreased by the addition of the graphite nanosheets. However, in the paper, the XRD analysis revealed that the graphite nanosheets were not graphene nanosheets. In general, chemical oxidation method (Hummers and Offeman) produces graphene by first inserting functional groups such as carbonyl, hydroxyl, and peroxy in carbon layers of graphite. The functional groups weakened the force between the carbon layers, which causes the graphene layers to peel off layer by layer from graphite. The resulting graphene oxide can be reduced to graphene by adding hydrazine into the graphene oxide solution [11].

However, the realization of the potential of the graphene is difficult because of the lack of the functional group in graphene. The abundant oxygenous groups in graphene oxide molecules make it feasible to interact with other functional groups [12]. So many works try to study the properties of the GO. Song et al. [13] investigated the tribological behaviors of the poly(ether ketone) (PEEK) composites filled with GO nanosheets. The result showed that the GO-Si-filled PEEK possessed an excellent friction reducing and antiwear properties when the applied load and the sliding speed are 2.94 N and 0.0628 m/s, respectively. The outstanding properties of the composites are possibly attributed to the self-lubricity of the GO-Si nanosheets. Tai et al. [14] fabricated a series of GO/ultrahigh molecular weight polyethylene (UHMWPE) through an optimized toluene-assisted mixing followed by hot-pressing. The tribological behavior of the GO/UHMWPE was investigated using high speed reciprocating friction testing machine. When the content of the added GO nanosheets was up to 1.0 wt%, the wear resistance of the composites increased lightly due to the formation of the transfer film of the UHMWPE. Li et al. [15] synthesized GO/nitrile rubber (NBR) nanocomposites using a solution-mixing method. Under dry sliding condition, the friction coefficient and wear rate of the GO/NBR composites were decreased dramatically with a lower concentration of GO. Possibly, the GO easily transferred from matrix to form a continuous transfer film during sliding, decreasing the friction coefficient and wear rate. Liu et al. [16] synthesized full exfoliation GO with an improved Hummers' method. The polyimide (PI) and PI/GO nanocomposites were also prepared via a polymerization of monomer reactants process. The friction and wear testing results showed that the addition of GO evidently improved the tribological properties of the PI. Song and Li [17] also synthesized GO nanosheets with modified Hummers and Offeman methods. The tribological behavior of the oxide graphene nanosheets as water-based lubricant additive was investigated using a UMT-2 ball-plate tribotester. With the addition of GO nanosheets in pure water, the antiwear ability was improved and the friction coefficient was decreased. They believed that the formation of a thin physical tribofilm on the substrate can explain the good friction and wear properties of GO nanosheets.

Based on the above discussion, the GO possesses an excellent tribological property, mixed into polymer or water-based lubricant. In this paper, the GO nanosheets were synthesized by modified Hummers and Offeman methods and were capped with OA using chemical method. The tribological properties of the PAO containing OACGO were investigated using quenched AISI 1045 steel/AISI 52100 steel couples. Furthermore, the mechanism of the antiwear was also discussed.

## 2. Experimental

GO, a two dimensional solid in bulk form, was prepared from natural graphite powder by oxidizing natural graphite powder in the presence of  $\text{KMnO}_4$  in concentrated  $\text{H}_2\text{SO}_4$  according to modified Hummer's method [18]. Simply, 4 g of

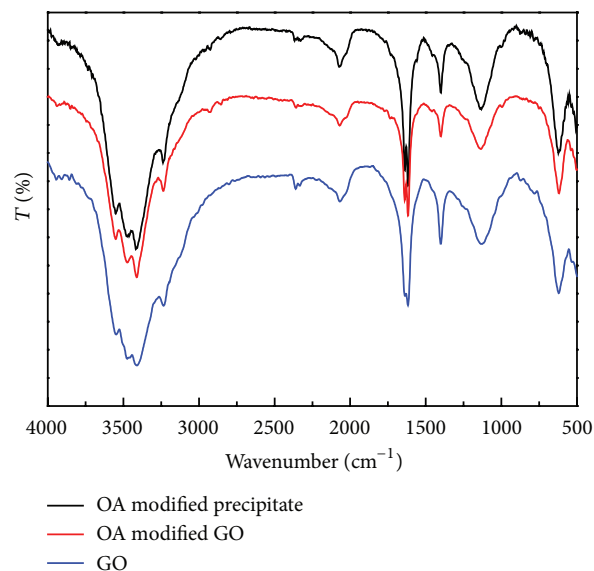


FIGURE 1: FT-IR spectra of the GO, OA modified GO, and OA modified precipitate.

graphite powder and 4 g of  $\text{NaNO}_3$  were added to 200 mL of cooled ( $0^\circ\text{C}$ ) concentrated  $\text{H}_2\text{SO}_4$  slowly with stirring, in a 1000 mL breaker. 30 g of  $\text{KMnO}_4$  was added gradually with stirring and cooling ( $0^\circ\text{C}$ ); then, the reaction was carried out for 90 min. For work up, the mixture was cooled to room temperature and poured into cold ( $0^\circ\text{C}$ ) deionized water. Successively, 30%  $\text{H}_2\text{O}_2$  was slowly added into the mixture until the solution turned bright yellow. The solid product was separated by centrifugation and washed repeatedly with 5% HCl solution and deionized water, until the PH of the mixture was neutral. The GO was obtained by centrifugation with the speed of 4000 round per minute, and the precipitate of the centrifugation was also retained for comparison.

3.0 g GO and its precipitate were put into 60 mL ethanol with ultrasonic cleaner to form homogeneous slurry, respectively. With 2 g OA, the homogeneous slurry was transferred into a round-bottom flask and stirred under reflux conditions for 0.5 h. Finally, the ethanol was distilled away under reduced pressure and washed with ultrasound several times to obtain the oleic acid capped GO and oleic acid capped precipitate (OACPG), respectively [19, 20].

The commercial PAO, kinetic viscosity of  $68 \text{ mm}^2/\text{s}$  at  $40^\circ\text{C}$ , was used as the base oil and the added content (mass fraction) of the individual OACGO, OACG, and OACPG were all selected with concentrations of 0.5%, 1.0%, 1.5%, and 2.0%. Every mixture forms a stable dispersion in PAO, and no sedimentation was observed after 7 days at room temperature. The friction and wear behavior of the quenched AISI 1045 steel lubricated with pure PAO and PAO containing additives (1.0 wt%) were investigated by SRV reciprocating ball-on-disc friction and wear tester. The upper balls of 10 mm in diameter were made of AISI 52100 steel. The lower stationary discs were made of quenched AISI 1045 steel ( $\text{Ø} 24 \text{ mm} \times 7.8 \text{ mm}$ ) with a surface roughness of  $0.03 \mu\text{m}$  and hardness of 640 HV. The sliding tests were executed at

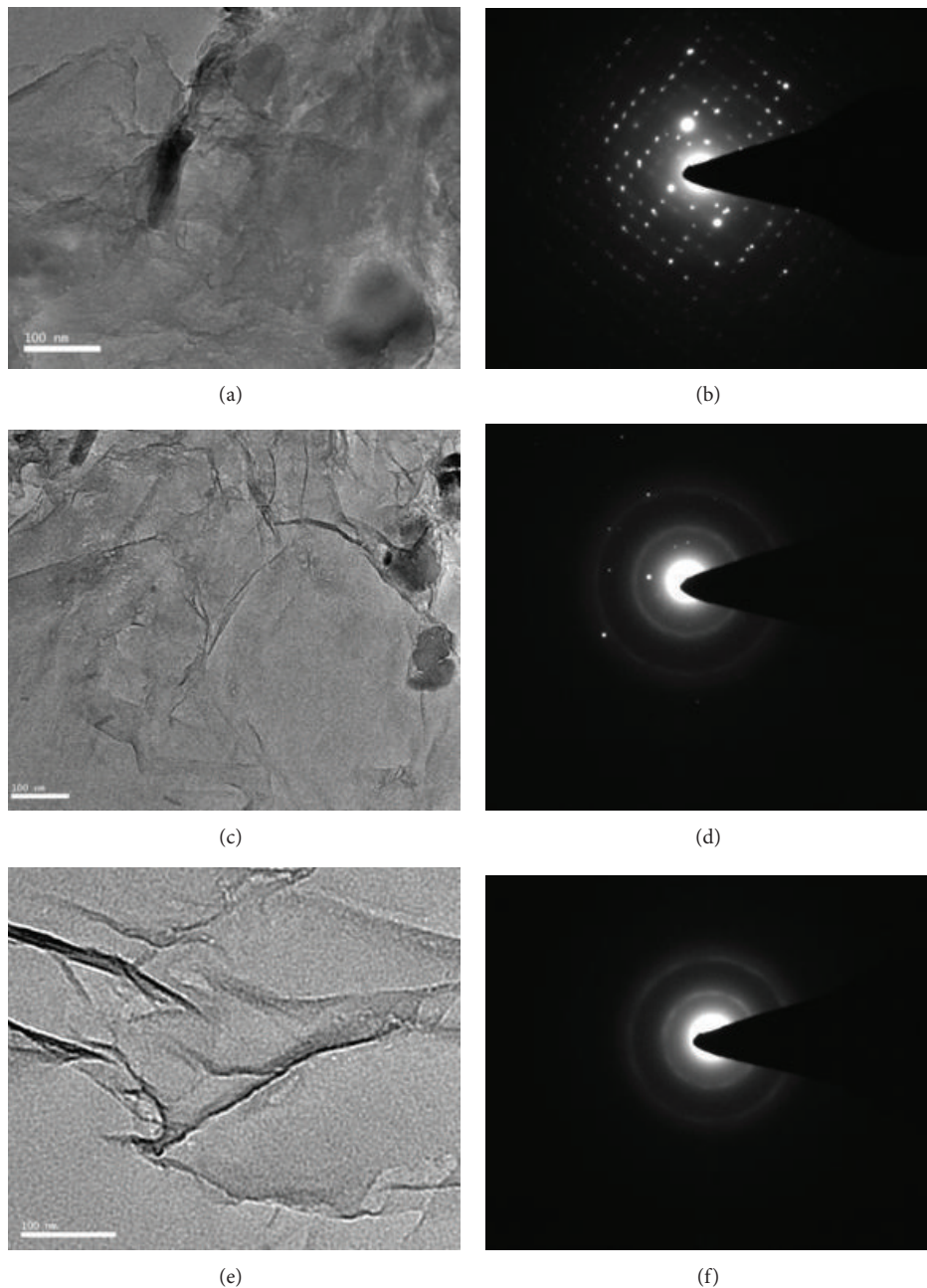


FIGURE 2: The TEM and SAED analysis of the graphite ((a), (b)), precipitate ((c), (d)), and GO ((e), (f)).

amplitude of 1 mm, test duration of 30 min, normal load of 40 N, and reciprocating frequencies of 10, 20, 30, 40, and 50 Hz at room temperature. Separate tests were performed for each frequency and three repeat measurements were performed, and the averaged coefficients of friction and wear rates are given herein. The antiwear properties of three lubricants were evaluated by MRS-10A four-ball machine (the ball, with a diameter of 12.7 mm, was made of AISI 52100 steel), and the testing conditions were selected as rotating rate of 1450 rpm, running duration of 30 minutes, load of 392 N, and room temperature. The FT-IR spectrum was analyzed in the range of  $500\text{--}4000\text{ cm}^{-1}$  by a Bruker IFS66v

spectrometer. Transmission electron microscopy (TEM) images of the samples were obtained by a JEM-1200 EX TEM. X-ray diffraction (XRD) was done on X'Pert-MRD X-ray diffractometer (40 kV, 30 mA, Cu  $K\alpha$  radiation). X-ray photoelectron spectroscopy (XPS) was executed on a PHI-5702 multifunctional X-ray photoelectron spectroscope to evaluate the chemical states of the worn surface. Al- $K\alpha$  radiation was used as the excitation source to determine the binding energies of the target elements at pass energy of 29.4 eV and a resolution of  $\pm 0.2$  eV. The binding energy of C1s (284.6 eV) was used as the internal reference [21]. The morphologies and elemental composition of the worn

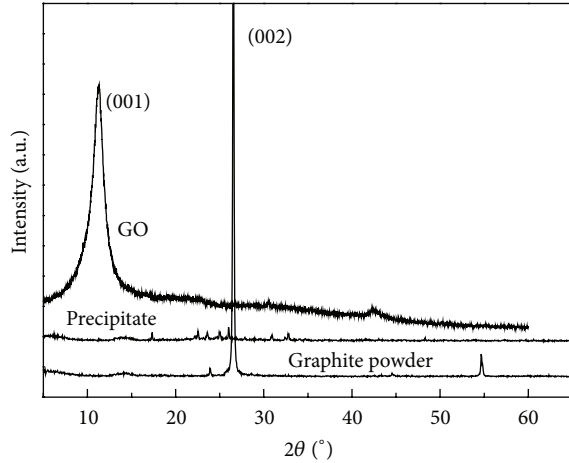


FIGURE 3: The XRD curves of the graphite, precipitate, and GO.

surfaces were analyzed by a JSM-6500LV scanning electron microscope equipped with an attachment for energy dispersive X-ray analysis (SEM-EDXA, Kevex Sigma, USA); the worn surfaces of AISI 1045 steels were ultrasonically washed with acetone and analyzed using SEM. The thermogravimetry (TG) test was carried out on Netzsch STA499 simultaneous thermal analyzer at a heating rate of  $10^{\circ}\text{C min}^{-1}$  under  $\text{N}_2$ . The wear volume loss of the lower discs was determined using a Microxam three dimensional surface profiler (3D) (ADE Corporation of America).

### 3. Results and Discussion

**3.1. Characterization of GO.** Figure 1 shows the FT-IR curves of the GO, OA modified GO, and OA modified precipitate. The absorbance band at about  $3425\text{ cm}^{-1}$  could be assigned to the O–H stretching vibration and the O–H stretching modes of intercalated water. The spectrum of  $1620\text{ cm}^{-1}$  indicates that  $\text{sp}^2$  of C=C was unoxidized [15, 16]. The bands at about  $1400\text{ cm}^{-1}$  and  $1140\text{ cm}^{-1}$  could be attributed to the C–OH stretching vibration and C–O stretching vibration [17]. As for the OA modified GO and precipitate, the bands at  $2925\text{ cm}^{-1}$  and  $2858\text{ cm}^{-1}$  indicate the band of C–H stretching of the alkyl chain [22].

Figure 2 shows the TEM images and corresponding ED (electric diffraction) patterns of the GO, precipitate, and graphite. Obviously, the GO was the result of the full oxidation of the graphite, so the crystal structure of the graphite was destroyed during the oxidation process. It can also be seen that the crystal structure of the precipitate was also destroyed seriously. The low contrast feature indicates the small thickness of the GO [23].

XRD is a valuable method to investigate the interlayer changes and the crystalline properties of the materials. Figure 3 shows the XRD profiles of the graphite, precipitate, and GO. The graphite revealed a sharp and intensive peak at  $2\theta = 26.6^{\circ}$ , exhibiting a highly ordered crystal structure with an interlayer spacing of  $0.33\text{ nm}$  [23]. After oxidation, the 002 diffraction peak of graphite powder disappeared, revealing

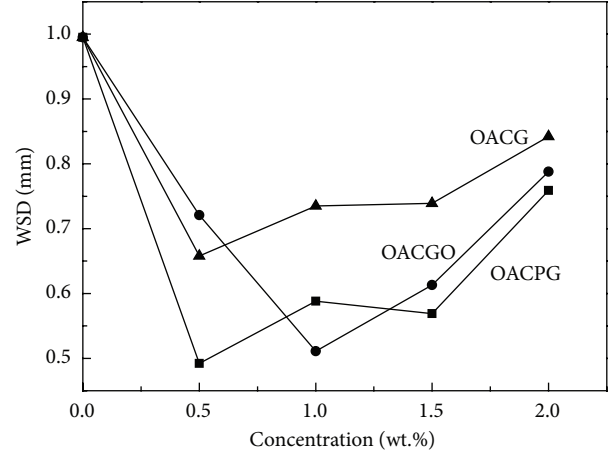


FIGURE 4: The WSD of the OACG, OACGO, and OACPG as additives.

the full oxidation of the graphite. GO pattern shows a weak characteristic peak at  $2\theta = 10.8^{\circ}$ , corresponding to interlayer spacing of  $0.7\text{ nm}$ . As for the precipitate, the 002 diffraction peak of graphite powder weakened very much, showing much oxidation of graphite.

**3.2. Friction and Wear Properties of OACGO.** Figure 4 shows the wear scare diameter (WSD) under the three additives at different contents with four-ball testing. It can be seen that the WSD decreased rapidly as the three compounds were added into base oil. Namely, the WSD of the lubricants containing OACPG decreased from  $1.0\text{ mm}$  to  $0.48\text{ mm}$  at the concentration of  $0.5\%$ . Moreover, the WSD of the PAO + OACGO was about  $0.5\text{ mm}$ , much lower than pure base oil. Comparing the three additives, we found that the WSD of the OACGO and OACPG were lower than that of OACG under the concentration higher than  $1.0\%$ .

Figure 5(a) shows the friction coefficient frequency curves of quenched AISI 1045 steel sliding against AISI 52100 steel balls under the lubrication of PAO, PAO + OACGO, and PAO + OACPG ( $1.0\%$  content) by SRV test. Under the lubrication of the PAO + OACGO and PAO + OACPG, lower friction coefficients were recorded than those under the lubrication of the pure PAO. For example, at a frequency of  $30\text{ Hz}$ , an average coefficient of friction for PAO + OACGO was about  $0.09$ , and it rose to  $0.36$  for pure PAO. Comparing the friction coefficient of PAO + OACGO and PAO + OACPG, we found that the friction coefficient of the PAO + OACGO was lower than that of the PAO + OACPG. In detail, the friction coefficient of PAO + OACPG was  $0.15$ , higher than that of PAO + OACGO. Figure 5(b) plots the wear rate of the AISI 1045 steel lubricated with the three lubricants. Obviously, the wear rate of the pure PAO was higher than the other two lubricants. At a frequency of  $20\text{ Hz}$ , the wear rate of the pure PAO was  $1.4 \times 10^{-2}\ \mu\text{m}^3/\text{Nm}$ , but those of PAO + OACGO and PAO + OACPG were  $0.8 \times 10^{-2}\ \mu\text{m}^3/\text{Nm}$  and  $0.2 \times 10^{-2}\ \mu\text{m}^3/\text{Nm}$ , respectively. The wear rate of PAO + OACGO was lower than that of PAO + OACPG under all the frequencies.

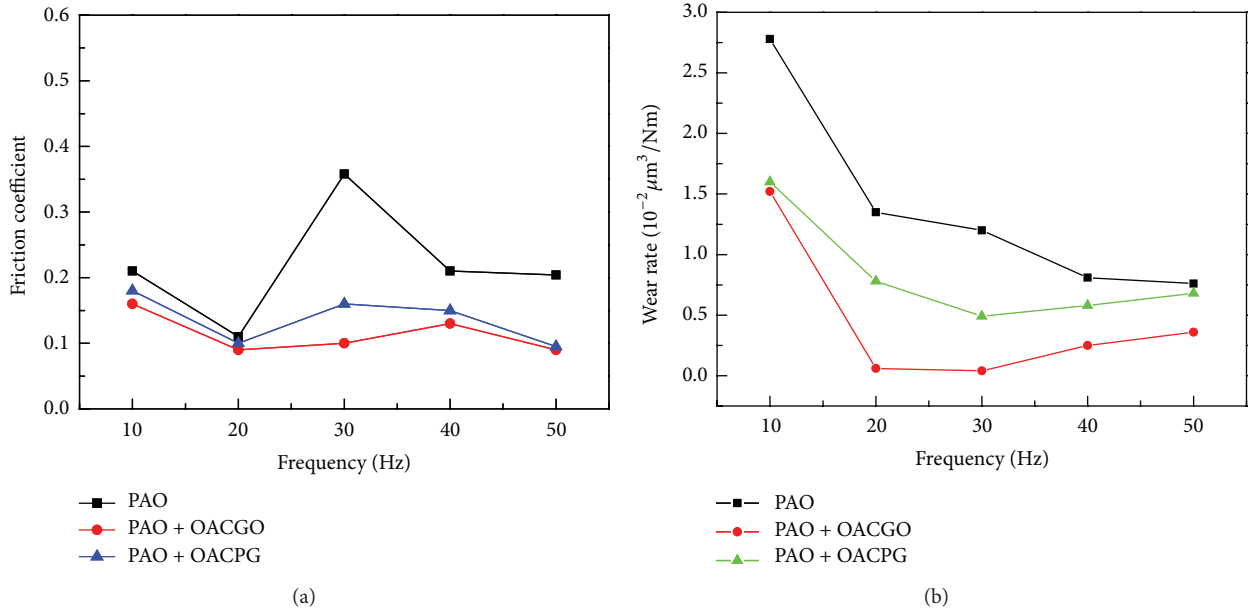


FIGURE 5: The friction coefficient and wear rate of the PAO, PAO + OACGO, and PAO + OACPG.

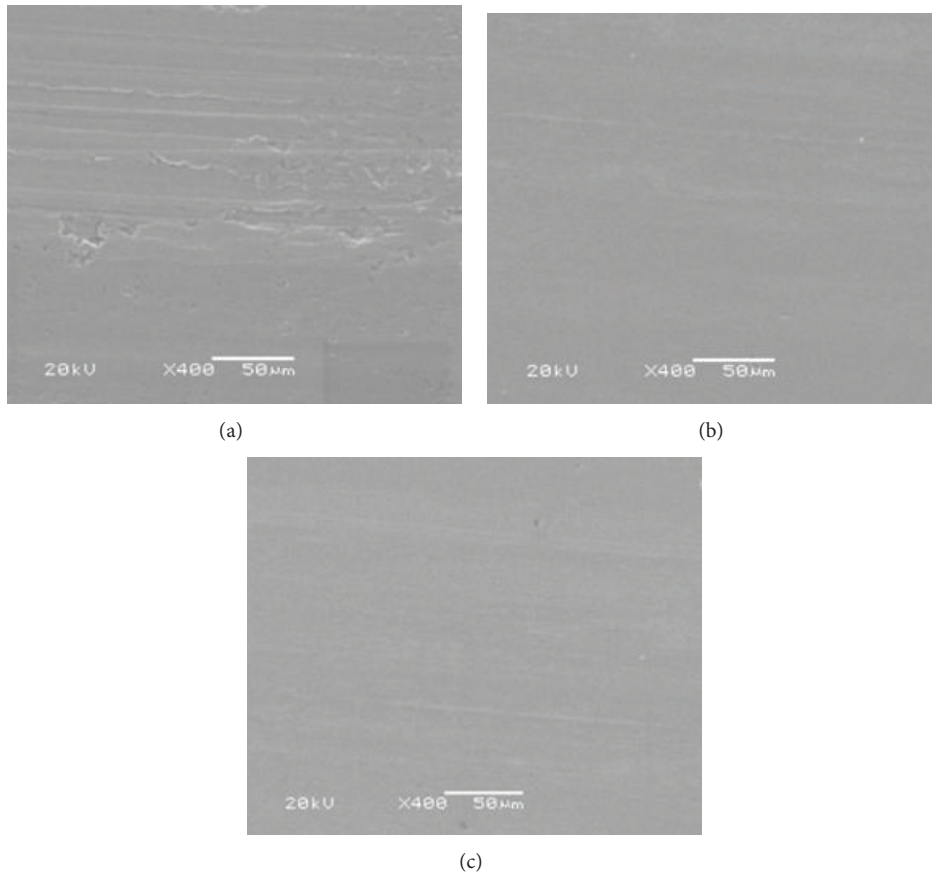


FIGURE 6: The SEM images of the worn surface of the low disc lubricated with PAO (a), PAO + OACGO (b), and PAO + OACPG (c).

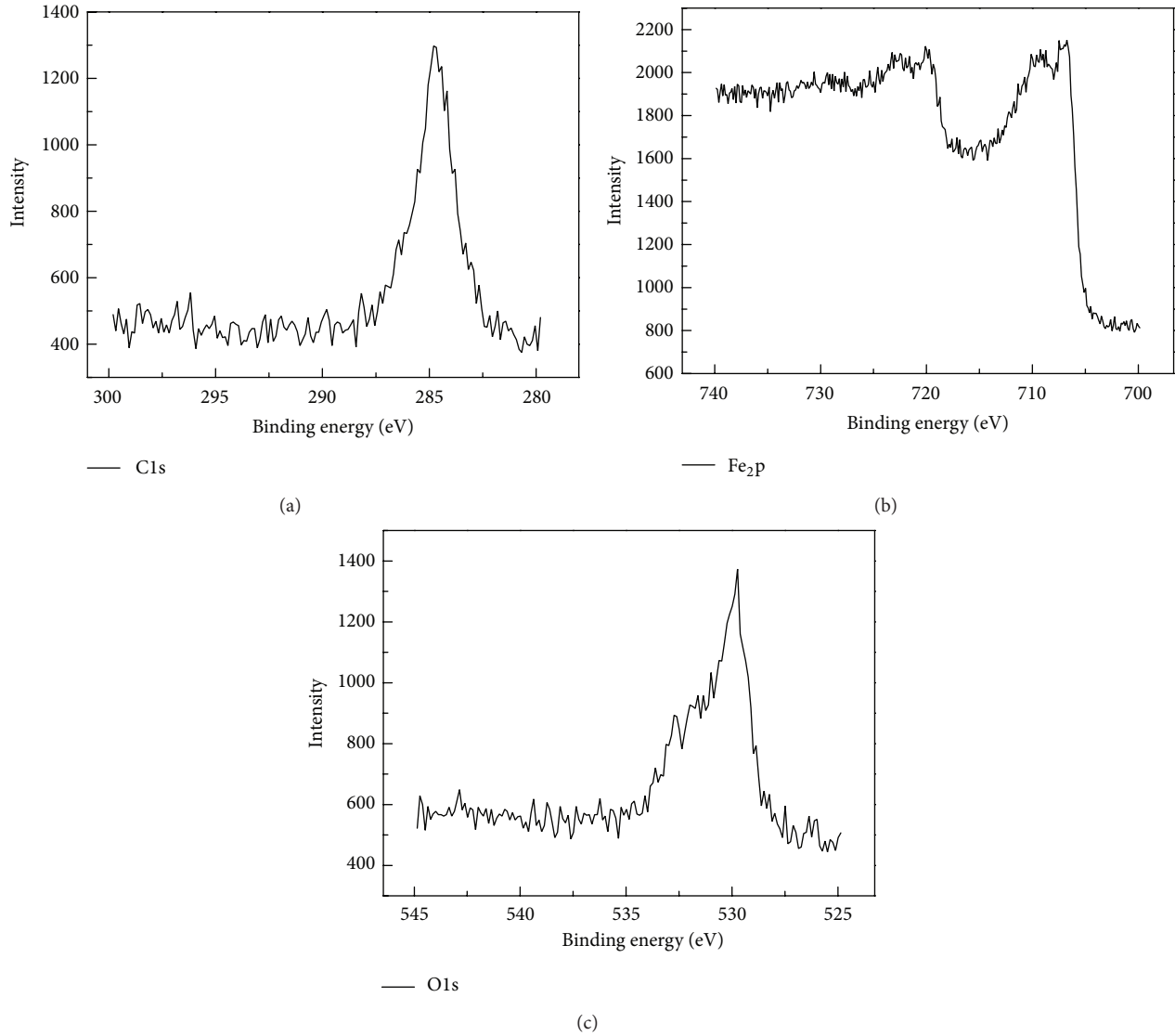


FIGURE 7: The XPS analysis of the PAO + OACGO lubricated AISI 1045 steel.

**3.3. SEM and XPS Analysis of the Worn Surface.** Figure 6 reveals the SEM images of the worn surfaces of the low disc of AISI 1045 steels lubricated with PAO, PAO + OACGO, and PAO + OACPG. As for the steel/steel pair, the worn surfaces of the lower disc under the lubrication of the PAO + OACGO and PAO + OACPG appear smoother and with slighter adhesion in comparison with that of the pure PAO at a frequency of 30 Hz for 30 minutes, corresponding well to the wear rate of the AISI 1045 steel and four-ball test (see Figures 4 and 5). Moreover, the wear scar of the PAO + OACGO was slighter than that of the PAO + OACPG.

The worn surfaces of the lower disc lubricated with PAO + OACGO were analyzed by XPS for acquiring more information about the tribochemical reactions during sliding. Figure 7 depicts the XPS spectra of C1s, O1s, and Fe<sub>2</sub>p on the worn surface of AISI 1045 steel lubricated with PAO + OACGO. O1s peak at 529.7 eV was assigned to metal oxides and Fe<sub>2</sub>O<sub>3</sub>. Fe<sub>2</sub>p peak from 706.5 eV to 710.2 eV was attributed to Fe

TABLE 1: The atomic concentration of elements on the worn surface of PAO and PAO + OACGO lubricated AISI 1045 steel.

Lubricants	Atomic concentration		
	C (%)	O (%)	Fe (%)
PAO + OACGO	57.46	16.40	26.14
PAO	40.55	19.57	39.88

and Fe<sub>2</sub>O<sub>3</sub>. The peak of C1s at 284.7 eV might be assigned to carbon [21]. So it is reasonable to induct that the tribofilm containing C, O, and Fe formed on the worn surface. To collect more information of the tribochemical reactions, the atomic concentrations of elements on the worn surface of PAO and PAO + OACGO lubricated AISI 1045 steel were shown in Table 1. Obviously, the atomic concentration of C on the worn surface of AISI 1045 steel lubricated with PAO + OACGO was 57.46%, higher than that with pure PAO. On

the other hand, the atomic concentration of the Fe on the worn surface lubricated with PAO + OACGO was 26.14%, lower than that of pure PAO of 39.88%. We can draw a conclusion that the tribofilm of the PAO + OACGO was thicker than that of pure PAO and the GO nanosheets exist on the worn surface. Similarly, Lin and Song [9, 13] suggested that the nanosheets entered the contact during sliding and a thin physical tribofilm was formed on the metal substrate. So the tribofilm could not only bear the load of the steel ball, but also prevent from directing contact with the metal surface. The antiwear ability was improved and the friction coefficient was reduced significantly. So it is reasonable to presume that the GO nanosheets entered the contact during sliding and formed a thick tribofilm on the worn surface of the AISI 1045 steel. The thick tribofilm possessed antiwear and friction reducing properties.

#### 4. Conclusions

The Following conclusions can be drawn from above results.

- (1) The XRD analysis showed that the 002 diffraction peak of graphite powder disappeared after oxidation. GO pattern showed a weak characteristic peak at  $2\theta = 10.8^\circ$ , corresponding to interlayer spacing of 0.7 nm.
- (2) With the addition of 1.0% OACGO in PAO, the WSD decreased from 1.0 mm to 0.52 mm. Moreover, the wear rate of the PAO + OACGO was also much lower than that of pure PAO.
- (3) XPS analysis showed that a thicker tribofilm formed during sliding with PAO + OACGO than that with pure PAO. It is presumed that the GO nanosheets entered the contact during sliding and formed a thick carbon film. The carbon film possesses the friction reducing and antiwear properties.

#### Conflict of Interests

The authors declare that there is no conflict of interests regarding the publication of this paper.

#### Acknowledgments

Thanks are due the financial support of this work by Natural Science Foundation of China (Grant No. 51172102) and Open Project of State Key Laboratory of Solid Lubrication, Lanzhou Institute of Chemical Physics, Chinese Academy of Sciences.

#### References

- [1] H. Y. Mao, Y. H. Lu, J. D. Lin et al., "Manipulating the electronic and chemical properties of graphene via molecular functionalization," *Progress in Surface Science*, vol. 88, no. 2, pp. 132–159, 2013.
- [2] Y. Q. Li, D. Y. Pan, S. B. Chen et al., "In situ polymerization and mechanical, thermal properties of polyurethane/graphene oxide/epoxy nanocomposites," *Materials and Design*, vol. 47, pp. 850–856, 2013.
- [3] S. Park and S. Kim, "Effect of carbon blacks filler addition on electrochemical behaviors of  $\text{Co}_3\text{O}_4$ /graphene nanosheets as a supercapacitor electrode," *Electrochimica Acta*, vol. 89, pp. 516–522, 2013.
- [4] Y. L. Zhang, Y. P. Liu, J. M. He et al., "Electrochemical behavior of graphene/Nafion/Azure I/Au nanoparticles composites modified glass carbon electrode and its application as nonenzymatic hydrogen peroxide sensor," *Electrochimica Acta*, vol. 90, pp. 550–555, 2013.
- [5] D. Berman, A. Erdemir, and A. V. Sumant, "Few layer graphene to reduce wear and friction on sliding steel surfaces," *Carbon*, vol. 54, pp. 454–459, 2013.
- [6] G. N. Ren, Z. Z. Zhang et al., "Influence of functional graphene as filler on the tribological behaviors of Nomex fabric/phenolic composite," *Composites A*, vol. 49, pp. 157–164, 2013.
- [7] K. J. Huang, L. Wang, J. Li, and Y. M. Liu, "Electrochemical sensing based on layered  $\text{MoS}_2$ -graphene composites," *Sensors and Actuators B*, vol. 178, pp. 671–677, 2013.
- [8] C. M. Praveen Kumar, T. V. Venkatesha, and R. Shabadi, "Preparation and corrosion behavior of Ni and Ni-graphene composite coatings," *Materials Research Bulletin*, vol. 48, pp. 1477–1483, 2013.
- [9] J. Lin, L. Wang, and G. Chen, "Modification of graphene platelets and their tribological properties as a lubricant additive," *Tribology Letters*, vol. 41, no. 1, pp. 209–215, 2011.
- [10] H. D. Huang, J. P. Tu, L. P. Gan, and C. Z. Li, "An investigation on tribological properties of graphite nanosheets as oil additive," *Wear*, vol. 261, no. 2, pp. 140–144, 2006.
- [11] F. Y. Ban, S. R. Majid, N. M. Huang, and H. N. Lim, "Graphene oxide and its electrochemical performance," *International Journal of Electrochemical Science*, vol. 7, pp. 4345–4351, 2012.
- [12] J. Ou, J. Wang, S. Liu et al., "Tribology study of reduced graphene oxide sheets on silicon substrate synthesized via covalent assembly," *Langmuir*, vol. 26, no. 20, pp. 15830–15836, 2010.
- [13] H. J. Song, N. Li et al., "Preparation and tribological properties of graphene/poly(ether ether ketone) nanocomposites," *Journal of Materials Science*, vol. 47, no. 17, pp. 6436–6443, 2012.
- [14] Z. Tai, Y. Chen, Y. An, X. Yan, and Q. Xue, "Tribological behavior of UHMWPE reinforced with graphene oxide nanosheets," *Tribology Letters*, vol. 46, no. 1, pp. 55–63, 2012.
- [15] Y. Li, Q. Wang, T. Wang, and G. Pan, "Preparation and tribological properties of graphene oxide/nitrile rubber nanocomposites," *Journal of Materials Science*, vol. 47, no. 2, pp. 730–738, 2012.
- [16] H. Liu, Y. Li, T. Wang, and Q. Wang, "In situ synthesis and thermal, tribological properties of thermosetting polyimide/graphene oxide nanocomposites," *Journal of Materials Science*, vol. 47, no. 4, pp. 1867–1874, 2012.
- [17] H.-J. Song and N. Li, "Frictional behavior of oxide graphene nanosheets as water-base lubricant additive," *Applied Physics A*, vol. 105, no. 4, pp. 827–832, 2011.
- [18] W. S. Hummers Jr. and R. E. Offeman, "Preparation of graphitic oxide," *Journal of the American Chemical Society*, vol. 80, no. 6, p. 1339, 1958.
- [19] Z. Jia and Y. Xia, "Hydrothermal synthesis, characterization, and tribological behavior of oleic acid-capped lanthanum borate with different morphologies," *Tribology Letters*, vol. 41, no. 2, pp. 425–434, 2011.
- [20] Z. F. Jia, Y. C. Su, Y. Q. Xia et al., "Synthesis, characterization, and tribological behavior of oleic acid capped calcium borate hydrate," *Tribology Transactions*, vol. 56, no. 3, pp. 521–529, 2013.

- [21] J. F. Moulder, W. F. Stickle, P. E. Sobol, and K. D. Bomben, *Handbook of X-Ray Photoelectron Spectroscopy*, Physical Electronics, 1995.
- [22] Y. Gao, X. Chen, H. Xu et al., "Highly-efficient fabrication of nanoscrolls from functionalized graphene oxide by Langmuir-Blodgett method," *Carbon*, vol. 48, no. 15, pp. 4475–4482, 2010.
- [23] C. Wang, L. Zhan, W.-M. Qiao, and L.-C. Ling, "Preparation of graphene nanosheets through detonation," *New Carbon Materials*, vol. 26, no. 1, pp. 21–25, 2011.

## Research Article

# 3D Hollow Sn@Carbon-Graphene Hybrid Material as Promising Anode for Lithium-Ion Batteries

Xiaoyu Zheng,<sup>1</sup> Wei Lv,<sup>2</sup> Yan-Bing He,<sup>2</sup> Chen Zhang,<sup>1</sup> Wei Wei,<sup>1</sup>  
Ying Tao,<sup>1</sup> Baohua Li,<sup>2</sup> and Quan-Hong Yang<sup>1,2</sup>

<sup>1</sup> School of Chemical Engineering and Technology, Tianjin University, Tianjin 300072, China

<sup>2</sup> Engineering Laboratory for Functionalized Carbon Materials, Graduate School at Shenzhen, Tsinghua University, Shenzhen 518055, China

Correspondence should be addressed to Wei Lv; [lv.wei@sz.tsinghua.edu.cn](mailto:lv.wei@sz.tsinghua.edu.cn)

Received 13 December 2013; Accepted 23 December 2013; Published 12 January 2014

Academic Editor: Zheng-Hong Huang

Copyright © 2014 Xiaoyu Zheng et al. This is an open access article distributed under the Creative Commons Attribution License, which permits unrestricted use, distribution, and reproduction in any medium, provided the original work is properly cited.

A 3D hollow Sn@C-graphene hybrid material (HSCG) with high capacity and excellent cyclic and rate performance is fabricated by a one-pot assembly method. Due to the fast electron and ion transfer as well as the efficient carbon buffer structure, the hybrid material is promising in high-performance lithium-ion battery.

## 1. Introduction

Metallic Sn has long been considered as a promising anode material for lithium-ion batteries (LIBs) due to its high theoretical specific capacity [1, 2]. However, Sn is plagued with a rapid capacity fading because of volume expansion induced pulverization during the lithiation and delithiation reactions, leading to the breakdown of electrical connection of anode particles [3, 4]. Generally, reducing the particle size to nanoscale is an effective way to minimize the volume change [5, 6]. In order to further decrease the volume change of Sn in the electrochemical reactions, hollow Sn nanospheres (NSs), whose tensile stress is ~5 times lower than that of Sn solid NSs with an equal volume, are proven to be a better choice in electrochemical reactions [7–10].

Besides aforementioned routes, many researches also indicate that dispersing Sn NSs into carbon matrix is another effective approach to improve and stabilize the cyclability, where the carbon matrix restricts the volume expansion of Sn and moreover acts as an electron conductor to increase the conductivity [11–14]. A Sn core/carbon shell nanostructure is a typical structure to combine the advantages of carbon and Sn from above consideration, in which the carbon coating layers not only enhance the conductivity of electrode and

buffer the volume variation but also help form a stable solid electrolyte interface (SEI) film.

Aggregation, which hinders the fast Li<sup>+</sup> transportation, is another problem for nanomaterials in real applications. Many latest results have shown that graphene nanosheets (GNs) are ideal substrates to well disperse NSs, which can also construct a flexible network through a “plane-to-point” mode to bridge the active material particles and form effective ion and electron transfer networks [15–18]. Furthermore, it is expected that such soft carbon layer could endure the volume change of the metal NSs and reduce the mechanical stress within the electrode to prevent its disintegration [10, 19, 20].

Herein, we integrate the above concerns into one hybrid structure, and a three-dimensional hollow Sn@carbon-graphene hybrid structure (abbreviated as HSCG) is obtained. In such an HSCG, hollow Sn NS was encapsulated in a carbon shell to form a core-shell sphere structure (hollow Sn@C) and these NSs are uniformly anchored onto the flexible GNs. On one hand, hollow Sn NSs are formed to decrease the intrinsic volume variation, and the carbon shell acts as a buffer layer to restrict the volume changes of Sn NS, which also improves the conductivity and helps the formation of stable SEI film. On the other hand, GNs are used as the substrate

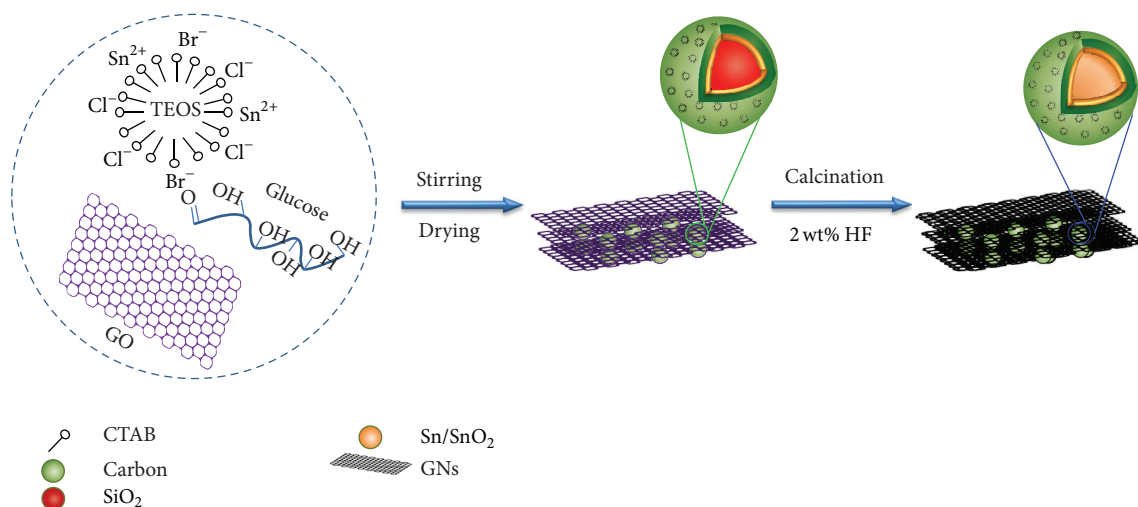


FIGURE 1: Scheme for the assembly process of hollow Sn@C-graphene hybrid nanostructure (HSCG).

to fix and isolate the NSs to avoid the aggregation and the presence of NSs prevents the restacking of GNs, which ensure the open ion transportation channels retention. The interlacing of GNs in the hybrid forms an interconnected conducting network, and the NSs are in a good contact with the GNs, which guarantee the electron transfer between the two components and the fabricated electrode. Furthermore, the GNs endure the volume change of the NSs at some extent. Therefore, the hybrid structure has combined the three above discussed characters, defined as fast ion transfer, interconnected conducting network, and efficient volume variation control in electrochemical performance improvement, and is a promising anode candidate for high performance LIBs [21, 22].

## 2. Experimental

**2.1. Preparation of 3D Hollow Sn@C-Graphene.** In a typical preparation process, 20 mL ammonia (26 wt%) was added into 20 vol% ethanol aqueous solution, and 2.4 g hexadecyltrimethylammonium bromide (CTAB) was then dissolved into the above solution with continuous stirring for 20 min. After that, 10 mL ethanol and 10 mL tetraethyl orthosilicate (TEOS) containing 5 g  $\text{SnCl}_2$  were dropwise introduced into the above solution under stirring for 48 h and the obtained mixture solution was denoted as Mixture A. Mixture B was obtained by sonicating 1 g glucose and 400 mg graphene oxide (GO) in 400 mL DI water with a probe sonicator (JY92-N, China, 300 W) for 1 h. Mixtures A and B were mixed under continuous stirring for 5 h followed by an overnight storage at room temperature. After dried at  $120^\circ\text{C}$ , the obtained mixture was calcined at  $800^\circ\text{C}$  for 4 h under  $\text{N}_2$  and then treated with HF followed by washing with ethanol and DI water. Finally, the HSCG was obtained after dried at  $120^\circ\text{C}$  (Figure 1).

**2.2. Structure Characterization.** XRD measurements were conducted at room temperature using a specular reflection mode (Bruker D-8, Cu  $\text{K}\alpha$  radiation,  $\lambda = 0.154056$  nm). SEM and TEM observations were performed by using Hitachi S-4800 (Hitachi, Japan) and JEM 2100F (JEOL, Japan),

respectively. Nitrogen cryoadsorption was measured by using BEL mini-instrument, and the specific surface area was obtained by Brunauer-Emmett-Teller analyses of the adsorption isotherm. Elemental mapping was performed using energy-dispersive X-ray spectroscopy (EDX) in conjunction with a TEM. Thermogravimetric analysis (TGA) was carried out using TG 8120 (Thermo Plus) with a heating rate of  $10^\circ\text{C}/\text{min}$  in a range of  $25\text{--}900^\circ\text{C}$  under air flow.

**2.3. Electrochemical Performance Measurement.** First, the as-prepared sample as active material was ground into fine powders. 80 wt% active materials, 10 wt% Super P, and 10 wt% PTFE were well mixed in ethanol solution to make uniform mixture slurry under sonication. Then, the mixture slurry was spread uniformly on nickel foam and dried at  $120^\circ\text{C}$  for 12 h under vacuum to obtain a loading density of active material in the range of  $2.2\text{--}2.5$   $\text{mg cm}^{-2}$ . Finally, coin cells (CR2032) were assembled in Ar filled glove box and the lithium foils were used as the anode, and 1M  $\text{LiPF}_6$  mixture solution (1:1 (v/v) of ethylene carbonate (EC) and dimethyl carbonate (DMC)) as the electrolyte.

The coin cells were tested at room temperature using battery tester (Lixing, China) and electrochemistry workstation (Gamry Instrument, USA). Note that the charge and discharge processes were conducted at the same current density with the voltage range of  $0.006$  V– $2.5$  V.

## 3. Results and Discussion

X-ray diffraction (XRD) analysis was performed to indicate the reduction process from  $\text{Sn}^{2+}$  to metallic Sn. As shown in Figure 2(a), the identified diffraction peaks that are located at  $30.7^\circ$ ,  $32.1^\circ$ , and  $44.9^\circ$  are attributed to the tetragonal Sn (200), (101), and (211) planes, respectively (JCPDS Card no. 04-0673). Obviously, the initial  $\text{Sn}^{2+}$  was reduced into crystalline Sn by carbon at high temperature. According to the energy-dispersive X-ray (EDX) analysis, the residual  $\text{SiO}_2$  weight fraction is lower than 3%, indicating that  $\text{SiO}_2$  has

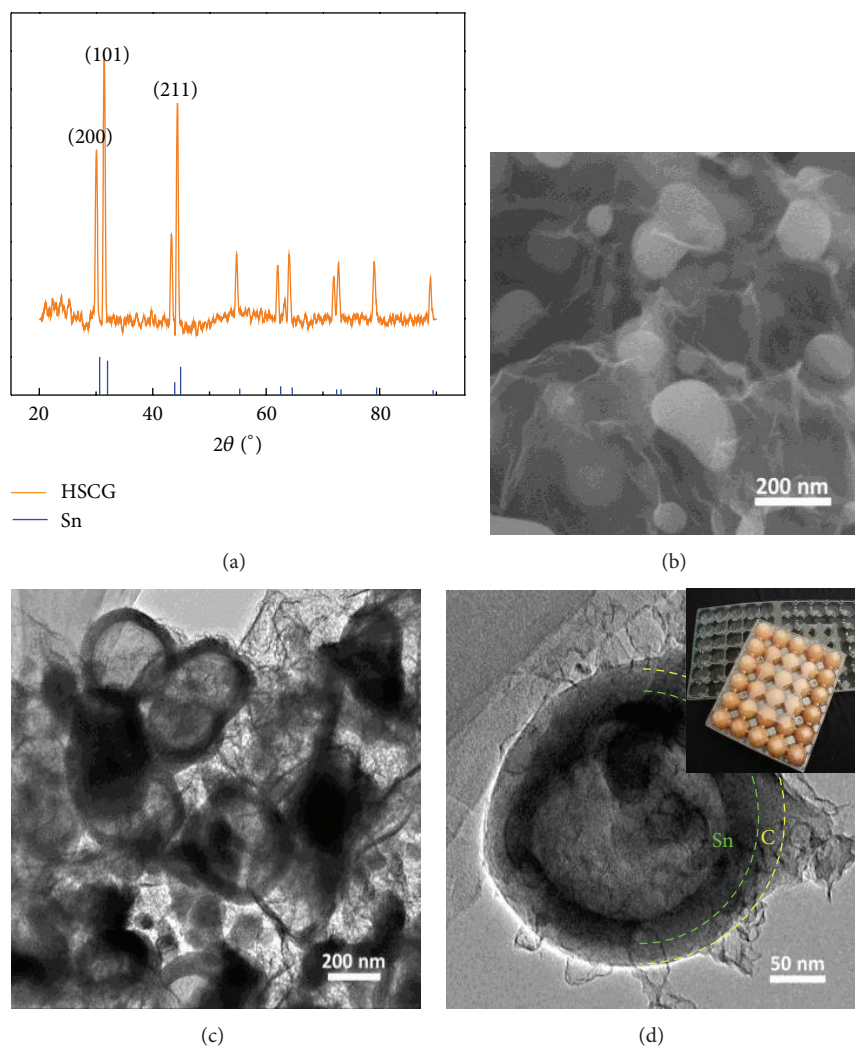


FIGURE 2: (a) XRD patterns of HSCG and crystalline Sn; (b) typical FESEM and (c and d) TEM images of HSCG. Inset of (d) shows eggs with an egg support, which is similar to HSCG nanostructure where a core-shell Sn@C is supported by planar graphene sheets.

mostly been etched off (Figure S1, ESI, available online at <http://dx.doi.org/10.1155/2014/974285>).

The morphologies of the HSCG were examined with field-emission scanning electron microscope (FESEM) and transmission electron microscope (TEM). Figure 2(b) clearly shows that NSs, which are with a narrow size distribution of 100~200 nm, are uniformly anchored onto the surface of GNs. These NSs acting as the spacers prevent the restacking of GNs and stabilize the individual GNs in single or few layers, inducing the retention of open ion transportation channels. Additionally, the separated NSs guarantee the fast and sufficient contact of electrolyte with the active sites. As revealed in the SEM image, the soft two-dimensional GNs bridge the active NSs through a “plane-to-point” mode, in which a flexible conducting network is essentially constructed in electrochemical reactions. The obtained sample shows a typical IV  $N_2$  adsorption-desorption isotherm with a significant hysteresis loop, indicating that HSCG possesses a mesoporous and macroporous structure (Figure S2, ESI).

The specific surface area of HSCG is  $29.51 \text{ m}^2 \text{ g}^{-1}$  calculated by Brunauer-Emmett-Teller method.

The TEM images (Figures 2(c) and 2(d)) further confirm the formation of aforementioned structure. As revealed in Figure 2(d), the carbon shell with a thickness of ~20 nm fully encapsulates the hollow Sn core to form a core-shell NS with the diameter of about ~200 nm. These NSs are tightly anchored onto the GNs even though a strong sonication treatment is used during the sample preparation for the TEM observations, suggesting a strong interaction between the NSs and GNs. Besides, the carbon shell is tightly attached to the Sn core, which is beneficial for mechanical reinforcement of the carbon buffer to restrict the volume expansion and enhance electronic conduction. Moreover, the void space of the hollow Sn@C is large enough to endure the volume changes during the electrochemical reaction. Such a hybrid structure, where core-shell Sn@C is supported by planar GNs, is similar to the structure of nonyolk eggs with the protection of egg support as shown in Figure 2(d) (inset).

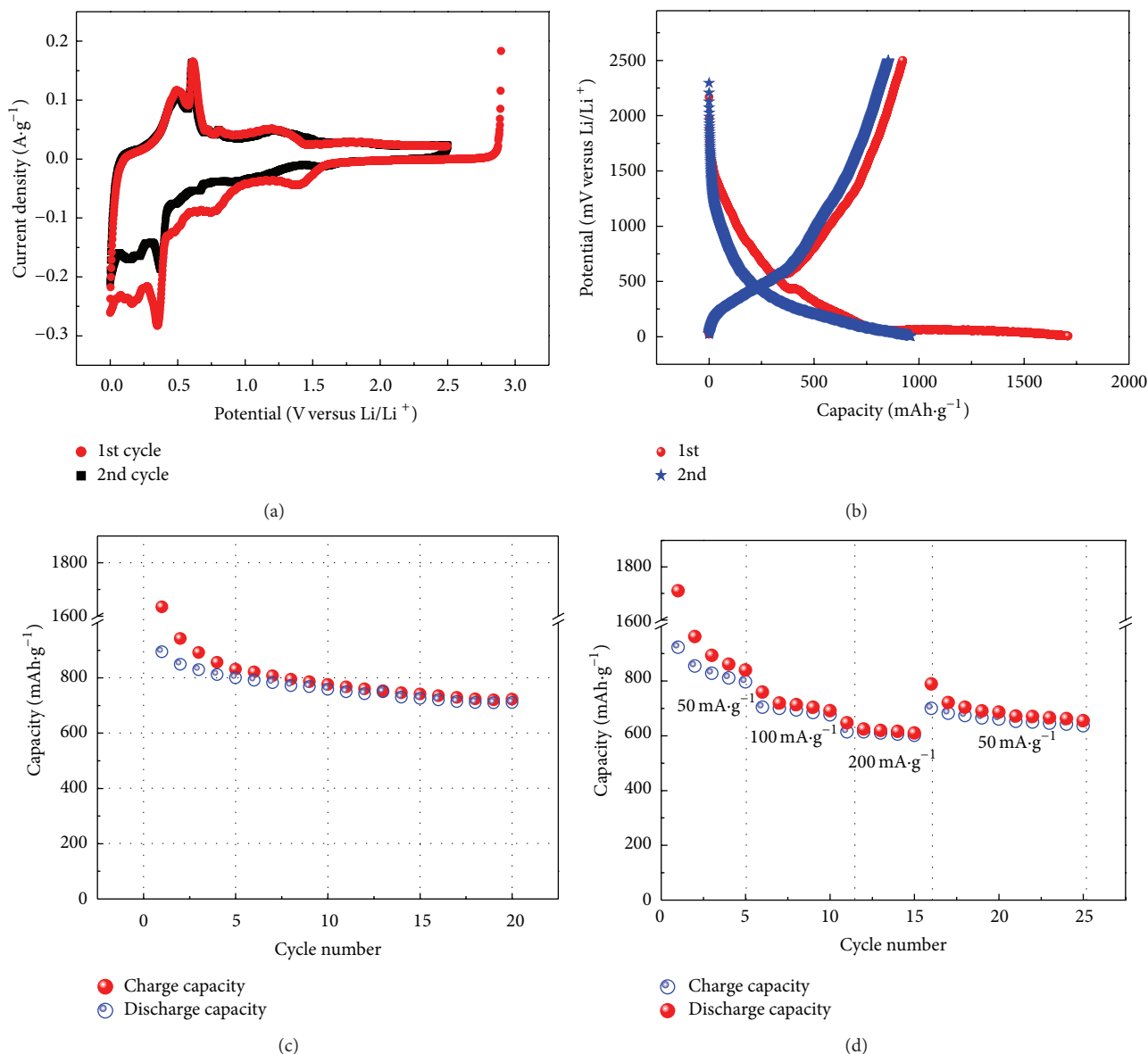


FIGURE 3: Electrochemical performance of HSCG. (a) CV profiles of the first and second cycles; (b) galvanostatic profiles at a current density of  $50 \text{ mA g}^{-1}$  with a cut-off potential between 5 mV and 2.5 V; (c) cycling profiles; (d) rate performance profile.

In order to determinate the carbon and tin fractions in HSCG, thermogravimetric analysis (TGA, Figure S3, ESI) was carried out under air atmosphere, and the result shows that HSCG contains about  $\sim 70$  wt% tin and  $\sim 27$  wt% carbon.

To reveal the advantages of HSCG, its lithium insertion/extraction process is characterized with cyclic voltammetry in the range of 0.005 to 2.5 V at a scan rate of  $0.1 \text{ mV s}^{-1}$  [23]. The CV behavior shown in Figure 3(a) is consistent with the previous reports [10, 24], indicating a similar electrochemical reaction occurred. It is found that the cathodic current in the first cycle is obviously larger than that of the 2nd cycle, especially from 1.5 to 0 V, which is mainly due to the reduction of electrolyte on the HSCG surface to form a SEI film and the irreversible reduction

of the tin oxide ( $\text{SnO}_2$ ) impurity. The broad cathodic peaks at 0.3–0.7 V are attributed to the multistep electrochemical reduction reactions (lithiation) of Sn with Li ion to form various Li-Sn alloys. The anodic peaks at 0.4–0.8 V originate from the delithiation process (from the formed Li-Sn alloy phases). Based on the above discussion, it is found that the HSCG electrode shows excellent anodic reversibility.

Figures 3(b) and 3(c) show the discharge-charge voltage profiles at a current density of  $50 \text{ mA g}^{-1}$ . The voltage profiles are consistent with that of Sn-based anodes. It is clear that the first discharge/charge capacities of the HSCG are  $\sim 1710.2$  and  $922.7 \text{ mAh g}^{-1}$ , respectively. The key point for such high capacity properties is derived from the synergic effect of hollow Sn@C structures with planar graphene sheets.

The hollow Sn@C structure accommodates the volume variation and prevents pulverization of Sn and it also acts as the spacer to avoid face-to-face aggregation of GNs. At the same time, the graphene interlinked with each other and with the carbon shell form a continuous conducting network. The initial irreversible loss ( $787.5 \text{ mAh g}^{-1}$ ) is mainly attributed to the formation of SEI film due to a relatively large interfacial surface of HSCG. At the second cycle, the HSCG anode still shows a large reversible capacity of about  $853.9 \text{ mAh g}^{-1}$ , revealing a high capacity retention of 92.6% with a coulombic efficiency of 88.8%. The charge/discharge property at the first two cycles is well consistent with the reactions observed from CV curves shown in Figure 3(a). After 10, 20, and 50 cycles, the reversible capacities are preserved at about 758.2, 710.0, and  $659.5 \text{ mAh g}^{-1}$ , respectively, indicating a capacity retention of 82.1%, 76.9%, and 71.5%. To the best of our knowledge, the capacities are amongst the highest values reported for Sn/C hybrid structure (see Figure S4) [22, 25, 26]. The enhanced performance of HSCG is derived from its unique infrastructure. Other than preventing the Sn NSs from aggregation, carbon shell and GNs both play the role of buffer in this hybrid to mitigate the large volume change of Sn particles associated with a conversion reaction electrode. The hollow structure of Sn also contributes to a reduction of the intrinsically large volume change.

The HSCG also shows a good rate capability and stability. As shown in Figure 3(d), at higher current densities of  $100 \text{ mA g}^{-1}$  and  $200 \text{ mA g}^{-1}$ , the specific discharge capacities can also reach  $759.2 \text{ mAh g}^{-1}$  and  $647.4 \text{ mAh g}^{-1}$ . When the current density goes back to  $50 \text{ mA g}^{-1}$ , the discharge capacity returns to  $788.7 \text{ mAh g}^{-1}$ , which is comparable to the initial capacity at  $50 \text{ mA g}^{-1}$ , indicating the electrode is stable and has high reversibility. The promotion of the rate capability is attributed to the open channels and formed conductivity network mentioned in the structure discussion. Moreover, the hollow Sn shell with improved surface-to-volume ratio and reduced transport lengths for both mass and transport further improves the rate performance.

#### 4. Conclusion

In summary, a novel 3D hollow Sn@carbon-graphene structure was designed and prepared by a one-pot assembly method. Such a unique hybridized nanostructure, which is similar to non-yolk eggs within a rigid egg support, is proved a highly active hollow metal@carbon structure attached on flexible and high-strength conductive GNs plane. The synergic effects, resulting from the combination of three kinds of selected infrastructures, contribute to a high reversible specific capacity of  $922.7 \text{ mAh g}^{-1}$  and excellent cyclic performance, while an outstanding rate capability is also achieved simultaneously due to the fast ion and electron transfer characteristic. This hybrid structure provides us a promising model for the design of high-performance anode material for LIBs.

#### Conflict of Interests

The authors declare that there is no conflict of interests regarding the publication of this paper.

#### Acknowledgments

The authors appreciate support from NSAF (no. U1330123), National Natural Science Foundation of China (nos. 51372167 and 51302146), Shenzhen Basic Research Project (nos. JC201104210152A and CYJ20130402145002430), and China Postdoctoral Science Foundation (2012M520012 and 2013T60111).

#### References

- [1] S. Yang, X. Feng, S. Ivanovici, and K. Müllen, "Fabrication of graphene-encapsulated oxide nanoparticles: towards high-performance anode materials for lithium storage," *Angewandte Chemie*, vol. 49, no. 45, pp. 8408–8411, 2010.
- [2] B. Luo, B. Wang, X. Li, Y. Jia, M. Liang, and L. Zhi, "Graphene-confined Sn nanosheets with enhanced lithium storage capability," *Advanced Materials*, vol. 24, no. 26, pp. 3538–3543, 2012.
- [3] C.-M. Park and K.-J. Jeon, "Porous structured SnSb/C nanocomposites for Li-ion battery anodes," *Chemical Communications*, vol. 47, no. 7, pp. 2122–2124, 2011.
- [4] H.-C. Shin and M. L. Liu, "Three-dimensional porous copper-tin alloy electrodes for rechargeable lithium batteries," *Advanced Functional Materials*, vol. 15, no. 4, pp. 582–586, 2005.
- [5] W. Lv, Y. Tao, W. Ni et al., "One-pot self-assembly of three-dimensional graphene macroassemblies with porous core and layered shell," *Journal of Materials Chemistry*, vol. 21, no. 33, pp. 12352–12357, 2011.
- [6] J. Liu, S. Z. Qiao, J. S. Chen, X. W. Lou, X. Xing, and G. Q. Lu, "Yolk/shell nanoparticles: new platforms for nanoreactors, drug delivery and lithium-ion batteries," *Chemical Communications*, vol. 47, no. 47, pp. 12578–12591, 2011.
- [7] Y. Yao, M. T. McDowell, I. Ryu et al., "Interconnected silicon hollow nanospheres for lithium-ion battery anodes with long cycle life," *Nano Letters*, vol. 11, no. 7, pp. 2949–2954, 2011.
- [8] W.-M. Zhang, J.-S. Hu, Y.-G. Guo et al., "Tin-nanoparticles encapsulated in elastic hollow carbon spheres for high-performance anode material in lithium-ion batteries," *Advanced Materials*, vol. 20, no. 6, pp. 1160–1165, 2008.
- [9] Y.-S. Lin, J.-G. Duh, and M.-H. Hung, "Shell-by-shell synthesis and applications of carbon-coated  $\text{SnO}_2$  hollow nanospheres in lithium-ion battery," *The Journal of Physical Chemistry C*, vol. 114, no. 30, pp. 13136–13141, 2010.
- [10] S. Liang, X. Zhu, P. Lian, W. Yang, and H. Wang, "Superior cycle performance of Sn@C/graphene nanocomposite as an anode material for lithium-ion batteries," *Journal of Solid State Chemistry*, vol. 184, no. 6, pp. 1400–1404, 2011.
- [11] Y. Qiu, K. Yan, and S. Yang, "Ultrafine tin nanocrystallites encapsulated in mesoporous carbon nanowires: scalable synthesis and excellent electrochemical properties for rechargeable lithium ion batteries," *Chemical Communications*, vol. 46, no. 44, pp. 8359–8361, 2010.
- [12] D. Deng and J. Y. Lee, "Reversible storage of lithium in a rambutan-like tin-carbon electrode," *Angewandte Chemie*, vol. 48, no. 9, pp. 1660–1663, 2009.

- [13] W. Lv, F. Sun, D.-M. Tang et al., "A sandwich structure of graphene and nickel oxide with excellent supercapacitive performance," *Journal of Materials Chemistry*, vol. 21, no. 25, pp. 9014–9019, 2011.
- [14] Y. Wang, M. Wu, Z. Jiao, and J. Y. Lee, "Sn@CNT and Sn@C@CNT nanostructures for superior reversible lithium ion storage," *Chemistry of Materials*, vol. 21, no. 14, pp. 3210–3215, 2009.
- [15] A. K. Geim and K. S. Novoselov, "The rise of graphene," *Nature Materials*, vol. 6, no. 3, pp. 183–191, 2007.
- [16] W. Lv, D.-M. Tang, Y.-B. He et al., "Low-temperature exfoliated graphenes: vacuum-promoted exfoliation and electrochemical energy storage," *ACS Nano*, vol. 3, no. 11, pp. 3730–3736, 2009.
- [17] F.-Y. Su, C. You, Y.-B. He et al., "Flexible and planar graphene conductive additives for lithium-ion batteries," *Journal of Materials Chemistry*, vol. 20, no. 43, pp. 9644–9650, 2010.
- [18] F.-Y. Su, Y.-B. He, B. Li et al., "Could graphene construct an effective conducting network in a high-power lithium ion battery?" *Nano Energy*, vol. 1, no. 3, pp. 429–439, 2012.
- [19] G. Zhou, D.-W. Wang, F. Li et al., "Graphene-wrapped  $\text{Fe}_3\text{O}_4$  anode material with improved reversible capacity and cyclic stability for lithium ion batteries," *Chemistry of Materials*, vol. 22, no. 18, pp. 5306–5313, 2010.
- [20] S. Chen, P. Chen, M. Wu, D. Pan, and Y. Wang, "Graphene supported Sn-Sb@carbon core-shell particles as a superior anode for lithium ion batteries," *Electrochemistry Communications*, vol. 12, no. 10, pp. 1302–1306, 2010.
- [21] Z.-S. Wu, W. Ren, L. Wen et al., "Graphene anchored with  $\text{Co}_3\text{O}_4$  nanoparticles as anode of lithium ion batteries with enhanced reversible capacity and cyclic performance," *ACS Nano*, vol. 4, no. 6, pp. 3187–3194, 2010.
- [22] G. Wang, B. Wang, X. Wang et al., "Sn/graphene nanocomposite with 3D architecture for enhanced reversible lithium storage in lithium ion batteries," *Journal of Materials Chemistry*, vol. 19, no. 44, pp. 8378–8384, 2009.
- [23] I. Stojković, N. Cvjetičanin, M. Mitrić, and S. Mentus, "Electrochemical properties of nanostructured  $\text{Li}_{1.2}\text{V}_3\text{O}_8$  in aqueous  $\text{LiNO}_3$  solution," *Electrochimica Acta*, vol. 56, no. 18, pp. 6469–6473, 2011.
- [24] L. Ji, Z. Tan, T. Kuykendall et al., "Multilayer nanoassembly of Sn-nanopillar arrays sandwiched between graphene layers for high-capacity lithium storage," *Energy & Environmental Science*, vol. 4, no. 9, pp. 3611–3616, 2011.
- [25] X. W. Lou, Y. Wang, C. Yuan, J. Y. Lee, and L. A. Archer, "Template-free synthesis of  $\text{SnO}_2$  hollow nanostructures with high lithium storage capacity," *Advanced Materials*, vol. 18, no. 17, pp. 2325–2329, 2006.
- [26] F. Wang, G. Yao, M. Xu, M. Zhao, Z. Sun, and X. Song, "Large-scale synthesis of macroporous  $\text{SnO}_2$  with/without carbon and their application as anode materials for lithium-ion batteries," *Journal of Alloys and Compounds*, vol. 509, no. 20, pp. 5969–5973, 2011.

## Research Article

# Electronic Structures and Optical Properties of Phenyl C<sub>71</sub> Butyric Acid Methyl Esters

Cai-Rong Zhang,<sup>1,2</sup> Li-Heng Han,<sup>1</sup> Jian-Wu Zhe,<sup>3</sup> Neng-Zhi Jin,<sup>3</sup> Yu-Lin Shen,<sup>3</sup> Li-Hua Yuan,<sup>1</sup> You-Zhi Wu,<sup>2</sup> and Zi-Jiang Liu<sup>4</sup>

<sup>1</sup> Department of Applied Physics, Lanzhou University of Technology, Lanzhou, Gansu 730050, China

<sup>2</sup> State Key Laboratory of Gansu Advanced Non-Ferrous Metal Materials, Lanzhou University of Technology, Lanzhou, Gansu 730050, China

<sup>3</sup> Gansu Computing Center, Lanzhou, Gansu 730030, China

<sup>4</sup> Department of Physics, Lanzhou City University, Lanzhou 730070, China

Correspondence should be addressed to Cai-Rong Zhang; zhcrxy@lut.cn

Received 20 September 2013; Accepted 11 November 2013

Academic Editor: Jinlong Jiang

Copyright © 2013 Cai-Rong Zhang et al. This is an open access article distributed under the Creative Commons Attribution License, which permits unrestricted use, distribution, and reproduction in any medium, provided the original work is properly cited.

Phenyl C<sub>71</sub> butyric acid methyl ester (PC<sub>71</sub>BM) has been adopted as electron acceptor materials in bulk heterojunction solar cells with relatively higher power conversion efficiency. The understanding of the mechanism and performance for the devices based upon PC<sub>71</sub>BM requires the information of conformations, electronic structures, optical properties, and so forth. Here, the geometries, IR and Raman, electronic structures, polarizabilities, and hyperpolarizabilities of PC<sub>71</sub>BM isomers are studied by using density functional theory (DFT); the absorption and excitation properties are investigated via time-dependent DFT with B3LYP, PBE0, and CAM-B3LYP functionals. The calculated results show that [6,6]PC<sub>71</sub>BM is more stable than [5,6]PC<sub>71</sub>BM due to the lower total energy. The vibrational modes of the isomers at IR and Raman peaks are quite similar. As to absorption properties, CAM-B3LYP functional is the suitable functional for describing the excitations of PC<sub>71</sub>BM because the calculated results with CAM-B3LYP functional agree well with that of the experiment. The analysis of transition configurations and molecular orbitals demonstrated that the transitions at the absorption maxima in UV/Vis region are localized  $\pi$ - $\pi^*$  transitions in fullerenes cages. Furthermore, the larger isotropic polarizability of PC<sub>71</sub>BM indicates that the response of PC<sub>71</sub>BM to applied external electric field is stronger than that of PC<sub>61</sub>BM, and therefore resulting into better nonlinear optical properties.

## 1. Introduction

The electronic devices based upon organic materials, such as organic radiofrequency identification, light emitting diode, memory devices, and solar cells, have attracted considerable attention in the past decade due to their potential to be lower-cost, light-weight, flexible, and large-area equipment. These devices usually contain heterojunction formed by electronic donor and acceptor materials. The properties of materials in these devices, including chemical structures [1], electronic structures [2], excited states [3], charge transfer, and charge transport [4], are of particular importance for their overall performance. To provide a better understanding toward the higher performance of device, it is necessary to

investigate the electronic structures of the materials, as well as the energy level alignment at the heterojunction interface [5]. The discovery of ultrafast photoinduced charge/energy transfer from a conjugated polymer to fullerene molecules and introducing bulk heterojunction (BHJ) stimulated the rapid development of organic photovoltaic (OPV) technology [4, 6–11]. Also, some fullerene hybrids show good nonlinear optical properties [12].

Among the fullerene derivatives in OPV, [6,6]-phenyl-C<sub>61</sub> butyric acid methyl ester (PC<sub>61</sub>BM) as the soluble electron acceptor was widely used to fabricate efficient BHJ organic polymer solar cells (PSCs) [13]. For instance, Svensson et al. reported the PSC with open circuit voltage ( $V_{oc}$ ) 1 V based on alternating copolymer PFDTBT blended with

PC<sub>61</sub>BM [14]. Inganäs et al. performed a systematic study of PSCs and found the efficiency about 2–3% using four different fluorene copolymers through changing the length of the alkyl side chains and chemical structures [15]. A series of highly soluble fullerene derivatives with varying acceptor strengths was applied in PSCs, and the  $V_{oc}$  of the corresponding devices was found to correlate directly with the acceptor strength of the fullerenes [16]. Unfortunately, PC<sub>61</sub>BM has very low absorption coefficients in UV/Vis region [17], which limits the light harvesting efficiency.

Phenyl C<sub>71</sub> butyric acid methyl ester (PC<sub>71</sub>BM), a higher fullerene analogue of PC<sub>61</sub>BM, displays improved light absorption in the visible region of spectrum [17, 18]. PC<sub>71</sub>BM was adopted as electron acceptor in BHJ solar cells with relatively higher power conversion efficiency (PCE) [19–25]. The substitution of PC<sub>61</sub>BM with PC<sub>71</sub>BM under the same standard test conditions in PSC increased current densities about 50% [26], as well as approached to 3.0% of PCE [17]. Recently, more than 10% PCE has been reported by PSCs of PCDTBT:PC<sub>71</sub>BM system [27].

PC<sub>71</sub>BM has similar geometry to PC<sub>61</sub>BM, and the fullerene cage of PC<sub>71</sub>BM contains ten C atoms more than that of PC<sub>61</sub>BM, but the performances of them in PSCs are quite different. The better understanding of the mechanism and performance for the devices based upon PC<sub>71</sub>BM requires the information of conformations, electronic structures, optical properties, and so forth. In this work, taking into account two kinds of possible isomers of phenyl C<sub>71</sub> butyric acid methyl esters, the geometries, electronic structures, vibrational properties, polarizabilities, and hyperpolarizabilities are calculated using density functional theory (DFT), and the absorption properties which relate to the character of excited states are addressed with time-dependent DFT (TDDFT) [28–34]; the comparative analyses for the isomers are also reported.

## 2. Computational Methods

The computations of the geometries and vibrational properties have been performed with Becke's three parameters gradient-corrected exchange potential and the Lee-Yang-Parr gradient-corrected correlation potential (B3LYP) [35–38], since the comparison with the MP2 geometries of several organic molecules confirmed the accuracy of B3LYP for the geometry optimizations [39]. In order to get the reliable calculations of absorption spectra and excited states, the hybrid functionals B3LYP and PBE0 [40–42], as well as long-range-corrected hybrid functional Coulomb attenuation method CAM-B3LYP [43], are adopted in TDDFT calculations. The comparison of absorption spectra between experiment and calculations demonstrates the better performance of CAM-B3LYP functional in describing the excited state properties of PC<sub>71</sub>BM. Thus, the electronic structures, polarizabilities, and hyperpolarizabilities are also analyzed using CAM-B3LYP functional. The nonequilibrium version of the polarizable continuum model (PCM) [44] is employed to take account of the solvent effects of toluene solution. The polarized split-valence 6-31G(d,p) basis sets are sufficient for calculating

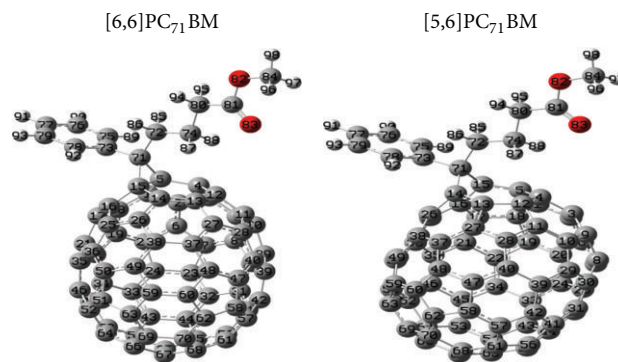


FIGURE 1: The optimized geometrical structures of [6,6]PC<sub>71</sub>BM and [5,6]PC<sub>71</sub>BM in gas phase (gray circles: C red circles: O; light gray circles: H).

the excitation of organic molecules [45], and introducing additional diffuse functions in basis sets generates negligible effects on the electron density and hence on the accuracy of DFT and TDDFT results [39]. All calculations were performed with 6-31G(d,p) basis sets without any symmetry constraints using the Gaussian 09 package [46].

## 3. Results and Discussion

**3.1. Geometrical Structures.** C<sub>70</sub> fullerene is composed of 12 five-C rings and 25 six-C rings with  $D_{5h}$  symmetry. However, when the C atom in the side chain of butyric acid methyl ester connects to C<sub>70</sub> cage, two possible isomers can be formed since the C atom can connect to not only the most “polar” carbon-carbon double bonds in C<sub>70</sub> (the adjacent edge of six-C rings), but also the carbon-carbon single bond in C<sub>70</sub> (the adjacent edge between five-C rings and six-C rings), and these two structures were denoted as [6,6]PC<sub>71</sub>BM and [5,6]PC<sub>71</sub>BM, respectively. The isomerization is similar to other fullerene derivatives [47].

The optimized geometries of [6,6]PC<sub>71</sub>BM and [5,6]PC<sub>71</sub>BM at the B3LYP/6-31G(d,p) level in gas phase are shown in Figure 1. The calculated total energy of [6,6]PC<sub>71</sub>BM is about 0.54 eV lower than that of [5,6]PC<sub>71</sub>BM. The NMR spectrum confirmed the stability of [6,6]PC<sub>71</sub>BM isomer [17]. The selected bond lengths, bond angles, and dihedral angles are listed in Tables s1 and s2 in Supplementary Material available online at <http://dx.doi.org/10.1155/2013/612153>. The calculated average bond lengths of single and double bonds in fullerene cage of PC<sub>71</sub>BM isomers are about 0.145 and 0.141 nm, respectively, which are very close to the corresponding values (0.145 and 0.140 nm) of C<sub>70</sub> fullerene obtained from the same level of theoretical calculation. The bond character of C5–C15 was changed from double bond (0.140 nm) in pure C<sub>70</sub> fullerene to single bond (0.163 nm) in [6,6]PC<sub>71</sub>BM due to forming a carbon trigon (C5–C15–C71) through the changes of orbital hybridization, and the change of C5–C15 bond length is similar to the cases of C<sub>60</sub>-TPA [48] and N-methyl-3,4-fulleropyrrolidine [49], while, in [5,6]PC<sub>71</sub>BM, the atomic distance between C14 and C15 is about 0.213 nm, which far exceeds the typical C–C

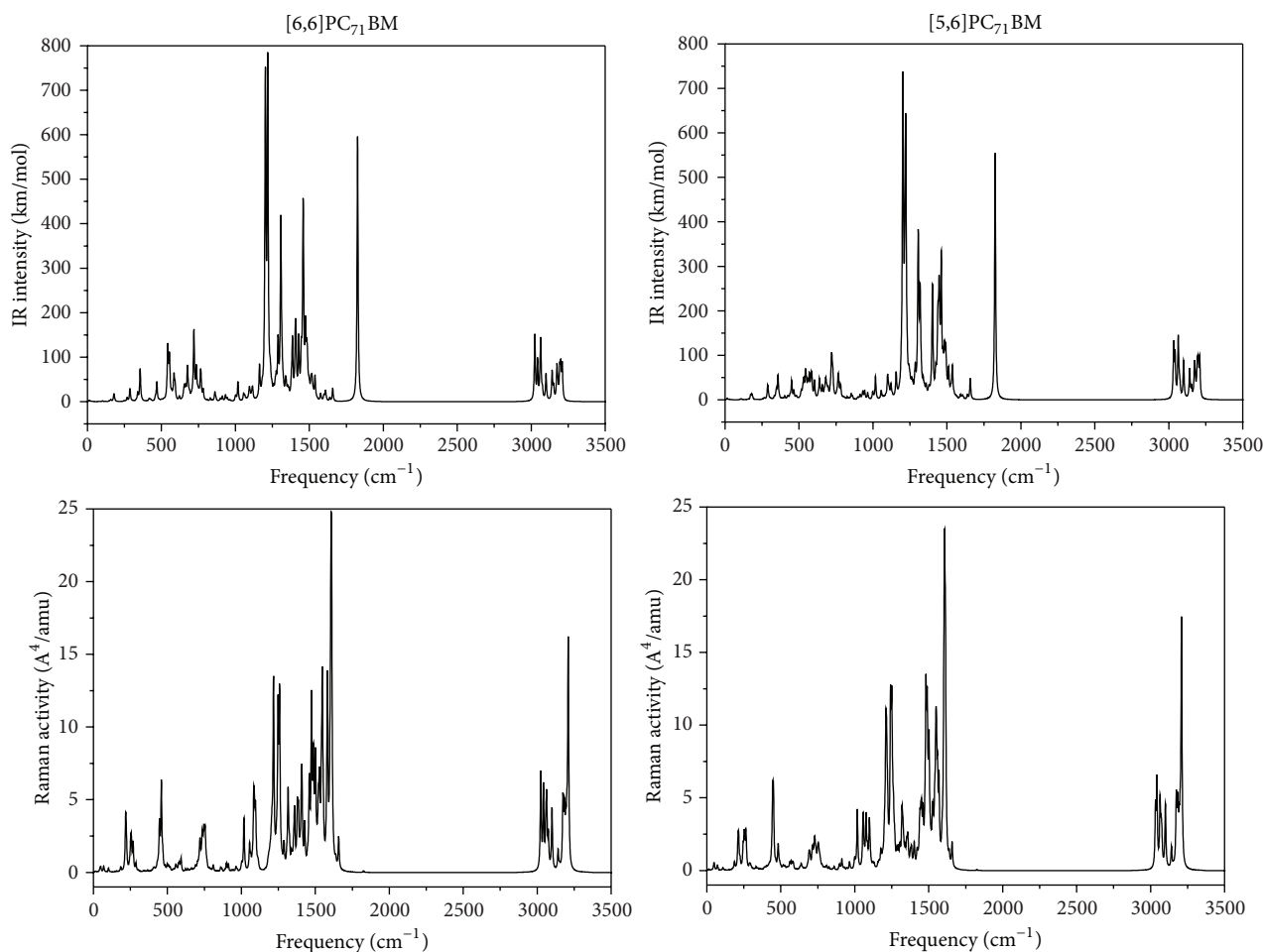


FIGURE 2: The IR and Raman spectra of [6,6]PC<sub>71</sub>BM and [5,6]PC<sub>71</sub>BM. The top panel is IR spectra, while the bottom panel is Raman spectra.

single bond length (0.154 nm). Therefore, the single bond of C14–C15 is broken in the isomer. This is the main difference between the two isomers and it may affect electronic and optical properties. The other corresponding geometrical parameters of these isomers are very similar because of the localized character of chemical bonds.

**3.2. IR and Raman.** In order to investigate the IR and Raman properties of PC<sub>71</sub>BM, the vibrational analyses are performed based upon the optimized structures of isomers. The IR and Raman spectra of [6,6]PC<sub>71</sub>BM and [5,6]PC<sub>71</sub>BM are shown in Figure 2. The calculated vibrational data indicates that there are no imaginary frequencies. This means that the optimized isomer structures are the minima of potential energy surface indeed.

The vibrational frequency ranges of [6,6]PC<sub>71</sub>BM and [5,6]PC<sub>71</sub>BM are 10~3210 cm<sup>-1</sup> and 13~3209 cm<sup>-1</sup>, respectively. For [6,6]PC<sub>71</sub>BM, the strongest IR peaks at about 1219 and 1203 cm<sup>-1</sup> correspond to the C–H bond-bending vibrational modes in butyric acid methyl ester group, while the IR peak at about 1826 cm<sup>-1</sup> comes from stretch mode of C–O bond in carbonyl group. As to [5,6]PC<sub>71</sub>BM, the vibrational modes of the strongest peaks at about 1222 and 1826 cm<sup>-1</sup> are

very similar to those of [6,6]PC<sub>71</sub>BM, whereas to Raman, for [6,6]PC<sub>71</sub>BM, the peak at about 1609 cm<sup>-1</sup> comes from the stretching mode of C–C bonds in the fullerene cage, and the peak at about 3210 cm<sup>-1</sup> relates to the stretching mode of C–H bonds in phenyl group. Again, the vibrational modes of peaks at about 1608 and 3209 cm<sup>-1</sup> for [5,6]PC<sub>71</sub>BM are very similar to those of [6,6]PC<sub>71</sub>BM. Furthermore, the strengths of IR and Raman at the strongest peaks of [6,6]PC<sub>71</sub>BM are slightly larger than those of [5,6]PC<sub>71</sub>BM due to its larger dipole moment. The vibrational modes at the IR and Raman peaks of PC<sub>71</sub>BM are very similar to those of PC<sub>61</sub>BM [50] due to the same moiety and the similarity of fullerene cages.

**3.3. Absorption Spectra and Electronic Structures.** The UV/Vis absorption of PC<sub>71</sub>BM was measured in toluene solution, and the absorption peaks locate at about 462 and 372 nm, respectively [17]. Also, the experiment demonstrated that the absorption coefficient of PC<sub>71</sub>BM is significantly higher than that of PC<sub>61</sub>BM in the visible region [17]. The better absorption properties of PC<sub>71</sub>BM are favorable for improving light harvesting efficiency in OPV. In order to select a suitable functional for the excitations of PC<sub>71</sub>BM, the B3LYP, PBE0, and CAM-B3LYP functionals are adopted in computing

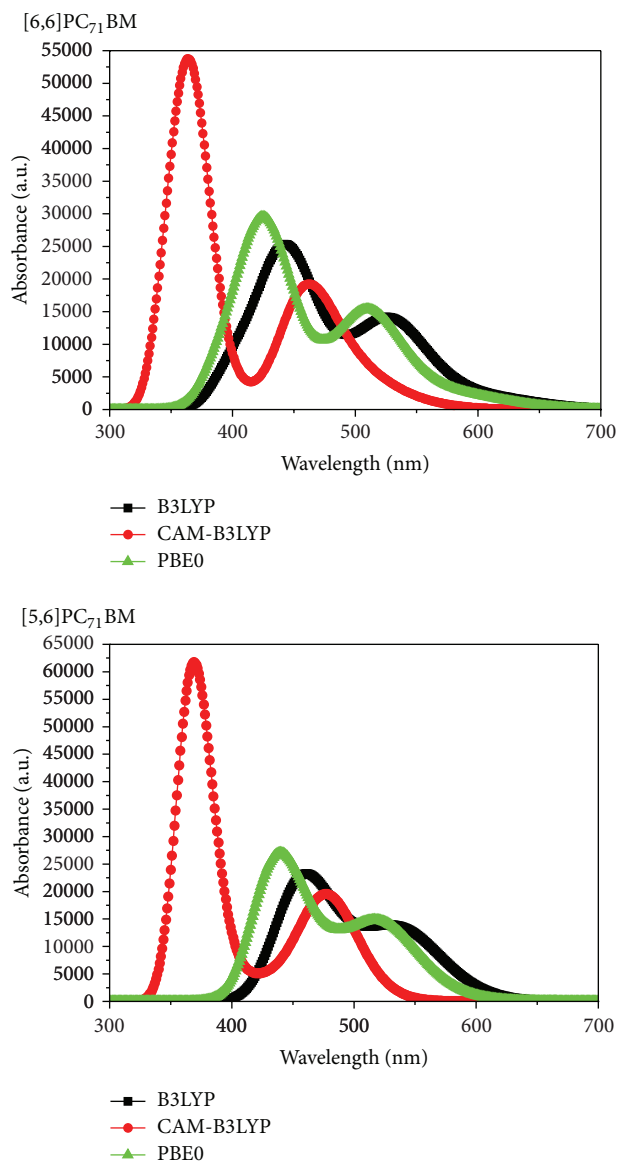


FIGURE 3: The simulated absorption spectra for [6,6]PC<sub>71</sub>BM and [5,6]PC<sub>71</sub>BM based upon TD-DFT results calculated with different functionals. The 0.15 eV of half-width at half-maximum was applied for simulating absorption spectra.

the absorption spectra of the isomers in toluene solution. The simulated absorption spectra for the two isomers of PC<sub>71</sub>BM are presented in Figure 3. Apparently, the excitation energies calculated with CAM-B3LYP are larger than the corresponding values calculated with PBE0 and B3LYP functionals due to the different methods for dealing with exchange and correlation energies. Comparing with the experimental results, we found that the CAM-B3LYP functional results agree well with the experimental data.

The excitation properties for the first excited state  $S_1$  and the excited states at absorption peaks in UV-Vis region for [6,6]PC<sub>71</sub>BM and [5,6]PC<sub>71</sub>BM in toluene are listed in Table 1, which includes the excitation energies (eV), wavelength (nm), oscillator strengths ( $f$ ) and the transition

MOs	[6,6]PC <sub>71</sub> BM	[5,6]PC <sub>71</sub> BM
HOMO-3		
HOMO-2		
HOMO-1		
HOMO		
LUMO		
LUMO + 1		
LUMO + 2		
LUMO + 3		

FIGURE 4: Isodensity plots (isodensity contour = 0.02 a.u.) of the frontier molecular orbitals of [6,6]PC<sub>71</sub>BM and [5,6]PC<sub>71</sub>BM with CAM-B3LYP functional.

configurations with coefficients larger than 10%. The results indicate that the excitation energies at the absorption maxima for the isomers are very close, and the excited states include several transition configurations. To understand the transition character, the molecular orbitals involved transitions in Table 1 are presented in Figure 4. The HOMOs are  $\pi$  orbitals between C-C bonds in fullerene cage, while the LUMOs are  $\pi^*$  orbitals in fullerene. Thus, the transitions in Table 1 are localized  $\pi$ - $\pi^*$  transitions in fullerenes cages. This is different from that of PC<sub>61</sub>BM, which has several intramolecular charge transfer transitions [50].

The exciton binding energy (EBE), an important quantity for the efficiency of excitonic solar cells, determines the charge separation in solar cells [51]. The EBE can be calculated as the difference between the electronic and optical band gap energies [52]. The electronic band gap is calculated as the energy difference between the HOMO and LUMO levels, while the first excitation energy is adopted as the optical gap [51, 53]. The molecular orbital energy levels and HOMO-LUMO gaps of PC<sub>71</sub>BM isomers are shown in Figure 5. The HOMO-LUMO gap of [6,6]PC<sub>71</sub>BM is about 4.34 eV, which is about 0.09 eV smaller than that of [5,6]PC<sub>71</sub>BM. The calculated EBE for [6,6]PC<sub>71</sub>BM and [5,6]PC<sub>71</sub>BM are 2.08

TABLE 1: The excitation energies (eV), wavelength (nm), oscillator strengths ( $f$ ), and the transition configurations with coefficients larger than 10% for the first excited state  $S_1$  and the excited states at absorption peaks in UV/Vis region for [6,6]PC<sub>71</sub>BM and [5,6]PC<sub>71</sub>BM in toluene.

	States	Transition configurations	$E$ (nm/eV)	$f$
[6,6]PC <sub>71</sub> BM				
CAM-B3LYP	$S_1$	H → L (56%); H → L + 1 (19%); H - 2 → L + 1 (13%)	548/2.26	0.0077
	$S_7$	H - 2 → L + 1 (56%); H → L + 1 (10%)	456/2.72	0.0770
	$S_{22}$	H → L + 3 (27%); H - 3 → L + 1 (17%); H - 2 → L + 3 (14%); H - 7 → L + 2 (12%); H - 3 → L (10%)	372/3.33	0.2047
B3LYP	$S_1$	H → L + 1 (73%); H → L (26%)	621/2.00	0.0020
	$S_8$	H - 2 → L + 1 (69%)	530/2.34	0.0635
	$S_{25}$	H - 5 → L + 2 (32%); H - 8 → L (25%); H → L + 3 (16%); H - 3 → L + 1 (10%)	444/2.79	0.0690
PBE0	$S_1$	H → L + 1 (89%)	597/2.08	0.0003
	$S_8$	H - 2 → L + 1 (69%)	512/2.43	0.0660
	$S_{25}$	H - 5 → L + 2 (24%); H - 7 → L + 2 (12%); H - 4 → L + 2 (11%)	425/2.92	0.0817
[5,6]PC <sub>71</sub> BM				
CAM-B3LYP	$S_1$	H → L + 2 (28%); H - 1 → L (22%); H - 2 → L + 1 (15%); H - 1 → L + 2 (12%); H → L (11%)	535/2.32	0.0003
	$S_5$	H → L (29%); H - 1 → L (25%); H - 2 → L (18%)	478/2.60	0.0864
	$S_{29}$	H - 3 → L + 2 (26%); H → L + 3 (23%); H - 1 → L + 3 (19%)	365/3.39	0.1991
B3LYP	$S_1$	H → L (87%)	608/2.04	0.0002
	$S_8$	H → L + 2 (39%); H - 2 → L (19%); H - 4 → L (13%)	544/2.28	0.0709
	$S_{26}$	H - 7 → L + 1 (29%); H - 6 → L (22%); H - 7 → L + 2 (14%)	458/2.71	0.0738
PBE0	$S_1$	H → L (81%)	586/2.12	0.0003
	$S_9$	H - 1 → L + 2 (44%); H - 2 → L + 1 (23%); H - 4 → L + 1 (10%)	526/2.36	0.0537
	$S_{26}$	H - 6 → L (26%); H - 7 → L + 1 (25%); H - 7 → L + 2 (11%)	438/2.83	0.0828

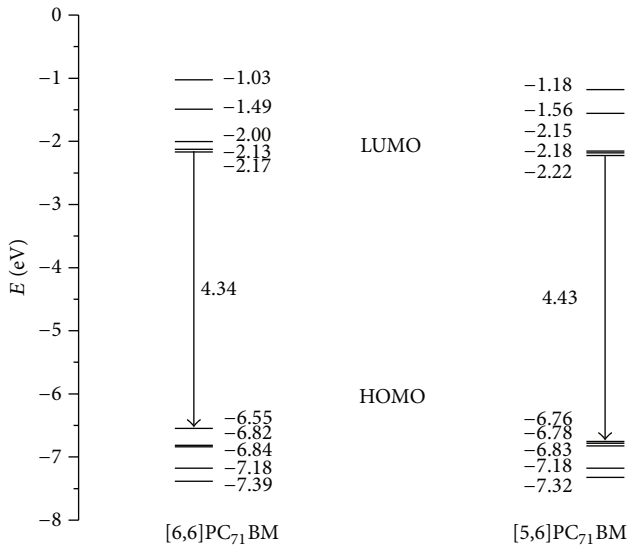


FIGURE 5: The calculated frontier molecular orbital energies and HOMO-LUMO gaps (in eV) at the CAM-B3LYP/6-31G(d,p) level in toluene solvent.

and 2.11 eV, respectively. The smaller EBE of [6,6]PC<sub>71</sub>BM is favorable for exciton dissociation in heterojunction.

**3.4. Polarizabilities and Hyperpolarizabilities.** Polarizabilities and hyperpolarizabilities characterize the response of a system in an applied electric field in some extent [54], such as the strength of molecular interactions, the cross sections

of scattering, collision processes, and the nonlinear optical properties of the system [55, 56]. The definition for the isotropic polarizability is

$$\alpha = \frac{1}{3} (\alpha_{XX} + \alpha_{YY} + \alpha_{ZZ}), \quad (1)$$

the polarizability anisotropy invariant is

$$\Delta\alpha = \left[ \frac{(\alpha_{XX} - \alpha_{YY})^2 + (\alpha_{YY} - \alpha_{ZZ})^2 + (\alpha_{ZZ} - \alpha_{XX})^2}{2} \right]^{1/2}, \quad (2)$$

and the average hyperpolarizability is

$$\beta_{||} = \frac{1}{5} \sum_i (\beta_{iiz} + \beta_{izi} + \beta_{zii}), \quad (3)$$

where  $\alpha_{XX}$ ,  $\alpha_{YY}$ , and  $\alpha_{ZZ}$  are tensor components of polarizability;  $\beta_{iiz}$ ,  $\beta_{izi}$ , and  $\beta_{zii}$  ( $i$  from  $X$  to  $Z$ ) are tensor components of hyperpolarizability. For [6,6]PC<sub>71</sub>BM, the calculated  $\alpha_{XX}$ ,  $\alpha_{YY}$ , and  $\alpha_{ZZ}$  are 818.5, 699.3, and 638.9 a.u., respectively, and the computed  $\beta_{XXZ}$ ,  $\beta_{YYZ}$ , and  $\beta_{ZZZ}$  are 67.0, -28.6, and -98.8 a.u., respectively. For [5,6]PC<sub>71</sub>BM, the corresponding tensor components are 817.1, 711.7, and 614.4 a.u., respectively, and the calculated  $\beta_{XXZ}$ ,  $\beta_{YYZ}$ , and  $\beta_{ZZZ}$  are -26.7, -2.4, and -108.4 a.u., respectively. In addition to the individual tensor components of the polarizabilities and the first hyperpolarizabilities, the calculated isotropic polarizability, polarizability anisotropy invariant, and average hyperpolarizability for [6,6]PC<sub>71</sub>BM are  $\alpha = 718.9$  a.u.,  $\Delta\alpha = 158.3$  a.u., and  $\beta_{||} = -36.2$  a.u., respectively, and

the corresponding values for [5,6]PC<sub>71</sub>BM are 723.4, 153.2, and -82.5 a.u., respectively. The values are larger than that of PC<sub>61</sub>BM ( $\alpha = 577.7$  a.u.,  $\Delta\alpha = 96.9$  a.u., and  $\beta_{\parallel} = -22.8$  a.u. (B3LYP/3-21G\*)) [50] due to the C<sub>70</sub> fullerene cage. This means that PC<sub>71</sub>BM has stronger response of external field and better nonlinear optical properties than that of PC<sub>61</sub>BM.

#### 4. Conclusions

In this work, the geometries, IR and Raman, electronic structures, polarizabilities, and hyperpolarizabilities of PC<sub>71</sub>BM isomers are studied by using DFT; the absorption and excitation properties are addressed via TDDFT with B3LYP, PBE0, and CAM-B3LYP functionals. Based upon the calculated results, we found the following: the lower total energy of [6,6]PC<sub>71</sub>BM suggests that [6,6]PC<sub>71</sub>BM is more stable than [5,6]PC<sub>71</sub>BM. The geometrical characters reveal that the C-C bond at the edge of six-C rings is changed from double bond in pure C<sub>70</sub> fullerene to single bond in [6,6]PC<sub>71</sub>BM, while the C-C bond at the edge between five-C and six-C rings is broken in [5,6]PC<sub>71</sub>BM. The wave numbers of strongest IR peaks of [6,6]PC<sub>71</sub>BM and [5,6]PC<sub>71</sub>BM are 1219 and 1222 cm<sup>-1</sup>, respectively. The Raman peaks of [6,6]PC<sub>71</sub>BM and [5,6]PC<sub>71</sub>BM locate at about 1609 and 1608 cm<sup>-1</sup>, respectively. The vibrational modes of [6,6]PC<sub>71</sub>BM and [5,6]PC<sub>71</sub>BM at IR and Raman peaks are quite similar and also very similar to that of PC<sub>61</sub>BM. Compared with the experimental absorption properties, it can be found that the CAM-B3LYP functional is the most suitable functional for describing excitations of PC<sub>71</sub>BM. The analysis of transition configurations and MOs demonstrated that the transitions at the absorption maxima in UV/Vis region are localized  $\pi$ - $\pi^*$  transitions in fullerenes cages. The calculated EBE for [6,6]PC<sub>71</sub>BM and [5,6]PC<sub>71</sub>BM are 2.08 and 2.11 eV, respectively. The smaller EBE of [6,6]PC<sub>71</sub>BM is favorable for exciton dissociation in heterojunction. Furthermore, the larger isotropic polarizability of PC<sub>71</sub>BM indicates that the response of PC<sub>71</sub>BM to applied external electric field is stronger than that of PC<sub>61</sub>BM, and therefore resulting into better nonlinear optical properties.

#### Acknowledgments

This work was supported by the Basic Scientific Research Foundation for Gansu Universities of China (Grant no. 1210ZTC055) and National Natural Science Foundation of China (Grant nos. 11164016 and 11164015).

#### References

- [1] Y. Lin, Y. Li, and X. Zhan, "Small molecule semiconductors for high-efficiency organic photovoltaics," *Chemical Society Reviews*, vol. 41, no. 11, pp. 4245-4272, 2012.
- [2] M. Linares, D. Beljonne, J. Cornil et al., "On the interface dipole at the pentacene-fullerene heterojunction: a theoretical study," *Journal of Physical Chemistry C*, vol. 114, no. 7, pp. 3215-3224, 2010.
- [3] Y. Yi, V. Coropceanu, and J.-L. Brédas, "Exciton-dissociation and charge-recombination processes in pentacene/C<sub>60</sub> solar cells: theoretical insight into the impact of interface geometry," *Journal of the American Chemical Society*, vol. 131, no. 43, pp. 15777-15783, 2009.
- [4] P. W. M. Blom, V. D. Mihailetschi, L. J. A. Koster, and D. E. Markov, "Device physics of polymer:Fullerene bulk heterojunction solar cells," *Advanced Materials*, vol. 19, no. 12, pp. 1551-1566, 2007.
- [5] L.-M. Chen, Z. Xu, Z. Hong, and Y. Yang, "Interface investigation and engineering—achieving high performance polymer photovoltaic devices," *Journal of Materials Chemistry*, vol. 20, no. 13, pp. 2575-2598, 2010.
- [6] G. Yu, J. Gao, J. C. Hummelen, F. Wudl, and A. J. Heeger, "Polymer photovoltaic cells: enhanced efficiencies via a network of internal donor-acceptor heterojunctions," *Science*, vol. 270, no. 5243, pp. 1789-1791, 1995.
- [7] F. Padinger, R. S. Rittberger, and N. S. Sariciftci, "Effects of postproduction treatment on plastic solar cells," *Advanced Functional Materials*, vol. 13, no. 1, pp. 85-88, 2003.
- [8] J. Xue, B. P. Rand, S. Uchida, and S. R. Forrest, "A hybrid planar-mixed molecular heterojunction photovoltaic cell," *Advanced Materials*, vol. 17, no. 1, pp. 66-71, 2005.
- [9] G. Li, V. Shrotriya, J. Huang et al., "High-efficiency solution processable polymer photovoltaic cells by self-organization of polymer blends," *Nature Materials*, vol. 4, no. 11, pp. 864-868, 2005.
- [10] G. Dennler, M. C. Scharber, and C. J. Brabec, "Polymer-fullerene bulk-heterojunction solar cells," *Advanced Materials*, vol. 21, no. 13, pp. 1323-1338, 2009.
- [11] N. Banerji, M. Wang, J. Fan, E. S. Chesnut, F. Wudl, and J. E. Moser, "Sensitization of fullerenes by covalent attachment of a diketopyrrolopyrrole chromophore," *Journal of Materials Chemistry*, vol. 22, no. 26, pp. 13286-13294, 2012.
- [12] P. Aloukos, K. Iliopoulos, S. Couris et al., "Photophysics and transient nonlinear optical response of donor-[60]fullerene hybrids," *Journal of Materials Chemistry*, vol. 21, no. 8, pp. 2524-2534, 2011.
- [13] H. Cha, D. S. Chung, S. Y. Bae et al., "Complementary absorbing star-shaped small molecules for the preparation of ternary cascade energy structures in organic photovoltaic cells," *Advanced Functional Materials*, vol. 23, no. 12, pp. 1556-1565, 2013.
- [14] M. Svensson, F. Zhang, S. C. Veenstra et al., "High-performance polymer solar cells of an alternating polyfluorene copolymer and a fullerene derivative," *Advanced Materials*, vol. 15, no. 12, pp. 988-991, 2003.
- [15] O. Inganäs, M. Svensson, F. Zhang et al., "Low bandgap alternating polyfluorene copolymers in plastic photodiodes and solar cells," *Applied Physics A*, vol. 79, no. 1, pp. 31-35, 2004.
- [16] C. J. Brabec, A. Cravino, D. Meissner et al., "Origin of the open circuit voltage of plastic solar cells," *Advanced Functional Materials*, vol. 11, no. 5, pp. 374-380, 2001.
- [17] M. M. Wienk, J. M. Kroon, W. J. H. Verhees et al., "Efficient methano[70]fullerene/MDMO-PPV bulk heterojunction photovoltaic cells," *Angewandte Chemie*, vol. 42, no. 29, pp. 3371-3375, 2003.
- [18] Z. Liu, F. Xue, Y. Su, and K. Varshneyan, "Electrically bistable memory device based on spin-coated molecular complex thin film," *IEEE Electron Device Letters*, vol. 27, no. 3, pp. 151-153, 2006.
- [19] Y. M. Chang and C. Y. Leu, "Conjugated polyelectrolyte and zinc oxide stacked structure as an interlayer in highly efficient and stable organic photovoltaic cells," *Journal of Materials Chemistry A*, vol. 1, no. 21, pp. 6446-6451, 2013.

- [20] H.-C. Chen, I.-C. Wu, J.-H. Hung et al., "Superiority of branched side chains in spontaneous nanowire formation: exemplified by poly(3-2-methylbutylthiophene) for high-performance solar cells," *Small*, vol. 7, no. 8, pp. 1098–1107, 2011.
- [21] M. Chen, W. Fu, M. Shi et al., "An ester-functionalized diketopyrrolopyrrole molecule with appropriate energy levels for application in solution-processed organic solar cells," *Journal of Materials Chemistry A*, vol. 1, no. 1, pp. 105–111, 2013.
- [22] Y.-C. Chen, C.-Y. Yu, Y.-L. Fan, L.-I. Hung, C.-P. Chen, and C. Ting, "Low-bandgap conjugated polymer for high efficient photovoltaic applications," *Chemical Communications*, vol. 46, no. 35, pp. 6503–6505, 2010.
- [23] P. Dutta, W. Yang, S. H. Eom, and S.-H. Lee, "Synthesis and characterization of triphenylamine flanked thiazole-based small molecules for high performance solution processed organic solar cells," *Organic Electronics*, vol. 13, no. 2, pp. 273–282, 2012.
- [24] J. Jo, A. Pron, P. Berrouard et al., "A new terthiophene-thienopyrrolodione copolymer-based bulk heterojunction solar cell with high open-circuit voltage," *Advanced Energy Materials*, vol. 2, no. 11, pp. 1397–1403, 2012.
- [25] D. C. Lim, K. D. Kim, S. Y. Park et al., "Towards fabrication of high-performing organic photovoltaics: new donor-polymer, atomic layer deposited thin buffer layer and plasmonic effects," *Energy & Environmental Science*, vol. 5, no. 12, pp. 9803–9807, 2012.
- [26] Y. Jiang, D. Yu, L. Lu et al., "Tuning optical and electronic properties of star-shaped conjugated molecules with enlarged [small pi]-delocalization for organic solar cell application," *Journal of Materials Chemistry A*, vol. 1, no. 28, pp. 8270–8279, 2013.
- [27] Y. Chen, M. Elshobaki, Z. Ye et al., "Microlens array induced light absorption enhancement in polymer solar cells," *Physical Chemistry Chemical Physics*, vol. 15, no. 12, pp. 4297–4302, 2013.
- [28] R. Bauernschmitt and R. Ahlrichs, "Treatment of electronic excitations within the adiabatic approximation of time dependent density functional theory," *Chemical Physics Letters*, vol. 256, no. 4–5, pp. 454–464, 1996.
- [29] C. Van Caillie and R. D. Amos, "Geometric derivatives of excitation energies using SCF and DFT," *Chemical Physics Letters*, vol. 308, no. 3–4, pp. 249–255, 1999.
- [30] C. Van Caillie and R. D. Amos, "Geometric derivatives of density functional theory excitation energies using gradient-corrected functionals," *Chemical Physics Letters*, vol. 317, no. 1–2, pp. 159–164, 2000.
- [31] F. Furche and R. Ahlrichs, "Adiabatic time-dependent density functional methods for excited state properties," *The Journal of Chemical Physics*, vol. 117, no. 16, pp. 7433–7447, 2002.
- [32] G. Scalmani, M. J. Frisch, B. Mennucci, J. Tomasi, R. Cammi, and V. Barone, "Geometries and properties of excited states in the gas phase and in solution: theory and application of a time-dependent density functional theory polarizable continuum model," *The Journal of Chemical Physics*, vol. 124, no. 9, Article ID 094107, 2006.
- [33] M. E. Casida, C. Jamorski, K. C. Casida, and D. R. Salahub, "Molecular excitation energies to high-lying bound states from time-dependent density-functional response theory: characterization and correction of the time-dependent local density approximation ionization threshold," *The Journal of Chemical Physics*, vol. 108, no. 11, pp. 4439–4449, 1998.
- [34] R. E. Stratmann, G. E. Scuseria, and M. J. Frisch, "An efficient implementation of time-dependent density-functional theory for the calculation of excitation energies of large molecules," *The Journal of Chemical Physics*, vol. 109, no. 19, pp. 8218–8224, 1998.
- [35] R. D. Adamson, J. P. Dombroski, and P. M. W. Gill, "Efficient calculation of short-range Coulomb energies," *Journal of Computational Chemistry*, vol. 20, no. 9, pp. 921–927, 1999.
- [36] A. D. Becke, "Density-functional exchange-energy approximation with correct asymptotic behavior," *Physical Review A*, vol. 38, no. 6, pp. 3098–3100, 1988.
- [37] A. D. Becke, "Density-functional thermochemistry. III. The role of exact exchange," *The Journal of Chemical Physics*, vol. 98, no. 7, pp. 5648–5652, 1993.
- [38] C. Lee, W. Yang, and R. G. Parr, "Development of the Colle-Salvetti correlation-energy formula into a functional of the electron density," *Physical Review B*, vol. 37, no. 2, pp. 785–789, 1988.
- [39] M. Pastore, E. Mosconi, F. De Angelis, and M. Grätzel, "A computational investigation of organic dyes for dye-sensitized solar cells: benchmark, strategies, and open issues," *Journal of Physical Chemistry C*, vol. 114, no. 15, pp. 7205–7212, 2010.
- [40] J. P. Perdew, K. Burke, and M. Ernzerhof, "Generalized gradient approximation made simple," *Physical Review Letters*, vol. 78, no. 7, pp. 1396–1396, 1997.
- [41] J. P. Perdew, K. Burke, and M. Ernzerhof, "Generalized gradient approximation made simple," *Physical Review Letters*, vol. 77, no. 18, pp. 3865–3868, 1996.
- [42] C. Adamo and V. Barone, "Toward reliable density functional methods without adjustable parameters: the PBE0 model," *The Journal of Chemical Physics*, vol. 110, no. 13, pp. 6158–6170, 1999.
- [43] T. Yanai, D. P. Tew, and N. C. Handy, "A new hybrid exchange-correlation functional using the Coulomb-attenuating method (CAM-B3LYP)," *Chemical Physics Letters*, vol. 393, no. 1–3, pp. 51–57, 2004.
- [44] M. Cossi and V. Barone, "Separation between fast and slow polarizations in continuum solvation models," *Journal of Physical Chemistry A*, vol. 104, no. 46, pp. 10614–10622, 2000.
- [45] D. Jacquemin, E. A. Perpète, I. Ciofini, and C. Adamo, "Accurate simulation of optical properties in dyes," *Accounts of Chemical Research*, vol. 42, no. 2, pp. 326–334, 2009.
- [46] M. J. Frisch, G. W. Trucks, H. B. Schlegel et al., Gaussian, Inc., Wallingford, Conn, USA, 2010.
- [47] W. H. Powell, F. Cozzi, G. P. Moss, C. Thilgen, R. J.-R. Hwu, and A. Yerin, "Nomenclature for the C<sub>60</sub>-I<sub>h</sub> and C<sub>70</sub>-D<sub>5h(6)</sub> fullerenes: (IUPAC recommendations 2002)," *Pure and Applied Chemistry*, vol. 74, no. 4, pp. 629–695, 2002.
- [48] T.-T. Wang and H.-P. Zeng, "Synthesis, characterization and theoretical calculation of the fulleropyrrolidines containing triphenylamine," *Chinese Journal of Chemistry*, vol. 24, no. 2, pp. 224–230, 2006.
- [49] C. Zhang, W. Liang, H. Chen, Y. Chen, Z. Wei, and Y. Wu, "Theoretical studies on the geometrical and electronic structures of N-methyl-3,4-fulleropyrrolidine," *Journal of Molecular Structure: THEOCHEM*, vol. 862, no. 1–3, pp. 98–104, 2008.
- [50] C.-R. Zhang, H.-S. Chen, Y.-H. Chen, Z.-Q. Wei, and Z.-S. Pu, "DFT study on methanofullerene derivative [6,6]-Phenyl-C<sub>61</sub> butyric acid methyl ester," *Acta Physico-Chimica Sinica*, vol. 24, no. 8, pp. 1353–1358, 2008.
- [51] B.-G. Kim, C.-G. Zhen, E. J. Jeong, J. Kieffer, and J. Kim, "Organic dye design tools for efficient photocurrent generation in dye-sensitized solar cells: exciton binding energy and electron acceptors," *Advanced Functional Materials*, vol. 22, no. 8, pp. 1606–1612, 2012.

- [52] B. A. Gregg, "Excitonic solar cells," *Journal of Physical Chemistry B*, vol. 107, no. 20, pp. 4688–4698, 2003.
- [53] G. D. Scholes and G. Rumbles, "Excitons in nanoscale systems," *Nature Materials*, vol. 5, no. 9, pp. 683–696, 2006.
- [54] C.-R. Zhang, H.-S. Chen, and G.-H. Wang, "Structure and properties of semiconductor microclusters  $\text{Ga}_n\text{P}_n(n=1-4)$ : a first principle study," *Chemical Research in Chinese Universities*, vol. 20, no. 5, pp. 640–646, 2004.
- [55] H. Cheng, J. K. Feng, A. M. Ren, and L. Jian-Jun, "Theoretical study of the structure, spectra and nonlinear third-order optical susceptibility of  $\text{C}_{74}$ ," *Acta Chimica Sinica*, vol. 60, no. 5, pp. 830–834, 2002.
- [56] H. Cheng, J.-K. Feng, A.-M. Ren, and J.-J. Liu, "Theoretical study of the structure, spectra and nonlinear optical susceptibility of  $\text{C}_{72}$ ," *Acta Chimica Sinica*, vol. 61, no. 4, pp. 541–546, 2003.

## Research Article

# Preparation of BiFeO<sub>3</sub>-Graphene Nanocomposites and Their Enhanced Photocatalytic Activities

J. F. Dai,<sup>1,2</sup> T. Xian,<sup>1,2</sup> L. J. Di,<sup>2</sup> and H. Yang<sup>1,2</sup>

<sup>1</sup> State Key Laboratory of Gansu Advanced Non-Ferrous Metal Materials, Lanzhou University of Technology, Lanzhou 730050, China

<sup>2</sup> School of Science, Lanzhou University of Technology, Lanzhou 730050, China

Correspondence should be addressed to H. Yang; [hyang@lut.cn](mailto:hyang@lut.cn)

Received 23 September 2013; Accepted 27 October 2013

Academic Editor: Jian Lin

Copyright © 2013 J. F. Dai et al. This is an open access article distributed under the Creative Commons Attribution License, which permits unrestricted use, distribution, and reproduction in any medium, provided the original work is properly cited.

BiFeO<sub>3</sub> nanoparticles were prepared via a polyacrylamide gel route. BiFeO<sub>3</sub>-graphene nanocomposites were fabricated by mixing BiFeO<sub>3</sub> nanoparticles and graphene into absolute ethanol solution followed by thermal drying. The TEM observation demonstrates that the BiFeO<sub>3</sub> nanoparticles are well anchored onto graphene sheets. The photocatalytic activities of the as-prepared samples were evaluated by the degradation of methyl orange (MO) under simulated sunlight irradiation. Compared to bare BiFeO<sub>3</sub> nanoparticles, BiFeO<sub>3</sub>-graphene nanocomposites exhibit enhanced photocatalytic activity. The outstanding photocatalytic performance is mainly ascribed to the efficient transfer of photogenerated electrons from BiFeO<sub>3</sub> to graphene, thus leading to an increased availability of h<sup>+</sup> for the photocatalytic reaction. In addition, hydroxyl (-OH) radicals were detected by the photoluminescence technique using terephthalic acid as a probe molecule and are found to be produced on the irradiated BiFeO<sub>3</sub> and BiFeO<sub>3</sub>-graphene nanocomposites; in particular, an enhanced yield is observed for the latter.

## 1. Introduction

Semiconductor-based photocatalysts have attracted considerable attention over the past decades due to their potential applications in solar energy conversion and environmental purification [1, 2]. Among them, TiO<sub>2</sub> has proven to be a powerful photocatalyst for the degradation of numerous organic compounds [3–5]. However, it can only respond to UV light owing to its wide bandgap (~3.2 eV). To efficiently make use of solar energy that consists largely of visible light, it is essential to explore visible-light-driven photocatalysts.

BiFeO<sub>3</sub>, exhibiting simultaneous ferroelectric and antiferromagnetic properties at room temperature, has been extensively studied as one of the most important multiferroic materials [6, 7]. Besides its multiferroic property, recent investigations have revealed that BiFeO<sub>3</sub> also exhibits visible-light responsive photocatalytic activity for the degradation of organic pollutants [8–13]. Generally, the overall photocatalytic activity of a photocatalyst depends on numerous factors. Among them, the effective separation of photogenerated electron-hole (e<sup>-</sup>-h<sup>+</sup>) pairs is very important in improving the photocatalytic activity. Graphene, being a

two-dimensional (2D) sheet of sp<sup>2</sup>-hybridized carbon atoms, possesses excellent properties including high electrical conductivity, electron mobility, thermal conductivity, mechanical strength, chemical stability, and so forth [14–16]. On account of its outstanding properties, graphene has been frequently used as an ideal support to integrate with a large number of functional nanomaterials to form unique nanocomposites with improved performances in the fields of photocatalysts [17–23], microsupercapacitors [24], field-emission emitters [25], and fuel cells [26]. Particularly, the combination of graphene with photocatalysts is demonstrated to be an efficient way to promote the separation of photogenerated e<sup>-</sup>-h<sup>+</sup> pairs and then enhance their photocatalytic activities [17–23]. In these graphene-photocatalyst composites, photogenerated electrons can be readily captured by graphene which acts as electron acceptor; thus, more photogenerated holes are increasingly available for the photocatalytic reactions. Therefore, many efforts have been devoted to incorporating graphene into BiFeO<sub>3</sub>-based composite materials.

Up to now, the BiFeO<sub>3</sub>-graphene composites are often prepared by hydrothermal method and sol-gel route. In

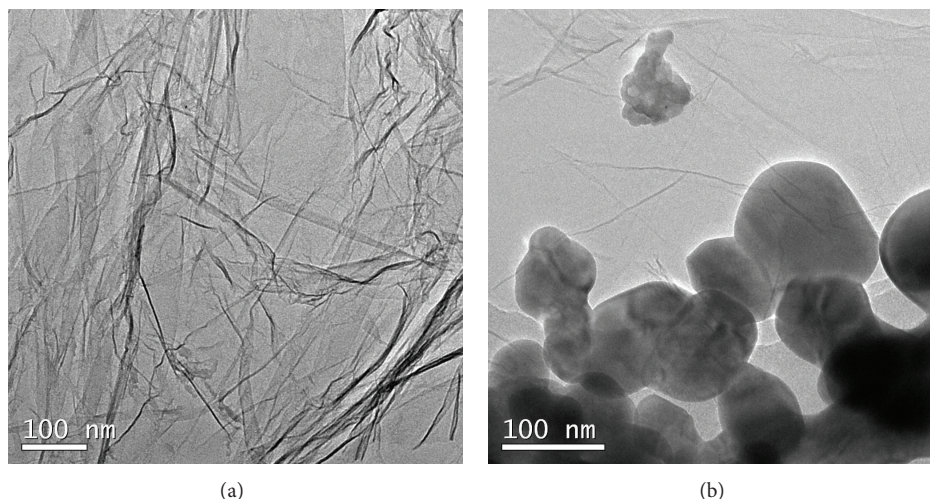


FIGURE 1: TEM images of graphene and BiFeO<sub>3</sub>-graphene(5%) nanocomposite.

the former method, the BiFeO<sub>3</sub> precursors were introduced into the dispersed aqueous of graphene or graphene oxide, followed by hydrothermal reaction, to yield BiFeO<sub>3</sub>-graphene composites [23, 27]. For the latter route, the sol containing precursors and graphene oxide was dried, and then the resultant was thermally treated at N<sub>2</sub> atmosphere, leading to the formation of BiFeO<sub>3</sub>-graphene hybrids [22]. However, it should be noted that the aforementioned processes are based on hydrothermal condition or high temperature thermal treatment procedure, which may damage the graphene lattice [28]. In this paper, we demonstrate that BiFeO<sub>3</sub> nanoparticles can be assembled onto graphene sheets by mixing BiFeO<sub>3</sub> nanoparticles and graphene into absolute ethanol solution followed by thermal drying. The photocatalytic activities of prepared samples were evaluated by the degradation of methylene orange (MO) under simulated sunlight irradiation. The production of <sup>•</sup>OH radicals on the irradiated BiFeO<sub>3</sub>-graphene photocatalyst was examined by the photoluminescence (PL) technique using terephthalic acid (TPA) as a probe molecule.

## 2. Experimental

The graphene used in this research was purchased from Nanjing XFNano Materials Tech Co. Ltd. BiFeO<sub>3</sub> nanoparticles were synthesized via a polyacrylamide gel route as described in the literature [29]. To assemble BiFeO<sub>3</sub> nanoparticles on graphene, number of BiFeO<sub>3</sub> nanoparticles and graphene were dispersed into absolute ethanol solution and ultrasonically treated for 10 min. The obtained mixture was dried at 60°C for 10 h in a thermostat drier, during which ethanol was vaporized, leaving behind BiFeO<sub>3</sub> nanoparticles well anchored on graphene nanosheets. By changing the graphene content, several BiFeO<sub>3</sub>-graphene nanocomposite samples with graphene weight fractions of 1%, 3%, 5%, 7%, and 9% were prepared.

The photocatalytic activity of the BiFeO<sub>3</sub>-graphene nanocomposites was evaluated by the degradation of MO under simulated sunlight irradiation from a 200 W xenon lamp

(incident light power: ~5 mW cm<sup>-2</sup>) at room temperature. The initial dye concentration was 10 mg L<sup>-1</sup> with a catalyst loading of 2.5 g L<sup>-1</sup>. Before illumination, the mixed solution was mildly stirred for 1 h in the dark in order to reach the adsorption-desorption equilibrium of MO on the catalyst. The concentration of MO after photocatalytic degradation was determined by measuring the absorbance of the solution at a fixed wavelength of 464 nm using a UV-visible spectrophotometer. Before the absorbance measurements, the reaction solution was centrifuged for 10 min at 4000 r min<sup>-1</sup> to remove the catalyst.

Terephthalic acid (TPA) was used as a probe molecule to examine <sup>•</sup>OH radicals formed on the irradiated BiFeO<sub>3</sub>-graphene photocatalyst. It is expected that TPA reacts with <sup>•</sup>OH to generate a highly fluorescent compound, 2-hydroxyterephthalic acid (TAOH). By measuring the PL intensity of TAOH that is pronounced around 429 nm, the information about <sup>•</sup>OH can be obtained. TPA was dissolved in 1.0 × 10<sup>-3</sup> mol L<sup>-1</sup> NaOH aqueous solution to make a 2.5 × 10<sup>-4</sup> mol L<sup>-1</sup> TPA solution, and then to the solution was added 2.5 g L<sup>-1</sup> photocatalyst. The mixed solution, after several minutes of ultrasound treatment in the dark, was illuminated under the 200 W xenon lamp. The reacted solution was centrifuged for 10 min at 4000 r min<sup>-1</sup> to separate the catalyst particles and was then used for the PL measurements at a fluorescence spectrophotometer with the excitation wavelength of 315 nm.

The morphology of the sample was observed using a field-emission transmission electron microscope (TEM). A fluorescence spectrophotometer was used to measure the photoluminescence (PL) emission spectra of the samples.

## 3. Results and Discussion

Figure 1(a) presents the TEM image of pure graphene, indicating that graphene has typical two-dimensional sheet structure with crumpled feature. Figure 1(b) shows the TEM image of BiFeO<sub>3</sub>-graphene(5%) nanocomposite. It can be seen that BiFeO<sub>3</sub> nanoparticles are assembled onto the graphene sheet.

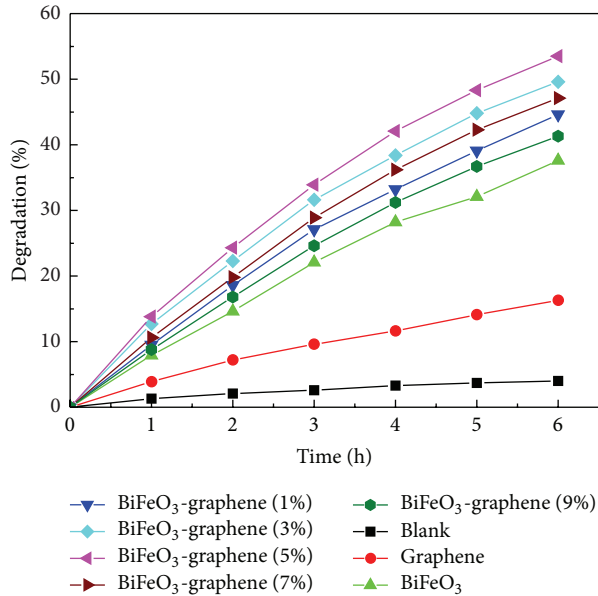


FIGURE 2: Photocatalytic degradation of MO as a function of irradiation time over bare BiFeO<sub>3</sub> nanoparticles and graphene and BiFeO<sub>3</sub>-graphene nanocomposites with graphene weight fractions of 1%, 3%, 5%, 7%, and 9%.

The BiFeO<sub>3</sub> nanoparticles mainly exhibit sphere-like shape and have an average particle size centered around 110 nm.

Figure 2 shows the photocatalytic degradation of MO over BiFeO<sub>3</sub>-graphene nanocomposites as a function of irradiation time ( $t$ ). The degradation percentage is defined as  $(C_0 - C_t)/C_0 \times 100\%$ , where  $C_0$  and  $C_t$  are the MO concentrations before and after irradiation, respectively. The blank experiment result is also shown in Figure 2, from which one can see that the MO is hardly degraded under simulated sunlight irradiation without photocatalysts, and its degradation percentage is less than 5% after 6 h of exposure. After 6 h irradiation in the presence of BiFeO<sub>3</sub> nanoparticles and graphene, about 37% and 16% of MO are observed to be degraded, respectively. When BiFeO<sub>3</sub> nanoparticles assembled on graphene, all samples of BiFeO<sub>3</sub>-graphene nanocomposites exhibit higher photocatalytic activity than bare BiFeO<sub>3</sub> nanoparticles. Moreover, the photocatalytic activity of nanocomposites increases gradually with the increase in graphene content from 1% to 5%. Further increase in graphene content leads to the decrease of photocatalytic activity.

Figure 3 shows the PL spectra of the TPA solution after reacting 6 h over the simulated sunlight irradiated BiFeO<sub>3</sub> and BiFeO<sub>3</sub>-graphene(5%) photocatalysts. The blank experiment result indicates that no PL signal is observed at 429 nm after irradiation without catalyst. With BiFeO<sub>3</sub> as photocatalyst, the PL signal centered around 429 nm is detected, revealing that  $\cdot\text{OH}$  radicals are generated on the irradiated BiFeO<sub>3</sub>. When BiFeO<sub>3</sub>-graphene(5%) nanocomposite is used as the photocatalyst, the PL signal intensity is slightly increased, which suggests that the yield of  $\cdot\text{OH}$  radicals is enhanced on the irradiated nanocomposite.

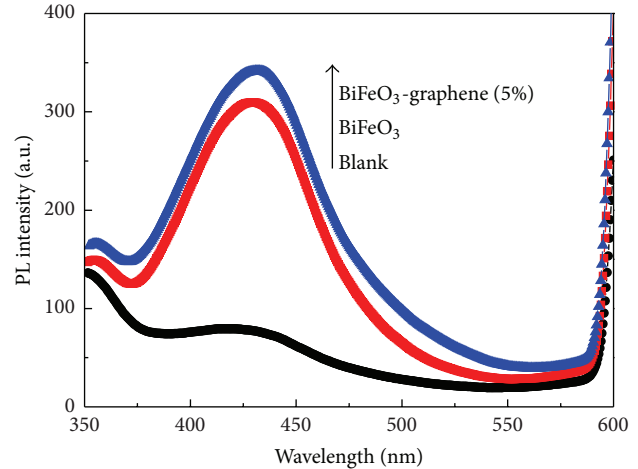


FIGURE 3: PL spectra of the TPA solution after reacting 6 h over the irradiated BiFeO<sub>3</sub> nanoparticles and BiFeO<sub>3</sub>-graphene (5%) nanocomposite.

Figure 4 schematically shows the photocatalytic mechanism of BiFeO<sub>3</sub>-graphene nanocomposite toward the degradation of MO. Under the simulated sunlight irradiation, the valence band (VB) electrons of BiFeO<sub>3</sub> are promoted to the conduction band (CB), inducing the production of  $e^-$ - $h^+$  pairs. The photogenerated electrons and holes then participate in a series of redox reactions to form a number of active species. However, the redox reaction processes are strongly related to the CB and VB edge potentials of BiFeO<sub>3</sub>. The VB potential of the BiFeO<sub>3</sub> can be calculated using the following relation [30]:

$$E_{\text{VB}} = X - E^e + 0.5E_g, \quad (1)$$

where  $X$  is the absolute electronegativity of the semiconductor,  $E_e$  is the energy of free electrons on the hydrogen scale ( $\sim 4.5$  eV), and  $E_g$  is the bandgap energy of the semiconductor (for the as-prepared BiFeO<sub>3</sub>,  $E_g$  is 2.06 eV [31]). The value of  $X$  for BiFeO<sub>3</sub> is obtained, by the arithmetic mean of the electron affinity and the first ionization of the constituent atoms reported in the literatures [32, 33], to be 5.93 eV. Thus, the CB and VB potentials of BiFeO<sub>3</sub> are calculated to be 0.4 and 2.46 V versus normal hydrogen electrode (NHE), respectively. It can be seen that the VB potential of sample is more positive than the redox potential of  $\text{OH}^-/\cdot\text{OH}$  (1.89 V/NHE), indicating that the photogenerated holes have strong oxidative ability and they can oxidize  $\text{OH}^-$  into  $\cdot\text{OH}$ . However, the CB potential of sample is not negative enough to reduce  $\text{O}_2$  to  $\text{O}_2^{\cdot -}$  ( $-0.13$  V/NHE) via  $e^-$ . As a result, it is reasonable to infer that  $\cdot\text{OH}$  radicals derived by the reaction of the photogenerated  $h^+$  with  $\text{OH}^-$  are the main active species responsible for the degradation of MO over simulated sunlight irradiated BiFeO<sub>3</sub>. Therefore, the effective separation of  $e^-$ - $h^+$  pairs and increased availability of  $h^+$  are the key points to improve the photocatalytic activity of the BiFeO<sub>3</sub>. When BiFeO<sub>3</sub> nanoparticles assembled on graphene, that is, an excellent electron acceptor and conductor, the photogenerated electrons readily transfer from the BiFeO<sub>3</sub> conduction

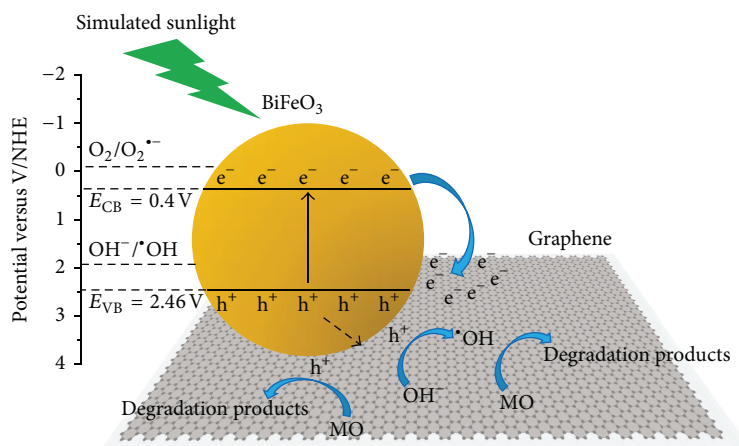


FIGURE 4: Schematic illustration of the photocatalytic mechanism of BiFeO<sub>3</sub>-graphene nanocomposite toward the degradation of MO.

band to graphene, which could suppress the recombination of photoexcited  $e^-h^+$  pairs, thus leading to the increase in the number of holes which participate in the photocatalytic reaction. The results shown in Figure 3 confirm the enhanced yield of  $\cdot\text{OH}$  radicals on the irradiated BiFeO<sub>3</sub>-graphene nanocomposite. As a result, with the introduction of an amount of graphene, the resulted BiFeO<sub>3</sub>-graphene nanocomposites exhibit an improved photocatalytic activity compared to bare BiFeO<sub>3</sub> nanoparticles. However, when the graphene content is further increased above its optimum value, the photocatalytic efficiency begins to exhibit a decreasing trend. This is ascribed to the following reasons: (i) the excessive graphene may shield the light and decrease the number of photon absorption on BiFeO<sub>3</sub> particles; (ii) the amount of available surface active sites tends to be reduced due to an increasing coverage of graphene onto the surface of BiFeO<sub>3</sub> particles.

#### 4. Conclusions

BiFeO<sub>3</sub> nanoparticles were prepared via a polyacrylamide gel method. BiFeO<sub>3</sub>-graphene nanocomposites were fabricated by mixing BiFeO<sub>3</sub> nanoparticles and graphene into ethanol followed by thermal drying at 60°C. It is found that the BiFeO<sub>3</sub> nanoparticles are well anchored onto graphene sheet. The photocatalytic experiments indicate that the BiFeO<sub>3</sub>-graphene nanocomposites exhibit higher photocatalytic activity for the degradation of MO under simulated sunlight irradiation than bare BiFeO<sub>3</sub> nanoparticles, which is attributed to the fact that the photogenerated electrons are captured by graphene, leading to an increased availability of  $h^+$  for the photocatalytic reaction.

#### Acknowledgments

This work was supported by the National Natural Science Foundation of China (Grant nos. 50962009 and 51262018) and the Hongliu Outstanding Talents Foundation of Lanzhou University of Technology (Grant no. J201205).

#### References

- [1] A. Mills, R. H. Davies, and D. Worsley, "Water purification by semiconductor photocatalysis," *Chemical Society Reviews*, vol. 22, no. 6, pp. 417–425, 1993.
- [2] M. R. Hoffmann, S. T. Martin, W. Choi, and D. W. Bahnemann, "Environmental applications of semiconductor photocatalysis," *Chemical Reviews*, vol. 95, no. 1, pp. 69–96, 1995.
- [3] J. H. Carey, J. Lawrence, and H. M. Tosine, "Photodechlorination of PCB's in the presence of titanium dioxide in aqueous suspensions," *Bulletin of Environmental Contamination and Toxicology*, vol. 16, no. 6, pp. 697–701, 1976.
- [4] S. Mozia, P. Brozek, J. Przepiorski, B. Tryba, and A. W. Morawki, "Immobilized TiO<sub>2</sub> for phenol degradation in a pilot-scale photocatalytic reactor," *Journal of Nanomaterials*, vol. 2012, Article ID 949764, p. 10, 2012.
- [5] Y. Han, H.-S. Kim, and H. Kim, "Relationship between synthesis conditions and photocatalytic activity of nanocrystalline TiO<sub>2</sub>," *Journal of Nanomaterials*, vol. 2012, Article ID 427453, 10 pages, 2012.
- [6] J. Wang, J. B. Neaton, H. Zheng et al., "Epitaxial BiFeO<sub>3</sub> multiferroic thin film heterostructures," *Science*, vol. 299, no. 5613, pp. 1719–1722, 2003.
- [7] G. Catalan and J. F. Scott, "Physics and applications of bismuth ferrite," *Advanced Materials*, vol. 21, no. 24, pp. 2463–2485, 2009.
- [8] F. Gao, X. Chen, K. Yin et al., "Visible-light photocatalytic properties of weak magnetic BiFeO<sub>3</sub> nanoparticles," *Advanced Materials*, vol. 19, no. 19, pp. 2889–2892, 2007.
- [9] R. Guo, L. Fang, W. Dong, F. Zheng, and M. Shen, "Magnetically separable BiFeO<sub>3</sub> nanoparticles with a  $\gamma$ -Fe<sub>2</sub>O<sub>3</sub> parasitic phase: controlled fabrication and enhanced visible-light photocatalytic activity," *Journal of Materials Chemistry*, vol. 21, no. 46, pp. 18645–18652, 2011.
- [10] S. Li, Y.-H. Lin, B.-P. Zhang, Y. Wang, and C.-W. Nan, "Controlled fabrication of BiFeO<sub>3</sub> uniform microcrystals and their magnetic and photocatalytic behaviors," *Journal of Physical Chemistry C*, vol. 114, no. 7, pp. 2903–2908, 2010.
- [11] J. Wei, C. Zhang, and Z. Xu, "Low-temperature hydrothermal synthesis of BiFeO<sub>3</sub> microcrystals and their visible-light photocatalytic activity," *Materials Research Bulletin*, vol. 47, no. 11, pp. 3513–3517, 2012.

- [12] Y. Huo, Y. Jin, and Y. Zhang, "Citric acid assisted solvothermal synthesis of BiFeO<sub>3</sub> microspheres with high visible-light photocatalytic activity," *Journal of Molecular Catalysis A*, vol. 331, no. 1-2, pp. 15–20, 2010.
- [13] C. Reitz, C. Suchomski, C. Weidmann, and T. Brezesinski, "Block copolymer-templated BiFeO<sub>3</sub> nanoarchitectures composed of phase-pure crystallites intermingled with a continuous mesoporosity: effective visible-light photocatalysts?" *Nano Research*, vol. 4, no. 4, pp. 414–424, 2011.
- [14] K. I. Bolotin, K. J. Sikes, Z. Jiang et al., "Ultra-high electron mobility in suspended graphene," *Solid State Communications*, vol. 146, no. 9-10, pp. 351–355, 2008.
- [15] A. A. Balandin, S. Ghosh, W. Bao et al., "Superior thermal conductivity of single-layer graphene," *Nano Letters*, vol. 8, no. 3, pp. 902–907, 2008.
- [16] I. W. Frank, D. M. Tanenbaum, A. M. Van Der Zande, and P. L. McEuen, "Mechanical properties of suspended graphene sheets," *Journal of Vacuum Science and Technology B*, vol. 25, no. 6, pp. 2558–2561, 2007.
- [17] X. Liu, L. Pan, Q. Zhao et al., "UV-assisted photocatalytic synthesis of ZnO-reduced graphene oxide composites with enhanced photocatalytic activity in reduction of Cr(VI)," *Chemical Engineering Journal*, vol. 183, pp. 238–243, 2012.
- [18] H. Fan, X. Zhao, J. Yang et al., "ZnO-graphene composite for photocatalytic degradation of methylene blue dye," *Catalysis Communication*, vol. 29, pp. 29–34, 2012.
- [19] S. Liu, J. Tian, L. Wang, Y. Luo, and X. Sun, "One-pot synthesis of CuO nanoflower-decorated reduced graphene oxide and its application to photocatalytic degradation of dyes," *Catalysis Science and Technology*, vol. 2, no. 2, pp. 339–344, 2012.
- [20] S. Song, W. Gao, X. Wang et al., "Microwave-assisted synthesis of BiOBr/graphene nanocomposites and their enhanced photocatalytic activity," *Dalton Transactions*, vol. 41, no. 34, pp. 10472–10476, 2012.
- [21] G. Chen, M. Sun, Q. Wei, Y. Zhang, B. Zhu, and B. Du, "Ag<sub>3</sub>PO<sub>4</sub>/graphene-oxide composite with remarkably enhanced visible-light-driven photocatalytic activity toward dyes in water," *Journal of Hazardous Materials*, vol. 244-245, pp. 86–93, 2013.
- [22] J. An, L. Zhu, N. Wang et al., "Photo-fenton like degradation of tetrabromobisphenol A with graphene BiFeO<sub>3</sub> composite as a catalyst," *Chemical Engineering Journal*, vol. 219, pp. 225–237, 2013.
- [23] Z. Li, Y. Shen, C. Yang et al., "Significant enhancement in the visible light photocatalytic properties of BiFeO<sub>3</sub>-graphene nanohybrids," *Journal of Materials Chemistry A*, vol. 1, pp. 823–829, 2013.
- [24] J. Lin, C. Zhang, Z. Yan et al., "3-dimensional graphene carbon nanotube carpet-based microsupercapacitors with high electrochemical performance," *Nano Letters*, vol. 13, no. 1, pp. 72–78, 2013.
- [25] Z. Yan, L. Ma, Y. Zhu et al., "Three-dimensional metal-graphene-nanotube multifunctional hybrid materials," *ACS Nano*, vol. 7, no. 1, pp. 58–64, 2013.
- [26] Y. Liang, Y. Li, H. Wang et al., "Co<sub>3</sub>O<sub>4</sub> nanocrystals on graphene as a synergistic catalyst for oxygen reduction reaction," *Nature Materials*, vol. 10, no. 10, pp. 780–786, 2011.
- [27] T. Li, J. Shen, N. Li, and M. Ye, "Hydrothermal preparation, characterization and enhanced properties of reduced graphene-BiFeO<sub>3</sub> nanocomposite," *Materials Letters*, vol. 91, pp. 42–44, 2013.
- [28] V. Singh, D. Joung, L. Zhai, S. Das, S. I. Khondaker, and S. Seal, "Graphene based materials: past, present and future," *Progress in Materials Science*, vol. 56, no. 8, pp. 1178–1271, 2011.
- [29] T. Xian, H. Yang, X. Shen, J. L. Jiang, Z. Q. Wei, and W. J. Feng, "Preparation of high-quality BiFeO<sub>3</sub> nanopowders via a polyacrylamide gel route," *Journal of Alloys and Compounds*, vol. 480, no. 2, pp. 889–892, 2009.
- [30] S. R. Morrison, *Electrochemistry at Semiconductor and Oxidized Metal Electrode*, Plenum Press, New York, NY, USA, 1980.
- [31] T. Xian, H. Yang, J. Dai, Z. Wei, J. Ma, and W. Feng, "Preparation and photocatalytic performance of nano-bismuth ferrite with tunable size," *Chinese Journal of Catalysis*, vol. 32, no. 4, pp. 618–623, 2011.
- [32] H. Hotop and W. C. Lineberger, "Binding energies in atomic negative ions," *Journal of Physical and Chemical Reference Data*, vol. 4, no. 3, pp. 539–576, 1975.
- [33] T. Andersen, H. K. Haugen, and H. Hotop, "Binding energies in atomic negative ions: III," *Journal of Physical and Chemical Reference Data*, vol. 28, no. 6, pp. 1511–1533, 1999.